SAPIENZA
UNIVERSITÀ DI ROMA

DEPARTMENT OF INFORMATION ENGINEERING, ELECTRONICS AND TELECOMMUNICATIONS

PhD Course in

INFORMATION AND COMMUNICATION TECHNOLOGY

- Applied Electromagnetics -

Assessment of Antenna Parameters for Current Drive in Thermonuclear Reactors by Radio-Frequency Power

PhD Thesis

Tutor: Prof. Alessandro Galli
Ext. Tutor: Ing. Roberto Cesario
Co-tutors: Dott. E. Giovannozzi
Ing. L. Panaccione

PhD
CANDIDATE
Luca Amicucci

YEAR 2016

Synopsis

The most challenging conceptual problem of thermonuclear energy research based on deuterium plasmas magnetically trapped in toroidal machines, named *tokamaks*, consists in how to control and actively shape during operations the current density radial profile of plasma column.

To achieve this control is of paramount importance, indeed, for the following reasons:

i) to prevent the onset of unstable modes that detriment the figures of stability and fusion power gain from thermonuclear reactions, which are necessary for a reactor;

ii) to remove the obstacle of tokamaks of being intrinsically inductive machines, i.e., capable of producing only transient plasma regimes, in front of the reactor's need of operating in steady-state.

In regard to the former problem, data of modelling and experiments available in the last 25 years showed that the growth rate of pernicious unstable plasma modes, of magneto-hydro-dynamic (MHD) nature, is strongly depressed when a relative maximum of the plasma current density is suitably located at radii close to the region that interests the unstable modes. They make challenging the possibility of achieving the desired thermal insulation that is necessary for allowing thermonuclear conditions of high temperatures (~100 million of degrees) and high density (~10^{20} m^{-3}) of plasma.

The limitation of pulsed operation was, instead, well known since the assessment (half century ago) of the tokamak concept, and this was soon perceived as the major conceptual obstacle against the development of a thermonuclear fusion reactor. Indeed, at that time, the further problem of the onset of unstable modes (which produces anomalous transport effects, on heat and matter, via micro-turbulence and MHD modes) did not appear yet.

The discovery in 1981 at Princeton (USA) of the lower hybrid current drive (LHCD) effect was considered very attractive for facing both the mentioned major problems of a reactor.

The LHCD effect consists in the capability of multimegawatt microwave power at several gigahertz, coupled to quasi-electrostatic natural modes of plasma, named lower hybrid (LH) waves, of non-inductively producing current in tokamak plasma. Consequently, the plasma current can flow with continuity in a tokamak under RF power injection.

The antenna consists in phased arrays of rectangular waveguides that suitably fit the gaps of the tokamak's magnet. Via electronic setting of the waveguide phasing, the refractive index ($n_{//}$, in the direction parallel to the confinement magnetic field) of the RF power spectrum can be usefully determined in order to Landau-resonate with a tail of the electron distribution of plasma electrons, for the temperature that corresponds to the radial layer where the current drive effect would be desirably produced. As further support of attractiveness of the LHCD effect, it should be considered that other methods utilising radiofrequency power in the ion-cyclotron and electron-cyclotron resonant frequencies, as well those that exploit strong power injection of energetic ion beams, present much lower efficiency in driving plasma current than that possible by the LHCD effect.

Unfortunately, for long time the LHCD effect was observed to occur successfully only when operating at too low plasma densities – of about a factor three lower than that required by reactor – despite of the many attempts carried out for decades in many laboratories in the world. In these experiments, the RF power was however successfully coupled by the antenna, but remained unexpectedly deposited at the plasma periphery, as a consequence of parasitic effects of plasma edge.

Only recently, an original research performed in the ENEA-Frascati Lab. – whose results have been published on Nature Communications: 5,55,2010 – has assessed a new method for enabling the occurrence of the LHCD effect at reactor graded high plasma densities. This method is based on previous theoretical predictions of reduced parasitic effect under higher temperature of plasma edge (ENEA Laboratory work published on Physical Review Letters in 2004). These works demonstrated that the parasitic damping of the coupled RF power is produced by non-linear wave-plasma interaction, named parametric instability (PI), which is capable of strongly altering (namely, broadening) the $n_{//}$ spectrum launched by the antenna. Consequently, the temperature required for Landau-resonance of the RF power spectrum with plasma electrons is strongly diminished, which causes absorption in the cold region of plasma periphery.
This Thesis is focused on helping solution of an important conceptual problem, which is part of this challenge, by means of a noticeable application of strong radiofrequency power coupled to quasi-electrostatic plasma waves (LH waves).

From the engineering point of view, results produced by an originally developed numerical code (LHPI) have backed solving the problem (existing for decades) of how to enable the antenna parameters determining the deposition of the coupled RF power (of several gigahertz) at a desired radial layer of the plasma column. This task would be ideally required indeed by an antenna.

With respect to other current drive tool, based on electron cyclotron resonance (at about 150 GHz), this cannot guarantee the coverage of the outer half radius of plasma necessary for a reactor.

Thanks to results reported here, new understanding is provided that for the first time enables a waveguide antenna for current drive in tokamaks to tailor the deposition in the plasma, in different operating conditions, by electronically acting on the launched spectrum (via feeding/phasing of waveguides).

In particular,

a) in case of too high plasma densities at the plasma edge, as occurs in running experiments, operation with higher temperature of plasma is recommended to avoid parasitic effects of spectral broadening.
b) in case of too high plasma temperature at the plasma periphery, as envisaged in a future reactor, the assessment of a new antenna parameter, $\Delta n_{//}$, allows however guaranteeing useful penetration of the coupled RF power into the plasma bulk.

More specifically, the following issues have been considered in the Thesis.

1) Available data of RF power spectral broadening, kept during experiments carried out on the EAST tokamak (China), have been interpreted on the basis of the parametric instability modelling. This work has been performed thanks to a new version of a numerical code (developed on the basis of a previously version available since 1989 at ENEA-Frascati) having much improved qualities of velocity and precision.
2) The work has also focused on the key problem of how to enable the occurrence of the LHCD effect also in conditions of high electron temperature of reactor plasmas. Indeed, precisely the high temperature that in a reactor is expected to occur even at large radii of the plasma column –

which usefully prevents the occurrence of the parasitic effects observed in the experiments – would also produce an undesired RF power deposition too far out in the plasma, owing too strong electron Landau damping, as shown by numerical results. This circumstance is in contrast with the primary goal of a reactor of being equipped by current profile control, so that the too high plasma temperature of reactor represents the remaining major conceptual problem preventing the exploitation of the LHCD tool.

This problem has been solved by the new outcome described in the Thesis. This result consists in having identified in a sufficiently narrow $n_{//}$ antenna power spectrum the way for reducing the wave-plasma interaction at high temperatures, thus enabling the penetration of the coupled RF power in the hot and dense regions of reactor plasmas. This diminished wave-plasma interaction is consequence of the content of standard quasi-linear theory of plasma waves: this aspect remained singularly undisclosed so far.

3) Finally, the thesis has analysed the problem of how to design an antenna capable of producing the required power spectra necessary for envisaging a current profile control system in a thermonuclear reactor. For carrying out this work, a numerical code has been utilised capable of treating waveguide antenna geometries however complex. Consequently, the desired sufficiently narrow $n_{//}$ power spectrum can be produced, indeed, by suitable array of active and passive phased array of rectangular waveguides. Moreover, the scan of the main antenna parameters (power reflection coefficient, directivity, etc,) performed assuming realistic conditions of plasma edge, has shown that all requirements should be satisfied for envisaging a current profile control system for a tokamak reactor based on the exploitation of the LHCD effect.

The lower hybrid current drive tool in now fully supported by know how necessary for enabling the current profile control in the warm and dense plasma of thermonuclear reactor.

The current drive method assessed here is of paramount importance for conceiving antennas to be implemented in the system of current profile control, which a reactor mandatorily requires.

Chapter 1

1 Energy and environment: the major problem of humanity

We show here the background at the basis of the motivation of research on thermonuclear fusion energy, following Ref. 1. All methods at the basis of energy production are examined. In regard to nuclear fission energy, this is based on a mechanism that occurs spontaneously at normal condition of ambient. Therefore, fission has this fundamental condition in common with all mechanisms utilised so far for energy production, i.e., of being a spontaneous phenomenon that nature permits occurring on earth.

Moreover, strictly speaking, the major drive of nuclear fission is the electromagnetic potential, not the nuclear one as occurs, instead, for fusion energy. For this reason, energy from fusion should be considered the only true nuclear energy This means that humanity does not have succeeded so far in producing, and directly exploiting, the true nuclear energy: this would require to win the most ambitious challenge of science and technology that has been ever imagined. This is represented, indeed, by research on nuclear fusion energy, contrary to what generally believed that the so-called fundamental science would be the most difficult one.

1.1 Introduction

Standard of living is directly proportional to energy consumption. Energy is essential for enabling all the human activities, i.e., for producing food, heating and lighting homes, operating industrial facilities, providing public and private transportation, enabling communication, etc. Despite this recognition, much of the world is in a difficult energy situation at the moment and the problems are getting worse. To put it simply, there is a steadily increasing demand for new energy production, more than can be met in an economically feasible and environmentally friendly manner within the existing portfolio of options. Some of this demand arises from increased usage in the industrialized areas of the world such as in North America, Western Europe, and Japan. There are also major increases in demand from rapidly industrializing countries such as China and India. Virtually all projections of future energy consumption conclude that by the year 2100, world energy demand will at the very least be double of present world usage.

A crucial issue driving the supply problem concerns the environment. In particular, there is continuously increasing evidence that greenhouse gases are starting to have an observable negative impact on the environment. In the absence of the greenhouse problem, increasing the use of coal, which is available in large amount, could significantly alleviate the energy supply situation. However, if the production of greenhouse gases is to be reduced in the future, there are limits to how much energy can be generated

from the primary fossil fuels: coal, natural gas, and oil. A further complication is that, as has been well documented, the known reserves of natural gas and oil will be exhausted in decades. The position taken here is that the greenhouse effect is indeed a real issue for the environment. Consequently, in the discussion below, it is assumed that new energy production will be subject to the constraint of reducing greenhouse gas emissions.

To better understand the issues of increasing energy supply while decreasing emissions, a short description is presented hereafter of each of the major existing energy options. As might be expected, each option has both advantages and disadvantages so there is no obvious single path to the future. This is where fusion enters the picture. Its potential role in energy production is put in context by comparison with the other existing energy options. Comparisons show that fusion has many attractive features in terms of safety, fuel reserves, and minimal damage to the environment. Equally important, fusion should provide large quantities of electricity in an uninterrupted and reliable manner, thereby becoming a major contributor to the world's energy supply. These major benefits have fuelled the dreams of fusion researchers for over half a century. However, fusion also has disadvantages, the primary ones being associated with overcoming the very difficult scientific and engineering challenges that are inherent in the fusion process. Moreover, the final challenge will be to integrate the obtained solutions into an economically competitive power plant that will allow fusion to fulfil its role in world energy production.

Therefore it would not be reasonable to indicate (as instead usually done in the divulgation of this matter by official fusion sites) in the next 30 – 100 years the term for the availability the fusion energy, since the time necessary for reaching the goal should be only assessed after having solved major conceptual problems. The latter will be summarised more ahead in this thesis.

Following Refs. 1–10, it is given hereafter a comparative description of the various existing energy options and a more detailed discussion of how fusion might fit into the future energy mix.

1.2 The existing energy options

The primary natural resources used to produce energy fall into three main categories: fossil fuels, nuclear fuels, and sunlight, which is the driver for most renewables. In general these resources can be used either directly towards some desired purpose or indirectly to produce electricity, which can then be utilized in a multitude of ways. The direct uses include heating for homes, commercial buildings, and industrial facilities and as fuel for transportation. Electricity is used in manufacturing and construction, as well as home, commercial, and industrial lighting and cooling.

One issue applicable to all sources of energy is efficiency of utilization, which directly impacts fuel reserves and/or cost. Clearly high efficiency is desirable and in practical terms this translates into conservation methods. Logically, conservation should be used to the maximal extent possible to help solve the energy problem.

It is worth to consider the final uses of energy. In the year 2001 industrialized countries such as the USA apportioned about 60% of their energy to direct applications and 40% to the production of electricity. Electricity is singled out because of its high versatility and the fact that this is the main area where fusion can make a contribution.

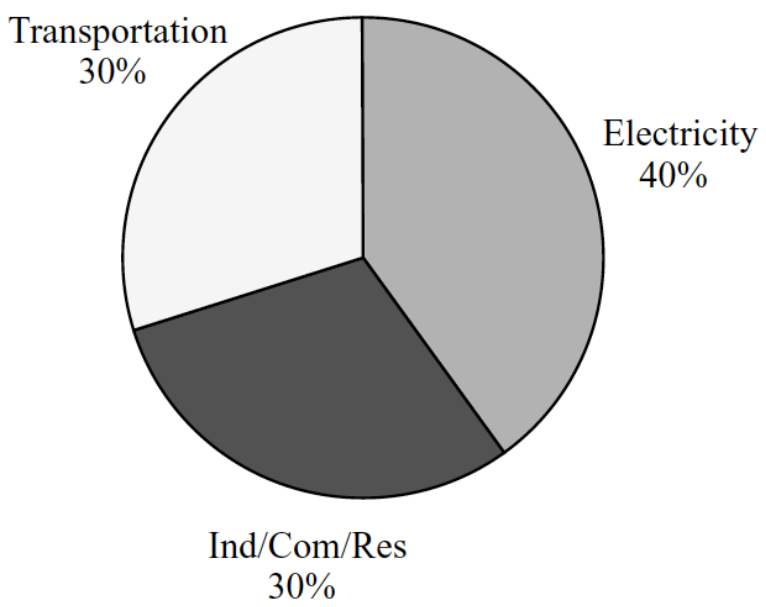

Figure 1.1 Apportionment of energy in the USA in 2001 (Annual Energy Review, 2001 Energy Information Administration, US Department of Energy).

Fossil fuels are the dominant contributor, providing about 70% of the electricity with 51% generated by coal. Nuclear, gas, and hydroelectric generation also made substantial contributions while wind, solar, and other renewable sources had very little impact (i.e. 0.4%).

In summary: *i*) most of the world's energy, including electricity, is derived from fossil fuels; *ii*) all fossil fuels produce greenhouse gases; *iii*) if greenhouse emissions are to be reduced in the future, even though energy demand is increasing, new energy capacity will have to be met by a combination of nuclear, hydroelectric, renewable (e.g. wind, solar, geothermal) sources, and conservation; *iv*) some major direct energy usages, such as heating by fossil fuels, could be replaced by electricity, although at an increased cost because of lower efficiency; *v*) transportation is a special problem because of the need for a mobile fuel. As discussed shortly electricity may be able to help here through the production of synthetic fuels, ethanol, or hydrogen, which ultimately may be used to replace gasoline and diesel fuel.

Increasing electricity production in an economic and environment-friendly way is a vital step in addressing the world's energy problems now and in the future. Fusion is one new energy source that has the potential to accomplish this mission. It would be, however, a long-term solution. In the interim, fossil fuels will remain the primary natural resources producing the world's electricity.

We describe hereafter in more detail the various existing energy options, particularly with respect to electricity, in order to put fusion in a proper context.

1.2.1 Coal

Coal is the main fossil fuel used to generate electricity (41% in the world in 2013, from: http://databank.worldbank.org/data/home.aspx). One major advantage of coal is that there are substantial reserves in many countries, capable of supplying the world with electricity at the current usage rate for hundreds of years. If fuel availability were the only energy issue, coal would be the solution for the foreseeable future. However, when environmental concerns are considered, coal becomes less desirable. Coal provides continuous, non-stop electricity by means of large, remotely located power plants. This vital non-stop property is known as "base load" electricity. For reference, note that a large power plant typically produces 1 GW of power, capable of supporting a city with a population of about 250 000 people. Two other important advantages of coal are that it is a well-developed technology and

that it is among the lowest-cost producers of electricity.

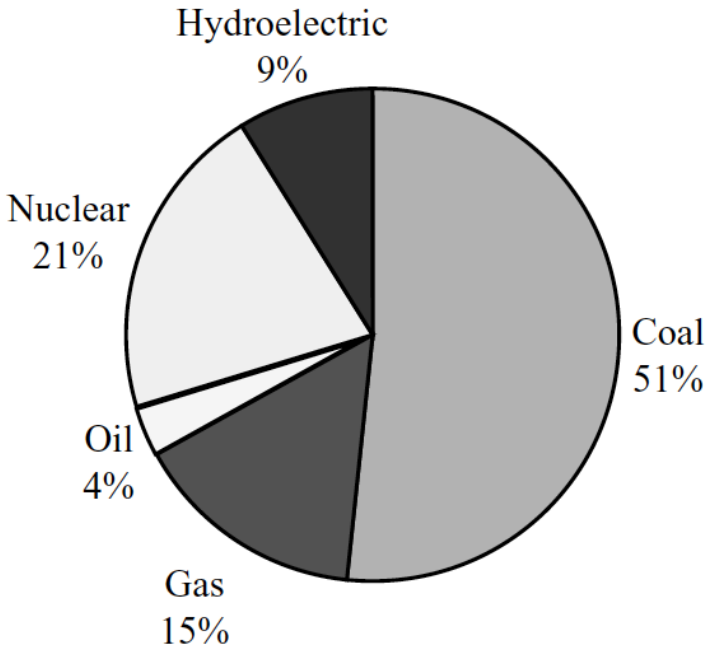

Figure 1.2 Breakdown of fuel consumption to generate electricity in the USA in 2001 (Annual Energy Review, 2001, Energy Information Administration, US Department of Energy).

Consider next the efficiency of converting coal to electricity. Burning any fossil fuel (i.e., coal, natural gas, or oil) is a chemical process whose main output is heat. A heat exchanger converts water to steam, which then drives a steam turbine connected to an electric generator, thereby producing electricity. The laws of thermodynamics imply that for reasonable operating temperatures, the maximum overall efficiency for converting heat to electricity is about 35–40%. More heat is lost out of the smokestack than the one converted to electricity. This unpleasant consequence is unavoidable and occurs whenever a steam cycle is used to produce electricity, as it is for coal and nuclear systems.

Resource	Energy reserves (Quads)	Total usage (y)	Self-usage (y)
Coal	10^5	200	900
Oil	10^4	20	60
Natural gas	10^4	20	100
U235 (standard)	10^4	20	300
U238, Th232 (breeder)	10^7	20 000	
Fusion (D–T)	10^7	20 000	
Fusion (D–D)	10^{12}	2×10^9	

Table 1.1. Estimate of energy reserves for various primary fuels. The total usage assumes that the source is used to supply the entire world's energy at a rate of 500 Quads per year (slightly higher than the 2001 rate). The self-usage assumes that each source is used to supply energy at its own individual 2001 usage rate. Also 1 Quad ≈ 1018 joules.

The main disadvantage of fossil fuel combustion is of environmental nature. Burning any fossil fuels leads to the unavoidable generation of carbon dioxide (CO2), which is largely responsible for the greenhouse effect. There are also several coal-specific environmental disadvantages. Because of impurities, when coal is burned it also releases fly ash (largely calcium carbonate), sulphur dioxide, nitrous oxide, and oxides of mercury, all of which are harmful to health. These emissions can be reduced, although not completely eliminated, by electrostatic precipitators and scrubbers. However, this increases the cost of electricity.

In summary, one can see that coal has both advantages (fuel reserves and cost) and disadvantages (greenhouse gases and emissions). Because of its advantages, and because there are no obviously superior alternatives, coal will remain a major contributor to electricity production for many years to come.

1.2.2 Natural gas

Natural gas is a fossil fuel that consists mainly of methane (CH_4). It is widely used to heat homes, commercial buildings, and industrial plants, as well as to produce electricity.

About 22% of the electricity produced in the world in 2013 is derived from natural gas (from: http://databank.worldbank.org/data/home.aspx).

The amount of liquefied natural gas required to power Boston for one year is comparable in volume to that of coal. With respect to coal, natural gas has both advantages (cleanest burning of any fossil fuel and low short-term cost) and disadvantages (greenhouse gases, limited reserves, and poor allocation of resources).

Overall, short-term financial incentives dominate the trade-offs and will likely lead to the continued use of natural gas for electricity production.

1.2.3 Oil

The production of electricity by oil in the world is about 4% in 2013 (in 1970-1980 it was 20%). Oil is the last of the fossil fuels to be discussed. It is an excellent fuel for transportation because of its portability and its large energy content. It is also the fuel of choice for heating when natural gas is not available. A large amount (i.e., 35%) of the energy used in the world is derived from oil, with much of it devoted to transportation usage. It is rarely used to directly produce electricity. As a measure of energy content note that 1 litre container filled with gasoline is capable of moving a typical automobile 10–20 km, indeed an impressive feat. Furthermore the total weight of a fully loaded 60 litres fuel tank is only about 60 Kg, a negligible fraction of the total weight of the automobile. A full tank can therefore efficiently move an automobile about 600– 1000 km, again, a truly impressive feat.

The second issue of interest is the cost of gasoline. It is surprisingly inexpensive compared to many other common liquids. Generally, the untaxed price per litre of gasoline is still less than that of bottled water. Gasoline would appear to be a bargain, even at present higher prices.

Nevertheless, there are disadvantages to the use of gasoline for transportation. First, since gasoline is a fossil fuel it produces a large amount of greenhouse gases, comparable in total magnitude to that of coal. Second, crude oil is only readily available in a few areas of the world. One major source is the Middle East, which is fraught with political instability. Third, the reserves of oil are much less than those of coal, on the order of several decades at present usage rates. The competition for oil between developing countries will likely increase in the future, raising costs and perhaps limiting supplies.

Are there ways to decrease the world's dependency on oil? There are possibilities, but they are not easy. Consuming less oil by using hybrid vehicles could make an important contribution and may be accepted by the public even though it raises the initial cost of an automobile. Consuming less oil by driving smaller automobiles with improved fuel efficiency could also make a large contribution, although many may be reluctant to follow this path, viewing it as a lowering of standard of living.

A different approach is based on the fact that gasoline can be produced from coal tars and oil shale, of which there are large reserves. The end product is known as "synfuel," but at present the process is not economical. Also since synfuel is a form of fossil fuel, the production of greenhouse gases still remains an important environmental problem.

Another approach is to use non-petroleum fuels produced by bioconversion. One method currently in limited use is the conversion of corn to ethanol, a type of alcohol. Although ethanol is a plausibly efficient replacement for gasoline, the costs of production are not. Large amounts of land are required and considerable energy must be expended to produce the ethanol, comparable to and sometimes exceeding the energy content of the final fuel itself.

There has also been considerable interest and publicity in developing the technology of using hydrogen in conjunction with fuel cells to produce a fully electric car, thus completely replacing the need for gasoline. Hydrogen has the advantages of: *i*) large reserve of primary fuel (e.g. water), *ii*) a high conversion efficiency from fuel to electric power, and, *iii*) most importantly the end product of the process is harmless water vapour rather than CO_2.

This may be the ultimate transportation solution but there are two quite difficult challenges to overcome.

First hydrogen itself is not a primary fuel. It must be produced separately, for instance by electrolysis, and this requires substantial energy. If the energy for the electrolysis of water is derived from fossil fuels much of the gain in reduced CO_2 emissions is cancelled. Second, the energy content of hydrogen at atmospheric pressure, including its higher conversion efficiency, is still much lower than that of gasoline, by a factor of about 1200. Therefore, to increase the energy content of hydrogen fuel to a value comparable to gasoline, the hydrogen must be compressed to the very high pressure of 1200 atm. This poses a very difficult fuel tank design problem for on-board storage of hydrogen. Another option is to store the hydrogen in liquid form, but this requires a costly on-board cryogenic system.

A third option is to develop room-temperature compounds that are capable of storing and rapidly cycling large quantities of hydrogen. The development of such compounds is a topic of current research, but success is still a long way into the future. One sees that the on-board storage of high-density hydrogen presents a difficult technological challenge.

In summary, there is no simple, short-term, attractive alternative to gasoline for transportation. Synthetic fuel, ethanol, and hydrogen are possible long-term solutions, but each has a mixture of unfavourable economic, energy balance, and environmental problems. Providing the energy to produce hydrogen or ethanol by CO_2-free electricity (e.g. by nuclear power) would be a big help but would not solve the other problems. In the short term the best strategy may be to increase the use of hybrid vehicles and to evolve towards smaller, more fuel efficient automobiles.

1.2.4 Nuclear power

The primary use of nuclear power is the large-scale generation of base load electricity by the fissioning (i.e., splitting) of the uranium isotope U_{235}. Although there is still public concern about the use of nuclear power, a more careful analysis shows that this form of energy is considerably more desirable than is currently perceived and will likely be one of the main practical solutions for the future production of CO_2 free electricity.

There are several comparisons with fossil fuel plants that show why nuclear power has received so much attention as a source of electricity. The first involves the energy content of the fuel. A nuclear reaction produces on the order of one million times more energy per elementary particle than a fossil fuel chemical reaction. The implication is that much less nuclear fuel is required to produce a given amount of energy. Specifically, the total volume of nuclear fuel rods needed to power Boston for one year would just about fit in the back of a pickup truck. This should be compared to the football stadium required for fossil fuels.

A second point of comparison is environmental impact. Nuclear power plants produce neither CO_2 nor other harmful emissions. This is a major environmental advantage.

Another issue is safety. Despite public concern, the actual safety record of nuclear power is nothing less than phenomenal. No single nuclear worker or civilian has ever lost his or her life because of a radiation accident in a nuclear power plant built in the Western world. The worst accident in a USA plant occurred at Three Mile Island. This was a financial disaster for the power company but only a negligible amount of radiation was released to the environment. The reason is that Western nuclear power plants are designed with many overlapping layers of safety to provide *defence in depth* culminating with a huge, steel reinforced containment vessel around the reactor to protect the public in case of a *worst* accident. The large loss of life and wide environmental damage resulting from the Chernobyl accident occurred because there was no containment vessel around the reactor.

Such a design would never be licensed to operate as a nuclear power plant in the West. Overall, safety is always a major concern in the design and operation of nuclear power plants, but the record shows that for Western power plants the problems are well under control.

Consider next the issue of fuel reserves. This is a complex issue. In the simplest view one can assume that U_{235} is the basic fuel and once most of it has been consumed in the reactor, the resulting “spent fuel” rods are buried in a permanent, non-retrievable repository. In this scenario there is enough U235 to provide electricity at the present rate for several hundred years. On the other hand the spent fuel rods contain substantial amounts of plutonium, which can be chemically extracted and then used as a new nuclear fuel. In fact, it is possible to use the resulting plutonium in such a way that it actually breeds more plutonium than is being consumed. The use of such “breeder” reactors extends the reserves of nuclear fuels to many

thousands of years. Breeders are more expensive than conventional nuclear plants and are not currently used because of the ready availability of low cost U_{235}. However, in the long term breeders may be one of the energy sources of choice.

Nuclear waste and how to dispose of it is another important issue. Here, too, there are subtleties. One point is that many of the radioactive fission products have reasonably short half-lives, on the order of 30 years or less. They need to be stored for about a century during which time they self-destruct by radioactive decay into a harmless form, an ideal end result. It is the long-lived, multi-thousand year wastes that receive much public attention and scrutiny. Several possible solutions have received serious consideration. The waste can be dissolved in glass (i.e., vitrification) and permanently stored. The fuel can be chemically reprocessed for re-use in regular or breeder reactors, thereby transforming much of the long-lived waste into useful electricity. Third, there are techniques that, while currently expensive, transmute long-lived, non-fissioning radioactive waste by products into harmless elements.

Also, a critical point is that the total volume of nuclear waste is very small. The total nuclear "rubbish" resulting from powering Boston for one year would fill up only a small fraction of a pickup truck. The conclusion is that there are a variety of technological solutions to the waste disposal problem. The main problems are more political than technological.

The last issue of importance is nuclear proliferation, which concerns the possibility that unstable governments or terrorist groups would gain access to nuclear weapons. At first glance one might conclude that reducing the use of nuclear power would obviously reduce the risks of proliferation. This is an incorrect conclusion. The key technical point to recognize is that the spent fuel from a reactor cannot be directly utilized to make a weapon because of the low concentration of fissionable material. Nevertheless, spent fuel is often reprocessed to make new fuel for use in nuclear reactors thereby increasing the fuel reserves as previously discussed. However, one intermediate step in reprocessing is the production of nearly pure plutonium, which at this point could be diverted for use as weapons. A major component of an effective non-proliferation plan should thus involve the detection and prevention of the diversion of plutonium for weapons use by unstable governments. In implementing such a plan two facts should be noted: reprocessing may have valuable energy and economic benefits, and reprocessing technology, while very expensive, is reasonably well established. Consequently any nation can justify the construction of a reprocessing facility based on energy needs, thereby opening up the possibility of a surreptitious diversion of a small amount of plutonium for use in weapons.

One approach might be for the major, stable nuclear powers in the world to carry out all the reprocessing in their own countries, and then sell the resulting fuel to smaller countries with legitimate energy needs.

The reality is that reprocessing has expanded in other countries to fill the gap suggesting that USA policy may have made the non-proliferation situation worse rather than better.

Therefore, nuclear non-proliferation is a very serious and important problem that must be addressed. Moreover, whether or not stable countries like the USA build more nuclear power plants will have little if any direct effect on non-proliferation and may actually divert attention away from the real issues.

To summarize, nuclear power has many underappreciated advantages as well as some disadvantages. Even some well-known environmentalists have started to support nuclear power as the only viable option for producing large quantities of CO2 free electricity. A short-term stumbling block to the construction of new nuclear power plants is the fact that while fuel costs are low, the capital costs are high because of

the complexity of the reactor. In a deregulated market this is a disincentive to new investment.

1.2.5 Hydroelectric power

Hydroelectric power is a widely used renewable source of energy. It provides 16% of the world's energy (20% in 1970–1980). The idea behind hydroelectric power is conceptually simple. At a geographically and technologically appropriate location along the path of a river, a dam is built creating a huge reservoir lake on the high side of the dam. As reservoir water pours over the dam because of gravity, it turns a turbine, which then drives an electric generator, producing electricity.

Hydroelectric power has many attractive advantages. First, no CO_2 or other serious pollutants are generated during the production of electricity. Second, large amounts of power are generated in a hydroelectric plant, comparable to that in a coal or nuclear plant. Third, the conversion efficiency of fluid kinetic energy to electricity is high since no thermal steam cycle is involved. Fourth, except in rare cases of extended drought, the power is available continuously for base load electricity. Fifth, the cost of electricity is low, typically comparable to that of coal plants. Sixth, and most importantly, the fuel reserves are effectively infinite. Hydroelectric power is clearly a renewable energy source.

There are two downsides to hydroelectric power. First, most of the suitable rivers already have dams. Therefore, expansion of hydroelectric power is difficult since there are few, if any, unutilized technologically attractive sites available. Second, although not a major problem for early dams, environmental issues will have a much larger impact on any future hydroelectric plants. The main issue is the large amount of land that is flooded to form the reservoir lake. Often this land could be used for agricultural or recreational purposes, so there is a trade-off that must be evaluated before changing its use to electricity production.

Overall, hydroelectric power will continue to make an important contribution to the supply of electricity although the possibilities for expansion are limited.

1.2.6 Wind power

Wind is another renewable energy source that has received much attention in recent years. Even so, it currently provides a negligible fraction of electricity in the world. Wind should almost certainly be used more than it is at present but for fundamental technological reasons it will not be the ultimate solution to the electricity generation problem.

The idea behind wind power is conceptually easy to understand. Wind striking the blades of a large windmill causes them to rotate. This rotational kinetic energy, by a series of gears, drives an electric generator producing electricity.

Wind has some important advantages. First, wind power is clearly a renewable energy source. Second, it produces electricity in a very clean manner. There is no CO_2 and there are no other harmful pollutants. Third, no steam cycle is involved. Therefore the conversion from wind kinetic energy to electricity is reasonably efficient. Fourth, although the cost of wind power, for reasons described below, is higher than for existing coal plants, it is still within a tolerable range. This is particularly true if one were to add in the additional, often hidden, environmental costs of fossil fuel plants.

There are, however, some disadvantages to wind power. First, the wind does not blow at a constant rate. If it is too weak, not much power is produced. If it is too strong, the blades must turn parallel to the wind to prevent them from spinning too fast and causing mechanical damage. Here too, not much power is produced. On average, a large, modern windmill produces about 35% of its maximum rated power. Much of the gain of not requiring a steam cycle is cancelled by the variability of the wind speed.

Second, the 35% availability factor implies that to produce an average of 1 GW of power requires a wind farm whose total power rating is about 3 GW. The problem is that the excess power produced during optimal wind conditions is very difficult and very expensive to store for use during poor wind conditions.

A third disadvantage is that the power intensity of the wind is very low as compared for instance to that in the centre of a coal furnace. Therefore producing a significant amount of power requires a large number of windmills spread over a large area. For instance, a modern wind farm, with an optimistic 40% availability factor would need to consist of about 56000 windmills occupying about 14000 square kilometres to produce the 35 GW required to power Rome.

Lastly, there are several environmental issues to consider. Windmills tend to be noisy and harmful to birds. There is also the issue of aesthetics. Engineers may find beauty in modern windmills, but the general public tends to view them as unattractive eyesores. Also they are quite large, with mounting towers on the order of 100 m and blades about 50 m in length.

This discussion suggests that wind power faces some extremely difficult challenges if it is ultimately to replace coal as a major source of electricity. A perhaps better role for wind is as a topping source of power, helping to meet peak demand during critical parts of the day and during the more extreme seasons of summer and winter. In this role wind might ultimately provide up to 20% of electricity. It could not provide more because the large fluctuations in wind speed and resulting wind power would likely cause instabilities on the national transmission grid.

1.2.7 Solar power

The last renewable source discussed is solar energy. As with wind, the threshold of 1% amount of world electricity has been presently exceeded for production derived from solar power. Nevertheless, solar power is often projected to be a potentially attractive alternative to fossil fuels. There are a number of special applications where solar power can be attractive, but for fundamental technological reasons it is unlikely that it will be the ultimate solution for the world's electricity problems.

Understanding how the sun is used to produce electricity involves a detailed knowledge of quantum mechanics and semiconductor theory and is beyond the scope of this book. For present purposes, assume that a carefully designed solar cell converts the sun's energy directly into electricity with a daylight-averaged efficiency of about 10%. There are two main advantages of producing electricity from the sun. First, the source of energy is clearly renewable and free. Second, neither CO_2 nor other harmful emissions are produced during the energy conversion process. In this sense solar power is very attractive from an environmental point of view.

The disadvantages of solar energy are similar to those of wind. First, the sun obviously shines brightly only during periods of cloud-free daytime. Consequently, producing base load power is not possible since there is no simple way to store excess energy during the day for use at night. Second, the sun's intensity is very low compared to that in a coal furnace. Therefore a large area of solar cells is required to produce a

significant amount of power. For example, an area of about 2000 square kilometres would have to be covered by solar panels to provide the 35 GW required by Rome. i.e., 10 % of the surface of Lazio.

Lastly, solar electricity is inherently expensive. The reason is that a truly large quantity of manufactured material is required to cover a whole city area. The cost of mining, transporting, and manufacturing this material is large and unavoidable.

The conclusion is that solar power faces some very difficult challenges if it were to be used to produce large quantities of electricity. There are other more attractive uses, such as for residential and some commercial heating. Here its contributions can be substantial and should be encouraged.

1.2.8 Conservation

Conservation can be defined as the more efficient use of our existing natural resources.

Clearly maximizing conservation is an important and worthwhile contribution to help alleviate existing and future energy problems. There are two ways that conservation can be implemented, one of which has a good chance of acceptance by the public respect to the other one, which is on much shakier ground. Although both approaches conserve energy, a clear line in the sand separates them. The attractive approach takes advantage of advances in technology to conserve fuel while maintaining performance in appliances, automobiles, and other equipment used in daily living. Examples of this approach include hybrid automobiles, more efficient appliances, additional insulation for older homes, etc.

The second and more difficult approach to conservation requires that citizens directly reduce their use of energy in certain aspects of their daily living. Often this is viewed as a reduction in standard of living. The public is in general much more reluctant to give up something to which they are already accustomed. Examples of this approach to conservation include smaller more gasoline efficient automobiles, smaller houses, increased used of public transportation, less use of air conditioning in summer, lower thermostat settings in the winter, etc.

With the continually increasing demand for new electricity, particularly by some of the developing nations, it is difficult to imagine that conservation can completely solve the world's future electricity generation problems. Nevertheless, it can reduce the magnitude of the problems. This would afford the nations of the world more time to develop and transition to new alternatives.

1.2.9 Summary on the available energy sources

The discussion in this section has shown that there are difficult energy problems facing the world that will probably become worse in the future. There is no obvious, single solution. Each of the existing energy options faces a mixture of difficult issues including limited reserves, CO_2 production, toxic emissions, waste disposal, excessive land usage, and high costs. In the end energy will be provided by a portfolio of options, hopefully chosen by logic rather than by crisis. One possible new addition to the portfolio that can potentially have a large impact is fusion, which is the next topic for discussion.

1.3 The role of fusion energy

Fusion is a form of nuclear energy. Its main application is the production of electricity in large base load power plants. The basic nuclear processes involved occur at the opposite end of the spectrum of atomic masses than fission. Specifically, fission involves the splitting of heavy nuclei such as U_{235}. Fusion involves the merging (i.e., the fusing) of light elements, mainly hydrogen (H) and its isotopes deuterium (D) and tritium (T). The fusion of hydrogen is the main reaction that powers the sun.

There are three main advantages of fusion power: fuel reserves, environmental impact, and safety. Consider first fuel reserves. There are two main reactions of interest that occur at a fast enough rate to produce electricity. These involve pure deuterium and an equal mix of deuterium and tritium. Deuterium occurs naturally in ocean water. There is 1 atom of deuterium for every 6700 atoms of hydrogen. Also deuterium can be easily extracted at a very low cost. If all the deuterium in the ocean were used to power fusion reactors utilizing a standard steam cycle there would be enough energy generated to power the earth for about 2 billion years at the present rate of total world energy consumption! Also, since fusion is a nuclear process, it would take only about five pickup trucks full of deuterium laced ocean water (HDO rather than H_2O) to power Rome for a year.

The deuterium–tritium (D–T) reaction produces more energy than a pure deuterium (D– D) reaction. However, the main advantage is that D–T reactions occur at a faster rate, thereby making it easier to build such a reactor. Consequently, all first generation fusion reactors will use D–T. In terms of reserves, the multi-billion years of deuterium applies to D–T as well as D–D reactors. However, since tritium is a radioactive isotope with a half-life of only about 12 years, there is no natural tritium to be found on earth. Instead, tritium is obtained by breeding with the lithium isotope Li^6, which is one of the components in the fusion blanket.

The overall reserves for D–T fusion are thus limited by the reserves of Li^6. Geological estimates indicate that there is on the order of 20 000 years of inexpensive Li^6 available on earth (assuming total world energy consumption at the present rate). Presumably, well before Li^6 is exhausted, the science and technology will have been developed to switch to D–D reactors.

The next advantage is the environmental impact of fusion. Fusion reactions produce no CO_2 or other greenhouse emissions. Fusion reactions also do not emit any other harmful chemicals into the atmosphere. The main end product of the fusion reaction is the harmless, inert gas helium. The biggest environmental issue in fusion is that one product of both the D–D and the D–T reaction is a high-energy neutron. These neutrons are captured in the fusion blanket so they pose no threat to the public. However, as they pass through structural material on their way to the blanket, the neutrons cause the structure to become activated.

Even so, this radioactive structural material has a short half-life so that the storage time required once it is removed is also short, on the order of 100 years. Overall, when one considers the entire environmental situation, fusion is a very attractive option with respect to fossil, nuclear, and renewable sources.

The last major advantage involves safety. Here, since fusion is a nuclear process, one is concerned about the possibility of a radioactive meltdown such as occurred in the Three Mile Island accident. The basic laws of physics governing fusion reactions make this impossible. Specifically, in a fission reactor the entire energy content corresponding to several years of power production is stored within the reactor core at

any instant of time. It is this huge energy content that makes a meltdown possible. A fusion reactor does not depend on maintaining a chain reaction in a large sitting mass of fuel. Instead, fuel must be constantly fed into the reactor at a rate allowing it to be consumed as needed. The end result is that at any instant of time the mass of fuel in a fusion reactor is very small, perhaps corresponding to the weight of several postage stamps. It is this small instantaneous mass of fuel that makes a meltdown impossible in a fusion reactor.

The conclusion from this discussion is that the potential advantages of fusion from the point of view of fuel reserves, environmental impact, and safety are indeed impressive.

As one might expect there are also several disadvantages to fusion that must be considered. These involve scientific challenges, technological challenges, and economics. The key issues are as follows.

The science of fusion is quite complex. Specifically, to burn D–T one is required to heat the fuel to the astounding temperature of 150×10^6 ^{o}K, hotter than the centre of the sun. At even much lower temperatures the fuel is fully ionized becoming plasma, a high-temperature collection of independently moving electrons and ions dominated by electromagnetic forces. Once heated some method must be devised to hold the plasma together. The primary method requires a clever configuration of magnetic fields, an admittedly nebulous idea to those unfamiliar with the science of plasma physics. Cleverness is mandatory, not an option. Too simple a configuration allows the plasma to be lost at a rapid rate, thus quenching fusion reactions before sufficient energy can be produced. Even with a clever configuration there are limits to the plasma pressure that can be confined without rapid losses through the magnetic field.

The combined requirement of confining a sufficient quantity of plasma for a sufficiently long time at a sufficiently high temperature to make net fusion power has been the focus of the world's fusion research program for the past 50 years. Unexpected difficulty of these scientific challenges represents the primary reason it has taking so long to achieve a net power producing fusion reactor.

There are also engineering challenges as well, which many believe are of comparable difficulty to those of scientific nature. First, improved low-activation materials need to be developed that can withstand the neutron and heat loads generated by the fusion plasma. Second, large high-field, high-current superconducting magnets need to be developed to confine the plasma. Superconducting magnets on the scale required for fusion have not yet been built. Third, new technologies to provide heating power have to be developed in order to raise the plasma temperature to the enormously high values required for fusion. This involves a wide variety of techniques ranging from very high-power neutral beams to millimetre wavelength megawatt microwave sources. Clearly a major research and development program is required to make fusion a reality.

The last disadvantage is economics. A fusion reactor is inherently a complex facility. It includes a fuel chamber, a blanket, and a complicated set of superconducting magnets. Also, since the structural material becomes activated, a large remote handling system is required for assembly and disassembly during regular maintenance. The use of tritium plus the structural activation mean that radiation protection is also required. These basic technological requirements imply that the capital cost of a fusion reactor will be larger than that of a fossil fuel power plant, and very likely also that of a fission power plant. This will tend to raise the cost of electricity to consumers. Balancing this are low fuel costs and low costs to protect the environment, both of which tend to reduce the cost of electricity to consumers.

It is clearly difficult to predict the cost of fusion energy as compared to other options 30–50 years in the future. One main complication is that a combination of fuel reserve problems and environmental remediation costs will likely increase the costs of these other options so that comparisons involve a number of simultaneously moving targets. Estimates of future fusion energy costs are in the vicinity of the other options, but because the uncertainties are large, they should be viewed with caution. The main value of these estimates is to show that it makes sense to continue fusion research. Fusion should not be eliminated because of an inherently absurd cost of electricity, nor will it be "too cheap to meter" as one might have hoped in the past.

1.4 Fission and fusion for energy

1.4.1 Fission

The usual method of producing fission energy is to bombard an atom of $_{92}U^{235}$, a relatively rare isotope of uranium, with a slow neutron (i.e., a neutron whose energy is approximately equivalent to room temperature: 0.025 eV). This process has two major advantages with respect to the production of energy, which can be understood by examining a typical fission reaction. Note that there are many different ways in which $_{92}U^{235}$ can be split and the reaction given below is typical in terms of the end products and the energy release:

$$_0n^1 + {}_{92}U^{235} \rightarrow {}_{54}Xe^{140} + {}_{38}Sr^{94} + 2({}_0n^1) + E$$

In this reaction the xenon and strontium are themselves unstable isotopes and in about two weeks decay to stable elements via several beta emissions. The final reaction becomes

$$_0n^1 + {}_{92}U^{235} \rightarrow {}_{58}Ce^{140} + {}_{40}Zr^{94} + 2({}_0n^1) + 6e- + E$$

The energy E released can be easily determined from a standard table of nuclear data. The total mass of the initial and final elements is found to be 236.053 u and 235.832 u respectively. Here, u = 1.660566 $x10^{-27}$ kg is the atomic mass unit. Using Einstein's relation, this translates into E = 206 MeV per nuclear reaction or 0.88 MeV per nucleon of $_{92}U^{235}$. Macroscopically the energy released is equivalent to $84x10^6$ MJ/kg representing an enormous gain of over one million compared to the burning of gasoline.

The three reasons why this powerful fission reaction can be converted into a practical method for producing electricity can now be identified. First, while it takes only one neutron to initiate a fission reaction the end products contain two neutrons. Actually, when averaged over all possible fission reactions, the average number of neutrons produced is slightly higher, approximately 2.4 per reaction. This neutron multiplication allows the build up of a chain reaction, which has the advantage of making a fission reactor self-sustaining for several years before the fuel has to be replaced. All that is required is a sufficient mass of fuel to minimize the loss of neutrons.

The second reason is associated with the fact that fission reactions are initiated by an electrically neutral particle, the neutron. This is important because a neutron can easily penetrate the electron cloud surrounding the atom and gain close proximity to the nucleus itself. The electromagnetic Coulomb force of the nucleus has no impact on the neutron and cannot repel it from the nuclear interaction region. The result is that it is relatively easy for low-energy neutrons to produce fission reactions with $_{92}U^{235}$, a

definite advantage in terms of energy balance, economics, and the ability to operate the reactor in a regime where the temperature is low enough that the fuel remains a solid.

Therefore, very importantly, the chain fission mechanism occurs spontaneously at normal condition of ambient, as occurs with other mechanisms at the basis of the energy production today, which are all spontaneous phenomena, permitted by nature on earth.

These reasons are why fission reactions are an effective means of producing nuclear energy for the practical production of electricity. However, strictly speaking, the major drive of nuclear fission is not nuclear but electromagnetic potential, as occurs instead in fusion, which should be considered the only true nuclear energy.

1.4.2 Fusion

Neutron initiated nuclear reactions in light elements cannot occur spontaneously, since they require some energy to be inputted in the process. (Indeed: ${}_0n^1 + {}_1H^2 \rightarrow {}_1H^1 + 2({}_0n^1) + E$. This reaction leads to the desired neutron multiplication. However, the energy released show that $E = -2.23$ MeV).

The D–T reaction involves the fusion of a deuterium nucleus with a tritium nucleus. It is the easiest of all the fusion reactions to initiate (although its initiation is still much more difficult than that of ${}_{92}U^{235}$ fission reactions). In terms of energy desirability issues, D–T reactions produce large numbers of neutrons and require a supply of tritium in order to be capable of continuous operation, but there is no natural tritium on earth. Furthermore, the tritium is radioactive with a half-life of 12.26 years. The D–T reaction, nevertheless, produces a significant amount of nuclear energy. It can be written as:

$D + T \rightarrow \alpha + n + 17.6MeV$

This corresponds to 3.52 MeV per nucleon and is macroscopically equivalent to 338×10^6 MJ/kg. In spite of the problems associated with tritium and neutrons, the D–T reaction is the central focus of worldwide fusion research, a choice dominated by the fact that it is the easiest fusion reaction to initiate.

Having made this choice how does one deal with the tritium and neutron problems? Many years of fission research have taught nuclear engineers how to handle material activation and radiation damage resulting from high-energy neutrons. The same holds true for radioactivity associated with tritium. The solutions are far from simple but they are by now well established.

The one outstanding problem is the tritium supply. The solution is to breed tritium in the blanket surrounding the region of D–T fusion reactions. The chemical element that is most favourable for breeding tritium is lithium. The nuclear reactions of primary interest are:

${}_3Li^6 + n(slow) \rightarrow \alpha + T + 4.8MeV,$

${}_3Li^7 + n(fast) \rightarrow T + \alpha + n - 2.5MeV.$

Both reactions produce tritium although the first reaction generates energy while the second one consumes energy. Also natural lithium comprises 7.4% ${}_3Li^6$ and 92.6% ${}_3Li^7$. Even though there is a much larger fraction of ${}_3Li^7$, nuclear data show that the ${}_3Li^6$ reaction is much easier to initiate and as a result it is this reaction that dominates in the breeding of tritium.

With respect to the $_3Li^6$ reaction, if there were no loss of neutrons, then each n consumed in fusion would produce one new T by breeding with the fusion produced neutron: the breeding ratio would be 1.00. In a practical reactor, however, there are always some unavoidable neutron losses. Thus, some form of neutron multiplication is required. Also needed is a method of slowing down the high-energy fusion neutrons since the reaction is most easily initiated with slow, low-energy neutrons.

For present purposes one should assume that the issues have been satisfactorily resolved. Consequently, breeding T from $_3Li^6$ solves the problem of sustaining the tritium supply, assuming adequate supplies of lithium are available. The known reserves of lithium are sufficiently large to last thousands of years so fuel availability is not a problem. On the longer time scale, the goal would be to develop D–D fusion reactors.

The large amounts of energy released in fusion reactions appear in the form of kinetic energy of the end products. It is important, particularly for the D–T reaction where one end product is electrically charged and the other is not, to determine how the energy is apportioned between the two end products. The apportionment can be easily determined by making use of the well-satisfied assumption that the energy and momentum of each end product far exceeds that of the initial fusing nuclei.

The end products consist of an alpha particle and a neutron with $m_\alpha / m_n = 4$. Thus the kinetic energy of the alpha particle is equal to (1/5) E = 3.5 MeV while that of the neutron is equal to (4/5)E = 14.1 MeV. The neutron energy is four times larger than that of the alpha particle. One can then rewrite the D–T fusion reaction in the slightly more convenient form:

$D + T \rightarrow \alpha(3.5\ MeV) + n(14.1\ MeV)$

We provide here a physical explanation of the observation that nuclear reactions are most readily initiated for either heavy elements (i.e., fission) or light elements (i.e., fusion) but not with intermediate elements. The explanation is presented in two parts.

First, an examination of the curve of binding energy vs. atomic mass, as obtained from experimental measurements, shows that the binding forces holding the nuclei of either light or heavy elements together are weaker than those of intermediate elements. This is the basic explanation of why it is easier to initiate nuclear reactions with elements at the extreme ends of atomic mass. Having established this conclusion, one can then address the second part of the explanation, which is concerned with why the binding energy curve actually has the shape it does. It is shown that the shape arises from a geometric competition between the strong short-range nuclear force and the weak long-range Coulomb force.

Consider a primary chemical element whose nucleus contains N neutrons and Z protons. Note that the integer sum $N + Z$ is very nearly, but not exactly, equal to the actual experimentally measured mass number A: $N + Z \approx A$, where $m_A = A\ u$ is the nuclear mass. A comparison of the actual nuclear mass with the total mass of the isolated individual particles making up the nucleus shows that

$$Nm_n + Zm_p > m_A$$

The difference in mass can be thought of as being converted into binding energy to hold the nucleus together. Specifically, the binding energy is defined as

$$E_B \equiv (Nm_n + Zm_p - m_A)c^2$$

An amount of energy equal to EB would have to be added to the nucleus to break it apart into its separate components. A somewhat more convenient quantity is the binding energy per nucleon, defined as E_B/A.

This quantity is a measure of the average energy binding each nucleon to the nucleus.

The shape of the binding energy curve is a consequence of a competition between the strong short-range

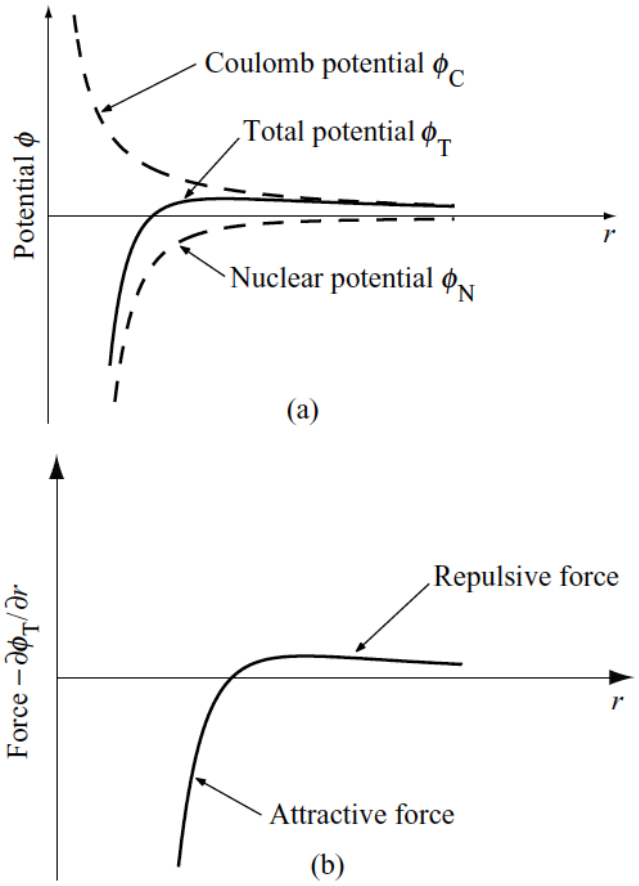

Figure 1.3. (a) The Coulomb, nuclear, and total potentials as functions of radius, and (b) the corresponding total force $F = -\partial\phi_T/\partial r$ as a function of radius.

nuclear force and the weak long-range Coulomb force. Schematic diagrams of the combined nuclear and Coulomb potential energies and the corresponding forces felt by a charged particle are shown in Figure 1.3.

Since the "attractive" direction for the force is along $-R$, the "attractive" Coulomb force is $-F^{(C)}R$, and is plotted as a function of A in Figure 1.4(a). As intuitively expected, the magnitude of the Coulomb force increases monotonically with A. More charges produce a larger force. Also, for large A, the force scales as $A^{1/3}$. This is a consequence of the fact that the total charge enclosed in the nucleus increases with R^3 while the geometric behaviour of the force decreases with R^{-2}. The net effect is proportional to the product of these contributions given by $R \sim A^{1/3}$. Consider next the nuclear force. Perhaps the simplest model (in terms of evaluating integrals) that one can construct to demonstrate the effects of a strong short-range force is that of a central force that scales as $-K/r^4$. The value of K can be determined by assuming that the nuclear and Coulomb forces are equal to each other in magnitude at a critical distance $r = r_c$ leading to $K = e^2 r_c^2 /4\pi\varepsilon_0$. Here, r_c is typically several nucleon radii; that is, $r_c = kr_0$ with k assumed to be a known dimensionless number of order unity. Observe that for $r < r_c$ the nuclear force dominates the Coulomb force, while for $r > r_c$ the reverse is true. These are the desired qualitative properties of a strong short-range force.

The "attractive" nuclear force $-F^{(N)}_R$ is plotted in Fig. 1.4(b) for k = 3.4. Note that the force increases with *A* for small *A*, eventually levelling off at large *A*. This behaviour is consistent with the following physical picture. For small nuclei, corresponding to small A, the attractive nuclear force increases as each new nucleon is added. However, after sufficient nucleons have been added, the nucleus becomes so large that new particles no longer feel the effect of distant nucleons because of the short-range nature of the nuclear force. In other words, the short-range nature of the force restricts new particles to feeling the effects of only a limited fixed number of nucleons (i.e., those lying approximately within a distance r_c), regardless of how large the total number of nucleons in the nucleus may be.

The total attractive nuclear force is plotted in Fig. 1.4(c). Observe that there is a qualitatively similar behaviour between this curve and the binding energy curve (E_B/A vs. *A*). The conclusion is that the shape of the binding energy curve is determined by a strong nuclear force whose attraction increases for small nuclei but which eventually saturates for large nuclei, ultimately becoming dominated by a weaker, but continually increasing repulsive Coulomb force. The result is that the binding energies for very light and very heavy elements are weaker than for intermediate mass elements. This explains why energy production from nuclear reactions is most effective at the ends of the spectrum of atomic masses.

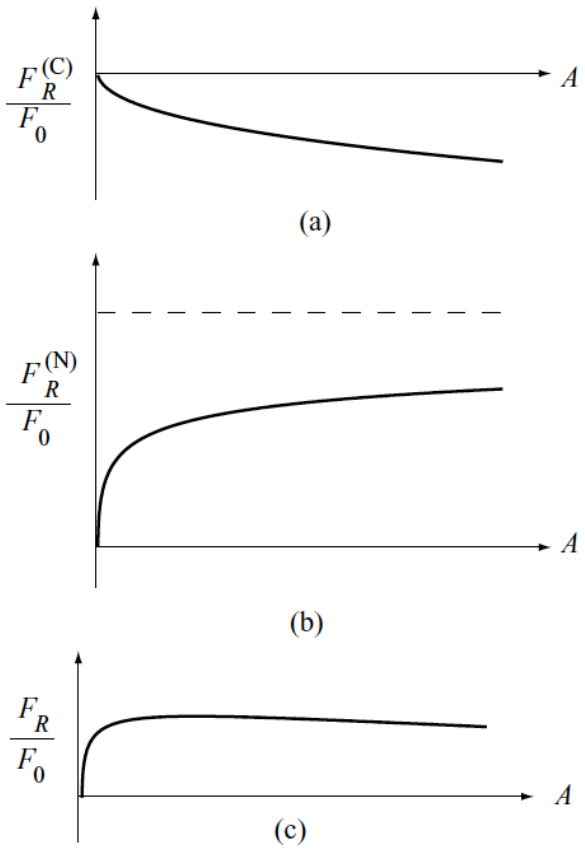

Fig. 1.4. Normalized attractive forces vs. mass number A: (a) the Coulomb force $-F^{(C)}_R$; (b) the nuclear force $-F^{(N)}_R$; and (c) the total attractive force: $F_R = -(F^{(C)}_R + F^{(N)}_R)$.

1.4.3 Summary of energy production

The chemical reactions occurring in the combustion of fossil fuels involve the rearrangement of the electron structure of the molecules involved, but conserve the individual chemical elements. The

reactions are dominated by the electromagnetic force and tend to release energies on the order of a fraction of an electron volt per atom per reaction.

Nuclear reactions on the other hand involve either the splitting or combining of the nuclei of the atoms involved, causing the transmutation of the initial fuel into new chemical elements. In these reactions the nuclear force dominates and energy releases on the order of mega-electron volts per nucleon per reaction are typical. Thus, nuclear reactions normally release about one million times more energy per reaction than chemical reactions.

There are two types of nuclear reactions, fission and fusion. Fission is easiest to achieve with very heavy elements, $_{92}U^{235}$ in particular. In these reactions, fission is initiated at room ambient condition by a slow neutron and the resulting reactions produce on average 2.4 new neutrons. This generates a chain reaction, which allows a self-sustaining mode of operation.

Neutrons are not effective initiators for light element fusion reactors as they are consumed rather than produced in fusion reactors. Instead fusion results from the direct interaction of two positively charged nuclei.

The need to overcome the repulsive Coulomb barrier in such reactions makes them more difficult to initiate than fission reactions. Fusion reactions do not occur at room ambient condition on Earth: this makes extremely challenging the research on thermonuclear fusion energy.

Since no chain reaction occurs, new fuel must be continually added to keep the operation continuous. The easiest way to initiate fusion is by the D–T reaction, which releases 17.6 MeV, 14.1 MeV in the neutron and 3.5 MeV in the alpha particle. The former elements are useful for extracting energy by the system, the latter reheat the plasma. The world's fusion energy research program is focused on the D–T reaction, the ease of initiation being of more importance than the problem of breeding tritium. Further in the future, the D–D reaction would be exploited, more advantageous in term of fully non-radioactive necessary fuel, and possible direct electric energy production by nuclear fusion reaction.

1.5 Summary of fusion

The reality of fusion power is still many years in the future. It is, nonetheless, worth pursuing because of the basic advantages of large fuel reserves, low environmental impact, and inherent safety. Most importantly, fusion should produce large amounts of base load electricity and thus has the potential to have a major impact on the way the nations of the world consume energy.

Two of the main disadvantages of fusion involve mastering the unexpectedly difficult scientific and technological problems. Great progress has been made in solving the scientific problems and large efforts are currently underway to address the technological challenges. Still the outcome is not certain. Many of the critical issues will be addressed in a new experiment known as the International Thermonuclear Experimental Reactor (ITER). This is an internationally funded facility whose construction begun in 2007. Details are shown in Chapter 2.

If successful, fusion power should be competitive cost-wise with other energy options although there is a large margin of error in making such predictions. Still the predicted costs are sufficiently reasonable that

this should not be a deterrent to completing the research necessary to assess the technological viability of fusion as a source of electricity.

The overall summary focuses on the issue of electricity production as it is in this context that fusion could play an important role. The accompanying conclusions are based on the following two realities concerning electricity consumption. First, the demand for electricity is large and is expected to increase in the future. Second, there is increasing evidence that the greenhouse effect is a real problem that must be considered.

The short-term demand for CO_2 free electricity will likely require the increased use of nuclear power to provide large amounts of base load power. Power can also be produced from natural gas, although this seems like a misuse of a fuel that is so ideally suited for heating applications. Hydroelectricity will continue to be an important contributor although, for the reasons discussed, further increases in capacity will be limited. A further important contribution to electricity production can be provided by the wind. However, this form of energy is more appropriate to meet peak demands because of the variable nature of the wind and the fact reserve wind energy cannot be easily stored at low cost. Solar power is currently too expensive except for special uses such as the heating of water, but encouraging development of more economic photovoltaic cells is presently in progress. Conservation can also play an important role in helping to reduce the magnitude of the problem, but by itself will not solve the problem of increasing electricity demand.

In the long term, fusion is an excellent new option that ultimately has the potential to become the world's primary source of electricity. This is the main mission of fusion.

However, difficult science and technology problems remain and cost may be an issue. Time will tell whether or not fusion research can fulfil its mission.

Chapter 2

2 Major challenges of the nuclear fusion energy research

We summarise here the most challenging aspects of nuclear fusion research, which are mostly of conceptual nature, not only technological.

The operation of a thermonuclear reactor would be based on the production of large plasma current (>10MA) in a toroidal device (tokamak) capable of magnetically trapping the plasma. This current should be mostly self-generated by plasma particle transport mechanism giving rise to the so-called bootstrap effect. This represents a very attractive opportunity considering the obstacle represented by the intrinsically inductive nature of tokamak machines utilised in fusion experiments. An inductive plasma current leads production, indeed, of transient regimes in front of the need of a reactor of operating in steady-state in order to provide available energy.

To produce and sustain a strong current mainly in the radial outer half of plasma column represents so far a major conceptual problem for envisaging a thermonuclear reactor. This thesis focuses on discussing results useful for contributing to solution of this problem.

This chapter is dedicated to introduce the concepts of tokamak and bootstrap current, giving an idea on how a suitable shape of the pressure radial profile of the plasma column is capable of maintaining this current in steady state, with no need of an ohmic transformer or external current drive.

2.1 Introduction

Research on nuclear fusion energy, now in progress, is based on deuterium-tritium plasmas magnetically trapped using the tokamak concept, which will be summarised in Sec. 2. This concept will be exploited in the projects: ITER (International Thermonuclear Experiment Reactor), ARIES, DEMO and ARC, which will be mentioned in Sec 4. The latter three projects aim to demonstrate the scientific, technical and economic feasibility of the new energy by the first working fusion power station.

The standard divulgation on this matter that is available by the official fusion sites is quite misleading. Indeed, it generally indicates that this research is aimed at creating a mechanism similar to that occurring in the Sun, but highlights only the need of achieving a high fusion gain, which is also required in an H-bomb. In addition, the challenge of this research would be mainly of technological type, whilst only minor conceptual problems would still need to be assessed.

Actually, these statements should be in principle reasonable only if it were possible to ignore the fact the large fusion energy gain must subsist in a reactor in the context of stability, as takes place in the Sun, see Figure 2.1. In a star, all fundamental forces of Nature cooperate, in fact, to yield nuclear fusion reactions in stable conditions, i.e., the mechanism goes ahead spontaneously without ceasing or exploding: the gravitation compensates the radiating pressure, the weak nuclear force that guarantees slow rate of neutrons production (necessary for synthetizing helium, so that this mechanism can goes ahead for billions of years), the electromagnetic force for establishing an equilibrate energy flow exchange between the different regions of the star and outside of that.

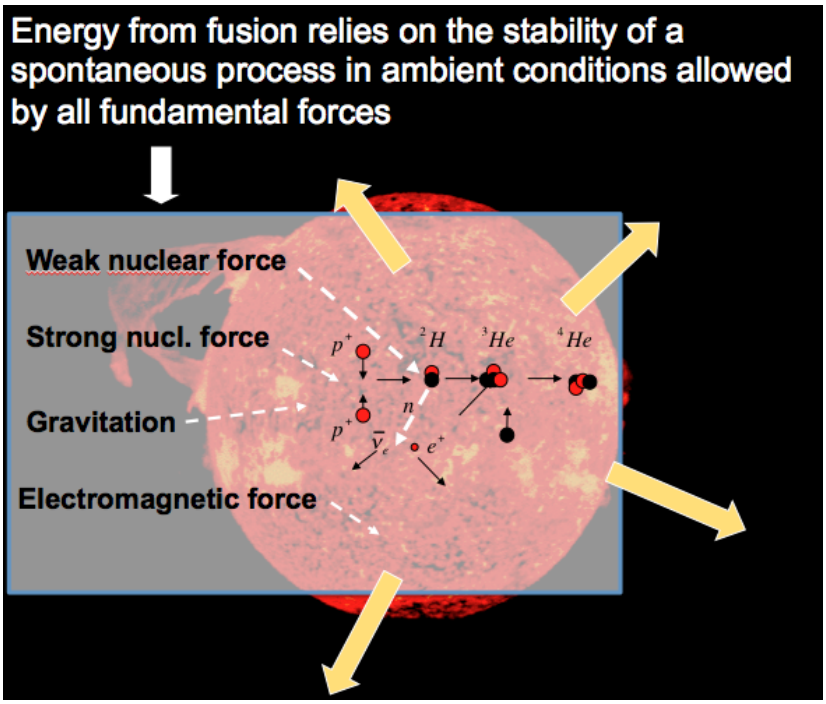

Figure 2.1. In the Sun, the cooperation of the fundamental forces allows the necessary fusion gain to be achieved in the context of stability.

On Earth, the same reactions cannot be utilised. Consequently, the urge of meeting condition for high and stable fusion gain (defined as Q=Produced power/Inputted power) in conditions in which it was never produced before represents the true challenge of nuclear fusion energy research. Fortunately, modelling and experimental results have shown that tokamak plasmas, own (quite incredibly) some capabilities of self-organising toward conditions of stable and good thermal insulation that are necessary for reactor. An example of this tendency is summarised ahead in the thesis.

Therefore, the major conceptual problem of a thermonuclear reactor is how to reach and maintain conditions of high-energy gain from fusion reactions and plasma stability for a long lasting (of at least several hours, as foreseen in the pulsed reactor option). For this aim, the plasma needs to have a high pressure. The high-pressure plasma is attained by means of a large current (>10MA) flowing through well thermally insulated plasma. Once this challenging scientific problem has been solved, the obtained solutions will merge into an economically competitive power plant that will allow fusion to fulfil its role in world energy production, which represents a formidable technological challenge.

2.2 The most promising concept for thermonuclear reactor: the tokamak

The tokamak is an axisymmetric torus with a large toroidal magnetic field (of several tesla). It is presently the leading candidate to become the world's first fusion reactor, since the achieved values of plasma pressure, thermal insulation at high temperature in a tokamak exceed those of any of the other concepts. Because of its performance, there is a large number of major tokamak experimental facilities operating or being constructed in the international fusion program.

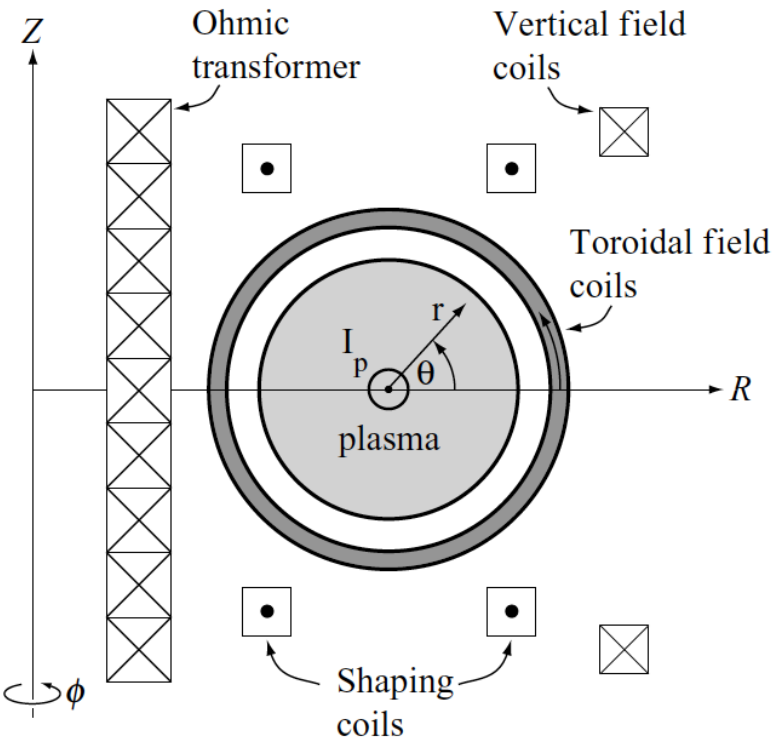

Fig. 2.2. Schematic diagram of a Tokamak

A schematic diagram of a tokamak is shown in Fig. 2.2. Observe that there are four basic magnet systems in the tokamak: (1) the toroidal field coils, which produce the large toroidal field; (2) the ohmic transformer, which induces the toroidal plasma current required for equilibrium and ohmic heating; (3) the vertical field system, which is required for toroidal force balance; (4) shaping coils, which produce a non-circular cross section to improve magneto-hydrodynamic (MHD) stability limits and alleviate plasma–wall impurity problems.

Typical operation of a tokamak discharge starts with the establishment of a large, steady, toroidal, magnetic field. Next, neutral gas is injected into the vacuum chamber and often pre-ionized. The transformer induced toroidal current is then ramped up to its maximum value and maintained for the "flat top" portion of the pulse. During flat top operation external heating power in the form of radio-frequency (RF) or neutral beams is applied to the plasma. The magnitude of the external power is usually substantially greater than that of the ohmic power. Most of the interesting experimental plasma physics occurs during the flat top period.

The characteristic equilibrium profiles of a tokamak during flat top operation are illustrated in Fig. 2.3. Note that the toroidal magnetic field has a slight diamagnetic dip, which is responsible for holding the plasma in radial pressure balance. A crucial feature is the behaviour of the safety factor, defined as the number of poloidal turns of a magnetic line along a full toroidal turn. The expression of this parameter is:

$$q \equiv \frac{2p}{lr} = \frac{rB_z(r)}{R_0 B_\theta(r)} \approx r\frac{B_\varphi}{R_0 B_\theta}$$

Use of the word "safety" is connected to magnetohydrodynamic (MHD) stability and configurations with high q(r) tend to be more stable, i.e., safer.

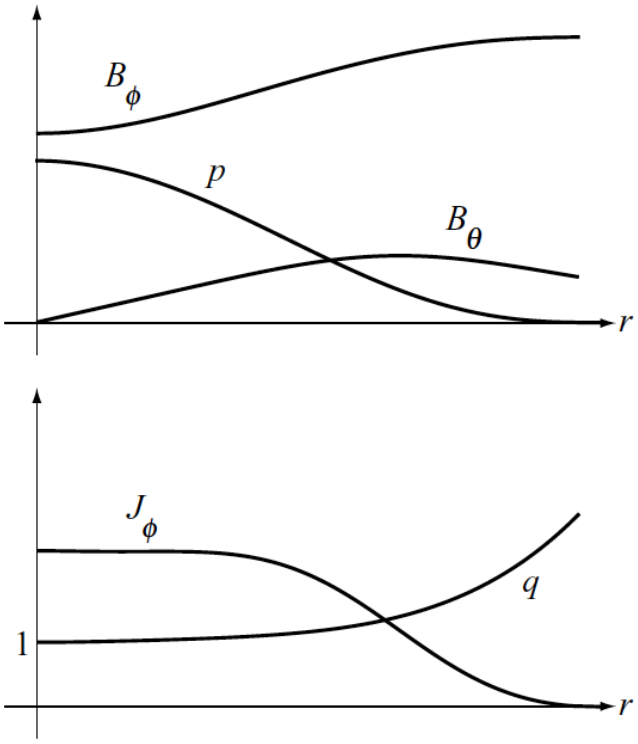

Fig. 2.3. Typical radial profiles in a tokamak in the large aspect ratio limit: R0/a >>1 →∞.

For a tokamak *q(r)* is an increasing function of radius and, most importantly, is always large: *q(r)* > 1 over almost the entire plasma, a consequence of the large toroidal magnetic field.

Another important parameter is the shear of the vector of the local magnetic field of confinement. The magnetic shear is defined as: $s = r\frac{dq}{dr}$. To assess the latter parameter is important for the following reason. A low local shear, at a radial layer where a relative maximum of the current density profile occurs, is condition useful for suppressing turbulence detrimental for the thermal insulation, which the plasma naturally exhibits along the radial direction [1].

In terms of reactor desirability, the tokamak has a number of advantages and a few problems. The main advantages are associated with good physics performance. The large toroidal field and correspondingly large edge safety factor lead to finite values of MHD stable β without a conducting wall and to reasonably high experimental values of the energy confinement time τE. The quantity β is the normalized plasma pressure defined as:

$$\beta \equiv \frac{2\mu_0 p}{B^2}\pi r^2$$

The energy confinement time τE is the characteristic time of decreasing temperature of the system after all power inputs have been switched-off.

Good confinement allows the plasma to heat up to high temperatures using only a moderate amount of external heating. In addition the resulting values of β lie in the regime of reactor interest. As an example, consider a high performance D–T shot on the Joint European Torus (JET) located near Oxford in the UK. At

$B_\phi \approx 3.6$T and external heating power $P_h = 25$ MW, JET has achieved the following performance for a pulse lasting several seconds: plasma central density: $n(0) \approx 0.4 \times 10^{20}$ m^{-3}, ion temperature: $Ti(0) = 28$ keV, electron temperature: $T_e(0) = 14$ keV, Averaged plasma pressure:$<\beta> \approx \beta(0)/3 \approx 0.018$, and $\tau E \approx 0.9$ s corresponding to $p\tau E \approx 0.84$ atm s. For comparison, recall that a value of $p\tau E \approx 8$ atm s is required for ignition. Clearly, existing tokamak experimental performance is starting to approach the regime of reactor interest.

2.2.1 Major drawback of the tokamak concept

The major problem of a tokamak, as conceptual basis of reactor, consists in its intrinsic limitation of producing only inductive, then transient, regimes of plasma current, whilst a reactor would operate in steady-state or at least in pulsed regimes of plasma current guaranteeing cycles of duration of several hours. Consequently the tokamak should be mandatorily equipped with systems of strong heating and current drive (CD) produced by means of externally injected strong powers of radio-frequency (RF) and beams of energetic neutral particles. In order to save the huge costs of these additional systems it is necessary exploit a strong fraction of plasma current that is produced by the so-called bootstrap effect [1]. In a tokamak plasma this current is self-produced via particle transport mechanism driven by the plasma pressure gradient, i.e., this current has the advantage of having non-inductive nature and flowing with continuity, which makes less demanding the requests of very expensive CD tools.

However for satisfying the important need of reactor of exploiting a large faction of bootstrap current, the radial plasma pressure profile of plasma column, which mostly dictates the radial profile of such self-generated current, should be maintained under control. This can be accomplished experimentally by programming the time dependence of the plasma current and the radial and time dependence of the external heating sources. Such a tailoring of the external sources of heating and current drive is capable to prevent the onset of strong unstable modes of magneto-hydro-dynamic (MHD) nature that are responsible of major cause of transport of energy and matter from the hotter regions of the plasma centre to the colder plasma region at the radial periphery, which detriments the key figure of thermal insulation of plasma column.

Therefore, an economic development of thermonuclear reactor based on the exploitation of a large non-inductive current self produced in tokamak plasma requires, as mandatory, an independent tool for tailoring the current density profile over the whole minor radius of plasma column. The radial outer half of plasma presently represents the major problem for full assessment of current profile control in a reactor. The main focus of this thesis is to contribute to the solution of this problem. Before facing it, we summarise hereafter the important bootstrap effect.

2.2.2 The bootstrap current

The bootstrap current J_B is one of the most interesting and important predictions of neoclassical transport theory. It is important because it is generated by the natural radial transport in the plasma, thereby

creating potentially steady state toroidal plasma current in a tokamak, without the need of expensive, external current drive. A tokamak without a substantial fraction of bootstrap current would very likely not be viable as a reactor for economic reasons.

The bootstrap current is also a quite subtle phenomenon since the final form of J_B is independent of collision frequency but yet is a consequence of collisional transport. An intuitive picture of the origin of the bootstrap current is presented in this paragraph. It is shown that the bootstrap current flows parallel and not anti-parallel to the main toroidal current. Also its magnitude can be quite substantial, theoretically capable of approaching 100% of the toroidal current. This is critical since bootstrap fractions on the order of $f_B > 0.7$ are probably required for economic viability.

The intuitive picture, which assumes for simplicity that the ions are infinitely massive, shows that three electron currents need to be considered. These are the magnetization current due to the trapped electrons, the magnetization current due to the passing electrons, and the current that flows because of the frictional momentum exchange between trapped and passing electrons. The computation of these currents requires a quite complex work of analysis and is omitted. As final result, the bootstrap current arises because of the collisional friction between the passing and trapped electrons. Collision effect is generally ignored in evaluating the magnetization current. Nevertheless, even if collisions are infrequent, when included in the steady state analysis, they impose a strong constraint on the electron currents. Specifically, the magnitudes of the trapped and passing particle currents must be such that the total momentum exchanged between all electrons is zero. In other words, when summing over both trapped and passing electrons momentum is exactly conserved in like particle collisions since the Coulomb interaction represents a purely elastic collision.

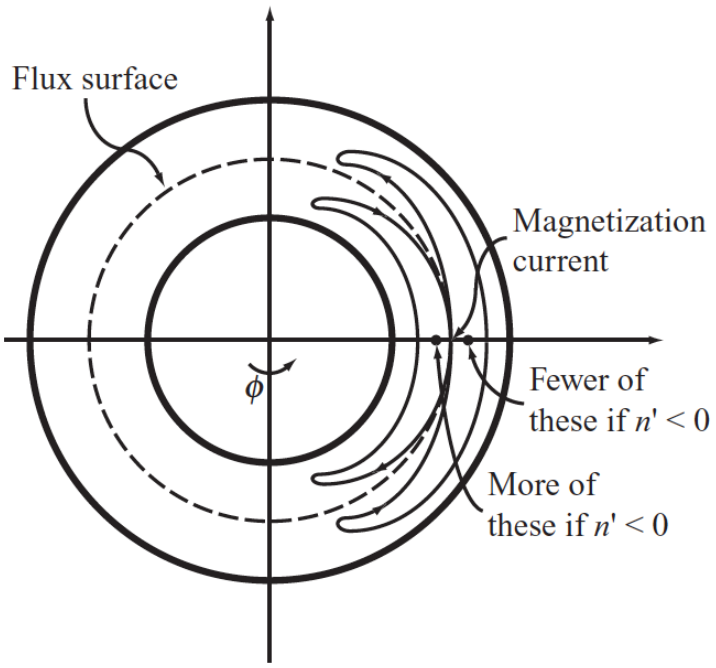

Figure 2.4. Top view of the tokamak showing the toroidal projection of two banana orbits. If $\partial n/\partial r < 0$, there are more inward that outward shifted banana orbits. This produces a net downward magnetization (for positive particles) at the point of tangency.

Therefore, the bootstrap current is carried by a flow of passing electrons generated by collisional friction with the trapped electron magnetization current. In summary, analysis shows that by properly considering the collisional momentum balance the final expression of the bootstrap current density is:

$$j_B = -4.71q\left(\frac{R_0}{r}\right)^{1/2}\frac{T}{B_0}\left(\frac{\partial n}{\partial r}+0.04\frac{n}{T}\frac{\partial n}{\partial T}\right)_s$$

where q is the safety factor and T is the sum of electron and ion temperatures.

The bootstrap fraction can be quite large and can theoretically overdrive the total current. In practice, however, the situation is more complicated. Analysis shows that the bootstrap current is maximised by a combination of high pressure and low toroidal current. However, low toroidal current shortens the energy confinement time making it harder to achieve high pressure. The final bootstrap fraction therefore involves a number of tradeoffs and a careful analysis including profile effects.

The main conclusion to be drawn from the analysis is that neoclassical-trapped particle effects lead to a transport driven toroidal plasma current carried by the passing particles. This bootstrap current is capable of being maintained in steady state without the need of an ohmic transformer or external current drive. Furthermore, tokamak experiments indicate that the neoclassical prediction of J_B is consistent with observations.

There is no obvious "anomalous" degradation of j_B due to micro-turbulence, which is indeed a favourable result as it opens up the possibility of steady state operation without the need for excessive amounts of external current drive power.

2.2.3 Problematic aspects of fusion energy from research performed in the past 50 years

The key issues involving scientific challenges, technological challenges, and economics are as follows.

The science of fusion is quite complex. Specifically, to burn D–T is required to heat the fuel to the astounding temperature of 150 million of degrees, hotter than the centre of the sun. At also much lower temperatures the fuel is fully ionized becoming plasma, a high-temperature collection of independently moving electrons and ions dominated by electromagnetic forces. Once heated some method must be devised to hold the plasma together. The primary method requires a clever configuration of magnetic fields, an admittedly nebulous idea to those unfamiliar with the science of plasma physics. Cleverness is mandatory, not an option. Too simple a configuration allows the plasma to be lost at a rapid rate, thus quenching fusion reactions before sufficient energy can be produced. Even with a clever configuration there are limits to the plasma pressure that can be confined without rapid losses through the magnetic field.

The combined requirement of confining a sufficient quantity of plasma for a sufficiently long time at a sufficiently high temperature to make net fusion power has been the focus of the world's fusion research program for the past 50 years. The unexpected difficulty of these scientific challenges is the primary reason it has taken so long to achieve a net power producing fusion reactor.

There are also engineering challenges, which many believe are of comparable difficulty to the scientific challenges. First, improved low-activation materials need to be developed that can withstand the neutron and heat loads generated by the fusion plasma. Second, large high-field, high-current superconducting magnets need to be developed to confine the plasma. Superconducting magnets on the scale required for

fusion have not been built yet.

Third, new technologies to provide heating power have to be developed in order to raise the plasma temperature to the enormously high values required for fusion. This involves a wide variety of techniques ranging from very high-power neutral beams to millimetre wavelength megawatt microwave sources. Clearly a major research and development program is required to make fusion a reality.

The last disadvantage is economics. A fusion reactor is inherently a complex facility. It includes a fuel chamber, a blanket, and a complicated set of superconducting magnets. Also, since the structural material becomes activated, a large remote handling system is required for assembly and disassembly during regular maintenance. The use of tritium plus the structural activation means that radiation protection is also required. These basic technological requirements imply that the capital cost of a fusion reactor will be larger than that of a fossil fuel power plant, and very likely also than that of a fission power plant. This will tend to raise the cost of electricity to consumers. Balancing this are low fuel costs and low costs to protect the environment, both of which tend to reduce the cost of electricity to consumers.

It is clearly difficult to predict the cost of fusion energy as compared to other options 30–50 years in the future. One main complication is that a combination of fuel reserve problems and environmental remediation costs will likely increase the costs of these other options so that comparisons involve a number of simultaneously moving targets. Estimates of future fusion energy costs are in the vicinity of the other options, but because the uncertainties are large, they should be viewed with caution. The main value of these estimates is to show that it makes sense to continue fusion research. Fusion should not be eliminated because of an inherently absurd cost of electricity, nor will it be “too cheap to meter” as one might have hoped in the past.

2.3 The future of fusion research

2.3.1 Macroscopic equilibrium and stability

The progress on plasma physics in tokamaks with respect to the basic ignition condition for a fusion reactor has been substantial, although there still remain challenging, unanswered questions.

The maximum achievable pressure against major disruptions in a given fusion concept is largely determined by macroscopic equilibrium and stability limits, which are well described by the MHD model. For the tokamak the theoretical predictions and experimental observations are, in general, in good agreement. The theory can therefore be used to reliably predict the pressure limits in next generation experiments.

In terms of performances of current devices, tokamak experiments operating in the standard mode have already achieved the values of β required in a reactor. These values are close to the maximum (no-wall) β limit. The corresponding plasma pressures are, however, less than those required in a reactor because the magnetic fields are smaller. A next generation, higher-field experiment, should be able to produce both high β and high pressure.

The main issue is that the high β pressure and current profiles produce a bootstrap fraction that is too low

to reduce the current-drive requirements to an acceptable level for economic viability in a reactor.

Avoiding this problem requires the achievement of high bootstrap fractions through advanced tokamak (AT) operation, which is based on the production of well-insulated internal radial region of plasma by means of appropriate control of the plasma current density radial profile. Unfortunately, the achievement of a high bootstrap fraction requires β values that exceed the no-wall β limit. A perfectly conducting wall can produce stability at these higher values of β. However, since a real wall has a finite resistivity, this leads to excitation of the resistive wall mode. Stabilization of the resistive wall mode is an important topic of research for both existing experiments and future large devices.

2.3.2 Thermal insulation of the plasma column

The dominant transport mechanism in tokamak plasmas is thermal conduction and is characterized by the energy confinement time τE in the ignition condition. Substantial progress in the basic understanding of core thermal transport has been made by a combination of analytic theory and large-scale computation. However, a first-principles prediction of τE is still not available and remains a grand challenge of present and future fusion research.

There are also several related transport problems involving the edge plasma that directly impact the core transport: the Greenwald density limit, the critical power threshold for the low (L) to high (H) mode transition, and edge localized modes (ELMs). In addition, the physics of internal transport barriers, which may be important for the lower-current AT operation, is not well understood.

At present, the determination of τE as well as the relevant criteria for the edge phenomena is based on empirical scaling relations. These relations work reasonably well in existing experiments and hopefully will reliably extrapolate to future generation tokamaks. In fact, the size and cost of a next generation experiment are directly dependent on the prediction of the empirical scaling relation for τE. Developing empirical scaling relations for thermal transport in the presence of a large population of energetic alphas is a major challenge for the future.

Lastly, it is worth noting that the theoretical prediction of the bootstrap current based on neoclassical transport theory seems to be in reasonably good agreement with experimental observations. An accurate prediction of J_B is critical for determining the requirements on the current-drive system for steady state operation. Understanding the effects of alpha particles on the self-consistent bootstrap current is another important challenge for future research.

2.3.3 Heating and current drive

Minimizing the demands on the pτE product in the ignition condition requires achieving a plasma temperature that maximizes the cross-section of fusion reactions. Reaching T ≈ 15 keV will be accomplished by a two-stage process, where initially auxiliary power heats the plasma to about T ~ 5–7 keV, after which the alphas dominate, completing the heating to T ≈ 15 keV. Several methods of auxiliary power that provide central heating have been tested in existing experiments: neutral beam heating, ion cyclotron heating (ICH), and electron cyclotron heating (ECH). Temperatures well in excess of T ~ 5–7 keV have been achieved in existing tokamaks in pure deuterium plasmas, usually at lower densities than

required in a reactor. Overall, the heating methods work reasonably well and are in good agreement with theoretical predictions. The implication is that a reasonable (in terms of power balance and cost) amount of auxiliary power should achieve the required heating mission in a next generation experiment or reactor. Also, based on present experimental experience, neutral beam heating is usually regarded as the simplest and most reliable heating method from a purely plasma physics point of view, and therefore will play a primary role in ITER.

The challenges of extrapolating heating methods to ITER and a reactor are largely technological. Neutral beam heating requires the development of high-energy, negative ion sources to act as drivers. ECH requires the development of high-power, steady state gyrotron sources. ICH requires an antenna structure very close to the plasma edge. These are all topics of current and future research.

A related issue concerns current drive, which enters the ignition condition implicitly through the assumption of steady state operation. Lower hybrid current drive (LHCD), which the Thesis is mostly focused on, is the most efficient method presently available. Also it drives current off-axis, which is an advantage in matching to the natural bootstrap profiles.

Even so, the absolute magnitude of the current-drive efficiency is too low to drive all the current in a tokamak reactor or ignition experiment. The conclusion is that a substantial bootstrap fraction will be required in order to reduce the current-drive requirements to a level compatible with reactor economics. Long-pulse current drive is thus an important research topic in present as well as next generation experiments.

2.3.4 Alpha particle plasma physics

The alpha particle physics discussed in the main text is primarily focused on issues of power balance and heating. There are very few data involving alpha particles since only two experiments, TFTR and JET, have actually operated with tritium, and then only for a limited period of time.

Because of the lack of data, alpha particle plasma physics is often referred to as the next (and hopefully last) frontier in plasma physics. Learning about alpha particle plasma physics is one the most important physics goals of a next generation ignition experiment. Of particular interest is whether the alpha pressure gradient will excite instabilities that would cause the alphas to be lost at an anomalously fast rate. This would be highly undesirable in that the alphas could be lost before transferring all their energy to the background plasma, thereby substantially increasing the difficulty of satisfying the steady state ignition condition.

Another issue involves the ability to externally control the pressure and current profiles by means of auxiliary heating and current drive. The difficulty here is that the alpha power in ignited plasma completely dominates the auxiliary and current-drive powers. Studies are needed to determine how effectively these relatively “small” external power sources control the profiles.

2.3.5 Fusion technology issues

A further topic of importance, not encountered in present experiments, is the removal of the alpha “ash”. As the alphas build up due to fusion reactions, they replace D–T fuel because of the charge neutrality requirement. Too many alphas dilute the D–T fuel, leading to a reduction in fusion reactions, which

adversely affects power balance. Rapidly removing the alphas is therefore an important challenge for future experiments. Lastly, the issue of burn control, should be automatic, needs to be addressed. This needs to be demonstrated experimentally to show the viability of stable, steady state operation.

As stated, great progress has been made in the basic understanding of plasma physics although important problems still remain that require investigation in a next generation ignition experiment. Equally importantly, an ignition experiment will have to start realistically addressing many of the fusion technology issues facing a reactor. Several of these issues are summarized below.

A critical issue is the interaction of the first wall with the flux of 14.1 MeV neutrons. It has been assumed that the neutron flux limits the wall loading on the first wall to PW ≤ 4 MW/m2. This is probably an optimistic bound with respect to existing materials but not an unrealistic goal by the time of the first fusion reactor. Recall that the maximum neutron wall loading is a crucial design parameter, directly impacting the cost of a reactor.

Unfortunately, there are only limited materials radiation data available because of the lack of 14 MeV sources. Most fusion researchers agree that progress towards a fusion reactor will require not only an ignition experiment such as ITER, but a dedicated materials testing facility to develop advanced materials capable of withstanding high wall loadings. This is the role of another future fusion facility known as the International Fusion Materials Irradiation Facility (IFMIF).

A second major technological problem involves the design of the divertor. Although a substantial number of data have been collected from existing tokamaks with divertors, the situation regarding ITER and fusion reactors is still not fully resolved. The reason is due to difficult trade-off issues involving the choice of target materials, the durability of the target, the action of the target back on the plasma, and the need to robotically replace divertor modules as they wear out.

A third issue of importance is related to superconducting magnet technology. Although there has been a great deal of experience building high-field, superconducting magnets, no one has yet built magnets on the scale needed for ITER or a fusion reactor. The size, coupled with the need to use the more difficult to fabricate superconducting material niobium–tin to achieve high values of toroidal magnetic filed, makes this a challenging technological problem.

A fourth technological issue involves the blanket. An experiment such as ITER will be the first to produce large amounts of fusion neutrons, thus requiring the presence of a blanket. Hopefully, the knowledge obtained from fission reactors will suffice with respect to the removal of neutron energy by means of a heat exchanger. However, there is almost no practical experience with respect to the breeding of tritium. This is an important technological issue since the world's supply of tritium is rather limited and it is very expensive to make in large quantities. Fifth, there are the technological issues associated with plasma heating: the development of negative ion drivers for neutral beam heating, the development of high-power gyrotrons for ECH, and the development of robust antenna designs for ICH.

Finally, in closing this section it is worth noting that many researchers view the technological and plasma physics problems facing fusion to be of comparable difficulty. Although technological solutions seem conceptually possible, it is clear that a facility such as ITER must be built to test these ideas in an actual practical device.

2.4 ITER

We give here a summary of the next major fusion experiment in the world fusion program, ITER, now in construction phase. Assuming ITER is built and is successful, one can then project ahead to the design and construction of a demonstration fusion power plant (DEMO).

To help understand ITER this section contains a brief history of the project and a description of the current proposed experiment. The story unfolds hereafter.

2.4.1 History

As early as the late 1970s fusion researchers around the world already recognized the importance of building a large-scale ignition experiment to investigate alpha physics and to start addressing many of the technological issues facing a reactor. An international collaboration was established to design such an experiment, which was named the International Tokamak Reactor (INTOR). The idea, which has a great deal of validity even today, is that a good way to learn about the issues facing an ignition experiment or a fusion reactor is to try to actually design one. The collaboration was highly successful in identifying many of the critical issues and suggesting important areas for future research. One difficulty faced by the INTOR group was that at the time of the design the world's large tokamaks had not yet been completed and as a consequence they did not have reliable scaling relations to predict the energy confinement time. The INTOR design, based on the best data available at the time, reached the conclusion that a plasma current of $I \approx 8$ MA would be sufficient to achieve its goals. Present understanding of energy confinement based on the H-mode (achievable when a sufficiently high heating power is injected to plasma for given condition of operating configuration) scaling implies that $I \approx 20$ MA is required for ignition.

Researchers knew about the uncertainties in INTOR and so the design was never put forward for actual construction. However, INTOR had established a precedent for international collaboration. Thus, at the Geneva Summit Meeting in 1985, Soviet Leader Mikhail Gorbachov suggested to US President Ronald Reagan that the USA and the USSR should initiate an international collaboration to design and build a next generation fusion ignition experiment. The European Community and Japan quickly joined the collaboration. The project was called ITER.

The first step in the project was the development of a conceptual design, which was given the official name of the Conceptual Design Activity (CDA). The CDA started in 1989 and was completed in 1991. It was viewed as a success in that the researchers did indeed agree that such a device could be built and its aims would be achieved. Critical design parameters were also specified.

Based on this success, a second agreement was signed to develop an actual engineering design for ITER. This was called the Engineering Design Activity (EDA) and spanned the period 1992–8. At the end of this period a detailed engineering design was delivered. The huge effort devoted to the EDA resulted in a technologically successful final design: that is, the final design was deemed credible from both an engineering and plasma physics point of view by a large number of expert reviewers. The final design called for a 20 MA tokamak with a major radius of 8.1 m. It would cost about $9B (in 2005 dollars) and take about 10 years to construct.

Although ITER was technologically credible, the various partners in the collaboration finally deemed its cost too high. This, coupled with the fact that energy was relatively inexpensive in the late 1990s, led to a situation in which none of the collaborators was willing to put forward a site on which construct ITER and

to serve as the host, which involved a considerably higher cost.

A decision was, therefore, made to design a smaller version of ITER with a corresponding reduced mission and cost. The hope was that a lower cost, perhaps combined with a more favorable future economic climate for energy research, would lead to approval of the project.

One of the main differences in missions is that the original ITER was designed to achieve full ignition (i.e., power gain: Q =∞), while in the new version this requirement was relaxed, with the reduced goal being high but not infinite Q (i.e., Q = 10). A further complication facing the reduced mission ITER was that the US Government decided to completely pull out of the ITER project in 1998.

The remaining partners continued their collaboration and by 2001 developed a successful engineering design for the reduced mission ITER. The new ITER design has a lower current of I = 15 MA and a smaller major radius of R_0 = 6.2 m. Its cost is about $4B (in 2005 dollars) and should take 8–10 years to build. By the time the design was completed energy prices had begun to increase and the climate for energy research had improved. The US re-joined the collaboration. Also joining were two new partners, China and Korea. Canada also considered becoming a partner.

Another very positive result was that after the new ITER design was completed, four countries offered sites for construction of the facility: Canada, France, Japan, and Spain.

The Canadian site was very attractive from a technological point of view. However, the population and corresponding tax base of Canada was too small to support the high level of funding required by the host country. Canada thus withdrew its offer of a site and is not at present an official member of the collaboration. The French and Spanish sites were both attractive technologically. Nevertheless, the European Union decided that a single entry would increase the likelihood of a European selection, and chose the French site at Cadarache as its official candidate. The Japanese proposed a technologically attractive site at Rokkasho at the north of Honshu Island.

The final competition was thus between the French and Japanese sites. Both the EU and Japan made very serious and attractive bids to become the host for the new ITER.

An initial vote, leading to a longstanding stalemate, had three partners (the EU, Russia, and China) supporting the French site and the other three partners (Japan, the US, and Korea) supporting the Japanese site. After an arduous and torturous set of negotiations, an international agreement was finally reached (in July 2005) to construct the new ITER at the French site in Cadarache. This was indeed a major milestone.

At the moment, ITER is under construction at Cadarache site and the progresses of the construction phase can be viewed at the website www.iter.org. The first Plasma is foreseen by the end of 2025.

2.4.2 Technical description

The primary physics mission of ITER is: to produce a stable, well-confined, Q = 10 plasma lasting for a sufficiently long duration to reach quasi-steady-state operation. A second physics mission is to achieve steady state operation using non-inductive current drive at Q >~ 5. With respect to technology, the construction of ITER would demonstrate the viability of large superconducting magnets, various plasma facing materials, and large-scale remote handling. It would also test the effectiveness of the divertor

design and begin to explore tritium breeding.

The actual ITER design is illustrated in a cutaway view in Fig. 2.5. An artist's sketch of the entire device is shown in Fig. 2.5. Note that ITER has a single null divertor and superconducting magnets constructed of niobium–tin. The magnetic field at the center of the plasma is B_0 = 5.3 T. To minimize the cost, the size of the machine has been minimized subject to the constraints of achieving Q = 10 operation with H-mode scaling in a plasma which is MHD stable without a conducting wall. This leads to a major radius R_0 = 6.2 m, a minor radius a = 2 m, and an aspect ratio R_0/a = 3.1. The current required to achieve the necessary confinement time is I = 15 MA. At Q = 10 operation the average density is 0.9 $x10^{20}$ m^{-3} and the temperature is of 11 keV.

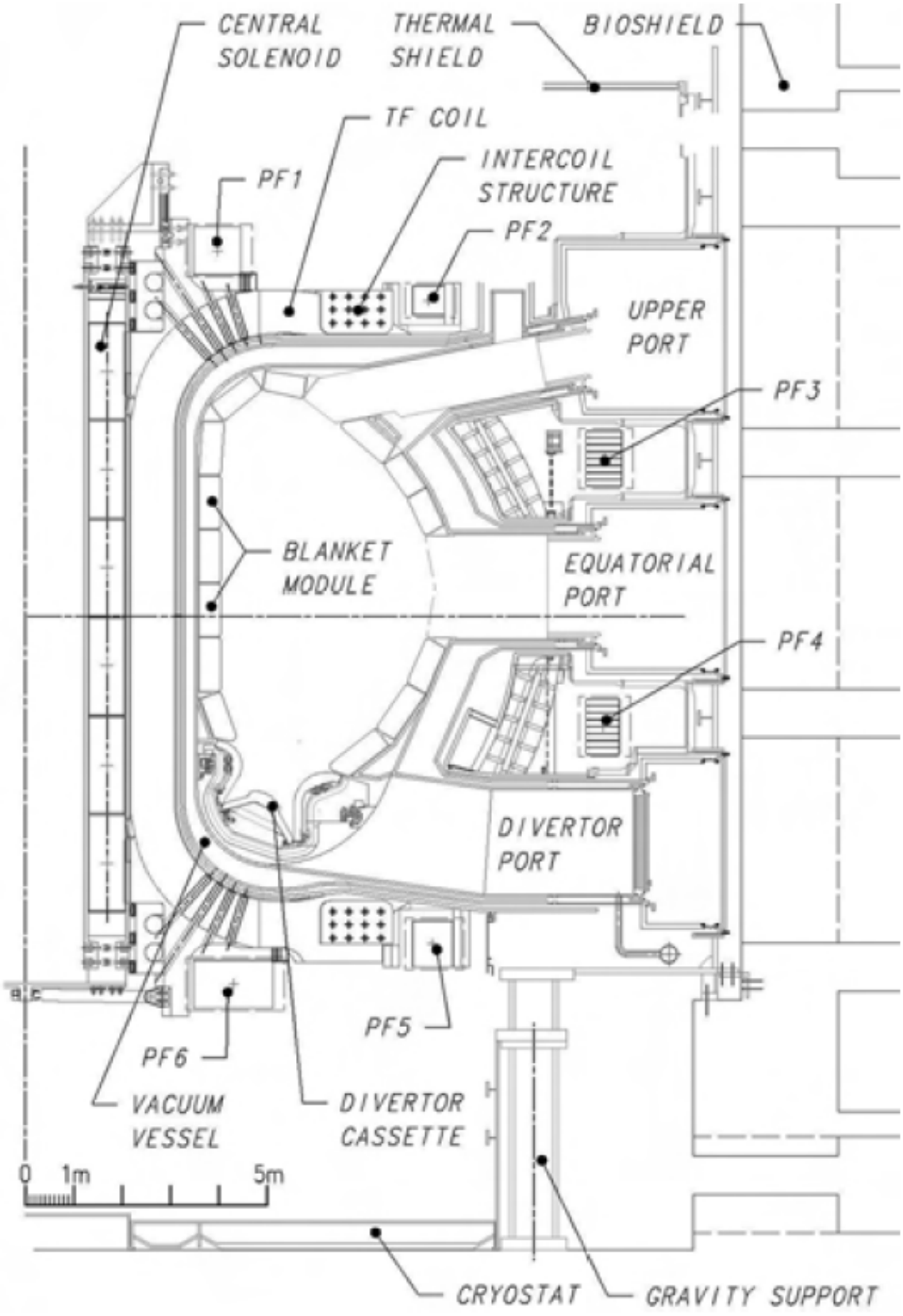

Figure 2.5. Cutaway view of ITER

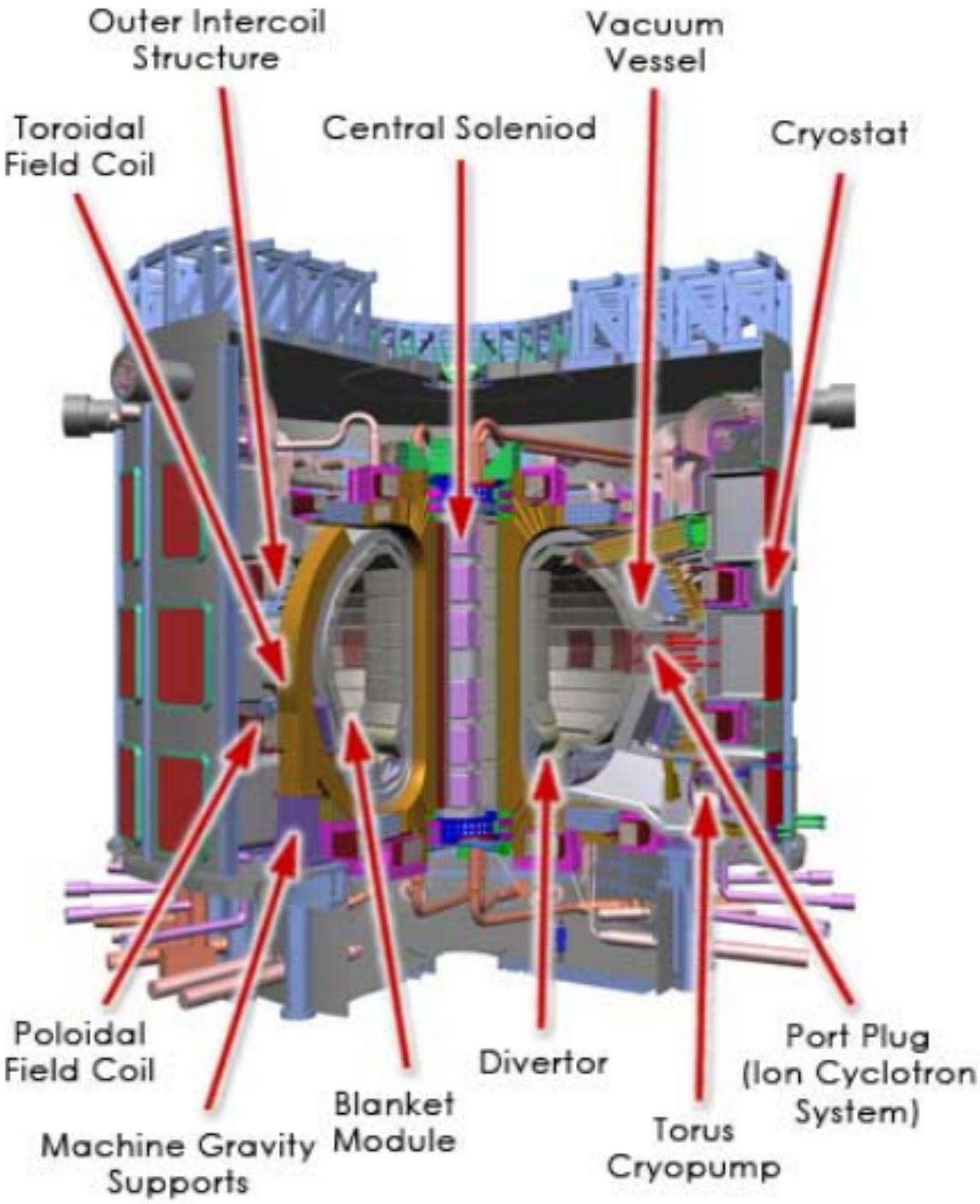

Figure 2.6. Sketch of ITER

For base operation, ITER will have three sources of auxiliary power: 33 MW of negative ion- driven neutral beams, 20 MW of ICH, and 20 MW of ECH. The neutral beams and ICH will be used primarily for heating. The ECH will be used, at least initially, to stabilize a localized resistive MHD instability known as the neoclassical tearing mode, should this mode limit the achievable value of β.

ITER will operate for pulse durations of about $\tau_{pulse} \approx 400$ s, driven entirely by the ohmic transformer. The bootstrap current is expected to be small and no current drive is planned for base operation. If successful, ITER should produce a Q = 10 plasma.

An overall summary of the basic parameters characterizing ITER is given in Table 2.1.

Table 2.1. Parameters for base operation of the ITER experiment

Parameters	**Symbol**	**Units**	**ITER**
Major radius	R_0	m	6.2
Minor radius	a	m	2.0
Aspect ratio	R_0/a	-	3.2
Elongation (95% flux surface)	κ	-	1.7
Toroidal magnetic field	$B_0 = B(R_0)$	T	5.3
Plasma current	I_P	MA	15
Safety factor (95% flux surface)	q_{95}	-	3.0
Average temperature $T_e \approx T_i$	T_k	KeV	11
Average electron density	n20	10^{20} m^{-3}	0.91
Energy confinement time	τ_E	s	3.7
Power gain	Q = Pf/Ph	-	10
Neutral beam power	P_{NBI}	MW	33
ICH power	P_{ICH}	MW	20
ECH power	P_{ECH}	MW	20
Ohmic pulse length	τ_{pulse}	s	400
Cost	C	billions	4.3

ITER is close to be a full-scale prototype fusion reactor in terms of size and performance. The main difference is that ITER is still largely an experimental facility and therefore has not been designed to have the very high duty factor associated with a steady state power-producing reactor.

In addition to the first stage of operation described in Table 2.1 there is a second stage of ITER operation that focuses on advanced tokamak (AT) operation aiming at near steady state operation by means of substantial current drive and profile shaping. Several different scenarios are envisaged and the parameters below describe a representative example of AT operation.

For the AT experiments a combination of bootstrap current and external current drive should produce very, very long pulses (i.e. 3000 s) or almost true steady state operation. The current drive will be provided by a combination of lower hybrid and electron cyclotron power. However, since ITER will not have sufficient current-drive power plus bootstrap fraction to achieve the entire 15 MA of base performance, the AT phase of the experiment will operate with somewhat reduced parameters. Specifically the total current will be reduced from 15 MA to about 9 MA, while the fusion gain will be reduced from Q = 10 to Q = 5.

Profile control should produce a hollow current density, a reversed shear safety factor, and bootstrap fractions on the order of $f_B \sim 0.4$. Also, the required confinement time to achieve Q = 5 will exceed the H-mode confinement time, implying the need for an improvement in transport due to the formation of internal transport barriers, again by means of profile control. Lastly, the anticipated value of β will be very close to the Troyon no-wall stability limit. Quite possibly the resistive wall mode may be excited, and would need to be feedback stabilized.

Observe that while performance is somewhat reduced from the base values, AT operation still represents

a major accomplishment in showing that a tokamak can sustain steady state operations in the presence of a large population of alpha particles.

Assuming that ITER is built and is successful in carrying out its goals, a full-scale demonstration power plant has been envisaged as described below.

2.5 A demonstration power plant (DEMO)

The current belief is that the information learned from ITER with respect to both plasma physics and fusion technology should be sufficiently complete and comprehensive to justify moving to the final step before commercialization. This final step is usually referred to as DEMO.

The transition from ITER to DEMO involves several important issues, mainly of a technological nature. The plasma physics issues should be similar to those for ITER since the devices will be of comparable size with comparable parameters. However, technologically DEMO must be able to demonstrate full steady state operation in a safe, reliable, and maintainable way. While individual components may extrapolate in a straightforward manner, integration of all these components into a working power plant will be a major goal of DEMO.

Another major goal of DEMO will be to demonstrate tritium breeding with a recovery ratio greater than unity. This is crucial since the world's supply of tritium is very limited. There are huge reserves of lithium that can be used to breed tritium in the blanket but it is essential to demonstrate that more tritium can be produced than is consumed.

Lastly, DEMO, through the utilization of advanced materials developed during the interim period, should be able to demonstrate the attractiveness of fusion with respect to the environment in general and radioactive waste in particular. This is, after all, one of the primary advantages of a fusion reactor.

DEMO is clearly decades away. If built and successful, the step after DEMO is a commercial fusion power plant. Because of its complexity, the capital cost of a fusion power plant will likely be relatively high. However, its fuel and operating costs should be low.

The net result is that the overall cost of electricity from a fusion power plant may indeed be competitive with other sources when such fusion plants become available.

In the immediate future the goal is to build and operate ITER. ITER is expensive but the ultimate attractiveness of fusion in terms of fuel supply and environmental impact suggests that this is a wise investment of research funds.

Further projects, namely, ARIES and ARC, have been proposed with the aim of demonstrating a future thermonuclear power station.

Chapter 3

3 The problem of current drive in a thermonuclear reactor

We focus here on the importance of driving current non-inductively, i.e., in a way capable of producing reactor relevant steady-state regime of plasma current. This is important not only owing to the limit of tokamaks plasma machinse of producing only transient regimes, but also because having an independent tool for driving current is essential for exploiting the bootstrap current (the non-inductive current self generated in the plasma by collisional friction between electrons trapped in the different trajectories imposed by the magnetic configuration). This option is fundamental condition for economic, then, viable development of a thermonuclear reactor.

Results of Ref. [64] (R. Cesario, L. Amicucci et al., Plasma Phys. Control Fusion 2013 55 (2013) 045005 (14pp)) have been considered.

The possibility of bringing out and maintaining the bootstrap current at the levels required by fusion plasma condition depends on the capability of plasma of achieving and keeping up a suitable ambient radial profile of pressure. This, in turn, can occur only if the plasma were free from the onset of pernicious unstable modes that are detrimental for plasma's thermal insulation, and, consequently, for the desired pressure profile. Theoretical and experimental results have demonstrated that the capability to impose the desired radial profile of the current is essential: it supports in time the conditions for the overall "current drive" that are necessary for the fusion plasma regime. An independent tool is required for that purpose.

In this chapter we describe the major problem of fusion research represented by the lack so far of a tool capable of driving current in the radial outer half of plasma column in a tokamak machine. Indeed, the available tools can efficiently cover only the inner radial half of plasma.

In the remaining of the Thesis we propose a possible solution of this problem by exploiting the lower hybrid current drive (LHCD) effect that, after its discovery, four decades ago, resulted problematic in being extrapolated at reactor relevant conditions of high density and temperatures of plasma.

3.1 How to exploit potentiality of tokamak plasmas in self-producing steady-state current

Originated in an inductively produced toroidal plasma, the bootstrap current has the attractive feature of having non-inductive nature, i.e., in principle, this current can circulate in steady-state thus contributing to an essential requirement of a reactor.

If properly exploited, this option could solve the dramatic problem of huge costs of multi-megawatt tools necessary for strongly heating the plasma and driving current of several tens of mega-amperes. However the bootstrap current cannot be set autonomously as it intimately depends on the pressure radial profiles of plasma that are created by the nuclear self-heating, mostly via collisional slowing-down of fusion alpha nuclei on thermal electrons. These profiles, in turn, dictate the character of turbulence and turbulent transport on the characteristic spatial-temporal scales of burning plasmas, which represent complex self-

organized systems.
In summary, fusion energy research has to manage with the problematic loop that links together: i) the redial profile of plasma current density, ii) the onset of unstable modes and, iii) their detrimental effect on the pressure profile that ultimately imposes the bootstrap current profile. The latter current must be a large enough fraction of the total plasma current in order to successfully manage with costs of the heating and current drive tools, condition essential for envisaging a thermonuclear reactor.
A major problem of the present research consists in how to actively drive current at outer radii of the plasma column, where a strong bootstrap fraction naturally develops in reactor relevant plasma configuration. Indeed, as shown in Chapter 2, bootstrap current is originated by the plasma pressure gradient which is stronger at the radial periphery of the plasma column since a reactor would operate with high values of density (~10^{20} m^{-3}) and temperature (>10 keV) even at large radii (normalised minor radius: r/a ~0.9). To control, especially at these layers, the onset of unstable modes, detrimental for maintaining local conditions of high density and temperature of plasma and, consequently, high fraction of bootstrap current, is of paramount importance for a reactor.
Unfortunately, the current drive tools envisaged so far for ITER have poor efficiency of current drive and insufficient accuracy in tailoring the current profile, as necessary for control of unstable modes. Most of the methods used to heat plasma can also be used to drive current. It therefore makes sense to extend the discussion of heating (done in Sec.2) to include current drive (discussed in Sec. 3).

Tools for current drive are based on the injection in the plasma of strong powers (of the order of hundred megawatt) of neutral beam (NB) and electron-cyclotron radio frequency (RF). This involves a wide variety of techniques ranging from very high-power neutral beams to millimetre wavelength of megawatt microwave sources.

3.2 Plasma heating

To understand the heating issues, we consider first ohmic heating. The toroidal current induced by the transformer in a tokamak produces ohmic heating. This is the simplest method in terms of the technology. However, the resistivity of a plasma decreases with temperature: $\eta \propto 1/T\ 3/2$. Thus, as the ohmic current increases the heating efficiency decreases. The analysis shows that for typical parameters in a tokamak reactor the maximum temperature achievable by ohmic heating is about T <~3 keV. This is not enough for the alpha power to dominate. Some other form of auxiliary heating is required.

The first option discussed is neutral beam heating. Here, a high-energy beam of either neutral deuterium or neutral tritium atoms is injected into the plasma. Heating takes place as follows. Neutral beam atoms are unaffected by the magnetic field. Thus beam atoms propagate in a straight line until they are ionized by collisions with the background plasma. Once ionized, the beam particles are confined by the magnetic field and gradually give up their energy to the plasma by Coulomb collisions. Since the heating mechanism depends on classical collisions it should reliably extrapolate to reactor grade plasmas. In terms of operation, the energy of the beam clearly must be much higher than the plasma temperature for good heating. The actual value of the energy is determined by the requirement that the beam be able to penetrate to the center of the plasma to produce central heating.

This requirement poses the main problem for neutral beam heating and is technological in nature. Existing neutral beam systems are driven by positive ion sources, which have good efficiency up to about 100 keV. This is sufficient for present day experiments. ITER and fusion reactors, because of their higher density and larger size, require 1 MeV beams for good penetration. This goal can be accomplished using a negative ion source to drive the neutral beam system. However, the technology is substantially more difficult and is not yet readily available. A major research and development program is underway to develop such negative ion sources and is expected to have been successful by the time they are needed for ITER.

A second option for auxiliary heating is the use of radio frequency (RF) waves. Here, high-frequency electromagnetic waves are launched into the plasma from an external source. The heating mechanism is similar to that in a microwave oven. When the applied frequency is carefully chosen to match the natural resonant frequency of the food, or in this case the plasma, there is a strong absorption of energy, which is converted into heat. There are several natural resonant frequencies of interest in plasma: the cyclotron frequencies of the electrons and ions, and their cyclotron harmonics. Heating at the resonant frequencies of the electrons is known as electron cyclotron heating (ECH). For the ions it is ion cyclotron heating (ICH). An interesting feature of ECH and ICH is that the resonant absorption takes place by a mechanism known as "collision-less damping." Absorption does not depend on collisions as in a microwave oven.

While both ECH and ICH can produce a strong absorption of energy at the centre of the plasma, both methods also face technological problems. For ECH the difficulty is that high-power, steady state gyrotron sources at the required frequency of 140 GHz are not yet readily available. For ICH the difficulty is that an antenna must be placed very close to the surface of the plasma to insure good coupling of the wave energy to the plasma. This leads to problems of arcing and plasma breakdown. Substantial research and development programs are underway and it is expected that successful solutions will have been found by the time they are needed for ITER.

Table 3.1. Approximate relative cost per watt of auxiliary heating power options

Option	***Requirement***	***Cost ($/W)***
Negative ion beam	1 MeV	4
ICH	40 MHz	2
ECH	140 GHz	6
LHCD	3 GHz	3

3.3 Current drive by neutral beam

This method consists in injecting neutral beams tangentially into the plasma, generating a toroidal momentum parallel to the direction of injection. Part of this momentum is transferred to electrons through collisions. Electrons flowing with a preferred momentum in the toroidal direction constitute an electric current in the opposite direction (because of the negative charge).

3.4 RF power-based current drive methods

A second method is to launch RF waves at an appropriate microwave frequency. The launching system (i.e., antennas or waveguides) must be designed so that the waves propagate preferentially in the toroidal direction. When this occurs, the waves drag electrons in the wave-troughs. The speeding up of slower electrons in the wave as it travels around the torus produces an electric current opposite to the direction of propagation. The situation is somewhat similar to a surfer catching a wave and then moving with the front.

Each of these methods is successful in driving currents non-inductively in present-day experiments, opening up the possibility of steady state operation with toroidal current. The main difficulty is that current drive is not as efficient as heating. It takes substantial power to drive a modest amount of current. The net result is that a reactor in which all the current must be driven non-inductively would likely lead to an unfavourable overall power balance.

Fortunately, in configurations such as the tokamak, there is a natural self-induced toroidal current arising from toroidal transport phenomena, i.e. the bootstrap current. This rather complex process, which has been observed in all high-performance tokamaks, can generate up to 90% of the total current. Consequently, if only a small fraction of the total current needs to be driven non-inductively, then the overall power balance may become acceptable.

In summary, a variety of methods involving neutral beams and RF power sources can be used to heat and non-inductively drive current in fusion experiments. Both types of methods have been successful for both tasks. From the reactor point of view, the current drive problem is more difficult because of the relatively low efficiency of converting power into toroidal current.

It should be noted that heating and current drive cover a very broad range of topics. The choice of topics discussed here is based on the strategy of focusing on methods that are likely to be relevant to ITER and fusion reactors. For heating these include ohmic heating, neutral beam heating, and electron and ion cyclotron heating. For current drive, the main topic of interest is lower hybrid current drive, to which the Thesis is mostly focused on.

3.5 Effect of current drive in preventing unstable plasma modes

We consider here results of Ref.: R. Cesario, Plasma Phys. Control. Fusion 55 (2013) 045005.
Tokamak experiments performed so far have highlighted the need, for a reactor, of controlling plasma instabilities that occur in the core (saw-tooth) and at large radii (neoclassical tearing and global MHD instabilities, and edge localised modes: ELMs) [1]. It is well known that the saw-tooth depends on the current fraction in the core, and this can be indirectly determined by the fraction imposed in the outer radial half of plasma. The latter is thus important for controlling all the aforementioned instabilities, as reviewed hereafter.

3.5.1 Edge localised modes (ELMs)

The behaviour of plasma eruptions, ELMs, which generally develop in H-mode, resulted linked to the plasma current density at radial layer close to pedestal [1]. The *pedestal* consists in a plasma structure where a large pressure gradient develops. This occurs at normalized minor radius, $x \equiv \frac{r}{a} \approx 0.9$, where *a* corresponds to the last closed magnetic surface (LCMS) of the plasma column. The large "Type I" ELMs seem, indeed, to be triggered by coupled peeling-ballooning modes: the ballooning mode is destabilised by pressure gradient, but stabilised by current density; the peeling mode is destabilised by current density, but stabilised by pressure gradient. The modes can couple, leading to a somewhat complicated stability boundary. In the pedestal, the current and the pressure gradient are coupled via the bootstrap current.
In experiments of JET, the ELMs behaviour resulted sensitive to the fraction of plasma current inductively injected at the edge by the technique of plasma current ramp-up. Signatures of ELM stabilisation were observed on EAST using LHCD. In the latter Reference, it was hypothesised that ELM stabilisation would be the effect of not-axisymmetric perturbation of the magnetic topology at the scrape-off plasma (SOL). However, we argue that such perturbation should be an effect, not the cause, of ELM dynamics, and that the true cause of ELM stabilisation could be, instead, the effect of the axisymmetric current driven by the LHCD tool at large radii, affecting the pedestal stability. Unfortunately, the plasmas shown in the Ref [18] are not supported by measurements of kinetic profiles necessary for performing LHCD analysis. This will be carried out in future work now in progress on EAST.

3.5.2 Global MHD instability

Strong, global MHD modes with low *n* (=1) and *m* (=2) manifest in experiments aimed at approaching reactor-relevant condition of confinement of large plasma volumes, and prevent the self-sustainment of on improved H-mode phase. Such phenomenon seemed prevented, indeed, prolonging the phase with high normalised β ($\beta_N \approx 2.8$) for the whole duration of the main heating power of experiments of JET, where ITER-relevant conditions of plasma configuration of high triangularity (d≃0.4) and low q_{95} (≃5) were produced, see Figure 3.1 (from Ref.: R. Cesario, et al., Plasma Phys. Controlled Fusion 2013).

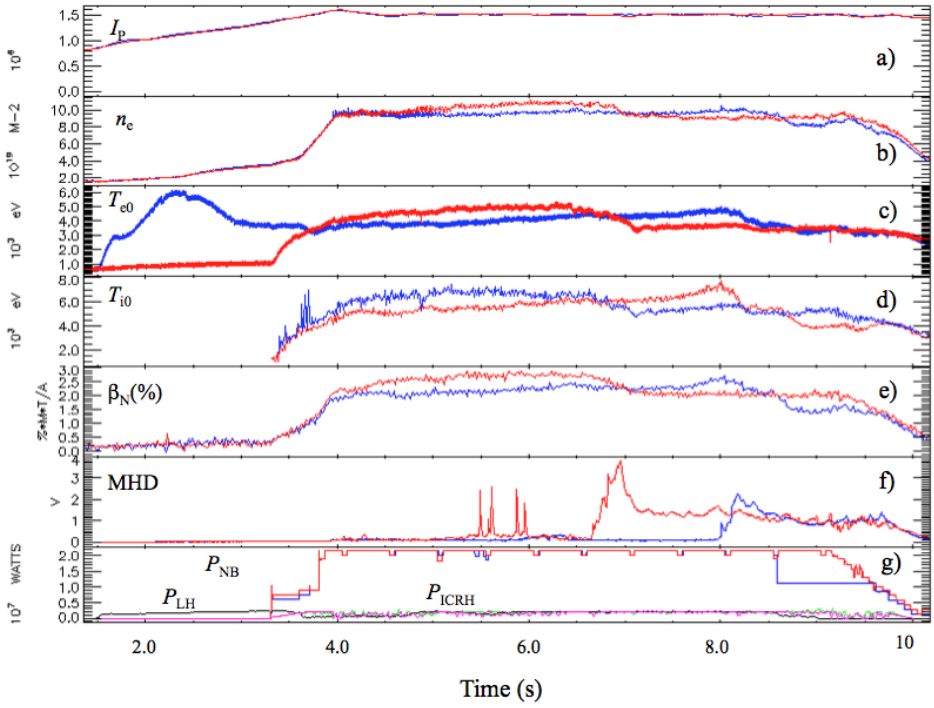

Figure 3.1 (from Ref. R. Cesario, L. Amicucci et al., Plasma Phys. Control. Fusion 55 (2013) 045005). Time traces of the main parameters of two experiments considered in the modelling: discharges 70069 (red lines), 70068 (blue lines). a) plasma current, b) line-averaged plasma density, central temperature of c) electrons (from ECE), d) ions, e) β_N, f) MHD (mode 2,1), g) NB power, ICRH power: discharge 70069 (magenta line), discharge 70068 (green line), LH power only in discharge 70068 (black line).

Discharges, whose main parameters waveforms are displayed in Fig. 3.1, are performed under same operating conditions suited for producing a low neutral density at the plasma edge before NB power (≈20MW) injection. In shot not exhibiting a sustained high b_N phase, some LHCD (of about 1MW) is coupled in prelude phase, which consequently produces a slightly reversed initial *q*-profile, with higher magnetic shear at large radii, which was recognised as not suitable for enabling self-sustainment of high β_N phase. The latter occurs, instead, in shot produced performing only the natural ohmic prelude, which is accompanied by initial lower shear. The high β_N phase lasts up to about half of the time duration of NB power injection, and collapses in concomitance of strong MHD instability.

The aforementioned behaviour was recognised to be a consequence of insufficient CD. Indeed, modelling analysis found the plasma with sustained high b_N phase to be stable to infinite-*n* ballooning modes, thanks to low magnetic shear condition produced by a higher bootstrap current than in the compared shot. Namely, this high performance plasma exhibited a bigger margin of stability minimum shear at the plasma periphery ($Ds_{min}\approx 4.0$, $b_{Nmax}\approx 2.8$ for discharge 70069) than the compared plasma with lower and not sustained b_N ($Ds_{min}\approx 2.3$, $b_{Nmax}\approx 2.6$ for discharge 70068) shown in Fig. 3.1 (Ds_{min} is the minimum distance in magnetic shear between the experimental plasma and the stability boundary). Such margin of stability is lost at the time (about 6.5s) of the onset of strong MHD.
Consequently, the bootstrap current fraction alone would not be sufficient for freezing the current profile, which, in these discharges, continues diffusing in contrast to stability requirement.

These results indicate that, in experiments aiming at approaching ITER-relevant regimes, the bootstrap current fraction, although essential for building condition of high confinement, is insufficient by itself for enabling the evolution of this phase in the necessary context of stability, in the lack of on independent and flexible CD tool at large radii.
Solution of this deficiency can be found considering the lower hybrid current drive (LHCD) effect, which this thesis in focused on.

Chapter 4

4 Plasma waves for driving current in reactor plasmas

We show here the analytical derivation of noticeable plasma waves named lower hybrid (LH) waves. The name refers to the mixed dynamic of both electrons and ions, which is associated to the coherent motion of plasma particles in the radiofrequency electric field. The analytical derivation of the LH waves would not clearly explain the reason of the "hybrid' term. This will be originally justified here and schematised using analogy with acoustic waves. This way, it is clearly understood the special features of LH waves of carrying strong power into the core of high density plasma, and drive current with high efficiency deriving from their essence of quasi-electrostatic, slow plasma waves.

LH waves are evanescent in the vacuum and exhibit the peculiar feature of efficiently transfer momentum to plasma electrons free of moving along the line of the static magnetic field, $\mathbf{B_0}$*, utilised for trapping the plasma into the toroidal chamber of tokamak machine. This produces the lower hybrid current drive (LHCD) effect.*

Wave equation shows that microwave power at several gigahertz can be coupled to these waves from the plasma edge by a suitable antenna capable of satisfying the conditions of: i) electric field polarisation: $\mathbf{E_{rf}}$ // $\mathbf{B_0}$*, ii) phase velocity slower than light speed and, iii) sufficiently high plasma density at the antenna-plasma interface (i.e.,* $n_{e\_ant} \gtrsim 10^{18}\ m^{-3}$*, suitable for operating frequencies of several gigahertz in order to overcome evanescence condition occurring in the vacuum and at too low plasma density).*

These constraints can be fully satisfied by antenna consisting of a phased array of rectangular waveguides, which optimally fits the gap between magnets of tokamak machines.

The LHCD effect is also summarised, consisting in the interaction of the launched antenna spectrum with finite extent of power spectrum in refractive index and the distribution function of plasma electrons.

The major problems presented by this method, and the relative solutions that have been recently found by ENEA-Frascati, will be discussed in the remaining part of the Thesis.

4.1 Introduction

The lower hybrid current drive (LHCD) effect was discovered in 1980 at Princeton (USA) on the basis of theoretical prediction [2,3]. It is the most efficient concept available so far for driving non-inductive current in tokamak plasmas, useful for producing the steady-state regime required by reactor.

This method utilises multi-megawatt RF power at the frequency of several gigahertz, externally launched in a reactor by means of antennas consisting in phased arrays of rectangular waveguides, faced to plasma edge. These antennas fit the tokamak's magnet gaps which represents a further advantage for developing

a compact fusion reactor, besides overcoming the pernicious limitation of transient operation imposed by inductive nature of the tokamak concept.

Since discovery, the LHCD tool was considered as essential for making viable a tokamak fusion reactor, but two major problems have made difficult so far the extrapolation of the LHCD effect to reactor plasma conditions.
The first problem, consisting in parasitic phenomena of plasma edge that prevent the launched RF power to penetrate into the high-density plasma bulk, has been recently solved [12] by experiments performed following the guidelines of previous theoretical predictions [13,14]. This issue will be discussed in the next Chapter.
The remaining major conceptual problem exhibited by the LHCD method consists in the circumstance that the high electron temperature ($T_e \approx 8$ keV), that in a reactor is foreseen even at large radii of the plasma column, would make the deposition of the RF power coupled by the antenna too far out in the plasma, as shown by numerical results [15]. This problem and relative solution [16] will be discussed in Chapter 6.

4.2 Wave equation of the lower hybrid (LH) plasma modes

We derive here the wave equation for the electric field $\underline{E}$ in the frequency range from the ion-cyclotron and electron cyclotron resonant frequencies. The relevant geometry is shown in Figure 4.1. The linear limit of wave is considered, i.e., the wave is assumed of small amplitude and no further perturbations are present in the plasma. The latter is considered under uniform magnetic field and cold, i.e., the constitutive relations are independent of temperature and particle velocities. Reference [11] has been followed. Algebraic manipulations, not contained in this Reference, have been explicated here with the aim of better understanding the way necessary for obtaining the important conditions for existence of lower hybrid waves.

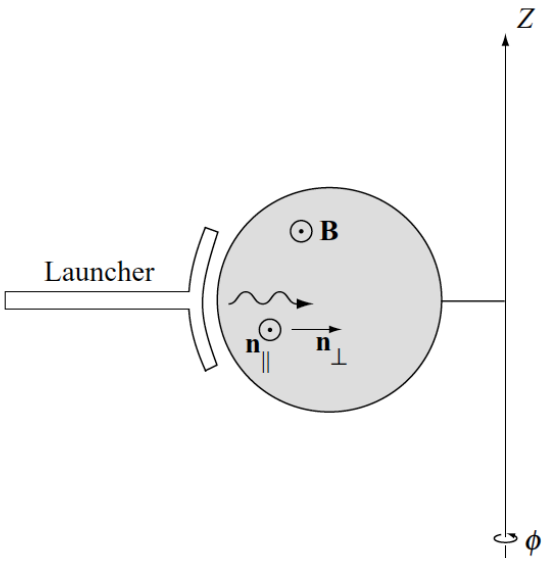

Figure 4.1. Schematic diagram of a low-field, outside launch in a toroidal geometry. Note the components of the refractive index vector: $n//$ and $n\perp$.

The Maxwell equations written in the Gaussian system are:

$$\begin{cases} \nabla \times \underline{E} = -\dfrac{1}{c}\dfrac{\partial \underline{B}}{\partial t} \\ \nabla \times \underline{H} = \dfrac{1}{c}\dfrac{\partial \underline{D}}{\partial t} + \dfrac{4\pi}{c}\underline{J} \\ \nabla \cdot \underline{D} = 4\pi\rho \\ \nabla \cdot \underline{B} = 0 \end{cases} \qquad \text{(4.1a,b,c,d)}$$

where we have considered: $\mu \cong \mu_0$ e $\varepsilon \cong \varepsilon_0$, $\mu \cong 1$ and $\varepsilon \cong 1$. The constitutive equations are:

$$\begin{cases} \underline{D} \cong \underline{E} \\ \underline{B} \cong \underline{H} \end{cases} \qquad \text{(4.2a,b)}$$

and Eqs. 4.1a,b,c,d can be written as:

$$\begin{cases} \nabla \times \underline{E} = -\dfrac{1}{c}\dfrac{\partial \underline{H}}{\partial t} \\ \nabla \times \underline{H} = \dfrac{1}{c}\dfrac{\partial \underline{E}}{\partial t} + \dfrac{4\pi}{c}\underline{J} \\ \nabla \cdot \underline{E} = 4\pi\rho \\ \nabla \cdot \underline{H} = 0 \end{cases} \qquad \text{(2.1a',b',c',d')}$$

The wave equation can be obtained utilising in Eq. 4.1a' the Schwarz theorem on the commutation of the partial derivatives:

$$\nabla \times \nabla \times \underline{E} = \nabla \times \left(-\frac{1}{c}\frac{\partial \underline{H}}{\partial t} \right) = -\frac{1}{c}\nabla \times \frac{\partial \underline{H}}{\partial t} = -\frac{1}{c}\frac{\partial}{\partial t}\left(\nabla \times \underline{H}\right)$$

From Eq.4.2b we obtain:

$$\nabla \times \nabla \times \underline{E} = -\frac{1}{c}\frac{\partial}{\partial t}\left(\nabla \times \underline{H}\right) = -\frac{1}{c}\frac{\partial}{\partial t}\left(\frac{1}{c}\frac{\partial \underline{E}}{\partial t} + \frac{4\pi}{c}\underline{J} \right) = -\frac{1}{c^2}\frac{\partial^2 \underline{E}}{\partial t^2} - \frac{4\pi}{c^2}\frac{\partial \underline{J}}{\partial t}$$

From the constitutive equation displaying the current density $\underline{J} = \underline{\underline{\sigma}} \cdot \underline{E}$, where $\underline{\underline{\sigma}}$ is the conductivity tensor, we have:

$$\nabla\times\nabla\times\underline{E}=-\frac{1}{c^2}\frac{\partial^2\underline{E}}{\partial t^2}-\frac{4\pi}{c^2}\frac{\partial\underline{J}}{\partial t}=-\frac{1}{c^2}\frac{\partial^2\underline{E}}{\partial t^2}-\frac{4\pi}{c^2}\frac{\partial\left(\underline{\underline{\sigma}}\cdot\underline{E}\right)}{\partial t}=-\frac{1}{c^2}\frac{\partial^2\underline{E}}{\partial t^2}-\frac{4\pi}{c^2}\underline{\underline{\sigma}}\cdot\frac{\partial\underline{E}}{\partial t}\Rightarrow$$

$$\Rightarrow\nabla\times\nabla\times\underline{E}=-\frac{1}{c^2}\frac{\partial^2\underline{E}}{\partial t^2}-\frac{4\pi}{c^2}\underline{\underline{\sigma}}\cdot\frac{\partial\underline{E}}{\partial t} \tag{4.3}$$

Consider the electric field in a form of plane wave:

$$\underline{E}(x,y,z,t)=\underline{E}_0e^{-j\left(\underline{k}\cdot\underline{r}-\omega t\right)}$$

and the respective time derivatives:

$$\begin{cases}\dfrac{\partial}{\partial t}\underline{E}_0e^{-j\left(\underline{k}\cdot\underline{r}-\omega t\right)}=\underline{E}_0e^{-j\underline{k}\cdot\underline{r}}\dfrac{\partial}{\partial t}e^{j\omega t}=\underline{E}_0e^{-j\underline{k}\cdot\underline{r}}j\omega e^{j\omega t}=j\omega\underline{E}_0e^{-j\left(\underline{k}\cdot\underline{r}-\omega t\right)}=j\omega\underline{E}\Rightarrow\dfrac{\partial}{\partial t}=j\omega\\ \dfrac{\partial^2}{\partial t^2}=j\omega\cdot j\omega=-\omega^2\end{cases} \tag{4.4}$$

we obtain:

$$\nabla\times\nabla\times\underline{E}=-\frac{1}{c^2}\left(-\omega^2\right)\underline{E}-\frac{4\pi}{c^2}\left(j\omega\right)\underline{\underline{\sigma}}\cdot\underline{E}=\frac{\omega^2}{c^2}\underline{E}-j\frac{4\pi\omega}{c^2}\underline{\underline{\sigma}}\cdot\underline{E} \tag{4.3'}$$

Using the notation: $\underline{E}=\underline{\underline{I}}\cdot\underline{E}$, where $\underline{\underline{I}}$ is the identity matrix we obtain:

$$\nabla\times\nabla\times\underline{E}-\frac{\omega^2}{c^2}\underline{E}+j\frac{4\pi\omega}{c^2}\underline{\underline{\sigma}}\cdot\underline{E}=\nabla\times\nabla\times\underline{E}-\frac{\omega^2}{c^2}\left(\underline{\underline{I}}\cdot\underline{E}\right)+j\frac{4\pi\omega}{c^2}\underline{\underline{\sigma}}\cdot\left(\underline{\underline{I}}\cdot\underline{E}\right)=$$

$$=\nabla\times\nabla\times\underline{E}-\frac{\omega^2}{c^2}\left(\underline{\underline{I}}-j\frac{4\pi\underline{\underline{\sigma}}}{\omega}\right)\cdot\underline{E}=0$$

where $\underline{\underline{I}} - j\frac{4\pi\underline{\underline{\sigma}}}{\omega} = \underline{\underline{K}}$ is the dielectric tensor.

The wave equation is:

$$\nabla \times \nabla \times \underline{E} - \frac{\omega^2}{c^2}\underline{\underline{K}} \cdot \underline{E} = 0 \qquad (4.5)$$

The dielectric tensor in a Cartesian system has the form [Stix, 1966]:

$$\underline{\underline{K}} = \begin{bmatrix} S & -jD & 0 \\ jD & S & 0 \\ 0 & 0 & P \end{bmatrix}$$

whose elements can be written in the relevant range of frequencies: $\omega_{ci} << \omega << \omega_{ce}$ in the form:

$$\begin{cases} S = 1 + \dfrac{\omega_{pe}^2}{\omega_{ce}^2} - \dfrac{\omega_{pi}^2}{\omega^2} \\ P = 1 - \dfrac{\omega_{pe}^2}{\omega^2} \\ D = \dfrac{\omega_{pe}^2}{\omega\omega_{ce}} \end{cases} \qquad (4.6)$$

Considering the wavevector notation: $\underline{k} = k_x\hat{i} + k_y\hat{j} + k_z\hat{k}$, Eq. 4.5 can be written as:

$$\nabla \times \nabla \times \underline{E} - \frac{\omega^2}{c^2}\underline{\underline{K}} \cdot \underline{E} = \nabla\left(\nabla \cdot \underline{E}\right) - \nabla^2\underline{E} - \frac{\omega^2}{c^2}\underline{\underline{K}} \cdot \underline{E} = 0 \qquad (4.5')$$

obtaining:

$$\nabla^2\underline{E} = \nabla^2\left(\underline{E}_0 e^{-j(\underline{k}\bullet\underline{r}-\omega t)}\right) = \underline{E}_0\nabla^2\left(e^{-j(\underline{k}\bullet\underline{r}-\omega t)}\right) = \underline{E}_0\left(\frac{\partial^2}{\partial x^2} + \frac{\partial^2}{\partial y^2} + \frac{\partial^2}{\partial z^2}\right)e^{-j\left(k_x x + k_y y + k_z z - \omega t\right)}$$

having utilised the relations:

$$\frac{\partial}{\partial x}\left\{e^{-j\left(k_x x+k_y y+k_z z-\omega t\right)}\right\}=-jk_x e^{-j\left(k_x x+k_y y+k_z z-\omega t\right)}=-jk_x e^{-j\left(\underline{k}\cdot\underline{r}-\omega t\right)}$$

$$\frac{\partial^2}{\partial x^2}\left\{e^{-j\left(k_x x+k_y y+k_z z-\omega t\right)}\right\}=-jk_x\left\{-jk_x e^{-j\left(k_x x+k_y y+k_z z-\omega t\right)}\right\}=-k_x^2 e^{-j\left(k_x x+k_y y+k_z z-\omega t\right)}=-k_x^2 e^{-j\left(\underline{k}\cdot\underline{r}-\omega t\right)}$$

Finally:

$$\begin{aligned}&\nabla^2\underline{E}=\underline{E}_0\left(\frac{\partial^2}{\partial x^2}+\frac{\partial^2}{\partial y^2}+\frac{\partial^2}{\partial z^2}\right)e^{-j\left(k_x x+k_y y+k_z z-\omega t\right)}=\\&=\underline{E}_0\left\{\frac{\partial^2}{\partial x^2}e^{-j\left(k_x x+k_y y+k_z z-\omega t\right)}+\frac{\partial^2}{\partial y^2}e^{-j\left(k_x x+k_y y+k_z z-\omega t\right)}+\frac{\partial^2}{\partial z^2}e^{-j\left(k_x x+k_y y+k_z z-\omega t\right)}\right\}=\\&=\underline{E}_0\left(-{k_x}^2-{k_y}^2-{k_z}^2\right)e^{-j\left(\underline{k}\cdot\underline{r}-\omega t\right)}=-k^2\underline{E}_0 e^{-j\left(\underline{k}\cdot\underline{r}-\omega t\right)}=-k^2\underline{E}\Rightarrow\nabla^2\underline{E}=-k^2\underline{E}\end{aligned}\qquad(4.7a)$$

In regard to the further differential operator term in Eq. 4.5' we have:

$$\begin{aligned}&\nabla\cdot\underline{E}=\nabla\cdot\left(\underline{E}_0 e^{-j\left(\underline{k}\cdot\underline{r}-\omega t\right)}\right)=\nabla\cdot\left\{\left(E_{0x}\hat{i}+E_{0y}\hat{j}+E_{0z}\hat{k}\right)e^{-j\left(k_x x+k_y y+k_z z-\omega t\right)}\right\}=\\&=\left(\frac{\partial}{\partial x}\hat{i}+\frac{\partial}{\partial y}\hat{j}+\frac{\partial}{\partial z}\hat{k}\right)\cdot\left\{\left(E_{0x}\hat{i}+E_{0y}\hat{j}+E_{0z}\hat{k}\right)e^{-j\left(k_x x+k_y y+k_z z-\omega t\right)}\right\}=\\&=\frac{\partial}{\partial x}\left\{E_{0x}e^{-j\left(k_x x+k_y y+k_z z-\omega t\right)}\right\}+\frac{\partial}{\partial y}\left\{E_{0y}e^{-j\left(k_x x+k_y y+k_z z-\omega t\right)}\right\}+\frac{\partial}{\partial z}\left\{E_{0z}e^{-j\left(k_x x+k_y y+k_z z-\omega t\right)}\right\}=\\&=-jk_x E_{0x}e^{-j\left(k_x x+k_y y+k_z z-\omega t\right)}-jk_y E_{0y}e^{-j\left(k_x x+k_y y+k_z z-\omega t\right)}-jk_z E_{0z}e^{-j\left(k_x x+k_y y+k_z z-\omega t\right)}=\\&=-j\left(k_x E_{0x}+k_y E_{0y}+k_z E_{0z}\right)e^{-j\left(\underline{k}\cdot\underline{r}-\omega t\right)}=-j\underline{k}\cdot\underline{E}_0 e^{-j\left(\underline{k}\cdot\underline{r}-\omega t\right)}=-j\underline{k}\cdot\underline{E}\Rightarrow\nabla\cdot\underline{E}=-j\underline{k}\cdot\underline{E}\end{aligned}\qquad(4.7b)$$

obtaining:

$$\begin{aligned}&\nabla\left(\nabla\cdot\underline{E}\right)=\nabla\left(-j\underline{k}\cdot\underline{E}_o e^{-j\left(\underline{k}\cdot\underline{r}-\omega t\right)}\right)=\left\{\frac{\partial}{\partial x}\hat{i}+\frac{\partial}{\partial y}\hat{j}+\frac{\partial}{\partial z}\hat{k}\right\}\left(-j\underline{k}\cdot\underline{E}_o e^{-j\left(\underline{k}\cdot\underline{r}-\omega t\right)}\right)=\\&=\left\{\frac{\partial}{\partial x}\hat{i}+\frac{\partial}{\partial y}\hat{j}+\frac{\partial}{\partial z}\hat{k}\right\}\left\{-j\left(k_x E_{0x}+k_y E_{0y}+k_z E_{0z}\right)e^{-j\left(k_x x+k_y y+k_z z-\omega t\right)}\right\}=\\&=-j\left(k_x E_{0x}+k_y E_{0y}+k_z E_{0z}\right)\left\{\frac{\partial}{\partial x}e^{-j\left(k_x x+k_y y+k_z z-\omega t\right)}\hat{i}+\frac{\partial}{\partial y}e^{-j\left(k_x x+k_y y+k_z z-\omega t\right)}\hat{j}+\frac{\partial}{\partial z}e^{-j\left(k_x x+k_y y+k_z z-\omega t\right)}\hat{k}\right\}=\\&=-j\left(k_x E_{0x}+k_y E_{0y}+k_z E_{0z}\right)\left\{-jk_x e^{-j\left(k_x x+k_y y+k_z z-\omega t\right)}\hat{i}-jk_y e^{-j\left(k_x x+k_y y+k_z z-\omega t\right)}\hat{j}+-jk_z e^{-j\left(k_x x+k_y y+k_z z-\omega t\right)}\hat{k}\right\}=\\&=\left\{j\underline{k}\cdot\underline{E}_0 e^{-j\left(k_x x+k_y y+k_z z-\omega t\right)}\right\}j\left(k_x\hat{i}+k_y\hat{j}+k_z\hat{k}\right)=j\underline{k}\cdot\underline{E}j\underline{k}=-\underline{k}\left(\underline{k}\cdot\underline{E}\right)\Rightarrow\nabla\left(\nabla\cdot\underline{E}\right)=-\underline{k}\left(\underline{k}\cdot\underline{E}\right)\end{aligned}$$

(4.7c)

Substituting in Eq. 4.5' we obtain:

$$\nabla\left(\nabla\cdot\underline{E}\right)-\nabla^2\underline{E}-\frac{\omega^2}{c^2}\underline{\underline{K}}\cdot\underline{E}=-\underline{k}\left(\underline{k}\cdot\underline{E}\right)+k^2\underline{E}-\frac{\omega^2}{c^2}\underline{\underline{K}}\cdot\underline{E}=0$$

and considering the definition of wave refractive index: $\underline{k}=\left(\omega/c\right)\underline{n}$, we have:

$$\nabla\left(\nabla\cdot\underline{E}\right)-\nabla^2\underline{E}-\frac{\omega^2}{c^2}\underline{\underline{K}}\cdot\underline{E}=-\underline{k}\left(\underline{k}\cdot\underline{E}\right)+k^2\underline{E}-\frac{\omega^2}{c^2}\underline{\underline{K}}\cdot\underline{E}=-\frac{\omega^2}{c^2}\underline{n}\left(\underline{n}\cdot\underline{E}\right)+\frac{\omega^2}{c^2}n^2\underline{E}-\frac{\omega^2}{c^2}\underline{\underline{K}}\cdot\underline{E}=$$
$$=-\frac{\omega^2}{c^2}\underline{n}\left(\underline{n}\cdot\underline{E}_0e^{-j(\underline{k}\cdot\underline{r}-\omega t)}\right)+\frac{\omega^2}{c^2}n^2\underline{E}_0e^{-j(\underline{k}\cdot\underline{r}-\omega t)}-\frac{\omega^2}{c^2}\underline{\underline{K}}\cdot\underline{E}_0e^{-j(\underline{k}\cdot\underline{r}-\omega t)}=0$$

Dividing by $-\omega^2/c^2$ e $e^{-j(\underline{k}\cdot\underline{r}-\omega t)}$ we write the wave equation expressed in function of $\underline{n}$:

$$\underline{n}\left(\underline{n}\cdot\underline{E}_0\right)-n^2\underline{E}_0+\underline{\underline{K}}\cdot\underline{E}_0=0 \qquad (4.8)$$

We consequently obtain:

$$\underline{n}\left(\underline{n}\cdot\underline{E}_0\right)=\underline{n}\left\{\left(n_x\hat{i}+n_y\hat{j}+n_z\hat{k}\right)\cdot\left(E_{0x}\hat{i}+E_{0y}\hat{j}+E_{0z}\hat{k}\right)\right\}=\underline{n}\left(n_xE_{0x}+n_yE_{0y}+n_zE_{0z}\right)=$$
$$=\left(n_x\hat{i}+n_y\hat{j}+n_z\hat{k}\right)\left(n_xE_{0x}+n_yE_{0y}+n_zE_{0z}\right)=$$
$$=\left(n_x^2E_{0x}\hat{i}+n_xn_yE_{0y}\hat{i}+n_xn_zE_{0z}\hat{i}\right)+\left(n_yn_xE_{0x}\hat{j}+n_y^2E_{0y}\hat{j}+n_yn_zE_{0z}\hat{j}\right)+\left(n_zn_xE_{0x}\hat{k}+n_zn_yE_{0y}\hat{k}+n_z^2E_{0z}\hat{k}\right)=$$
$$=E_{0x}\left(n_x^2\hat{i}+n_xn_y\hat{j}+n_xn_z\hat{k}\right)+E_{oy}\left(n_xn_y\hat{i}+n_y^2\hat{j}+n_yn_z\hat{k}\right)+E_{oz}\left(n_xn_z\hat{i}+n_yn_z\hat{j}+n_z^2\hat{k}\right)=$$
$$=\left(\hat{i}\quad\hat{j}\quad\hat{k}\right)\left[\begin{pmatrix}n_x^2 & n_xn_y & n_xn_z\\ n_yn_x & n_y^2 & n_yn_z\\ n_zn_x & n_zn_y & n_z^2\end{pmatrix}\begin{pmatrix}E_{0x}\\E_{0y}\\E_{0z}\end{pmatrix}\right] \qquad (4.9a)$$

For calculations we need considering the second term:

$$n^2\underline{E}_0=\left(n_x{}^2+n_y{}^2+n_z{}^2\right)\left(E_{0x}\hat{i}+E_{0y}\hat{j}+E_{0z}\hat{k}\right)=$$
$$=E_{0x}\left(n_x{}^2+n_y{}^2+n_z{}^2\right)\hat{i}+E_{0y}\left(n_x{}^2+n_y{}^2+n_z{}^2\right)\hat{j}+E_{0z}\left(n_x{}^2+n_y{}^2+n_z{}^2\right)\hat{k}= \qquad (4.9b)$$
$$=\left(\hat{i}\quad\hat{j}\quad\hat{k}\right)\left[\begin{pmatrix}n_x^2+n_y^2+n_z^2 & 0 & 0\\ 0 & n_x^2+n_y^2+n_z^2 & 0\\ 0 & 0 & n_x^2+n_y^2+n_z^2\end{pmatrix}\begin{pmatrix}E_{0x}\\E_{0y}\\E_{0z}\end{pmatrix}\right]$$

and the last term:

$$\underline{\underline{K}}\cdot\underline{E}_0=\left(\hat{i}\quad\hat{j}\quad\hat{k}\right)\left[\begin{pmatrix}S & -jD & 0\\ jD & S & 0\\ 0 & 0 & P\end{pmatrix}\begin{pmatrix}E_{0x}\\E_{0y}\\E_{0z}\end{pmatrix}\right] \qquad (4.9c)$$

Substituting the relations 4.9a,b,c in Eq. 4.8, we obtain the tensorial equation

$$\underline{n}\left(\underline{n}\cdot\underline{E}_0\right)-n^2\underline{E}_0+\underline{\underline{K}}\cdot\underline{E}_0 =$$

$$=\begin{pmatrix}\hat{i} & \hat{j} & \hat{k}\end{pmatrix}\left[\begin{pmatrix} n_x^{\,2} & n_xn_y & n_xn_z \\ n_yn_x & n_y^{\,2} & n_yn_z \\ n_zn_x & n_zn_y & n_z^{\,2}\end{pmatrix}\begin{pmatrix}E_{0x}\\E_{0y}\\E_{0z}\end{pmatrix}\right]+$$

$$-\begin{pmatrix}\hat{i} & \hat{j} & \hat{k}\end{pmatrix}\left[\begin{pmatrix} n_x^{\,2}+n_y^{\,2}+n_z^{\,2} & 0 & 0 \\ 0 & n_x^{\,2}+n_y^{\,2}+n_z^{\,2} & 0 \\ 0 & 0 & n_x^{\,2}+n_y^{\,2}+n_z^{\,2}\end{pmatrix}\begin{pmatrix}E_{0x}\\E_{0y}\\E_{0z}\end{pmatrix}\right]+$$

$$+\begin{pmatrix}\hat{i} & \hat{j} & \hat{k}\end{pmatrix}\left[\begin{pmatrix} S & -jD & 0 \\ jD & S & 0 \\ 0 & 0 & P\end{pmatrix}\begin{pmatrix}E_{0x}\\E_{0y}\\E_{0z}\end{pmatrix}\right]=$$

$$=\begin{pmatrix}\hat{i} & \hat{j} & \hat{k}\end{pmatrix}\left[\begin{pmatrix} n_x^{\,2} & n_xn_y & n_xn_z \\ n_yn_x & n_y^{\,2} & n_yn_z \\ n_zn_x & n_zn_y & n_z^{\,2}\end{pmatrix}-\begin{pmatrix} n_x^{\,2}+n_y^{\,2}+n_z^{\,2} & 0 & 0 \\ 0 & n_x^{\,2}+n_y^{\,2}+n_z^{\,2} & 0 \\ 0 & 0 & n_x^{\,2}+n_y^{\,2}+n_z^{\,2}\end{pmatrix}+\begin{pmatrix} S & -jD & 0 \\ jD & S & 0 \\ 0 & 0 & P\end{pmatrix}\right]\begin{pmatrix}E_{0x}\\E_{0y}\\E_{0z}\end{pmatrix}=0$$

By summation of the matrices within square brackets we obtain:

$$\underline{n}\left(\underline{n}\cdot\underline{E}_0\right)-n^2\underline{E}_0+\underline{\underline{K}}\cdot\underline{E}_0=\begin{pmatrix}\hat{i} & \hat{j} & \hat{k}\end{pmatrix}\left[\begin{pmatrix} S-n_y^2-n_z^2 & n_xn_y-jD & n_xn_z \\ n_xn_y+jD & S-n_x^2-n_z^2 & n_yn_z \\ n_xn_z & n_yn_z & S-n_x^2-n_y^2\end{pmatrix}\begin{pmatrix}E_{0x}\\E_{0y}\\E_{0z}\end{pmatrix}\right]=\begin{pmatrix}0\\0\\0\end{pmatrix}$$

and:

$$\begin{pmatrix} S-n_y^2-n_z^2 & n_xn_y-jD & n_xn_z \\ n_xn_y+jD & S-n_x^2-n_z^2 & n_yn_z \\ n_xn_z & n_yn_z & S-n_x^2-n_y^2\end{pmatrix}\begin{pmatrix}E_{0x}\\E_{0y}\\E_{0z}\end{pmatrix}=\begin{pmatrix}0\\0\\0\end{pmatrix}\Rightarrow\Lambda\cdot\underline{E}_0=0 \qquad (4.10)$$

The equation admits not trivial solutions (i.e., E_0=0) for: $\det\Lambda=0$

By applying the Sarrus's rule:

$$\det\Lambda=\begin{vmatrix} S-n_y^2-n_z^2 & n_xn_y-jD & n_xn_z \\ n_xn_y+jD & S-n_x^2-n_z^2 & n_yn_z \\ n_xn_z & n_yn_z & S-n_x^2-n_y^2\end{vmatrix}\begin{matrix} S-n_y^2-n_z^2 & n_xn_y-jD \\ n_xn_y+jD & S-n_x^2-n_z^2 \\ n_xn_z & n_yn_z\end{matrix}=$$

$$=D^2\left(n_x^2+n_y^2-P\right)+\left(n_x^2+n_y^2-n_z^2-S\right)\left[n_z^2P+S\left(n_x^2+n_y^2-P\right)\right] \qquad (4.11)$$

Then, in order to obtain not trivial solutions of Eq. 4.8 we must have:

$$\det\Lambda=D^2\left(n_x^2+n_y^2-P\right)+\left(n_x^2+n_y^2-n_z^2-S\right)\left\{n_z^2P+S\left(n_x^2+n_y^2-P\right)\right\}=0.$$

4.3 Dispersion relation of the lower hybrid (LH) waves

Considering the notations:

$$\begin{cases} n_{//}^2 = n_z^2 \\ n_{\perp}^2 = n_x^2 + n_y^2 \\ n^2 = n_{//}^2 + n_{\perp}^2 \end{cases}$$

we have:

$$Sn_{\perp}^4 + n_{\perp}^2\left(D^2 + Pn_{//}^2 + Sn_{//}^2 - PS - S^2\right) - D^2P + Pn_{//}^4 - 2PSn_{//}^2 + PS^2 =$$
$$= Sn_{\perp}^4 + n_{\perp}^2\left[D^2 + \left(n_{//}^2 - S\right)\left(P + S\right)\right] + P\left[\left(n_{//}^2 - S\right)^2 - D^2\right] = 0$$

where:

$$\begin{cases} A = S \\ B = D^2 + \left(n_{//}^2 - S\right)\left(P + S\right) \\ C = P\left[\left(n_{//}^2 - S\right)^2 - D^2\right] \end{cases}$$

which can be written in compact form:

$$An_{\perp}^4 + Bn_{\perp}^2 + C = 0 \qquad (4.12)$$

Eq. 4.12 is the wave dispersion relation that shows the link between $n_{\perp}$ and $n_{//}$. Solutions of Eq. 4.12 are given by:

$$n_{\perp F,S}^2 = \frac{-B \pm \sqrt{B^2 - 4AC}}{2A} \qquad (4.13)$$

where the following conditions can subsist:

$$\begin{cases} B^2 > 4AC \equiv \Delta > 0 \\ B^2 = 4AC \equiv \Delta = 0 \\ B^2 < 4AC \equiv \Delta < 0 \end{cases}$$

The relevant propagating modes correspond to $\Delta > 0$ which produces two distinct solutions corresponding to fast and slow waves in Eq. 4.13.

In detail, considering the positive sign in Eq. 4.13 and producing Taylor expansion at the first order, we obtain:

$$n_{\perp F}^2 = \frac{-B+\sqrt{B^2-4AC}}{2A} = \frac{-B}{2A} + \frac{1}{2A}\sqrt{B^2-4AC} = \frac{-B}{2A} + \frac{B}{2A}\sqrt{1-\frac{4AC}{B^2}}$$

at the first order we have: $\sqrt{1-x} \cong 1-\frac{x}{2}$ when $|x|<1$ then $\sqrt{1-\frac{4AC}{B^2}} \cong 1-\frac{2AC}{B^2}$ owing to: $\left|\frac{4AC}{B^2}\right| << 1 \Rightarrow B^2 >> 4AC$. Consequently:

$$n_{\perp F}^2 = \frac{-B}{2A} + \frac{B}{2A}\sqrt{1-\frac{4AC}{B^2}} \cong \frac{-B}{2A} + \frac{B}{2A}\left(1-\frac{2AC}{B^2}\right) = -\frac{B}{2A} + \frac{B}{2A} - \frac{C}{B} = -\frac{C}{B} = -\frac{P\left\{\left(n_{//}^2-S\right)^2 - D^2\right\}}{D^2+\left(n_{//}^2-S\right)\left(P+S\right)}$$

(4.14a)

For the slow wave solution, in the limit $\Delta >> 0 \Rightarrow B^2 >> 4AC$ we obtain:

$$n_{\perp S}^2 = \frac{-B-\sqrt{B^2-4AC}}{2A} \cong \frac{-B-\sqrt{B^2}}{2A} = \frac{-B-B}{2A} = -\frac{B}{A} = -\frac{D^2}{S} - \frac{1}{S}\left(n_{//}^2-S\right)\left(P+S\right) \qquad (4.14b)$$

where the following condition holds: $\left(P+S\right)$ $S << P$ since the operating frequency lies in the range between the ion and electron cyclotron resonant frequencies:

$$\begin{cases} \omega_{ci} << \omega << \omega_{ce} \\ \omega_{pe} >> \omega_{pi} \\ \omega << \omega_{pe} << \omega_{ce} \end{cases}$$

By defining:

$$\zeta^{-1} = \frac{\omega_{pe}^2}{\omega^2}$$

we have:

$$\begin{cases} P = 1-\zeta > 0 \\ S = 1+\frac{\omega_{pe}^2}{\omega_{ce}^2} - \frac{\omega_{pi}^2}{\omega^2} = 1+\zeta^{-1}\frac{\omega^2}{\omega_{ce}^2} - \zeta^{-1}\frac{\omega_{pi}^2}{\omega_{pe}^2} \cong 1 \end{cases} \Rightarrow \left(\left|S\right| = \left|1+\frac{{\omega_{pe}}^2}{{\omega_{ce}}^2} - \frac{{\omega_{pi}}^2}{\omega^2}\right|\right) << \left(\left|P\right| = \left|1-\frac{\omega_{pe}^2}{\omega^2}\right|\right)$$

obtaining the approximated solutions of Eq. 4.14 a,b:

$$n_{\perp S}^2 \cong -\frac{D^2}{S} - \frac{P}{S}\left(n_{//}^2 - S\right) \qquad (4.14'a)$$

$$n_{\perp F}^2 \cong \frac{D^2 - \left(n_{//}^2 - S\right)^2}{\left(n_{//}^2 - S\right) + \dfrac{D^2}{P}} \qquad (4.14'b)$$

The slow wave has a resonance defined by: $\omega_{LH} = \omega_{pi} \Big/ \sqrt{1 + \omega_{pe}^2 / \omega_{ce}^2}$ [1] corresponding to $S(\omega) = 0$; Indeed:

$$S(\omega)\Big|_{\omega=\omega_{LH}} = 0 \Rightarrow n_{\perp S}^2 \to \infty \qquad (4.15)$$

$$S(\omega) = 1 + \frac{\omega_{pe}^2}{\omega_{ce}^2} - \frac{\omega_{pi}^2}{\omega^2} \to S(\omega)\Big|_{\omega=\omega_{LH}} = 1 + \frac{\omega_{pe}^2}{\omega_{ce}^2} - \frac{\omega_{pi}^2}{\omega_{LH}^2} = 1 + \frac{\omega_{pe}^2}{\omega_{ce}^2} - \frac{\omega_{pi}^2}{\dfrac{\omega_{pi}^2}{1 + \dfrac{\omega_{pe}^2}{\omega_{ce}^2}}} = 1 + \frac{\omega_{pe}^2}{\omega_{ce}^2} - 1 - \frac{\omega_{pe}^2}{\omega_{ce}^2} = 0$$

and:

$$n_{\perp S}^2 \cong -\frac{D^2}{S} - \frac{1}{S}\left(n_{//}^2 - S\right)\left(P + S\right) = -\frac{D^2}{S} - \frac{n_{//}^2 P}{S} - n_{//}^2 + P + S\Big|_{S=0} \to \infty$$

The term “lower” needs for distinguishing from another resonance, the upper hybrid resonance, which further plasma wave exhibits at much higher frequencies, close to the electron cyclotron resonant frequency.

For fusion relevant plasma densities (~10^{20} m^{-3}), Eq. 4.15 shows that LH waves are propagating plasma modes with frequencies of several gigahertz.

Considering the phase velocity:

$$v_{f//} = \frac{\omega}{k_{//}} = \frac{c}{n_{//}}$$

we have:

$$v_{f//} < c \Rightarrow n_{//} > 1 \text{ for the slow wave}$$

and $v_{f//} > c \Rightarrow n_{//} < 1$ for the fast wave.

We show now the solutions of Eq. 4.12 in terms of slow and fast waves. For the slow wave case, relevant to LHCD effect in object, we can use the following approximation:

$$\Delta >> 0 \Rightarrow B^2 >> 4AC$$

Consider the negative sign in Eq. 4.13. By the condition $\Delta >> 0 \Rightarrow B^2 >> 4AC$ we obtain:

$$n_{\perp S}^2 = \frac{-B-\sqrt{B^2-4AC}}{2A} \cong \frac{-B-\sqrt{B^2}}{2A} = \frac{-B-B}{2A} = -\frac{B}{A} = -\frac{D^2}{S} - \frac{1}{S}\left(n_{//}^2 - S\right)\left(P+S\right) \qquad (4.14b)$$

Since we consider operation frequencies in the range $f \in (0,5GHz - 8GHz)$, the following conditions hold:

$$\begin{cases} \omega_{ci} << \omega << \omega_{ce} \\ \omega_{pe} >> \omega_{pi} \\ \omega << \omega_{pe} << \omega_{ce} \end{cases}$$

Considering the ratio:

$$\zeta^{-1} = \frac{\omega_{pe}^2}{\omega^2}$$

we have:

$$\begin{cases} P = 1-\zeta > 0 \\ S = 1 + \dfrac{\omega_{pe}^2}{\omega_{ce}^2} - \dfrac{\omega_{pi}^2}{\omega^2} = 1 + \zeta^{-1}\dfrac{\omega^2}{\omega_{ce}^2} - \zeta^{-1}\dfrac{\omega_{pi}^2}{\omega_{pe}^2} \cong 1 \end{cases} \Rightarrow \left(\left|S\right| = \left| 1 + \frac{\omega_{pe}{}^2}{\omega_{ce}{}^2} - \frac{\omega_{pi}{}^2}{\omega^2} \right| \right) << \left(\left|P\right| = \left| 1 - \frac{\omega_{pe}^2}{\omega^2} \right| \right)$$

obtaining:

$$n_{\perp S}^2 \cong -\frac{D^2}{S} - \frac{P}{S}\left(n_{//}^2 - S\right) \qquad (4.14'a)$$

$$n_{\perp F}^2 \cong \frac{D^2 - \left(n_{//}^2 - S\right)^2}{\left(n_{//}^2 - S\right) + \dfrac{D^2}{P}} \qquad (4.14'b)$$

The slow wave exhibits a resonance at:

$$\omega_{LH} = \omega_{pi} \Big/ \sqrt{1 + \omega_{pe}^2 / \omega_{ce}^2} \text{ for } S(\omega) = 0.$$

Indeed:

$$S(\omega)\Big|_{\omega=\omega_{LH}} = 0 \Rightarrow n_{\perp S}^2 \to \infty \qquad (4.15)$$

$$S(\omega) = 1 + \frac{\omega_{pe}^2}{\omega_{ce}^2} - \frac{\omega_{pi}^2}{\omega^2} \to S(\omega)\Big|_{\omega=\omega_{LH}} = 1 + \frac{\omega_{pe}^2}{\omega_{ce}^2} - \frac{\omega_{pi}^2}{\omega_{LH}^2} = 1 + \frac{\omega_{pe}^2}{\omega_{ce}^2} - \frac{\omega_{pi}^2}{\dfrac{\omega_{pi}^2}{1 + \dfrac{\omega_{pe}^2}{\omega_{ce}^2}}} = 1 + \frac{\omega_{pe}^2}{\omega_{ce}^2} - 1 - \frac{\omega_{pe}^2}{\omega_{ce}^2} = 0$$

$$n_{\perp S}^2 \cong -\frac{D^2}{S} - \frac{1}{S}\left(n_{//}^2 - S\right)\left(P+S\right) = -\frac{D^2}{S} - \frac{n_{//}^2 P}{S} - n_{//}^2 + P + S\Big|_{S=0} \to \infty$$

4.4 Sketch of the lower hybrid wave

LH waves are quasi-electrostatic modes ($\mathbf{E}_{RF}$ almost aligned to $\mathbf{B}_{RF}$), with phase velocity smaller than the light speed ($n_{//}$>1, $n_{\perp}$>1). Consequently plasma electrons moving at relatively large velocities (typically with v//= 3 – 5 times the thermal velocity) along the magnetic lines of the confinement magnetic field can "feel" the wave electric field, which consequently accelerates the electrons building up plasma current.

Figure 4.2 displays a sketch of LH waves evidencing the "hybrid" dynamic associated the coherent motions of the plasma ions and electrons in the wave electric field. The figure schematises, in the plane perpendicular to the static magnetic field of a tokamak plasma, a quasi-electrostatic (quasi-longitudinal) oscillation, i.e., with electric field and wavevector almost aligned. Moreover the refractive index is very large, which represents a LH wave close to resonance condition occurring at high plasma densities, see Eq. 4.15.

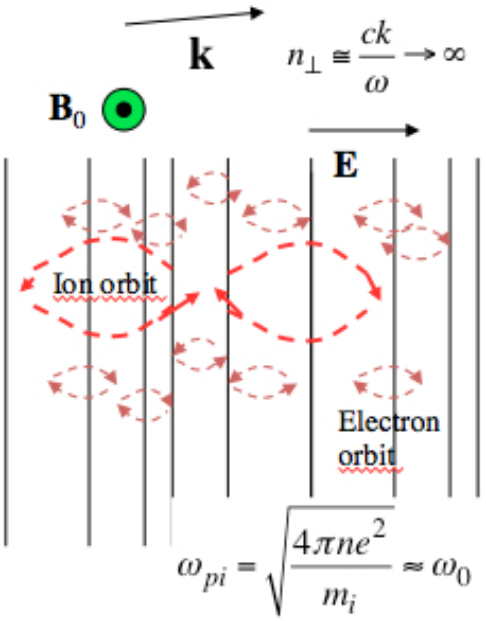

Figure 4.2. Sketch of the ion and electron dynamics in the field of a lower hybrid wave in the plane perpendicular to the static magnetic field of tokamak plasma. The operating frequency ($\omega_0/2\pi$) of the RF system that couples power to these plasma waves is chosen close to the ion plasma frequency ($\omega_{pi}/2\pi$).

The motion of the plasma ions and electrons is imposed to stay in circular orbits by the respective cyclotron resonance conditions; these orbits instantaneously degenerate in ellipses as effect of the RF electric field. Consequently, in the direction perpendicular to the static magnetic field, the plasma behaves as a dielectric that originates sound-like waves produced by the mutual contributions of the ion

and electron dynamics. This corresponds to the case of lower hybrid waves and justifies their name. The dielectric-like behaviour is useful for carrying power into reactor relevant plasmas of high densities and this power can be diverted in current driven by electrons free of moving in the direction parallel to the confinement magnetic field. For this reason, LH waves are capable of carrying power externally coupled to the plasma, and driving current in the direction parallel to the static magnetic field. The complex interaction that establish between the power antenna spectrum having finite size and the electron distribution function, described by quasi-linear (QL) theory [12], is at the basis of the LHCD effect summarised in the next Section.

4.5 The lower hybrid current drive (LHCD) effect

The LHCD mechanism is of greatest importance for driving current in reactor plasma by RF power launched in tokamak plasmas. Indeed, the auxiliary heating methods, based on the injection of strong power of neutral beams (NB), or radio-frequencies at the electron cyclotron (EC) or ion cyclotron (IC) frequencies should be modified to drive a steady state current in the plasma, exhibiting poor efficiency (defined as the number of amperes driven per watt of auxiliary power) especially at outer radii of the plasma column. In this region of the plasma it is where is very important to drive current in order to match the natural bootstrap profiles. This allows lower the cost of too many CD tools and, at the same time, to control the current profile that is necessary to suppress unstable modes, detrimental for achieving higher thermal insulation of large plasma volume, which is mandatory for a thermonuclear reactor.

This problem can be solved by method known as LHCD. Besides the mentioned reasons there is a further reason for this choice: the physics of LHCD is of scientific interest in its own right, representing a very clever way to solve a difficult problem.

The basic idea of LHCD is to launch RF waves into the plasma from the low-field side (outer radii of plasma column) with a strongly asymmetric spectrum in $k_{//}$, see Fig. 4.3.

With such a spectrum, the waves travel predominantly in one direction around the torus (against the direction of the ohmic current flow). For LHCD the wave frequency is typically between the electron and ion cyclotron resonant frequencies.

In this frequency range there is no cyclotron damping. However, for appropriately chosen parameters there can be a strong $l = 0$ Landau wave-particle resonance (at $\omega = k_{//}v_{e//}$) acting on the tail of the distribution function of plasma electrons with parallel velocities meeting the condition $v_{e//} \sim c/n_{//}$ which is provided by the slow wave property of LH waves. At this resonance the electrons absorb energy from the wave, that is, electrons with velocity $\pm v_{e//}$ absorb equal but opposite momentum at $\omega = \pm k_{//}v_{e//}$. In this condition, indeed, electrons feel the wave electric field as an almost constant force that

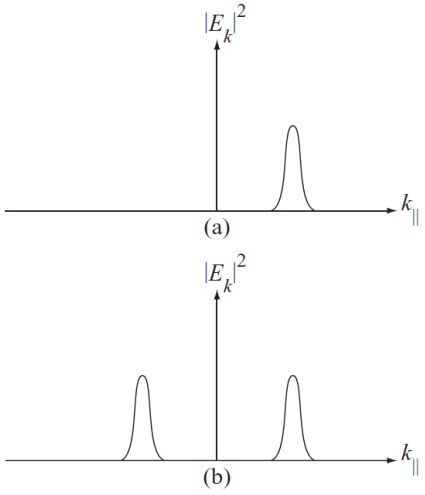

Fig. 4.3. Fourier spectrum of the electric field energy for: the case of (a) current drive (asymmetric) and (b) heating (symmetric).

accelerate them, see Figure 4.4.

If the spectrum is asymmetric, there is also a net transfer of momentum to the electrons. This is in contrast to a heating spectrum, which is typically symmetric in $k_{//}$ and consequently imparts no net momentum to the electrons. For an asymmetric spectrum the gain in electron momentum corresponds to a net toroidal electron fluid flow, or equivalently a net toroidal current. This is the desired current in "current drive."

Note that one must continuously supply RF power to sustain the driven current. The reason is that the heating up of slow electrons and the slowing down of fast electrons produces a distortion of the distribution function away from a Maxwellian in the vicinity of the resonant velocity. Specifically, the electron distribution function (EDF) becomes flattened near $u_{e//} = \omega / k_{//}$ as shown in Fig. 4.4.

Coulomb collisions act to restore the distribution function to a Maxwellian, reducing the current drive to zero. Only by continuously driving the system with auxiliary power can restore the asymmetry in the distribution function and the corresponding current drive be maintained. The ratio of the driven current to the auxiliary power required to sustain the current is the critical parameter defining the efficiency of current drive. Experiments have shown for the LHCD efficiency: η_{CD} ≡ driven current/auxiliary power ~ 0.05 A/W.

From subtle plasma physics point, worth noting concerns the mechanism for driving current. The electrons involved in LHCD are shown to be those with velocities satisfying $u_{e//} \gtrsim 3u_{the}$, where

$$u_{the} = \sqrt{\frac{kT_e}{m_e}}$$

is the electron thermal velocity. The electrons are somewhat out on the tail of the distribution function. As they heat and absorb momentum these electrons tend to enhance the tail of the distribution function as compared to a pure Maxwellian. Now, since the Coulomb collision frequency scales as $\nu_{ei} \sim 1/ \nu_{e//}^3$, most of the current is carried by electrons with a higher $u_{e//}$, the Coulomb frictional drag is reduced, implying that there is less friction trying to restore the distribution function to a Maxwellian. The conclusion is that less power is required to sustain the current drive (i.e., the efficiency is higher) than one might have expected based solely on the classical collisional frequency ν_{ei}.

The task now is to design an LHCD system capable of driving a specified amount of non-inductive current to create steady state operation.

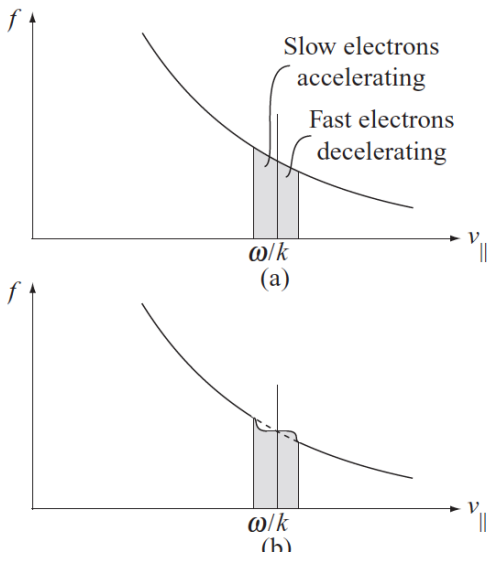

Figure 4.4. (a) Schematic diagram of the electron distribution function (EDF) in the vicinity of the resonant particles. (b) The acceleration of slow particles plus the deceleration of fast particles tends to flatten the distribution function near ω = $k_{//}u_{e//}$.

Specifically, one wants to determine the following properties of the LHCD system: (1) the amplitude and radial profile of the driven current $j_{LHCD}(r)$, (2) the frequency of the lower hybrid waves ω, and (3) the parallel wave number of the lower hybrid waves $k_{//}$.

Analysis necessary for assessing the LHCD effect is summarized hereafter, on the basis of QL theory [12]. The mere linear wave theory is incapable, indeed, to get by the effect of a RF power spectrum of finite wavenumber width in modifying the electron distribution function (EDF). The analysis allows to highlight a typical effect of a feedback mechanism that, mediated by EDF distorted by the RF electric field, determines the non-linear modality of how spectral components with slower phase velocities gradually promote the absorption of the faster ones, i.e., of the full spectrum launched by the antenna.

Considering slab plasma geometry where gradients vary along the above-defined *x* direction, the damping of a quasi-electrostatic LH wave is described by the equation [13,14]:

$$\frac{1}{P_0}\frac{dP_0}{dx} = \Gamma_{QL} \tag{4.16}$$

where P_0 is the normalized power at around the peak of the spectrum, and Γ_{QL} is the quasi-linear damping rate inferred from the 1-D distribution function of plasma electrons, given by the expression (calculated for the resonant velocity: $u_{||} = u_{||0} \equiv \frac{\omega}{k_{||}u_{the}}$

$$\Gamma_{QL} = \sqrt{\frac{\pi}{2}}\frac{u_{||0}\omega_{pe}^2}{\left(k_\perp^2 + k_{||}^2\right)u_{the}^2}\frac{\zeta\nu_{coll}^{ee}\left(u_{||}\right)_{u=u_0}}{\zeta + u_{||0}^3 D(u)\big|_{u_{||}=u_{||0}}} e^{-\int_u^{\left.\frac{\zeta u}{\left[\zeta+u_{||}^3 D(u_{||})\right]}du_{||}\right|_{u=u_0}}} \tag{4.17}$$

where ν_{coll}^{ee} is the electron-electron collision frequency [14], $\zeta = \frac{2+Z_i}{2}$, Z_i is the effective ion charge, and $D(u_{||})$ is the QL diffusion coefficient given by:

$$D\left(u_{||}\right) = \sum_{k_{||}}\left(\frac{e}{m_e}\right)^2\left|E_{||}\left(k_{||}\right)\right|^2\pi\delta\left(\omega - k_{||}u_{||}\right) \tag{4.18}$$

where $E_{||}$ is the relevant component of the wave electric field.

The expression:

$$D(u)\big|_{u=u_0} = \frac{4\pi^2e^2}{c^2m_e^2}\frac{1}{k_\perp u_{the}^2(x)}p_{RF} \tag{4.19}$$

is the QL diffusion coefficient calculated at the centre of the QL plateau (i.e., for $u_{||}=u_{||0}$), and p_{RF} is the RF

power density. The level of the plateau is fixed by the exponential of Eq. 4.17 via the value:

$$k_{//\max} = \left(k_{0//} + \frac{2\omega}{c} \Delta n_{//} \right) \tag{4.20}$$

that is the highest value of the launched spectrum where $\frac{D\left(u_{\|}\right)}{v_{coll}^{ee}\left(u_{\|}\right)}$ falls below one from values typically higher than 1000 in the plateau. The damping rate in the limit of the linear wave theory is [14]:

$$\Gamma_{lin} = \sqrt{\frac{\pi}{2}} \frac{u_0 \omega_{pe}^2}{\left(k_{\perp}^2 + k_{//}^2\right) u_{the}^2} e^{-\frac{1}{2}u_0^2} \tag{4.21}$$

Eqs. 4.17 and 4.21 show that higher RF power densities have the effect of diminishing the QL damping, as described in Ref. [15], which would favour a radially inner deposition in reactor plasmas. However this effect cannot be utilised since operations at higher RF power density are limited by breakdown at the antenna mouth, as observed in tokamak experiments using LH wave power and operating in a wide operating frequency range (from 0.5 GHz to 8 GHz) [16]. This limit increases with frequency, and it is of about 80 MW/m^2 at 5 GHz (the latter corresponds to the design requirement of high power sources under development [17]). For this reason, in the present work we have considered the conservative value of about 30 MW/m^2 for guaranteeing safe antenna operations.

Owing to complexity of wave-plasma mechanisms, having also non linear character, numerical computations performed by suitable codes is necessary for assessing the LHCD effect in realistic cases of experiment, as shown in Chapter 8 for solving an important problem. Indeed, for reactor-like parameters the damping is so strong that most of the lower hybrid wave power is absorbed in a relatively narrow penetration layer near the plasma edge, implying that current can only be driven at values of minor radius, *r*, not too different from the radial plasma size, *a*, which should be not useful for having sufficient flexibility necessary for current profile control in a reactor. This problem has been solved by new results presented in Chapter 8 of the Thesis.

4.6 Basic principles of RF heating and current drive

Although this Thesis focuses mainly on the technique of lower hybrid current rive, we give hereafter a summary of all methods utilised for radiofrequency heating in tokamak plasmas.

Launching RF waves into the plasma is a successful technique for: (1) raising the temperature to the level required for ignition, or (2) driving a steady state non-inductive current. Furthermore, RF source technology appears to extrapolate favourably into the reactor regime. The idea is conceptually similar to using a microwave oven to cook foods. In the case of fusion if the launched frequency is carefully chosen, the RF waves resonate with one of the natural frequencies of the plasma, leading to a large absorption of power that appears in the form of heat and additionally, under certain conditions, as non-inductive current.

We concisely describe: (1) the two most promising RF heating methods, electron cyclotron heating (ECH), (2) ion cyclotron heating (ICH) and (3) the power sources for lower hybrid current drive (LHCD). The relevant issues are indicated hereafter in form of questions:

1) What types of RF sources and launching structures are needed to propagate waves into the plasma?

2) At what frequency should the RF waves be launched in order to produce maximum absorption for heating or maximum current for current drive?

3) How does one insure that the RF power for heating is absorbed in the centre of the plasma where it is most needed?

4) What fraction of the incident heating power is absorbed in the plasma and what is the absorption mechanism?

5) How does one insure that the RF power for current drive is absorbed near the outer edge of the plasma where it is most needed to match the natural bootstrap profile?

6) What is mechanism for driving such a current?

7) How many Watts of LHCD power are required to drive *1A* of current?

The answers to these questions are essential in order to assess the desirability of RF heating and current drive with respect to economic viability and the recirculating power fraction in a fusion reactor.

We give a brief description of the sources and launching structures used for ECH, ICH and LHCD in order to obtain an overview of the relevant technology. Next, some of the general principles of electromagnetic wave propagation in arbitrary media are reviewed.

These principles are then applied to the "cold" plasma model, which gives a surprisingly reliable description of the way waves propagate to the centre of the plasma. However, the cold plasma model does not accurately describe the way in which waves are absorbed or drive current in plasma. This requires an analysis of "collision-less" damping, which, although sounds like an oxymoron, is actually what happens in plasmas.

The main conclusions obtained by theory (which cannot be detailed here for sake of brevity) are that both ECH and ICH are capable of efficient plasma heating (i.e., a large fraction of absorption). For reactor parameters, the main difficulty with ECH is the lack of high-power, steady state sources at the requisite high frequencies. For ICH, there is no difficulty with sources. The main problem is the need for an antenna inside the vacuum chamber close to the plasma edge. The ICH issues involve electromagnetic shielding and the prevention of arcing near the antenna. Large research and development programs are underway to address both the ECH source problem and the ICH antenna problem and solutions should be available when needed for ITER.

For LHCD the sources and launching structures are readily available and the main technological problem is the need to place the launching structure very close to the plasma surface. The largest problem is that the conversion of power to current is not very efficient, implying the need for a substantial bootstrap current to achieve an economically viable steady state reactor.

4.7 RF sources and launching structures

Most of the analysis of RF heating involves learning how electromagnetic waves launched from the outer edge of the plasma propagate to a desired location in the plasma where they can be absorbed by

collision-less damping: in the centre for heating and near the edge for current-drive. Before proceeding along this path, it is instructive to begin with a brief discussion of the various RF sources currently available, and the methods by which energy are transmitted from these sources to the plasma edge.

The basic RF heating or current-drive configuration is illustrated in Fig. 4.5 which shows a source sending waves along a transmission path to a launching structure at the plasma edge.

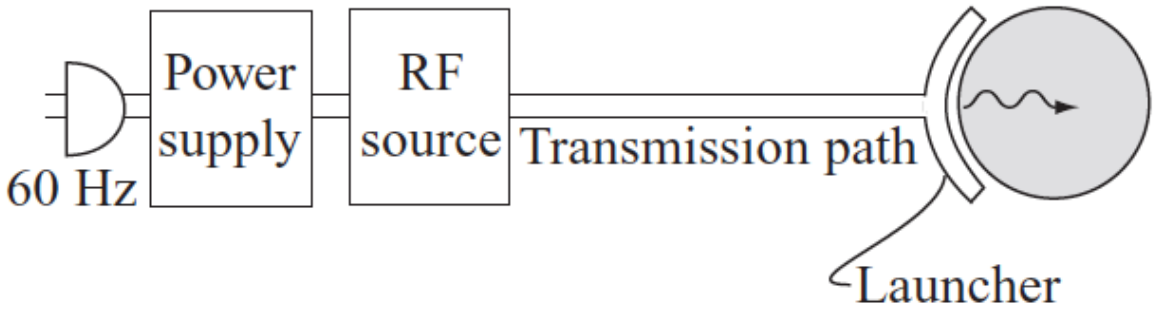

Figure 4.5. Schematic diagram of an RF heating or current-drive system.

4.7.1 RF Sources

The source is driven by a high-voltage power supply, which in turn is driven by standard 60 Hz power. The type of source utilized depends by the operating frequency. Here it is useful to keep in mind that, as their names imply, ECH and ICH require RF waves at the electron and ion cyclotron frequencies respectively. For a magnetic field B0 = 5 T, these frequencies are given by:

- $f_{ce} = \omega_{ce}/2\pi$ = 140 GHz;
- $f_{ci} = \omega_{ci}/2\pi$ = 38 MHz (for deuterium);
- f_{LH} = 3 GHz;

Lower hybrid waves correspond to an intermediate frequency.

These frequencies must be matched with the typical frequencies generated by various types of RF sources as follows:

- high-power vacuum tubes: f < 100 MHz
- klystrons (microwaves): f ~ 1–10 GHz
- gyrotrons (sub-millimetre waves): f ~ 10–300 GHz

Each type of source is illustrated in Fig. 4.6.

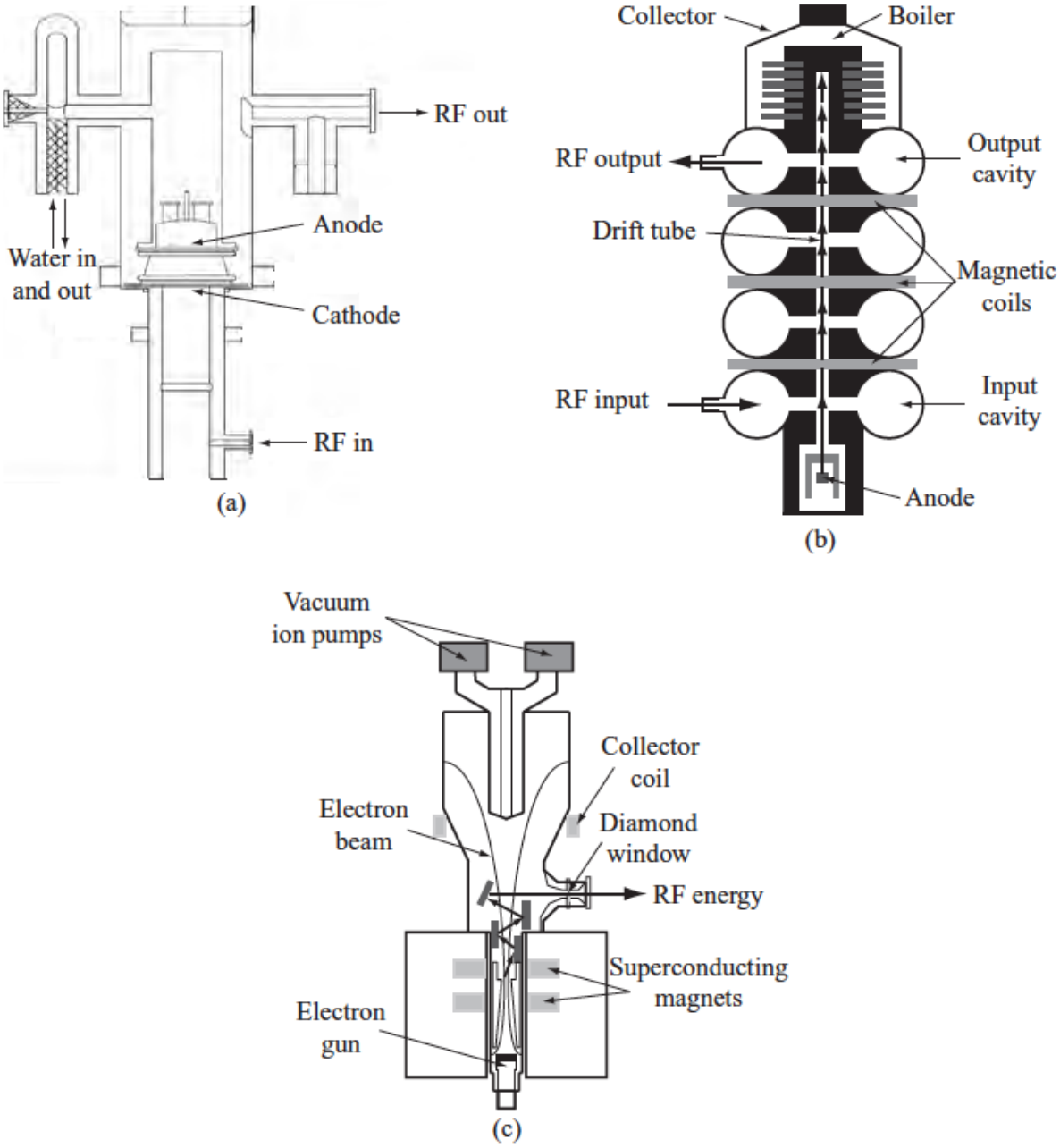

Figure 4.6. (a) High-power ICH vacuum tube; (b) LHCD klystron; c) ECH gyrotron

Observe that ICH is driven by high-power vacuum tubes, while ECH requires gyrotrons. Klystrons drive intermediate frequencies, which are required for LHCD. In terms of the technology, high-power, steady state vacuum tubes and klystrons are well developed and readily available. Gyrotrons are well on the way, but further development is still required. The goal is to develop a robust, reliable 140 GHz, 1 MW, steady state gyrotron.

4.7.2 Transmission path

Consider next the transmission path. There are three basic ways in which electromagnetic energy can be

transmitted from the source to the plasma: standard electrical wire, a two-wire transmission line, and waveguides. The appropriate choice of a transmission method involves a comparison of the wavelength of the RF power with the characteristic dimensions of the transmitting circuit as shown in Fig. 4.7. The different regimes of applicability are as follows.

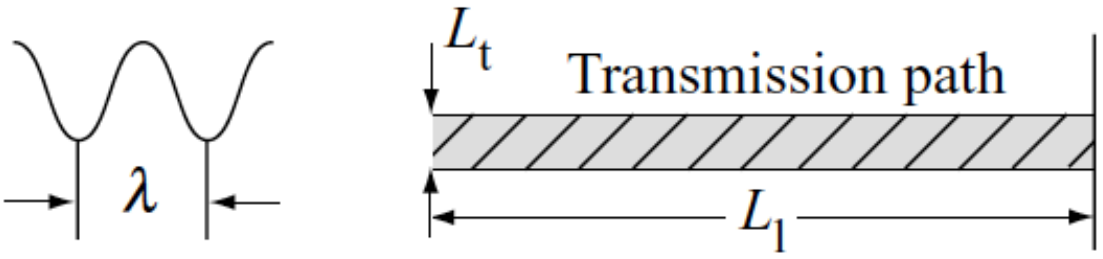

Figure 4.7. Comparison of three characteristic lengths: (1) the wavelength λ, (2) the transverse dimension of the transmission circuit, Lt, (3) the length of the transmission path L_1.

Normal household and industrial AC circuits require standard twisted-wire electrical cable to carry power. This is the appropriate choice when:

$$\lambda >> L_1 >> L_t$$

For example if f = 60 Hz, then $\lambda = c/f$ = 5000 km, which clearly satisfies the above criterion. When analysing AC circuits it is a good approximation to neglect the displacement current in Maxwell's equations.

Parallel wire or coaxial transmission lines are routinely used to guide TV and FM signals. This method is the appropriate choice when:

$$L_1 \gtrsim \lambda >> L_t$$

A typical ICH frequency $f = 40\ MHz$ corresponds to $\lambda = c/f$ = 7.5 m, which satisfies the above inequality. The analysis of transmission line circuits shows that the displacement current must be maintained in Maxwell's equations. The RF power propagates as a pure transverse electromagnetic wave (TEM) whose field structure, as the name implies, has no component of electric or magnetic field parallel to the direction of propagation: $E_1 = B_1 = 0$. It is critical to use two wires to guide the electromagnetic waves.

Lastly, waveguides are used to transmit RF power when the wavelength lies in the range:

$$L_1 >> L_t \sim \lambda.$$

For ECH a typical frequency in a reactor is $f = 140\ GHz$ and corresponds to $\lambda = c/f = 2.1\ mm$. For lower hybrid waves: f is of the order of $3\ GHz$ and $\lambda = c/f$ = 10 cm. Thus, ECH power is transmitted by means of a waveguide with a relatively small cross sectional dimension. Usually an "oversized waveguide" is used to minimize ohmic dissipation in the waveguide walls. Lower hybrid waves are transmitted using standard size waveguides.

For both of these cases the displacement current must be maintained in Maxwell's equations and the power propagates as either a transverse electric (TE) or transverse magnetic (TM) wave; that is, either B_1 or E_1 must be non-zero. At these high frequencies transmission of power requires only a hollow metal

tube (i.e., a waveguide), which is usually rectangular or circular in cross section. No central conductor is needed.

In practice, transmission lines and waveguides have been studied, developed, and widely used for many, many years. The conclusion is that once an appropriate RF source is available, its power can be readily transmitted to the launcher at the plasma edge.

4.8 Launchers

The launcher is a structure that acts as the interface between the transmission circuit and the edge of the plasma. Its shape also depends critically on the wavelength being used. For ICH, waves are launched into the plasma by means of an antenna placed inside the vacuum chamber. For LHCD, the corresponding structure is a waveguide array. For ECH, an RF mirroring system is used. Examples of each are illustrated in Fig. 4.6.

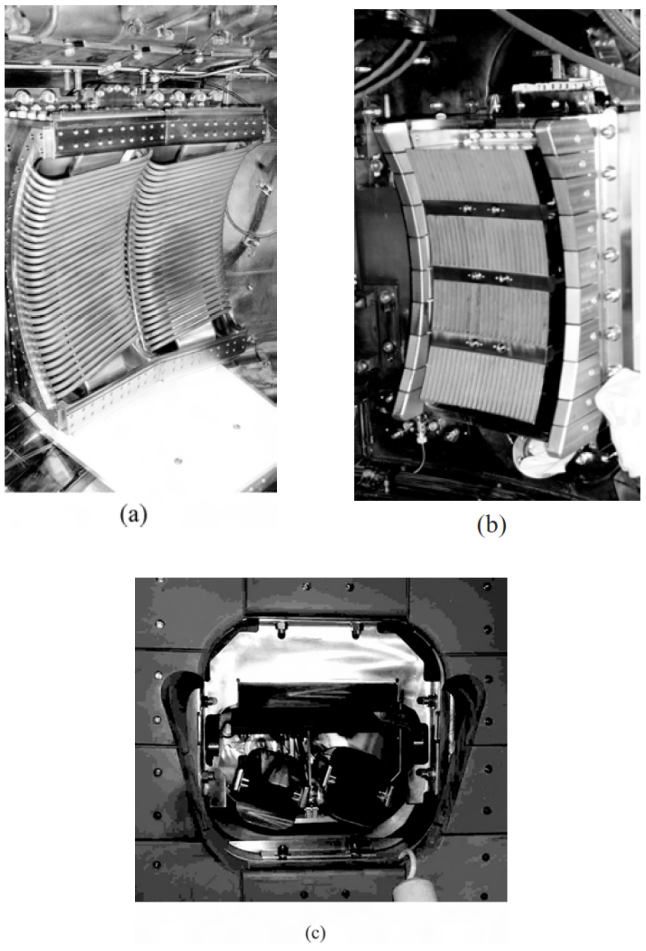

Figure 4.8. Launching structures for: (a) an ICH antenna, (b) an LHCD waveguide array, (c) an ECH mirroring system

In general, for ICH, ECH, and LHCD it is highly desirable, for reasons of geometric accessibility, to launch waves from the outside of the plasma as illustrated in Fig. 4.9. There is just too much hardware in the centre of most configurations to allow unimpeded access to the plasma edge. In addition to this general requirement, there are several specific issues facing each type of launchers, which are described below.

For ICH, the biggest problem is the proximity of the metal structure of the antenna to the plasma. High voltages are required to launch large amounts of power and these voltages can cause arcing and plasma breakdown near the antenna, both undesirable effects. One cannot just move the antenna further away from the plasma, because, as expected by theory, close proximity is required or else the ICH waves do not couple strongly to the plasma. The design of a well-shielded antenna capable of preventing high-voltage arcing is an important technological problem for ICH. It also worth noting that, since the DC magnetic field in the plasma is tangential to the vacuum chamber, the geometric structure of the antenna determines the value of $k_{//}$ of the electromagnetic waves as they enter the plasma. In other words, as the waves start to propagate into the plasma the frequency ω and parallel wave number $k_{//}$ are known from the RF source and antenna structure respectively.

For LHCD, the issues are somewhat different. A generic problem is to spread the RF power over a large enough area so that high-voltage breakdown problems do not occur, a situation somewhat driven by the small transverse dimensions of a single waveguide and the need to place the launching structure near the plasma edge for good coupling. This requires a large number of waveguides in the launching array. An equally difficult problem is maintaining an insulated vacuum interface between the plasma and the waveguides. The solution involves inserting sealed windows of a carefully chosen material at the end of each waveguide in the array to isolate the launcher from the plasma. The difficulty is that large amounts of RF power must pass through this window. Very little of it should be reflected back, otherwise the efficiency would rapidly decrease. Very little of it should be absorbed in the window, otherwise damage will occur due to thermal stresses. The development of high-power windows is an important technological problem for LHCD. Lastly, again as for ICH, the geometric arrangement and relative phases of the electromagnetic waves at the edge of the launching array set the value of $k_{//}$ for the waves as they enter the plasma. Thus, here too both ω and $k_{//}$ are known at the plasma edge.

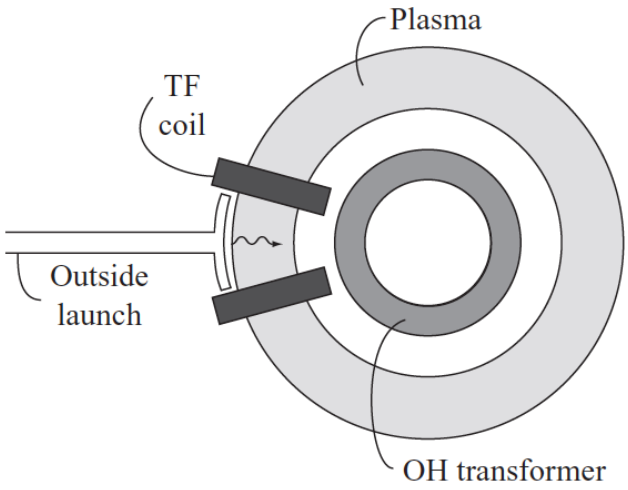

Figure 4.9. Schematic diagram of the top view of a tokamak showing an outside, low-field launch. Note the hardware congestion on the inside of the torus because of the converging geometry and the presence of the OH transformer.

ECH has a similar set of issues as LHCD, although there is good coupling even when the launching structure is moved away from the plasma. Quasi-optic structures are generally used as launchers.

ICH, ECH, and LHCD have been used to heat and drive current in present day plasma experiments. The technological problems described above have been satisfactorily resolved, although with considerable effort, in these pulsed experiments. ICH is more prevalent than ECH because of the ready availability of high-power, reliable sources at reasonable cost.

Even so, ECH is being used in a number of existing experiments around the world. LHCD is gaining attention, although it has not been investigated as thoroughly as ICH. The reason is that current drive has not until recently been viewed as being as critical a problem as heating.

Chapter 5

5 Parasitic phenomena for RF power propagation: the parametric instability

Following Ref. [13] (R Cesario, L Amicucci, 2014), it is here summarised the phenomenon of parametric instability (PI), responsible for preventing the lower hybrid current drive in experiments that approach condition of high plasma densities relevant for thermonuclear reactor, as modelling and experimental results demonstrate. Modelling tools described here have been originally developed at the ENEA Frascati Laboratory and have been utilised for successfully interpreting recent experimental data of experiments, as shown in the next Chapters 6 and 7.

In particular, new software has been produced by work performed for the present Thesis useful for assessing, much faster than by previous numerical code version, frequencies and growth rates of coupled modes producing the instability. This upgrade has enabled producing for the first time the works of modelling necessary for comparing, in useful time, cases of several plasma discharges available also from different machines.

5.1 Introduction

Early experiments on the use of radiofrequency LH power with the aim of heating the plasma ions, as previously predicted by theory [18], did not succeed obtaining penetration of the radiofrequency power into the plasma core, despite the utilised antennas worked properly in coupling power to plasma. The LH ion heating scheme, which consequently does not have been tested so far, requires high plasma density ($n_{e\_av} \sim 1.5 \times 10^{20}$ m^{-3}) in order to enable mode conversion of LH wave into an hot ion mode that occurs at radial layer where a high harmonic of the ion-cyclotron (IC) resonant frequency is located. The failure of the early LH experiments does not have been fully understood yet. The parametric instability described here can justify these unsuccessful results as consequence of parasitic effect on wave propagation and damping. Moreover, this study allows opening the path for overcoming the obstacle that for long time has prevented envisaging an LHCD tool capable of operating at the high plasma densities required by a reactor. This important issue will be described in Chapter 6.

Early experiments aimed at plasma ion heating by LH wave power and those more recently performed for extrapolating LHCD effect at high density present the same failure of RF power penetration, have in common the circumstance that huge spectral broadening of the operating frequency line occurs in RF probe spectrum measurements [25,26,21]. The RF probe diagnostic consists in a small loop antenna generally located outside the vacuum vessel and faced to a port.

The phenomenon of spectral broadening was interpreted as effect of the non-linear plasma-wave phenomenon of parametric instability (PI) [19,20]. This mechanism is produced by the coupled LH power

(the so-called pump wave), is driven by low frequency density fluctuations of thermal background, and produces LH sidebands shifted by a certain amount from the nominal frequency and $n_{//}$ values of the injected wave.

Data from modelling based on the PI mechanism, Refs. [22,23], showed that, at low densities, the consequent spectral broadening represents an important contribution in bridging the $n_{//}$ gap in LHCD, whilst, in standard operations at high densities it is responsible of the observed parasitic damping of the coupled LH power, due to stronger PI effect.

Consequently, by using the LH^{star} code [21] (which is the only tool available so far that calculates the LH deposition profile taking into account the effect of physics of the edge produced by PI) it was predicted that LHCD experiments approaching reactor-graded high plasma densities can have success only provided that relatively high electron temperature in the outer plasma should be produced. According to these predictions, experiments performed on FTU (Frascati Tokamak Upgrade) at high density, showed that the diminished PI-produced spectral broadening effect was accompanied by clear effects of penetration of the coupled LH power to the core [24]. These results will be summarised In Chapter 6.

We give details on how, in the LH^{star} code, the broadening of the spectrum launched by the antenna has been evaluated, and the LH deposition profiles modelled, for the relevant FTU cases. We give the reader also a useful synopsis on the mechanism that is at the basis of the complex PI concept.

The PI-produced spectral broadening is expected to affect both the domains of frequency and $n_{//}$, which is consistent, respectively, with observations of RF probe and LH-wave-accelerated plasma electron effect. FTU results proved for the first time that the temperature profile of plasma periphery, spectral broadening and LHCD effects are quantities intimately connected together, and that a high electron temperature in the outer plasma region is condition useful for both diminishing the spectral broadening and enabling the LHCD effect at high density. We provide here new proofs, by modelling and experimental data, on the abovementioned causal link.

5.2 Spectral broadening and sidebands in early experiments

Results of early LH experiments aimed at the ion heating have represented a fundamental support to the more recent modelling predictions that enabled the assessment of the new method for LHCD at high density. It is useful to summarise here the main features of RF probe spectra, which were observed in early experiments that tested the plasma ion heating scheme by LH wave [18].

RF probes were installed for the first time in LH experiments aimed at the ion heating, then also in experiments producing the LHCD effect. In order to test the ion-heating scheme, plasma densities (line-averaged: $n_{e\_av} \sim 1.5 \times 10^{20}$ m^{-3}) higher than in LHCD experiments ($n_{e\_av} \approx 0.2 \times 10^{20}$ m^{-3} – 0.5 10^{20} m^{-3}) were required. Moreover, the operating frequency (f_0) was relatively lower (0.5MHz–2.45 GHz) in the former case than in the latter (3.7 GHz–8 GHz). Consequently, at the high densities required by the ion heating scenario, the RF probe spectra showed an enormous broadening of the operating frequency line, orders of magnitude higher than the RF power source line width, and much bigger than that observed in the electron heating and current drive regime. The huge broadening occurring at high densities was accompanied by several *ion-cyclotron* sidebands, signatures of LH waves shifted from the operating line frequency f_0 by harmonics of the ion-cyclotron frequency in the outer plasma. These sidebands exhibit a typical non monotonic envelop in case of experiments operating at very high density (typically, $n_{e\_av} > 1.2$ 10^{20} m^{-3} for f_0=2.45 GHz). An example of such spectra observed during the LH experiments on FT (Frascati Tokamak) aimed at heating ions is shown in the Fig. 5.1 (from Ref. 22).

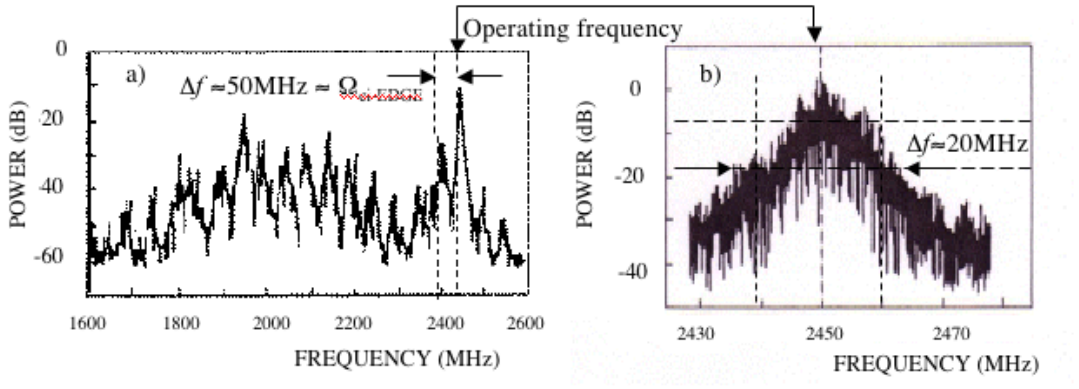

Fig. 5.1. Typical frequency spectra of the RF probes obtained during the experiment aimed at heating the plasma bulk ions on the FT tokamak. Fig 5.1a: broadband spectrum exhibiting the *ion-cyclotron* sidebands (span filter bandwidth: 20 MHz). Fig 5.1b: pump broadening (span filter bandwidth: 5 MHz).

The broadband frequency spectrum, Fig. 5.1a, shows the *ion-cyclotron* sidebands (with maximum of the sidebands located at the tenth harmonic). The spectrum around the operating line frequency is shown in Fig. 5.1 b. Such spectra were interpreted in terms of the non-linear mechanism of PI occurring in the outer plasma, namely, sidebands of PI produced by the launched LH power (pump wave) and low frequency evanescent modes (quasi-modes) of the thermal background of density fluctuations. The quasi-modes lye in the ion-sound and ion-cyclotron frequency ranges.

The typical envelope of the ion-cyclotron frequency-shifted LH sideband waves, observed in the RF probe spectrum, was found in agreement with PI modelling performed considering data of FT experiments aimed at the ion heating [22]. By this modelling, the sideband envelope would be produced by cascade of two PI channels, one of which is driven by ion-sound quasi-modes. The latter broadens the pump wave spectrum at around f_0, and produces LH sidebands shifted from the pump up to about 20 MHz, consistent with data of Fig. 5.1b. These LH waves act as a further pump having $n_{//}$ higher than the nominal antenna spectrum peak. This virtual pump, having slower phase velocity, have the peculiar behaviour of producing a cascading spectrum of LH sidebands that present the highest growth rates at around the 10^{th} harmonic of the ion-cyclotron frequency in the outer plasma. This modelling prediction is consistent with the spectrum of Fig. 5.1a. Only thanks to this upshift of the LH antenna spectrum, it is possible, by PI modelling, to interpret the whole available RF probe data. As further effect, the up-shifted LH spectrum, consequence of the cascading PI effects in the outer plasma, is suitable for producing a strong Landau damping with local plasma particles, which justifies the lack of penetration of the coupled LH power in the plasma interior.

In summary, the modelling prediction and interpretation useful for assessing the LHCD method at high density on FTU, is based on the same PI-produced $n_{//}$ spectral broadening effect, that was expected originating PI-cascade signatures in the spectra of Fig. 5.1a, as well as bridging the $n_{//}$ gap in LHCD, to the point of preventing, at high densities, the LH power penetration to the core.

In the following section, we show data of spectral broadening measured by RF probe during LH experiments at high density on FTU. These results are important for interpreting the behaviour of LH power penetration in the core on the basis of the PI model that will be described in Sec.5.4.

5.3 Spectral broadening in recent LHCD experiments at high density on FTU

We show new results of FTU experiments indicating that higher temperature in the outer plasma produces both a reduced spectral broadening and stronger LHCD effects, in a range of parameters larger

than in results related before [24]. Moreover, we give the important information on how the spectral broadening was measured in a way able to detect, just above the noise power level, the contribution of sidebands with markedly downshifted frequencies with respect to the pump. Following the PI modelling described in the next section, as these sidebands have relatively high $n_{//}$, their contribution, produced when a certain PI threshold condition is exceeded, is essential for determining the LH spectral broadening and the consequent interaction of the LH power with plasma particles.

The experiments in FTU benefit from the use of an LH spectral broadening monitor provided by a radio frequency probe located outside the machine at a port several metres from the LH antenna.

The RF probe spectra, obtained in experiments exploring the full range of plasma densities of FTU, did not ever exhibit LH sidebands shifted by harmonic of the IC frequency, as instead occurred in operations at 2.45 GHz on FT. Only a significant spectral broadening was observed in LHCD experiments performed at high densities on FTU. Similarly, the IC-frequency-shifted sidebands did not appear also in the early LH operation at 8 GHz on FT [25]. This behaviour is consistent with PI modelling that expects a much lower amplification factor of PI relevant to IC-shifted sidebands (see Sec. 5.4).

Figure 5.2 shows the frequency spectrum from RF probe obtained in two experiments of FTU aimed at producing LH current drive effect at high density. Two different regimes of outer plasma temperatures are considered, respectively, the standard (Fig. 5.2a, with $n_{e\_av} \approx 1.05 \times 10^{20}\ m^{-3}$) and that with higher T_{e_outer} (Fig. 5.2b, with $n_{e\_av} \approx 1.9 \times 10^{20}\ m^{-3}$).

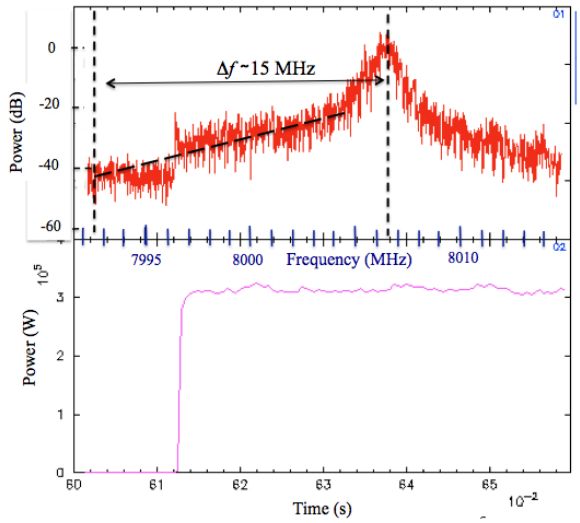

Figure 5.2a RF probe spectral broadening and LH power time trace in standard regime (FTU plasma discharge 32164)

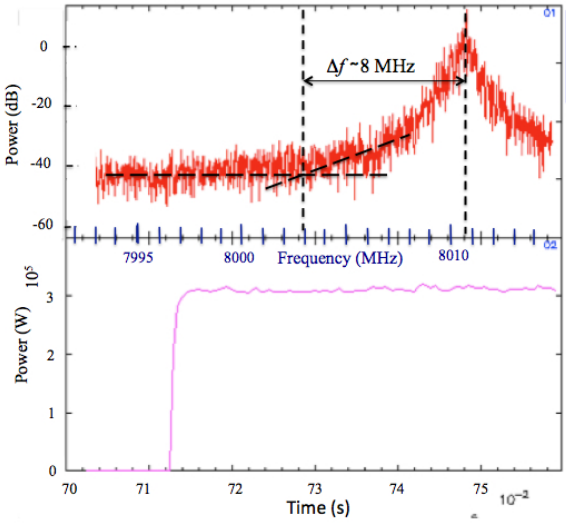

Figure 5.2b RF probe spectral broadening and LH power time trace in high T_{e_outer} regime (FTU plasma discharge 32555)

The figure shows the time trace of the power level measured by the RF probe in the frequency range spanned by the spectrum analyser, which has been properly set considering the switch-on time point of the coupled LH power waveform. This setting is useful, indeed, for distinguishing from the noise level the contribution of spectral broadening of LH sideband waves shifted by large frequencies from the operating line frequency.

In Figure 5.2a, the spectral broadening should be of about 15 MHz (or more, at around 35 dB below the pump power level). Indeed, at the LH power switch-on time point, the sideband power level is considerably higher than that of the noise. In the high T_{e_outer} regime case, Fig. 5.2b, the spectral broadening reduces to about 7 MHz, despite of the higher value (of about 35%) of plasma density that would produce instead, in standard regime, a broadening also huger than that of Fig 5.2a.

The peak in the spectrum of Fig. 5.2a is slightly lower (of at least 3 dB) than in case of Fig. 5.2b, indicating that a stronger pump power depletion occurs in the former case (with no LH power penetration). This

observation is consistent with narrower spectrum and higher peak occurring in RF spectra of experiment on FT (Frascati Tokamak), in regime performed with lower plasma density and characterised by stronger LH heating effect on the core electrons [26].
In the next section we show that the related strong dependence of the LHCD effect and the RF probe spectral broadening on T_{e_outer} are consistent with predictions made by numerical simulations of PI.

5.4 Modelling of parametric instability

We show here details of the modelling tool useful for performing theoretical predictions of spectral broadening and for determining the consequent effect of the coupled LH power on propagation and damping. Such work resulted useful for assessing on FTU the new method for enabling the LHCD effect at high plasma density [24].
The non-linear coupling of the LH wave (with angular frequency ω_0), which is fed by strong externally coupled RF power, occurs for interaction with low frequency modes ($\omega<<\omega_0$) of the thermal background of density fluctuations. The non-linear coupling occurs under conditions determined by solutions of parametric dispersion relation (PDR), which will be derived in the next subsection.
The PI of a LH pump wave with potential $\Phi_0 e^{-i(\omega_0 t - \mathbf{k}_0\cdot\mathbf{r})}$ is driven by a low frequency mode $\Phi e^{-i(\omega t - \mathbf{k}\cdot\mathbf{r})}$ and can show by the growth of two LH sideband waves $\Phi_{1,2} e^{-i(\omega_{1,2} t - \mathbf{k}_{1,2}\cdot\mathbf{r})}$, where $\mathbf{k}_{2,1}=\mathbf{k}\pm\mathbf{k}_0$, $\omega_{2,1}=\omega\pm\omega_0$ are the selection rules provided by momentum and energy conservation of the coupled modes (the index 1, 2 refer to the lower and upper sidebands, respectively). We assume $\mathbf{k_0}=k_{0x}\mathbf{x}+k_{0z}\mathbf{z}$, $\mathbf{k_{1,2}}=k_{1,2x}\mathbf{x}+k_{1,2z}\mathbf{y}+k_{1,2z}\mathbf{z}$, and utilise the relation $\mathbf{n}=\mathbf{k}c/\omega_0$ between refractive indexes and wavevectors. Moreover, the following notation is utilised: $k_\perp\equiv|k_x\mathbf{x}+k_y\mathbf{y}|$ for k-values relevant to each mode. The plasma is modelled as a slab including the region of the edge close to the antenna mouth. The solutions of the PDR are obtained considering a radial plasma layer that extends from the antenna mouth to the plasma centre. The x direction coincides with the (radial) direction of the plasma gradients, and y, z correspond to the poloidal and the toroidal directions, respectively. The PI analysis is based on the solution of the Vlasov and Poisson equations for coupled electrostatic modes up to the second order. The following ordering has been considered: the Maxwellian distribution function corresponds to the zero order, the variation produced by the pump wave to the first order, and the perturbation of the low frequency modes to the second order ($\Phi_0>>\Phi, \Phi_{1,2}$).
In order to perform PI modelling, the following three steps have been performed.
i) Identify frequency, $Re(\omega)$, and growth rate, $Im(\omega)\equiv\gamma$, of the coupled modes that characterise the PI. This analysis is carried out solving the PDR. This equation, for the LH frequency range, was originally derived by Porkolab in the approximation of pump as dipole, i.e., with wavenumber k_0=0 [19]. Later, by using the ponderomotive potential concept [29], the more useful form of PDR that retains the effect of finite k_0, which is utilised in the LH^{star} code, was obtained [30,31].
About propagation or evanescence of modes involved in PI, the following general conditions have been assessed as result of the solution of PDR in a wide range of parameters of different machines. For the low frequency driving mode, the condition of evanescence holds: $|\varepsilon_{Re}(\omega_1\mathbf{k})|>>0$, where ε is the dielectric function. For LH sidebands, both the conditions $\gamma>0$ and $|\varepsilon_{Re}(\omega_{1,2},\mathbf{k}_{1,2})|\approx 0$ are necessary for the growth of instability. Generally, this condition occurs for both the lower and upper sidebands only when these modes have frequencies lying within a small shift ($\lesssim$1MHz) from the pump. This condition reflects in the occurrence of LH sideband waves that produce a symmetric spectral broadening. In this case the PI

involves four modes, one of which, that at low frequency, is evanescent. Conversely, for PIs characterised by larger frequency shifts (~10MHz) the upper sideband is evanescent (like the low frequency quasi-mode, i.e., $|\varepsilon_{Re}(\omega_2,\mathbf{k}_2)|>>0$), and an asymmetric and downshifted spectral broadening is thus produced. This case corresponds to the hugely broadened RF probe spectra observed in standard LH regimes at high density, like that shown in Fig. 3a. Importantly, this asymmetry could not be explained by linear scattering mechanism [32], but reveals clear signature of different mode-coupling behaviours between interacting waves. The framework of the non-linear PI phenomenon is useful to properly take into account the experimental data from the RF probe.

ii) The effective growth factor for quasimodes-driven PI, is calculated by taking into account convective losses produced by plasma inhomogeneity [20,28,21] and finite spatial extent of then pump wave region.

iii) The pump depletion effect, i.e., the power fraction of the coupled RF power pump that goes to LH sideband waves, is estimated on the basis of perturbative method [33].

The abovementioned steps of analysis are fully performed by the LHPI (lower hybrid parametric instability) module of the LH^{star} code [21], for computing the broadening of the spectrum launched by the antenna. The broadened spectrum acts as *initial spectrum* for the RAY^{star} module, that performs the 2-D ray tracing analysis retaining toroidal geometry effects, and the Fokker-Planck analysis [34].

We summarise in Sec 5.4.1 the derivation of the PDR in the form used by LH code, to helps the reader to have a complete synopsis of the PI modelling. In Sec. 5.4.2 we show solutions of the PDR for cases relevant to the FTU experiment, which exhibit the important dependence of the PI growth rate on the electron temperature. Sec. 5.4.3 and 5.4.5 consider the remaining steps ii) and iii) of analysis, which reveals, for the case of FTU experiment, how the PI converts the initial LH waves into high $n_{//}$ LH waves with higher efficiency when T_e-edge is low, and how these high $n_{//}$ waves are absorbed at the peripheral region, reducing the capability of the LH waves of driving current into the plasma.

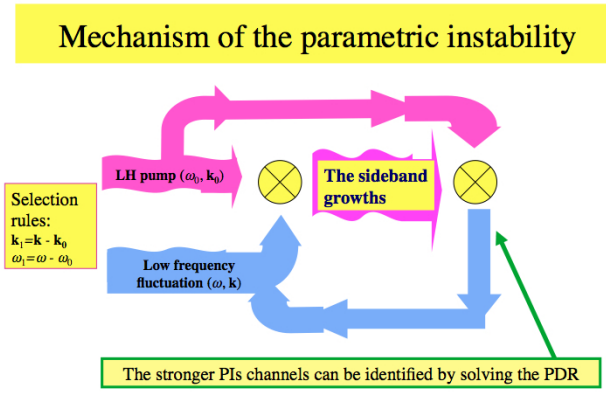

Figure 5.3. Sketch of the beating wave mechanism in PI. The LH pump wave beats with a low frequency density fluctuation, producing a sideband wave. The sideband beats with the pump and produces a low frequency contribution that, for pump electric field exceeding a certain threshold value, and in conditions determined by PDR solution and convective losses (see Sec 4.2), reinforce the original low frequency perturbation, so that the PI manifests.

5.4.1 The parametric instability mechanism: derivation of the parametric dispersion relation

We follow analytical formalism of Ref. [30] based on the use of the ponderomotive potential [29].

An important concept for the PI mechanism is the *ponderomotive force*. We consider a particle with mass m and charge q in presence of a pump oscillating quasi-electrostatic field (i.e., with wavevector and electric field vector almost aligned): $\mathbf{E}[\mathbf{x}(t),t]$, and in presence of a uniform magnetic field $\mathbf{B}_0$. The limit of homogeneous unbounded slab plasma is assumed in this step of analysis. The particle motion equation is:

$$m\frac{\partial \mathbf{v}(t)}{\partial t} = q\left\{\mathbf{E}\left[\mathbf{x}(t),t\right] + \frac{\mathbf{v}\times\mathbf{B}_0}{c}\right\} \quad 5.1$$

Assuming that the electric field and oscillating motion are composed by the contributions at high (hf) and low (lf) frequencies, the corresponding vectors of velocity and displacement can be written in the form:

$$\mathbf{v}(t) = \mathbf{v}_{hf}(t) + \mathbf{v}_{lf}(t) + \mathbf{v}_0(t) \quad 5.2$$

$$\mathbf{x}(t) = \mathbf{x}_{hf}(t) + \mathbf{x}_{lf}(t) + \mathbf{x}_0(t) \quad 5.3$$

where the suffix "0" denotes the unperturbed orbit.

The equation for high frequency motion is given, by linear approximation, by:

$$m\frac{\partial \mathbf{v}_{hf}(t)}{\partial t} = q\left\{\mathbf{E}_{hf}\left[\mathbf{x}_0(t),t\right] + \frac{\mathbf{v}_{hf}(t)\times\mathbf{B}_0}{c}\right\} \quad 5.4$$

For the low frequency motion, we retain only terms up to the first order in $\mathbf{x}_{hf}$ that give the low frequency contribution:

$$m\frac{\partial \mathbf{v}_{lf}(t)}{\partial t} = q\left\{\mathbf{E}_{lf}\left[\mathbf{x}_0(t),t\right] + \left[\mathbf{x}_{hf}(t)\cdot\nabla\mathbf{E}_{hf}\left(\mathbf{x}_0(t),t\right)\right]_{lf} + \frac{\mathbf{v}_{lf}\times\mathbf{B}_0}{c}\right\} \quad 5.5$$

The term:

$$\left[\mathbf{x}_{hf}(t)\cdot\nabla\mathbf{E}_{hf}\left(\mathbf{x}_0(t),t\right)\right]_{lf} \quad 5.6$$

indicates the ponderomotive force and represents the fundamental channel that, in PI, transfers energy and momentum from the high to low frequency non-linearly coupled modes, some of which could be not propagating modes, i.e, they are quasi-modes. In Figure 4 a sketch of the PI mechanism is displayed.

We now explore the PI mechanism for an electron with charge $-e$ and mass m_e in presence of a pump wave electric field $\frac{\mathbf{E}_0 + \mathbf{E}_0^*}{2}$, where the asterisk denotes complex conjugate, and

$$\mathbf{E}_0 = \left(\mathbf{E}_{0//} + \mathbf{E}_{0\perp}\right)\exp\left(i\mathbf{k}_0\cdot\mathbf{x} - i\omega_0 t\right) \quad 7$$

Assuming that the ion and electron motions are independent, the unperturbed values of the complex electron drift velocity, $\mathbf{v}_{D0}$, and displacement, $\mathbf{x}_{D0}$, are given by solving the equation of motion at the order of variation imposed by the pump wave electric field:

$$\mathbf{v}_{D0} = -\frac{e}{m_e}\left(\frac{i\omega_0\mathbf{E}_{0\perp}}{\omega_0^2 - \omega_{ce}^2} + \frac{\vec{\omega}_{ce}\times\mathbf{E}_{0\perp}}{\omega_0^2 - \omega_{ce}^2} + i\frac{E_{0//}}{\omega_0}\right) \quad 5.8$$

$$\mathbf{x}_{D0} = \frac{\mathbf{v}_{D0}}{-i\omega_0} \quad 5.9$$

The dependence of the drift velocity on the pump field is given by:

$$\mathbf{v}_{D0} = \frac{i\omega_0}{4\pi n_e}\mathbf{K}_e\cdot\mathbf{E}_0 \quad 5.10$$

where $\mathbf{K}_e$ is the electron contribution to the dielectric tensor:

$$\varepsilon(\omega,\mathbf{k}) = \mathbf{1} + \mathbf{K}_e + \mathbf{K}_i \quad 5.11$$

We consider a density perturbation (of the Maxwellian equilibrium thermal background n_{e0}) with frequency $\omega << \omega_0$ and wavevector **k,** given by:

$$n_e = n_{e0}\exp\left(i\mathbf{k}\cdot\mathbf{x} - i\omega t\right) \qquad 5.12$$

by the continuity equation we obtain the non linear contributions at high frequencies, considering the selection rules: $\mathbf{k}_{2,1}=\mathbf{k}\pm\mathbf{k}_0$, $\omega_{2,1}=\omega\pm\omega_0$, which represent momentum and energy conservation laws for the coupled modes:

$$n_{e1} = \frac{in_e}{4\pi n_{e0}} k_1 \mathbf{E}_0^* \qquad 5.13$$

$$n_{e2} = \frac{in_e}{4\pi n_{e0}} k_2 \mathbf{E}_0 \qquad 5.14$$

The suffixes 0, 1, 2 refer, respectively to the high frequency domains of pump wave and to the lower and upper sidebands, while the quantities without suffix refer to the low-frequency mode.
By the Poisson equation, we obtain the potentials of the lower and upper sideband waves:

$$\phi_1 = \frac{-in_e}{n_{e0}k_1^2\varepsilon(\omega_1,\mathbf{k}_1)}\mathbf{k}_1\cdot\mathbf{K}_e^*\cdot\mathbf{E}_0^* \qquad 5.15$$

$$\phi_2 = \frac{-in_e}{n_{e0}k_2^2\varepsilon(\omega_2,\mathbf{k}_2)}\mathbf{k}_2\cdot\mathbf{K}_e\cdot\mathbf{E}_0 \qquad 5.16$$

Using Eqs. 5.9 and 5.10, we obtain:

$$\phi_1 = -\frac{4\pi i e n_e}{k_1^2\varepsilon(\omega_1,\mathbf{k}_1)}\mathbf{k}_1\mathbf{x}_{D0}^* \qquad 5.17$$

$$\phi_2 = -\frac{4\pi i e n_e}{k_2^2\varepsilon(\omega_2,\mathbf{k}_2)}\mathbf{k}_2\mathbf{x}_{D0} \qquad 5.18$$

From Eq. 5.6 we can now obtain the ponderomotive electric field considering the oscillating contributions at low frequency (ω, $\mathbf{k}$). These terms give:

$$\frac{\mathbf{E}_P + \mathbf{E}_P^*}{2} = \frac{\mathbf{x}_D + \mathbf{x}_0^*}{2}\cdot\nabla\left(\frac{\mathbf{E} + \mathbf{E}^*}{2}\right) \qquad 5.19$$

where both $\mathbf{x}_D$ and $\mathbf{E}$ contain oscillating terms with ω_0, $\mathbf{k}_0$., ω_1, $\mathbf{k}_1$, and ω_1, $\mathbf{k}_1$.
Assuming that the sideband potentials would have small amplitude

$$\phi_0 >> \phi_1, \phi_2$$

so that:

$$|\mathbf{x}_{D0}| >> |\mathbf{x}_{D1}|,\ |\mathbf{x}_{D2}|$$

from Eq. 5.19 we obtain:

$$-\frac{1}{2}\nabla\phi_P = -\frac{1}{4}\left[\mathbf{x}_0\nabla\left(\nabla\phi_1\right) + \mathbf{x}_0^*\nabla\left(\nabla\phi_2\right)\right] \qquad 5.20$$

Considering Eqs. 5.17 and 5.18, we obtain:

$$\nabla\phi_P = -2\pi e n_e\left[\mathbf{x}_{D0}\cdot\mathbf{k}_1\nabla\left(\mathbf{x}_{D0}^*\cdot\mathbf{k}_1\right) + \mathbf{x}_{D0}^*\cdot\mathbf{k}_2\nabla\left(\mathbf{x}_{D0}^*\cdot\mathbf{k}_2\right)\right] \qquad 5.21$$

and

$$\phi_P = \pi e n_e\left[\frac{\left|\mathbf{k}_1\cdot\mathbf{x}_{D0}\right|^2}{k_1^2\varepsilon(\omega_1,\mathbf{k}_1)} + \frac{\left|\mathbf{k}_2\cdot\mathbf{x}_{D0}\right|^2}{k_2^2\varepsilon(\omega_2,\mathbf{k}_2)}\right] \qquad 5.22$$

which represents the ponderomotive force acting on the plasma electrons.

Including the ponderomotive potential in the kinetic equation for the electron distribution function, we obtain:

$$\frac{\partial f_e}{\partial t} + \mathbf{v}_{hf} \cdot \nabla_x f_e - \frac{e}{m_e}\left[-\nabla\left(\Phi + \Phi_P\right) + \frac{\mathbf{v}\times\mathbf{B}}{c}\right]\nabla_v f_e \qquad 5.23$$

The perturbed electron density is:

$$n_e = \frac{k^2 \chi_e\left(\omega,\mathbf{k}\right)}{4\pi e}\left(\phi + \phi_P\right) \qquad 5.24$$

where c_e is the linear electron susceptibility given by the expression:

$$\chi_e = 1 + \frac{2\omega_{pe}^2}{k^2 v_{the}^2}\left[1 + \frac{\omega + \omega_e^*}{k_z v_{the}}\sum_n Z\left(\frac{\omega - n\omega_{ce}}{k_z v_{the}}\right) I_n\left(b_e\right) e^{-b_e}\right] \qquad 5.25$$

where

$$\omega_e^* = \frac{k_y v_{the}^2}{2\omega_{ce} L_n} \quad , \quad \omega_i^* = -\frac{k_y v_{thi}^2}{2\omega_{ci} L_n} \qquad 5.26$$

are the electron and ion diamagnetic frequencies, L_n is the density scale length, and

$$b_e \equiv \frac{k_\perp^2 v_{the}^2}{2\omega_{ce}^2} \quad , \quad b_i \equiv \frac{k_\perp^2 v_{thi}^2}{2\omega_{ci}^2} \qquad 5.27$$

Due to the large ion mass, the effect of the ponderomotive force can be neglected. The kinetic equation for the ion distribution function is:

$$\frac{\partial f_i}{\partial t} + \mathbf{v}_{hf} \cdot \nabla_x f_i + \frac{eZ_i}{m_i}\left[-\nabla\Phi + \frac{\mathbf{v}\times\mathbf{B}}{c}\right]\nabla_v f_i \qquad 5.28$$

The perturbed ion density is:

$$n_i = -\frac{k^2 \chi_i\left(\omega,\mathbf{k}\right)}{4\pi Z_i e}\phi \qquad 5.29$$

where c_i is the linear ion susceptibility given by the expression:

$$\chi_i = 1 + \frac{2\omega_{pi}^2}{k^2 v_{thi}^2}\left[1 + \frac{\omega + \omega_i^*}{k_z v_{thi}}\sum_n Z\left(\frac{\omega - n\omega_{ci}}{k_z v_{thi}}\right) I_n\left(b_i\right) e^{-b_i}\right] \qquad 5.30$$

From the Poisson equation we obtain:

$$k^2\phi = 4\pi e\left(Z_i n_i - n_e\right) \qquad 5.31$$

and

$$\varepsilon(\omega,\mathbf{k})\left(\phi + \phi_P\right) = \left[1 + \chi_i\left(\omega,\mathbf{k}\right)\right]\phi_P \qquad 5.32$$

Using Eq. 5.24 and 5.22 for eliminating f_P, we obtain:

$$\left\{\varepsilon(\omega,\mathbf{k})+\frac{\chi_e(\omega,\mathbf{k})\left[1+\chi_i(\omega,\mathbf{k})\right]}{4}\left[\frac{\mu_1^2}{\varepsilon(\omega_1,\mathbf{k}_1)}+\frac{\mu_2^2}{\varepsilon(\omega_2,\mathbf{k}_2)}\right]\right\}\Phi=0 \qquad 5.33$$

where

$$\mu_{1,2}=\frac{e}{m_e}\frac{k}{k_{1,2}}\sqrt{\left[\frac{\left|\mathbf{k}_{1,2\perp}\times\mathbf{E}_{0\perp}\right|^2}{\omega_0^4\omega_{ce}^4}+\frac{\left(\omega_0^2\mathbf{k}_{1,2\perp}\cdot\mathbf{E}_{0\perp}-\omega_{ce}^2k_{1,2//}E_{0//}\right)^2}{\omega_0^4\omega_{ce}^4}\right]} \qquad 5.34$$

are the coupling coefficients. Eq. 5.34 shows an inverse dependence of PI intensity on the operating frequency.

Eq. 5.33 has not trivial solutions under the condition:

$$\varepsilon(\omega,\mathbf{k})+\frac{\chi_e(\omega,\mathbf{k})\left[1+\chi_i(\omega,\mathbf{k})\right]}{4}\left[\frac{\mu_1^2}{\varepsilon(\omega_1,\mathbf{k}_1)}+\frac{\mu_2^2}{\varepsilon(\omega_2,\mathbf{k}_2)}\right]=0 \qquad 5.35$$

Eq. 5.35 is the parametric dispersion relation (PDR) in the form used in the LHPI module of the LH^{star} code.

Assuming: $\mathbf{k_0}=k_{0x}\mathbf{x}+k_{0z}\mathbf{z}$, $\mathbf{k_{1,2}}=k_{1,2x}\mathbf{x}+k_{1,2z}\mathbf{y}+k_{1,2z}\mathbf{z}$, and using the relation $\mathbf{n}=\mathbf{k}c/\omega_0$ between refractive indexes and wavevectors, the coupling coefficients of Eq. 5.34 can be written as:

$$\mu_1=\frac{n}{n_{1,2\perp}}\sqrt{\left(\frac{\omega_{ce}}{\omega_0}\frac{n_{1,//}u\sin\delta_0}{c}-\frac{\omega_0}{\omega_{ce}}\frac{n_{1\perp}u\cos\delta_0\cos\delta_1}{c}\right)^2+\left(\frac{n_{1\perp}u\cos\delta_0\sin\delta_1}{c}\right)^2} \qquad 5.36$$

$$\mu_2=\frac{n}{n_{2\perp}}\sqrt{\left(\frac{\omega_{ce}}{\omega_0}\frac{\left(n_{1,//}+2n_{0//}\right)u\sin\delta_0}{c}-\frac{\omega_0}{\omega_{ce}}\frac{\left(n_{1\perp}\cos\delta_1+2n_{0\perp}\right)u\cos\delta_0}{c}\right)^2+\left(\frac{n_{1\perp}u\cos\delta_0\sin\delta_1}{c}\right)^2} \qquad 5.37$$

where $\delta_0\equiv atg\left(\frac{k_{0//}}{k_{0\perp}}\right)$, , $\delta_1\equiv\angle(\mathbf{n}_1,\mathbf{n}_0)$

$$u\left[\mathrm{cm/s}\right]=\frac{c}{B_0\left[gauss\right]}\sqrt{\left\{\frac{8\pi\omega_{LH}^{-2}n_{0//}\sqrt{\frac{m_i}{m_e}P_0\left[kW\right]}}{\left(cL_y\left[cm\right]L_z\left[cm\right]\sqrt{\left(\omega_{LH}^{-2}-1\right)^3\left(1+\frac{\omega_{pe}}{\omega_{ce}}\right)^2+\omega_{pi}^{-2}}\right)\cdot10^{-10}}\right\}} \qquad 5.38$$

where $\omega_{LH}^2\equiv\omega_{pi}^2\left(1+\frac{\omega_{pe}^2}{\omega_{ce}^2}\right)$ is the cold lower hybrid resonant frequency, P_0 is the coupled RF power, L_y and L_z are the dimensions of the launcher in the poloidal and toroidal directions. Eq. 5.33 has been written in the useful form that displays the angle δ_1 relevant to the lower sideband. The latter gives, indeed, the most important contribution of PI to large LH $n_{//}$ spectral broadening.

Eqs. 5.38 –5.35 display the equations in the form used in the LHPI module of the LH^{star} code, which solves the PDR for practical calculations, utilising input data from experiments. Eq. 5.35 is numerically solved considering as independent variable the $k_\perp$ of the quasimodes driving the instability and, as dependent variable, the complex frequency of this mode, i.e., $\omega+i\gamma$, where γ is the growth rate of the sidebands, since in the relation $\omega_{2,1}=\omega\pm\omega_0$ the pump wave frequency ω_0 is a real quantity.
In the homogeneous and unbounded plasma limit considered here, PI originates in condition of $\gamma>0$, which indicates that the sideband grows exceeding the linear Landau damping, implicitly contained in the imaginary part of frequency. In the next subsection we show that a more stringent condition should occur in realistic condition of experiment.
In order to solve Eq. 5.35 the technique of the Stokes plot was originally utilised [35], now replaced by a more flexible tool.
As evident from Eq. 5.34, the coupling coefficients contain the contributions of the non linearity originated by the fluid equations of continuity and motion: the first term corresponds to the ***ExB*** non-linearity produced in direction parallel to the confinement magnetic field by the ponderomotive force, whilst the second term contains the contributions from polarisation drift and parallel motion. In literature only the ***ExB*** contribution is generally retained as, for the considered cases of: $\delta_1\equiv\angle(\mathbf{k}_{1\perp}, \mathbf{k}_{0\perp})\sim\pi$, or $\delta_2\equiv\angle(\mathbf{k}_{2\perp}, \mathbf{k}_{0\perp})\sim\pi$, this contribution is much bigger than others. However this condition does not apply for PI effects that are produced mainly by the parallel contribution in the lower density layer of the SOL. However, small $\delta_{1,2}$ values have the effect of also reducing the convective losses effect, thus enhancing the PI growth factor that directly determines the LH spectral broadening. This issue is discussed in Sec. 5.4.3.
To properly consider all relevant non-linear contributions of mode coupling (i.e., the coupling coefficients of PDR in the complete form), and to choose the numerical, rather analytical, approach for solving this equation, represent essential prerequisites for producing spectral broadening modelling consistent with the available data for RF probe measurements. In literature, instead, works aimed at obtaining only analytical expressions of the growth rate of a certain PI channel generally appear. This approach is quite useless for performing a complete spectral broadening modelling. Moreover these works did not retain the important effect of convective loss produced by plasma inhomogeneity [20,21], which determines the main features of spectral broadening and will be considered in Sec. 5.4.2.

The derivation of the parametric dispersion relation shows the central role of the electron temperature in defining the condition of the occurrence of PI-produced spectral broadening, which was considered for formulating the theoretical prediction [27,28] utilised for assessing the new method for LHCD at high plasma density [24]. Indeed, for deriving the expression of the perturbed electron density, Eq. 5.24, which is produced by ponderomotive potential, Eq. 5.22, the non-linear contribution of electrons has been only retained due to the large inertia of ions. It implies that, for given amplitude of the pump electric field, the non-linear mode coupling is weaker for higher temperature due to the inverse dependence of the susceptibility on the electron temperature via the velocity term of Eq. 5.25.

5.4.2 Solutions of the parametric dispersion relation

For each run of analysis, the solutions of the PDR (Eq. 5.35) give, for the low-frequency quasi-mode driving the PI channel, the complex frequency for any $k_\perp$. The other relevant parameters, $k_{//}$, B_0, ω_0, n_e, T_e, T_i, $\delta_{1,2}$ are kept fixed run by run.

The following typical plasma periphery parameters of the FTU LHCD experiment have been considered for the analysis related here: LH operating frequency f_0= 8.0 GHz, toroidal magnetic field (considered at a normalised minor radius $r/a \approx 0.8$) B_T= 4.54 T, coupled LH power P_{LH}= 0.35 MW, $n_{0//}$ =2 with a width of 0.4. The radiating area of the waveguide antenna is: *Ly* (=0.14m) x *Lz* (=0.07m). The two reference high-density plasmas of see Sec. 5.2 produced, respectively, in the standard and high T_{e_outer} regimes have been considered. The density and temperature profiles of Figure 5.1 have been considered.

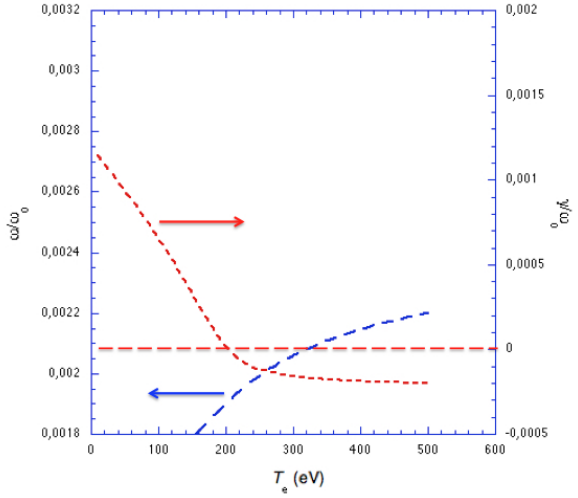

Figure 5.6a. Frequency and growth rates corresponding to solutions of the parametric dispersion relation (Eq. 35) with growth rate maximised with respect to $n_\perp$ of the low frequency quasi-mode driving the PI channel. The parallel component of the refractive index of the low frequency-quasi-mode is: $n_{//}$=7.

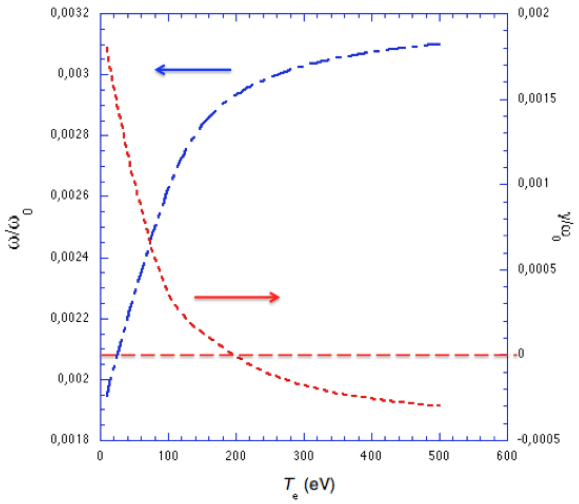

Figure 5.6b. Same parameters as in Fig. 6a, but $n_{//}$=15.

For the considered plasma parameters, solutions of Eq. 5.35 that have maximum growth rate with respect to $k_\perp$ (of the low frequency quasi-mode that drives the instability), represent the strongest and the more relevant PI contribution. We refer to these as *solutions with maximum growth rate*. Frequencies and growth rates corresponding to these solutions are plotted versus the electron temperature in Figure 5.6. Two values of the quasi-mode $n_{//}$ ($>n_{0//}$=2), which are relevant for possibly broadening the pump wave spectrum) have been considered, respectively, $n_{//}$ =7 and $n_{//}$ =15.

The growth rates displayed in Figure 5.6 diminish for high temperatures, becoming negative (giving stable solutions of Eq. 35) for T_e>200 eV. This condition corresponds to more internal radial regions or warmer conditions of outer plasma, as those produced in the new LHCD regime assessed on FTU [5]. No significant effects on the growth rate have been found by changing the ion temperature, which has kept fixed at 10 eV.

Figure 5.7 shows the necessary condition for possible occurrence of the important effect that broadens the LH $n_{//}$ spectrum by PI: LH sideband waves with $n_{//}$ higher than the nominal antenna value can be originated.

However, the spectral broadening actually occurs only provided that convective losses should be not strong enough to prevent the amplification of sideband waves. In PIs, the latter is consequent indeed to

the spatial propagation. The effect of higher growth rate for high $n_{//}$, found in the homogeneous plasma limit, considered in results of Fig. 5.7, is compensated by stronger convective loss that occur for high $n_{//}$ due to plasma inhomogeneity. This issue is described in the next subsection.

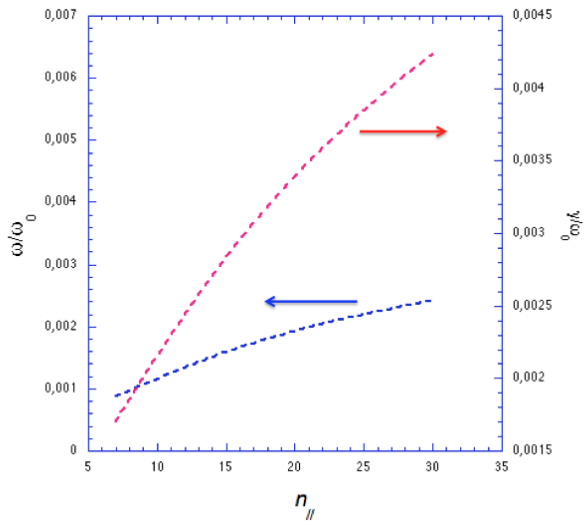

Figure 5.7. Trend of the growth rate maxima with respect to the parallel refractive index of the lower sideband, keeping fixed the other parameters. n_e=0.02 10^{20} m^{-3}, T_e = T_i =10 eV.

5.4.3 Convective loss produced by plasma inhomogeneity

The original analysis of convective loss due to plasma inhomogeneity effect for PI driven by a low frequency quasimode is contained in Refs. [28] and [21] which generalise the case of Ref. [20] that treats only PI driven by a resonant low frequency mode, not relevant for tokamak plasmas. We summarise hereafter the main concepts of analysis shown in Refs. [21].

In order to evaluate the amount of the RF power coupled by the antenna that is transferred by PI to LH sideband waves, the non-linearly coupled wave equations should be considered in the WKB limit. The approximations of unbounded and uniform plasma homogeneously illuminated by the LH pump wave, utilised in the previous two subsections, should be removed for taking into account the convective loss effect occurring in realistic conditions of experiment. We show that Convective loss limits the growth of PI that would occur at radial layers of plasma periphery, as expected by homogenous analysis.

As the LH wave energy flux is assumed contained in well-defined resonant cones [14], so that the plasma cannot be considered homogeneously illuminated by the LH pump, the finite spatial extent of pump wave region represent a cause of PI. This issue will be summarised in the next subsection. Here we focus on the effect of plasma inhomogeneity that tends to prevent the growth of the sidebands especially for large shifts in $n_{//}$ and frequency from the pump values. This convective loss contribution is indeed produced by the mismatch in frequency and wave-vector of waves that, once produced, propagate away from the original interaction layer, thus tending to lose the optimum matching conditions that satisfy the parametric dispersion relation. Consequently, the larger is the shift of sideband parameters from those of the pump, the stronger is the convective loss. A cut-off condition on the LH sideband $n_{//}$ that determines the size of the broadening of the LH launched spectrum is thus produced.

We assume for simplicity that only the lower sideband should be present in the PI, as it persists also for relatively large frequency shift from the pump wave frequency, as discussed in Sec. 5.1. However the analysis should be easily extended to include the upper sideband.

We limit the analysis to PI driven by low frequency quasimode (in the ion sound or ion-cyclotron frequency range) [14]. We also consider only a small effect of pump power depletion (less than 10%) in favour of sidebands, consistently to perturbative model approach.
For coupled mode equations of waves involved in PI, we can write [20]:

$$\varepsilon_1(\omega_1,\mathbf{k}_1)\phi_1 = \alpha_1\left(\phi_0\right)\phi \qquad 5.39$$

$$\varepsilon(\omega,\mathbf{k})\phi = \alpha\left(\phi_0\right)\phi_1 \qquad 5.40$$

where α, α_1 are the coupled coefficients.
In order to include the effect of phase detuning produced by plasma inhomogeneity we follow Ref. [28]. Eqs. 5.35, 5.36 can be generalised to include slow space-time variations of complex wave amplitudes. In the WKB limit, we can write:

$$\left(\frac{\partial}{\partial t} + v_{\mathrm{g1x}}\frac{\partial}{\partial x} + \Gamma_1\right)\phi_1 = -\mathrm{i}\frac{\alpha_1}{\frac{\partial\varepsilon_{1\mathrm{Re}}}{\partial\omega_1}}\phi e^{i\int M_x\,dx} \qquad 5.41$$

$$\left(\varepsilon + \mathrm{i}\frac{\partial\varepsilon}{\partial\omega}\frac{\partial}{\partial t} - \mathrm{i}\frac{\partial\varepsilon}{\partial k_x}\frac{\partial}{\partial x}\right)\phi = \alpha\phi_1 e^{i\int M_x\,dx} \qquad 5.42$$

where: $a=eF/F_1$, $a_1=F_1/F$, G_l is the linear damping of the sideband wave. Considering the effect of plasma inhomogeneity (assumed to occur in the *x* direction) the *k*-matching condition of the coupled modes, $\mathbf{M} \equiv \mathbf{k} - \mathbf{k}_0 - \mathbf{k}_1 = \mathbf{0}$, holds only at the interaction point *x*=0. Expanding away from this layer and assuming homogeneous the plasma in the y, z direction, i.e, $M_y \equiv M_z \equiv 0$, the small phase mismatch $M = M_x \equiv k_x - k_{0x} - k_{1x}$ can be expressed as:

$$M \approx \frac{dM}{dx}\Big\|_{x=0} x \qquad 5.43$$

Consequently, away from *x*=0, the condition of frequency matching of the interacting mode, $\omega - \omega_0 - \omega_1 \equiv 0$, is conserved, while a phase mismatch $M \neq 0$ due to the plasma inhomogeneity, increasing linearly with distance from the interaction point, is produced.

Utilising the expressions:

$$\phi = pe^{-\mathrm{i}\frac{dM_x}{dx}\frac{x^2}{4}} \qquad 5.44$$

$$\phi_1 = p_1 e^{\mathrm{i}\frac{dM_x}{dx}\frac{x^2}{4}} \qquad 5.45$$

the WKB Eqs. 5.41 and 5.42 can be integrated obtaining the spatial evolution of the sideband:

$$p_1(x) = p_{10}e^{\frac{\gamma\pi}{\frac{1}{\varepsilon_\mathrm{I}}\frac{\partial\varepsilon_{\mathrm{Re}}}{\partial k_x}\frac{dM_x}{dx}\mathrm{v}_{g1x}}} \qquad 5.46$$

and the spatial amplification growth factor due to plasma inhomogeneity for PI driven by a low frequency quasimode is [14]:

$$A_{INHOM} = \frac{\gamma\pi}{\left|\frac{1}{\varepsilon_{\mathrm{Im}}}\frac{\partial\varepsilon_{\mathrm{Re}}}{\partial k_x}\right|\frac{dM_x}{dx}\mathrm{v}_{g1x}} \qquad 5.47$$

For PI of significance, the condition A_{INHOM} >1 should occur, which defines the threshold imposed by the plasma inhomogeneity effect. For determining the phase mismatch parameter M_x, we consider that pump and sideband waves satisfy the linear LH wave dispersion relation: $e_{Re}(w_{0,1},\mathbf{k}_{0,1})=0$, which is equivalent to:

$$k_{0,1x} \approx \sqrt{\frac{m_i}{m_e}}\frac{\omega_{\mathrm{LH}}(x)}{\omega_0}k_{0,1/z} \qquad 5.48$$

From Eq. 5.48 we obtain the wavevector components $k_{0,1x}$ of the propagating modes involved in PI, which are useful for evaluating the phase mismatch. Regarding the driving low frequency quasimode, it is indeed an evanescent wave that exists only in presence of the pump wave, so that it does not have to satisfy a dispersion relation like Eq. 5.48. We can thus assume that a quasimode with $k_{\mathrm{x}} \approx k_{0\mathrm{x}} + k_{1\mathrm{x}}$, useful to minimise the phase mismatch (M~0), should be however available both in the interaction point (x=0) and at a certain small distance (Dx>0) away from it. We can also assume the condition $k_{1z} \sim k_{0z}$ that makes small the mismatch far away from the interaction point, as required by expansion of Eq. 5.43. Thus, by Eq. 5.48, we express, for slab plasma with weak inhomogeneity, the phase mismatch in terms of the small shift in frequency ($w=w_0-w_1$, $w<<w_0$) of sideband with respect to the pump wave. The spatial derivative of M_x in Eq. 5.47 is:

$$\left.\frac{dM_x}{dx}\right\|_{x=0} \approx \sqrt{\frac{m_i}{m_e}}\left.\frac{d\omega_{\mathrm{LH}}}{dx}\right\|_{x=0}\frac{\omega}{\omega_0^2}k_{1\mathrm{z}} \qquad 5.49$$

Consequently, the growth factor can be written as:

$$A_{INHOM} \approx \frac{\pi\omega_0^2}{\sqrt{\frac{m_i}{m_e}}\left|\frac{1}{\varepsilon_{\mathrm{Im}}}\frac{\partial\varepsilon_{\mathrm{Re}}}{\partial n_\perp}\right|\left.\frac{d\omega_{\mathrm{LH}}}{dx}\right\|_{x=0}\omega\mathrm{v}_{g1x}}\frac{\gamma}{n_{1//}} \qquad 5.50$$

In order to solve Eq. 5.50, solutions of PDR (Eq. 533) with large growth rate are necessary, i.e., calculated for plasma edge parameters. In particular, a solution characterised by relatively small shifts in frequency and wavevector component of the sideband from the pump wave (i.e., $w<<w_0$, and $k_{1z} \gtrsim k_{0z}$), should be considered, accordingly to conditions required for deriving Eq. 5.50.

The calculation of the amplification growth factor has been performed considering that the wave interaction begins close to the antenna–plasma interface, and eventually continues deeper in the plasma. The density profile in the scrape-off layer has been assumed with radial dependence:

$$n_e(x) \approx n_{e0}e^{\frac{x}{\lambda}} \qquad 5.51$$

where n_{e0} (=0.79 ×10^{18} m^{-3}) is the critical density at the layer $w_{pe} \approx w_0$ (LH wave cut-off) and l is the density characteristic length. For FTU plasmas, the available Langmuir probe measurements give l~2cm and plasma density ~1.0 ×10^{18} m^{-3} measured close to the radial antenna position, a few millimetres inside the plasma. At the antenna-plasma interface, Eq. 5.51 estimates a density of about 0.9×10^{18} m^{-3}. At this layer we initiate the analysis of contributions of both the convective effect due to plasma inhomogeneity and finite extent of the pump wave region. The latter effect will be discussed in the next subsection.
We discuss hereafter the assumptions considered for interpolating the available data of electron temperature relevant to the SOL and the main plasma (available from distances ≳5 cm away from the antenna).
Data from diagnostics of edge and periphery of the main plasma (Sec. 5.2) show that in the standard high density regime of FTU the electron temperature is very low (<100eV), within a wide radial gap (of about 13 cm). Langmuir probes mounted on the antenna measure: T_{e_outer}~10 eV. We assume that the latter value would persist in the whole SOL.
For the high T_{e_outer} regime, we consider the higher temperature (~15 eV) measured at the antenna layer, and assume that relatively high values (100 eV – 300 eV) occur deeper in the plasma (2 cm – 5 cm far away from the antenna. These assumptions give results of PI-produced spectral broadening consistent with the RF probe data of Sec. 5.3, as shown hereafter.

For a parallel refractive index of sideband $n_{1//}$=5 (which is not too far from the pump value, accordingly to assumptions kept for deriving Eqs. 5.49, 5.50), the solution of the parametric dispersion relation individuates a PI driving low frequency quasimode with perpendicular refractive index $n_{\perp} \equiv ck_{\perp}/\omega_0 \cong 2.65$, frequency $\omega/\omega_0 \approx 2.69\times10^{-4}$, and PI homogeneous growth rate $g/\omega_0 \approx 2.10\times10^{-3}$. Other parameters useful for calculating the amplification factor are: $e_{Re} \approx 1.01\times10^{3}$, $e_{Im} = 4.02\times10^{1}$. Consequently, Eq. 5.50 gives: $A_{INHOM} \approx 40$. A slightly lower value ($A_{INHOM} \approx 35$) is obtained for the case of high T_{e_outer} regime, due to smaller growth rate occurring at the antenna-plasma interface, as consequence of higher local temperature. We make the assumption that Eq. 5.50 would conserve some validity also for relatively large wavevector component of the sideband, as it is reasonable assuming that for sidebands with more noticeable difference in wave parameters with respect to the pump, convective loss due to phase mismatch should be correspondently stronger (consequence of wave propagation in inhomogeneous plasma away from the interaction point). The mechanism of dependence of the amplification factor on the sideband $n_{//}$, described by Eq. 5.50 is important for determining the broadening of the launched LH $n_{//}$ spectrum that penetrates to the plasma core. By Eq. 5.50, we thus estimate: $A_{INHOM} \approx 13$ for $n_{1//}$=30.

5.4.4 Convective loss produced by finite spatial extent of the pump wave region

The contribution of convective loss produced by the finite spatial extent of pump wave region is calculated using the homogeneous slab plasma limit. Following Ref. 20, the group velocities of pump and sideband and the respective propagating regions of energy fluxes have been taken into account. The *x* direction, on the *x* (radial), *z* (toroidal) plane, is perpendicular to the pump wave group velocity. The wave potential can be considered uniform in the region illuminated by the antenna, $f_0=P_0$ for $-L/2<x<L/2$ and $f_0=0$ otherwise, where *L* is the width of the pump wave region in the *x* direction. At the boundary, $f_0=P_0$ for $0<z<2a$ and $f_0=0$ otherwise, where $2a$ is the dimension of the antenna in the toroidal direction. The

sideband potential, which corresponds to thermal fluctuations, is $f_1=P_1$ for all z. Substituting f in Eqs. 5.41, 5.42, we obtain (in the homogeneous plasma limit):

$$\left(\frac{\partial}{\partial t}+v_{g1x}\frac{\partial}{\partial x}+\Gamma\right)\phi_1=-\mathrm{i}\frac{\alpha_1}{\dfrac{\partial\varepsilon_{1\mathrm{Re}}}{\partial\omega_1}}\phi_1 \qquad 5.52$$

In steady-state, Eq. 5.41 can be integrated to obtain the contribution of the growth factor that retains convective loss due to finite extent of the pump wave region. The amplification growth factor is:

$$A_{FPE}=\frac{\gamma(\mathbf{k_1},E_0,\omega_0,\omega_1)L}{v_{g_{1\xi}}} \qquad 5.53$$

Considering the propagation of the coupled LH power spectrum from the antenna–plasma interface to the plasma interior, the effective amplification growth factor should be evaluated performing the spatial average $\overline{A_{FPE}}$ over the region of SOL and plasma periphery where PI can occur (i.e., $\gamma>0$). For FTU plasmas, this region radially extends up to about 5 cm away from the antenna. It is worth to notice that the largest amplification factor contribution occurs in the outer plasma with lower density of SOL: here, the amplification factor is less sensitive to the $n_{//}$ parameter than in more internal layers.

Consequently, for the standard high plasma density regime we obtain $\overline{A_{FPE}}$ ~15 for $n_{1//}$=5, and higher values ($\overline{A_{FPE}}$ ~25) for higher $n_{1//}$ (=30) as effect of correspondently higher growth rate. In the high $T_{\mathrm{e\_outer}}$, regime, due to the markedly higher electron temperature in the SOL and periphery and consequent smaller growth rate, we obtain $\overline{A_{FPE}}$ ~ 13 for $n_{1//}$=7, and $\overline{A_{FPE}}$ ~ 4 for $n_{1//}$=30.

5.4.5 Pump power depletion

The competition of the aforementioned convective loss mechanisms determines the condition of the growth of PI sideband above the noise level and, consequently, the broadening of the launched LH power spectrum. For a certain spectral component of sideband, the effective growth factor, given by the minimum between A_{INHOM} and $\overline{A_{FPE}}$ should be large enough:

$$A=\min\left(A_{INHOM},\overline{A_{FPE}}\right)>1 \qquad 5.54$$

By Eq. 5.54 and results of Secs. 5.1–5.3, for FTU standard high-density regime, convective loss due to plasma inhomogeneity determines the PI amplification factor of sidebands with high $n_{//}$ (A = A_{INHOM} ~13 for $n_{1//}$=30). Thus, plasma inhomogeneity effect is mainly important for determining the size of the LH spectral broadening at high-density standard regimes, as predicted in Refs. [27, 28]. Finite extent of pump wave region effect is instead dominant for low $n_{//}$ (A= $\overline{A_{FPE}}$ ~16 for $n_{1//}$=5), and in the high $T_{\mathrm{e\_outer}}$ regime (A= $\overline{A_{FPE}}$ ~13 for $n_{1//}$=7, and A= $\overline{A_{FPE}}$ ~4 for $n_{1//}$=30).

The effective amplification growth factor of Eq. 5.54 is useful for evaluating the amount of the RF power coupled by the antenna that is transferred by the PI mechanism to the sideband waves. We are interested to sidebands originated by the background of thermal density fluctuations.

Following Ref. 5.38, we approximate the sideband electric field by the field energy contained in the wavenumber space limited by $k_{z\max}\approx\dfrac{\omega}{v_{the}}$ and $k_{\perp\max}\approx k_{z\max}\sqrt{\dfrac{m_e}{m_i}}\dfrac{\omega_0}{\omega_{LH}}$, which is given by the expression:

$$E_{1s}^2 \cong \frac{T_e}{4\pi\lambda_{\mathrm{De}}^3}\frac{\omega_0}{\omega_{LH}}\sqrt{\frac{m_e}{m_i}} \qquad 5.55$$

The fraction of pump power going to the sideband depends exponentially on the amplification factor, and can be estimated by the following expression:

$$\eta \approx \frac{E_{1s}^2 k_{\perp 0}}{2E_0^2 k_{\perp 1}} e^A \qquad 5.56$$

Since the considered model is valid only for small fractions of pump depletion ($\eta \lesssim 10\%$), due to the considered perturbative analysis limit, Eq. 5.56 cannot treat cases of large pump depletion, but is useful for determining the small pump power fraction that is transferred from the pump to sidebands that have large $n_{//}$, i.e., close to the $n_{1//\_\text{cut-off}}$ value. Consequently, for FTU standard high-density regime, we obtain: $n_{1//\_\text{cut-off}} \sim 30$ that corresponds to $\eta \sim 6\%$. For this refractive index, the sidebands exhibit large growth rate ($\gamma/\omega_0 \approx 5\times10^{-2} - 2\times10^{-2}$, for density 1.0×10^{19} m^{-3} – 0.1×10^{19} m^{-3}) at frequencies shifted up to about 20 MHz from the pump wave. An unrealistically huge depletion ($\eta \sim 40$) is obtained, instead, for values in the middle of the broadened spectrum ($n_{1//}$=15).

In the high $T_{\text{e\_outer}}$ regime, consequent to smaller growth rate produced by higher electron temperature, the depletion is small for sidebands with low $n_{//}$ ($\eta \sim 1\%$ for $n_{1//}$= 7, $\omega/2\pi \sim 5$ MHz), and is not significant for higher $n_{//}$.

Cases of strong pump depletion ($\eta >> 1\%$) should be treated considering, more properly, the non-linear evolution of coupled wave equations (including that of the pump wave), which enables considering the saturation effect of PI. This analysis was performed in Ref. [36] for case of sideband originated by the noise of generator, and a more general work is still in progress.

The PI mechanism is essential for modelling the LH deposition profile in realistic condition of experiment. Indeed, quasi-linear effect promotes the deposition of the whole LH power spectrum coupled by the antenna via LH sideband waves of the broadened $n_{//}$ spectrum although they have relatively small amplitude of the electric field [37].

Consequently, larger is the broadening in parallel refractive index, more peripheral is the deposition, as occurs in standard high-density regime of FTU [24,21].

5.4.6 The new software package for solving the parametric dispersion relation

We have verified that approximate analytical solutions of the parametric dispersion relation, Eq. 5.35, cannot allow performing a useful modelling of the parametric instability phenomenon that appears in the experiments. Consequently, useful modelling work should be performed only by means of appropriate numerical code. Such a tool was originally developed at ENEA Frascati Lab., with several upgrades, in the period 1988 – 2003, written in Fortran 77 language. However, a huge time was necessary for completing calculations relevant to only one case of plasma parameters.

Eq. 5.35 should be numerically solved considering as independent variable the $k_\perp$ of the quasimodes driving the instability and, as dependent variable, the complex frequency of this mode, i.e., $\omega+i\gamma$, where γ is the growth rate of the sidebands (in the selection rules linking the coupled mode frequencies involved in the instability, $\omega_{2,1}=\omega\pm\omega_0$, the pump wave frequency, ω_0, is a real). Such a calculation should

be performed keeping as fixed parameters the following quantities for a given values operating frequency of the RF power system and dilution of plasma ion species: $n_{//}$; the nominal amplitude value of the RF electric field at the peak of the launched antenna spectrum; the angle δ_1 defined in Eqs. 5.36, 5.37; the local values of plasma density; temperatures of plasma ions and electrons; the static magnetic field of plasma confinement. Consequently, considering the radial profiles of the latter four parameters and the need of identifying frequencies and growth rate of the PI coupled modes for a sufficiently wide range of $n_{//}$ and δ_1 values, a huge number of code runs were needed for a realistic case of experiment. Unfortunately, the limits of the Fortran 77 version enabled performing a complete set of runs only by work of several days. Consequently it was practically impossible to produce, in reasonable time, results useful for considering and comparing further cases of plasma discharges of a same machine and, a fortiori, cases of different machines.

This major problem has been recently solved upgrading the old program by a new release written in Fortran 2003. In summary, vectors allocable are present in the types defined by users and the procedures have arguments of allocable type. In addition, in order to improve flexibility, the definition of global variables has been avoided preferring the option of types defined by users. The old F77 program has been also improved by: i) inserting several IMPLICIT NONE that force all variable to be declared; ii) defining a single new module aimed at performing much faster than before the central function of the old program that consists in the search of a guess of solution of the parametric dispersion relation; iii) eliminating all COMMON and transforming them in types defined by users. This way, the program can run under openMP, i.e, parallel thread do not risk detrimentally affect each other the memory.

As result, Eq. 5.35 is solved in the complex plane using $k_{\perp}$ as independent variable and the complex frequency as dependent variable. Since Eq. 5.35 consists of analytical function, the contour rule has been used for finding the solutions. For a complex function, the number of zeros (N) minus the number of poles (P) is given by:

$$N - P = -i\frac{1}{2\pi}\oint\frac{f'(z)}{f(z)}dz \qquad 5.57$$

In the lack of poles this reduces to the number of zeros. In case of contour given by points, we approximate the integral by a sum, considering that:

$$f'(z_{i+1/2}) = \frac{f(z_{i+1}) - f(z_i)}{z_{i+1} - z_i} \qquad 5.58$$

and

$$f(z_{i+1/2}) = \frac{f(z_{i+1}) - f(z_i)}{2} \qquad 5.59$$

We obtain:

$$N - P = -i\frac{1}{\pi}\sum_i\frac{f(z_{i+1}) - f(z_i)}{f(z_{i+1}) + f(z_i)} \qquad 5.60$$

Since the approximate solution necessary for assessing a guess for given parameters, a little precision is sufficient. Consequently, we have chosen considering present a zero if the value of *N* is larger than 0.5. Program starts from a sufficiently wide contour that contains at least one root. The contour is divided in two parts and the one containing the root is maintained. To respect proportions, divisions are performed alternatively in vertical and horizontal sense. For simplicity, a rectangular contour is used as starting

shape with the number of points located on a side proportional to a power of two (>1): consequently, for any further division, only half of contour points should be recalculated.

After given number of divisions, the function is approximated by a plane $\alpha(z - z_0)$ using data relevant for the last contour. By this approximation the root z_0 is obtained.

The program (written in Fortran 2003) consists of two modules: *mdl_ideple*, which is an interface build around the old program in Fortran77, *contour_mdl*, which manages the integration along contours and the search of roots: *mdl_command_line*, that reads the command row where the input and output directories should be specified, and *mdl_fullexp* which is dedicated to overall manage the program.

Two files represent the input, one consisting of several parameters that do not change during a single run of program, the other with the plasma radial profiles of density, temperature (of ions and electrons) and confinement magnetic field. Input parameters include the range of complex values z where roots of Eq. 5.35 should be found and the range of $n_\perp$, which is the refractive index of the driving quasimode, along direction perpendicular to the confinement magnetic field.

The core of the program is based on two cycles: the more external acts on the radial profiles and the more internal on $n_\perp$. The latter has been inserted within a parallel section OpenMP and allows the program using all the available cores. In the output, each value of the profile is associated to the found root, provided that this solution should be present in the previously set range, as a function of the $n_\perp$ value.

For given radial position of plasma parameter profiles, by varying $n_\perp$ the complex root enters into the range of search of the roots and, as $n_\perp$ varies further, the root changes and comes out the range. Correspondently, it is written a file with the value of the solution consisting in the $n_\perp$ and the complex frequency that represent a zero of the parametric dispersion relation (PDR), Eq 5.35. Moreover, a summary file is written that stores, for every radial position, the value of $n_\perp$ that corresponds to solution of PDR with maximum growth rate, i.e., the maximum value of the imaginary part of the complex frequency. The latter values identify the parametric instability that occurs with larger intensity in the limit of homogeneous, unbounded plasma.

5.5 Interpretation of experimental results

The typical RF probe spectra observed during LH experiments at high plasma densities in the standard and high T_{e_outer} regimes of FTU are compared in Figure 5.8. In standard regime (red curve), the broadening at around the operating frequency shows a marked downshift up to about 15 MHz. The high T_{e_outer} regime is characterised by a noticeably less pronounced and more symmetric spectral broadening (green curve), of about 5 MHz. No LHCD effect is observed to occur in the core in the standard regime condition, although the plasma density is lower ($n_{e\_av} \approx 1.1\times10^{20}$ m^{-3}) than in the latter one ($n_{e0}\approx5\times10^{20}$, $n_{e\_0.8}\approx0.8\times10^{20}$, $n_{e\_av}\approx2\times10^{20}$).

The spectral asymmetry occurring in standard regime is interpreted as sign of the upper sideband of PI that is not propagating for large frequency shift (of a few megahertz) from the operating pump frequency (see the introduction of Sec 5). The lower sidebands present up to about 15 MHz in Fig. 5.8 (red curve) are quite consistent with PI-produced spectral broadening results of Sec. 5.4 relevant to standard regime ($n_{//\_cut0off}\sim30$, $\omega/2\pi \sim 20$ MHz).

For the high T_{e_outer} regime, the broadening exhibited by the green curve of Fig. 5.8 is consistent with spectral broadening modelling result ($n_{//\_cut\text{-}off} \sim 7$, $\omega/2\pi \sim 5$ MHz).

As the fraction of power transferred to sidebands in the core of the spectrum is not evaluable (due to the obtained too large values of the amplification growth factor) we assume that a pump depletion of 50% in the range $2.3 \lesssim n_{//} \lesssim 28$ would contribute in building the *initial spectrum* to be utilised for modelling the LH deposition profile for standard regime case. A similar assumption has been considered for the T_{e_outer} regime case in the range $2.3 \lesssim n_{//} \lesssim 4.5$.

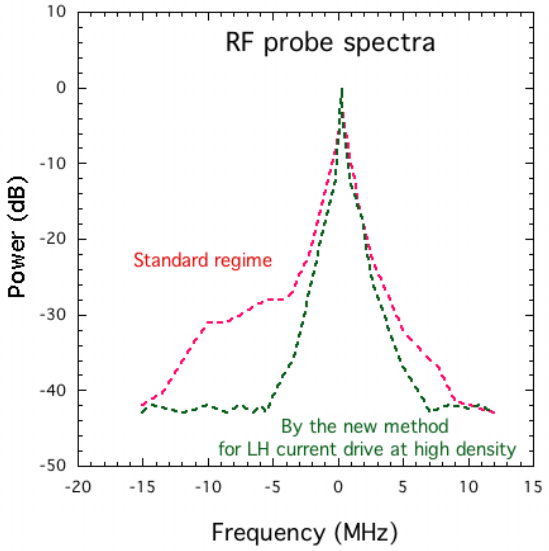

Figure 5.8. Frequency spectra of the signal collected by the radiofrequency probe. The zero frequency corresponds to the LH operating frequency of the FTU experiment (8 GHz). Green curve: high T_{e_outer} regime (new method for LHCD at high plasma density). Red curve: low T_{e_outer} regime (standard operation).

5.5.1 Modelling of LH deposition profile

We provide hereafter information that integrates contents of Ref. [24], relevant to modelling results obtained considering data of LHCD experiments at high density on FTU.

The *initial spectra* shown in the previous section have been used as inputs to the LH^{star} code for modelling the LH-driven current density profile, via ray-tracing in toroidal geometry and Fokker-Plank analysis [21]. In this condition, the effect of $n_{//}$ up-shift due to ray propagation in toroidal geometry takes place. Since, for the considered experiment parameters, LH rays meet reflections from the LH cut-off layers at the edge – where the geometric optic limit fails – the ray-tracing technique cannot be utilised for determining the $n_{//}$ up-shift produced by propagation effect. We have however assumed that this mechanism would produce a marked up-shift (to $n_{//}=5$) for the high T_{e_outer} case. According to numerical simulation results, the coupled LH power is mostly deposited at $r/a \approx 0.4$, as shown by green curve of in Figure 9 (from Ref. [21]). Numerical simulation also shows that LH waves accelerate plasma electrons, mainly in the same radial layer at $r/a \approx 0.4$, at energies in the 40 keV÷80 keV range, consistent with the available FEB (fast electron Bremsstrahlung) energetic spectra [24].

For the FTU standard regime, the computed LH power deposition is localised at the very plasma edge, red curve of Fig. 5.9. In this case, very low energy electrons are produced by the coupled LH power (<10 keV, out of the FEB camera range of detection). It is worth to notice that the LH^{star} code considers only plasmas confined in closed magnetic surfaces. The approximation of including the antenna–plasma interface has been thus made, so that the layer r/a=1.0 – 0.9 would correspond to the SOL. The locally accelerated electrons (corresponding to the red curve case) should be therefore virtually considered having poor confinement, which is insufficient for producing detectable changes in the local temperature.

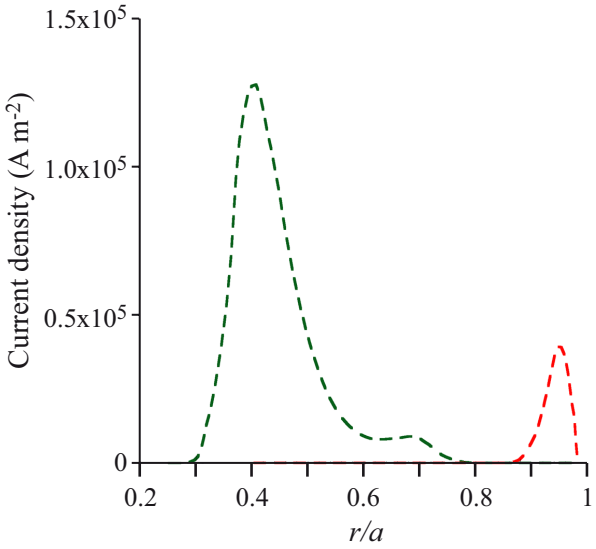

Fig. 5.9. LH-driven current density profiles in the standard and high T_{e_outer} regimes. r/a is the normalised minor radius of the plasma column. The profiles have been obtained by modelling with the LH^{star} code, considering two different the plasma discharges: standard regime (red curve), high T_{e_outer} regime (green curve).

5.6 Spectral broadening in other experiments and proposed interpretations for LH effects at high density

An asymmetric downshifted spectrum of the RF probe signal, similar to that found in the standard high density regime of FTU, was observed also in C-Mod, JET and EAST [38,39]. In these experiments a dependence of both the spectral broadening and the occurrence of LHCD effects in the core was found, consistent with results obtained on FTU, following theoretical predictions of PI modelling [27,28].

Linear wave scattering from plasma density fluctuations [32] could not explain the RF probe spectral asymmetry, which is typical of the non linear PI phenomenon; moreover, linear scattering was recognised to be largely insufficient for explaining the markedly low LHCD effect at high density in C-Mod [40]. On FTU, it is possible that the linear wave scattering effect would broaden the radiofrequency probe spectrum up to about 2 MHz (at around 20 dB below the RF power peak), in both regimes (standard and high density).

Modelling works that provided an interpretation of LHCD results at high density invoking mechanisms different from PI, are discusses hereafter.

The linear scattering by density fluctuations [32] was found insufficient for interpreting the reduction of the LHCD effect at high density observed on Alcator C Mod [40]. In the frame of the same theory, a model was proposed for interpreting the available data of RF probe spectra and LH effects during the LHCD experiments at high density on FTU [41]. However, this method is intrinsically useless for predicting data from experiments, since the outputs of the described model are tailored on the basis of the same experiment data that should be predicted (i.e., spectral broadening and LHCD effects).

Collisional effect [14] was invoked as responsible of reducing in FTU the LHCD effects when operating at relatively low electron temperature at the plasma periphery, as result of a 1-D ray-tracing-Fokker-Planck tool [42]. However, in this tool, the assumed geometric optic approximation fails at the cut-offs layers located near the edge, in the considered regimes of FTU (and other machines) characterised by LH multi-radial pass. Consequently, results that depend on assumptions, necessary for continuing the analysis after LH ray reflections, are obtained indeed. For this reason, in order to test results of a certain modelling tool, available data of experiments in both single and multi-pass regimes should be considered. This correct approach is routinely followed using the LH^{star} code, as shown, e.g., in Ref. [21] Regarding the role of collisional damping [14] in producing the strong deposition of the coupled LH power at the plasma column periphery, observed in standard FTU regimes at high densities, this contribution was considered not decisive. Indeed, taking into account remarkable cases of plasma discharges of JET, in which LH effects in the core did not occur (like in the FTU standard regime) the LH absorption was expected to occur in a single radial pass, thus making negligible the collisional damping effect [43].

We can thus conclude that parametric instability is the most relevant phenomenon that can produce the observed undesired absorption of the coupled LH power.

A further work will be dedicated to the case of possible LHCD experiments on ITER in order to extend previous study. It is worth to notice here that FTU discharges performed in standard regime are characterised by outer layer of plasma column in which the electron temperature profile approaches the conditions envisaged so far for the scrape-off layer of ITER [43]. The coupled LH power would be thus asked propagating in the SOL (whose size is of the order of ten centimetres) in which the electron temperature would be less than about 100 eV. This condition is similar to the FTU case of standard regime of Fig. 1. Consequently, the FTU plasma represents a useful reference test for designing a possible LHCD experiment on ITER. Considering that the operating LH frequency in FTU (8 GHz) is higher than that envisaged for ITER (5 GHz, which means that stronger PI effects are expected to occur in ITER), results obtained in standard high density regime on FTU allow excluding that any LHCD effect would occur in the core of ITER, if the SOL electron temperature profile will be confirmed (in particular the profile for steady-state scenario), or in case operation with higher electron temperature in the SOL would be prevented for some reason. LHCD effect would be, instead, successfully performed in ITER by operations producing low electron temperature ($\gtrsim$100 eV) only within a radial layer of the order of one centimetre close the antenna mouth. At smaller radii, temperatures higher of at least a factor three should be necessary.

Considering the similarity with ITER of the FTU density and temperature profiles in the radial outer plasma region, new experiments are planned on FTU, aimed at assessing the conditions useful for LHCD regimes in ITER, on the basis of the modelling of the PI-produced spectral broadening.

5.7 Discussion

The fundament of modelling that produced theoretical predictions [27,28] useful for assessing on FTU the new method for enabling the LHCD effect at reactor-graded high plasma density [24] has been described. Namely, we have provided information necessary for using the tool that determines frequencies and growth rates of PI coupled modes and, taking into account convective loss effects, calculates the parametric-instability-produced broadening of the spectrum launched by the antenna. The consequent initial $n_{//}$ spectrum is used in the LH^{star} code for obtaining the LH deposition profiles via quasilinear effect.

Using the same approach, previous works relevant to LHCD experiments of JET performed at relatively low density obtained lower values of the PI amplification factor, so that the model limitation was not

exceed and the spectral broadening effect was properly estimated. This mechanism was recognised important for obtaining an LH deposition profile modelling in agreement with available data of diagnostics.

The present case of experiments at high density of FTU produces, instead, large PI amplification factor values that correspond to unrealistically huge pump power depletion. Consequently, the width of the initial LH spectrum has been estimated (considering that little power fraction is carried by sidebands having refractive index near the $n_{//\_cut\text{-}off}$), but only an assumption has been made about the whole power fraction carried by the broadened LH spectrum.

New data from FTU experiments, produced in a broader range of density ($0.8\times10^{20}\,m^{-3}\gtrsim n_{e\_av}\gtrsim1.2\times10^{20}\,m^{-3}$) than in cases referred before [5], show that the higher is the electron temperature of plasma periphery, the stronger is the LHCD effect and, together, reduced is the spectral broadening. Moreover, the examples of solutions of the parametric dispersion relation and spectral broadening calculations shown here are made for different conditions of the edge, and indicate that relatively low electron temperature of plasma edge is condition that enables LH sidebands with high $n_{//}$ to broaden the launched spectrum. The causal link between electron temperature in the outer plasma layer, spectral broadening and LHCD effect has been now supported by further data of modelling and experiment.

Considering that the PI growth rate reduces for higher operating frequencies and FTU utilises the highest frequency so far, the results presented here indicate that, in order to have more chances of producing LHCD effect at high density, the condition of operating with sufficiently warm plasma edge should be considered, possibly, also more stringently than for the FTU case.

Details have been provided about the method utilised, in performing the RF probe measurements, for distinguishing from the noise level the contribution of spectral broadening of LH sideband waves shifted by large frequencies from the LH operating value. Consistency of the frequency spectrum and PI-produced spectral broadening data has been found.

Incidentally, the utilised technique of RF probe can assess the spectral broadening in a more proper way than that based on the measure of the RF power reflected back from the plasma to the antenna [45]. The latter technique cannot contain, indeed, the necessary information on the noise level, since a huge attenuation (≳50 dB) is generally present in the antenna measurements. Moreover, this approach can produce artefacts in the mixer of spectrum analyser, when the instrument is improperly set with low attenuation at the entrance for trying establishing the noise level.

Experiments performed following the new track opened by the FTU results have shown a dependence of both the spectral broadening and occurrence of LHCD effects in the core consistent with the FTU outcomes. Comparison with other interpretations of the LH effects observed at high densities allow concluding that parametric instability would represent the main cause of the observed undesired absorption of the coupled LH power.

Next experiments on FTU will test modelling prediction expecting that, by coupling ECRH radiofrequency power, the electron temperature in outer plasma region would be slightly enhanced. This effect would be useful, together with tools already tested for this aim on FTU, for enabling LHCD at high density towards steady-state conditions.

Standard high-density regimes of FTU exhibit electron temperatures of plasma edge close to those envisaged so far for ITER. We expect that a successful LHCD experiment in ITER requires the occurrence of relatively cold plasma ($T_e\lesssim100$ eV) within a small radial layer (of the order of one centimetre) close the antenna mouth, while noticeably higher temperatures ($T_e \gtrsim 300$ eV) would occur deeper in the plasma. Modelling results relevant for a possible LHCD experiment in ITER will be presented in a dedicated work.

The related results confirm the advance produced at Frascati in providing the know how, supported by modelling of relevant non-linear physics of plasma edge, useful for extending the range of usefulness of the lower hybrid current drive effect to regimes of critical importance for fusion reactors.

Chapter 6

6 Problem solution n.1: how to drive current at high plasma density of thermonuclear reactor

We consider here important modelling and experimental results (published on Ref. 24: R Cesario, L Amicucci, et al., Nature Communications, 2010, and Ref. 21: R Cesario, L Amicucci, et al., Nuclear Fusion 2014) showing how, after decades of unsuccessful attempts, a new method has been assessed to make possible the lower hybrid current drive (LHCD) at reactor relevant, high plasma densities.

This successful experiment, carried out on FTU (Frascati Tokamak Upgrade), has been designed on the basis of results of the parametric instability modelling tool, described in Chapter 5. Several years before performing the experiments, such modelling work allowed formulating theoretical prediction on how to reduce parasitic effect preventing the radiofrequency power penetration into high-density plasma core. The new method requires operation with higher temperature of plasma edge, expected useful for reducing the undesired effect of huge parametric instability-produced frequency broadening of the launched antenna spectrum that makes opaque the plasma to RF power penetration. Consequently, LHCD at high plasma density ($5x10^{20}$ m^{-3}, higher than that envisaged for International Thermonuclear Experiment Reactor: ITER) has been produced, as never observed before, accompanied by the expected marked reduction of spectral broadening.

6.1 Experimental results

Experimental results presented here confirm the theoretical predictions and extend the range of usefulness of the LHCD effect to regimes of importance for fusion power plants.

High-density plasmas have been produced in a wide range of parameters (toroidal magnetic field: B_T= 5T-8T, plasma current: I_P = 0.36 MA – 0.7 MA) and in standard conditions consisting in the plasma displaced towards the toroidal (internal) limiter, the vessel wall coated with boron and the plasma fuelled by gas injection. The FTU plasma major radius on axis is R_0=0.935m and the minor radius of main plasma at the last closed magnetic surface (LCMS) is a=0.285m. The generated LH-accelerated supra-thermal electrons have been detected by a fast electron Bremsstrahlung (FEB) camera using hard X-ray emission detection [29]. Figure 6.1 shows the trend of the hard X-ray emission level due to LH-accelerated electrons at different plasma densities.

The experimental points connected by dashed lines refer to plasmas with three different sets of plasma current and magnetic field in the standard conditions. The dotted line refers to plasmas in a new regime described later in the paper. In the standard regime the FEB signal remains at the noise level for $n_{e\_av} \gtrsim 1.3 \times 10^{20}\,m^{-3}$. In these conditions the coupled LH power appears to be fully deposited at the very edge of the plasma. This behaviour cannot be explained in terms of LH wave inaccessibility since these experiments

have an antenna spectrum higher than the critical value ($n_{//crit} \approx 1.75$) for LH wave mode-conversion into fast waves.

To produce higher T_{e_outer} the flexibility of FTU has been exploited to use a lithium-coated vessel and proper gas fuelling operations described in the Method Summary section. For these conditions, hereafter referred to as the "high T_{e_outer} regime", the experimental points denoted by dotted lines in Figure 6.1 were produced, indicating a change in the behaviour of the accelerated electrons compared with the standard regime. In this new regime the LH effect persists to densities a factor two higher than in standard regime.

Figure 6.2 shows the Plot of hard X-ray emission at different plasma densities and the radial profiles of the hard X-ray signal detected for three high-density plasmas ($n_{e\_av} > 1.5 \times 10^{20}$ m^{-3}) in the high T_{e_outer} regime. The energy range of the LH-accelerated plasma electrons is 40 keV – 200 keV and the coupled LH power is deposited in the core, mainly at r/a = 0.3 – 0.4. The radial profiles of the LH-driven current density are expected to have the same shape as the hard X-ray profile, as routinely assumed in tokamak experiment modelling. The high T_{e_outer} regime plasmas have densities much higher than in the standard regime (increased by 40% - 90%) and much lower core electron temperatures will consequently occur at the same plasma current. Since it is necessary to have regimes with similar core T_e when comparing LH effects, slightly lower plasma current has been used in the standard regime (reduced by 10% - 35%, the lowest current case referring to the one with lowest target density). In this way the following typical conditions have been produced: $T_{e0} \approx 1$keV in the standard regime; and $T_{e0} \approx 0.7$keV in the new regime plasmas with 70% higher density.

The time traces of the main plasma parameters of four relevant FTU experiments are shown in Figure 6.3. Fig.6.3a compares plasma discharges of the two regimes with similar parameters. At the start of the LH pulse significantly different T_{e_outer} is obtained (more than a factor two at $r/a \approx 0.65$ - 0.95, see boxes 3 and 4 of Fig.6.3a). This difference (and the reason for the name "high T_{e_outer} regime") was predicted to be sufficient to reduce the PI-induced spectral broadening and to favour LH penetration into the plasma core [11,12].

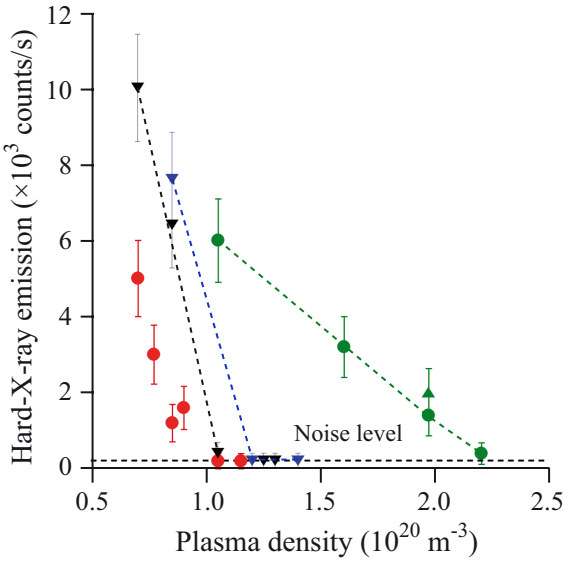

Figure 6.1. Plot of hard X-ray emission at different plasma densities. The fast electron Bremsstrahlung (FEB) camera on the central equatorial chord has been used. The standard

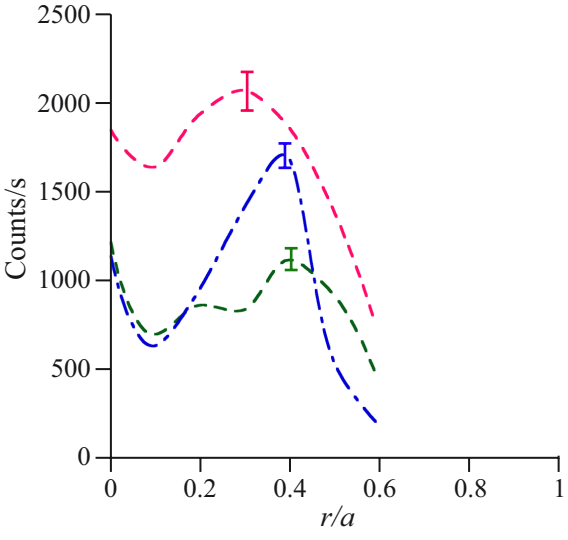

Figure 6.2. Radial profiles of the hard X-ray level in high-density plasmas performed in high T_{e_outer} regime. r/a is the normalised plasma radius, a is the plasma minor radius at

(dashed lines) and high T_{e_outer} (dotted line) regimes are shown. Different operating conditions are used in the standard regime: toroidal magnetic field B_T=5.2 T and plasma current I_P=0.36 MA (red squares), B_T=5.9 T, I_P=0.51 MA (black triangles), B_T=7.1 T, I_P=0.51 MA (blue triangles). The circles and triangle in green refer to the high T_{e_outer} regime, performed with B_T=5.9 T and I_P=0.59 MA. The coupled LH power is P_{LH}=0.35 MW in all cases, except P_{LH}=0.52 MW in the case indicated by the green triangle.

the last closed magnetic field surface. The cases of three different operating plasma densities are shown: n_{e_av} =1.6×10^{20} m^{-3} (red curves), n_{e_av} =1.7×10^{20} m^{-3} (blue curves), n_{e_av} =1.9×10^{20} m^{-3} (green curves) have been considered. Radiofrequency power coupled to the plasma: P_{LH} = 0.35 MW. Toroidal magnetic field: B_T=5.9 T, plasma current: I_P=0.59 MA. The error bar corresponds to one standard deviation.

In both experiments the LH power (0.35 MW) was coupled during the plasma current flat-top (starting at t≈0.1 s) when the line-averaged density was n_{e_av}≈1.4×10^{20} m^{-3} for the standard regime and n_{e_av}≈1.9×10^{20} m^{-3} for the high T_{e_outer} regime. In the case of the high T_{e_outer} regime the hard X-ray signal becomes markedly higher than the noise level during the LH pulse (see Fig. 6.3a, box 5), a sign that the coupled LH power has penetrated and interacted with the plasma core. The standard regime does not show this signature. In high T_{e_outer} regime experiments performed with the same parameters as the one in Fig 6.3a, but with a higher coupled LH power (0.52 MW instead of 0.35 MW), show a more pronounced increase in the hard X-ray signal (by a factor of two) and a higher central temperature (by 35%) as seen in Fig.6.3b. A clear increase of the central electron temperature also occurs during the LH power-coupling phase giving a further indication that, in high T_{e_outer} regime, the LH power penetrates to the plasma core.

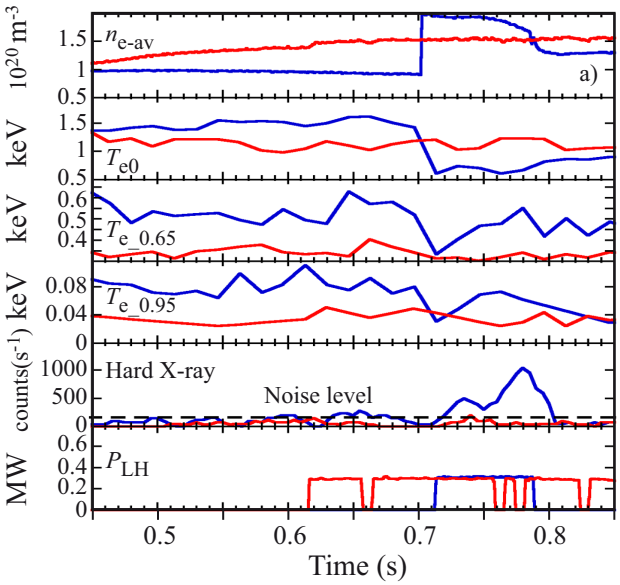

Figure 6.3a. Time evolution of the main plasma parameters. a) Two high-density plasma discharges are shown. Standard regime (plasma discharge 32323, red colour), high T_{e_outer} regime (plasma discharge 32555, blue colour). Toroidal magnetic field B_T=6.0 T. Plasma current: I_P=0.52 MA in pulse 32323, and I_P=0.59 MA in plasma discharge 32555. Plasma density (box 1), central (box2) and edge electron temperature (at r/a≈0.65 - box 3, at r/a≈0.95 - box 4), hard-X level (box 5), LH power (box 6). r/a is the normalised plasma radius, a is the plasma minor radius at the last closed magnetic field surface.

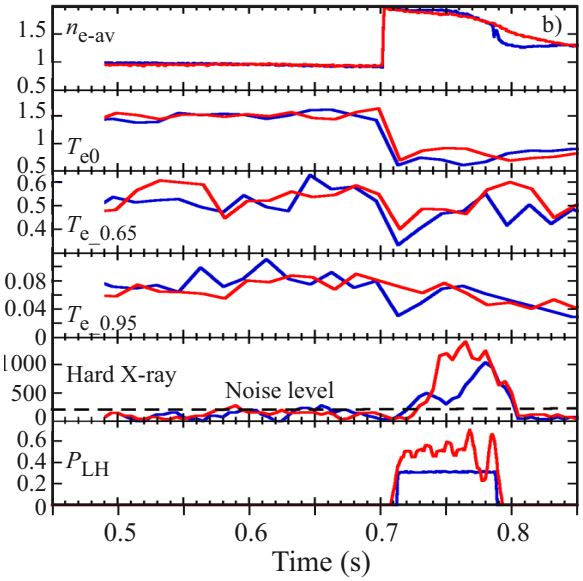

Figure 6.3b. Two high-density plasma discharges performed in the high T_{e_outer} regime are shown. Same operating parameters (B_T=6.0 T, I_P=0.59 MA), but different coupled LH power: 0.35 MW (plasma discharge 32555, blue colour), 0.52 MW (plasma discharge 32557, red colour). Plasma density (box 1), central (box 2) and edge electron temperature (at r/a≈0.65 - box 3, at r/a≈0.95 - box 4), hard-X level (box 5), LH power (box 6).

The hard X-ray signal starts to strongly decrease at t=0.78s when the LH power is still on and the edge temperature, $T_{e\_0.95}$, has decreased (from 80 eV to 50 eV) to values close to the corresponding standard regime (see box 4 of Figs 6.3a and 6.3b). This indicates that higher T_{e_outer} enhances the LH wave interaction with a high-density plasma core and that the plasma edge should be further heated to sustain the LHCD effects for longer times.

Kinetic profiles evolution is compared in Figure 6.4 for two pairs of experiments performed in the standard and high T_{e_outer} regimes.

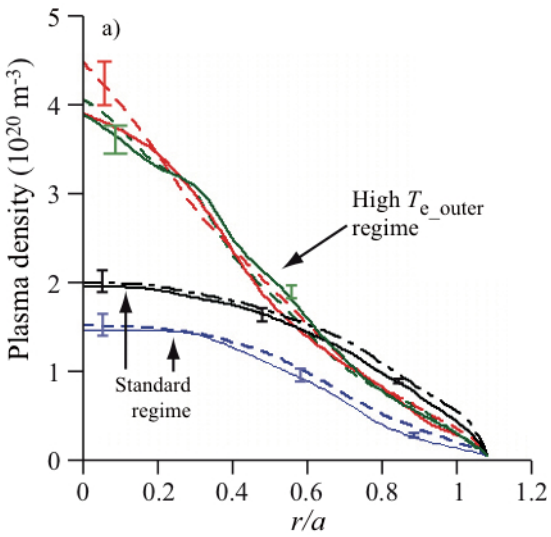

Figure 6.4a. Evolution of the plasma density and temperature radial profiles. The same data of plasma discharges described in Fig. 3 of Ref. 5 are displayed. a) Plasma density profiles in standard and high T_{e_outer} regimes. r/a is the normalised plasma radius, a is the plasma minor radius at the last closed magnetic field surface. Two standard regime plasmas are considered: plasma discharge 32323 (B_T=6.0 T, I_P=0.52 MA), black curves: before LH phase (t=0.61s, continuous curve) and during LH phase (t=0.64s, dashed curve); plasma discharge 32164 (B_T=5.2 T, I_P=0.36 MA), blue curves: before LH phase (t=0.61s, continuous curve) and during LH phase (t=0.64s, dashed curve). Two high T_{e_outer} regime plasmas are considered: plasma discharge 32555 (B_T=6.0 T, I_P=0.59 MA), green curves: before LH phase (t=0.71 s, continuous curve), during LH phase (t=0.74 s, dashed curve); plasma discharge 32557 (B_T=6.0 T, I_P=0.59 MA), red curves: before LH phase (t=0.71 s, continuous curve), during LH phase (t=0.74s, dashed curve). The error bar corresponds to one standard deviation.

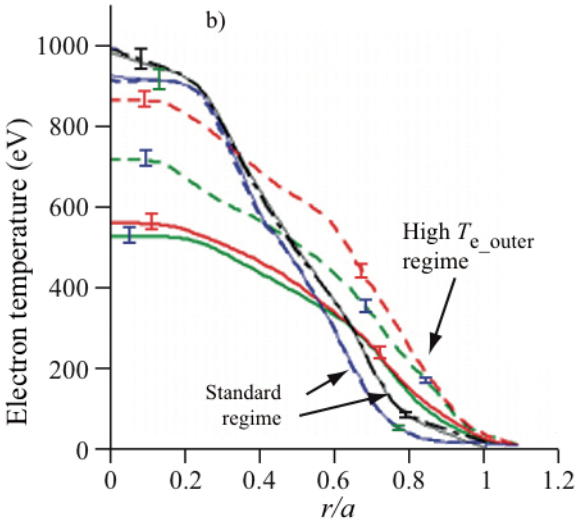

Figure 6.4b. Electron temperature profiles. Standard regime: plasma discharge 32323 (B_T=6.0 T, I_P=0.52 MA), black curves: before LH phase (t=0.61s, continuous curve), during LH phase (t=0.64s, dashed curve); plasma discharge 32164 (B_T=5.2 T, I_P=0.36 MA), blue curves: before LH phase (t=0.61s, continuous curve), during LH phase (t=0.64s, dashed curve). High T_{e_outer} regime: plasma discharge 32555 (B_T=6.0 T, I_P=0.59 MA), green curves, before LH phase (t=0.71 s, continuous curve), during LH phase (t=0.74 s, dashed curve); plasma discharge 32557 (B_T=6.0 T, I_P=0.59 MA), red curves: before LH phase (t=0.71 s, continuous curve), during LH phase (t=0.74s, dashed curve). The radial size of the scrape-off plasma (between LCMS and LH antenna mouth) is of 0.022 m. The error bar corresponds to one standard deviation.

For each experiment two time points are considered, one just before and one during the LH power-coupling phase. The density profiles in Fig 6.4a are obtained using a multi-chord CO_2 and CO laser scanning interferometer. Both discharges in the standard regime have high plasma densities (n_{e_av}>1×10^{20} m^{-3}) for which the signatures of LH-accelerated electrons are not observed (see Fig. 6.1). In the standard regime case the core plasma density is significantly lower than in the high T_{e_outer} case, but in one of the standard regime plasmas the density at the periphery is slightly higher. This allows the role played by different edge plasma densities to be compared in the two regimes. Figure 6.4b shows the electron temperature profile in the outer plasma region using electron cyclotron emission (ECE) Michelson interferometer and Thomson Scattering (TS) diagnostics, the latter only being used when LH-generated hard X-rays disturbing the ECE diagnostic are produced. Langmuir probes have been used to diagnose the SOL kinetic profiles. In both standard regime plasmas the electron temperature was T_e≲100 eV within a radial gap of about 10 cm (far away from the antenna location), which is about a factor of two lower than in the cases in the high T_{e_outer} regime. During the LH power coupling phase the density profiles exhibit only minor changes. The T_e profile remains unchanged in the standard regime while higher temperatures are produced in the high T_{e_outer} regime, increasing with LH coupled power. These results further confirm the consistency of higher T_{e_outer} operation with the occurrence of LH wave effects in the plasma core in high-density plasmas.

Importantly, the occurrence of LHCD effect at high density described before is accompanied by reduction of the spectral broadening phenomenon, as shown in Figure 5.2 of Chapter 5, as previously predicted by theory [27]. We show here the dependence of both the LHCD effect and the LH spectral broadening on the electron temperature of the outer plasma [21]. Data have been systematically kept in FTU in a wide range of plasma densities. Plasma discharges performed with same parameters of toroidal magnetic field (6T) and plasma current (0.5MA) have been selected, in which a different electron temperature at the periphery occurred, as consequence of different regimes of recycling. These differences were produced using boronised or lithised vessel, and operations laying the plasma column on the toroidal or the poloidal limiters. Figure 6.5 displays the level of the hard-X ray emission measured by the fast electron Bremsstrahlung (FEB) camera and the LH spectral broadening measured by RF probe versus the electron temperature in the outer plasma (at normalised minor radius of about 0.7). The plasma density (n_{e_av} ≈0.8×10^{20} m^{-3}) is lower than in cases shown in Fig. 6.1 (n_{e_av} ≲1.9×10^{20} m^{-3}). Consequently, we conclude that in LHCD regimes performed in a wide range of densities (0.8×10^{20} m^{-3}≲n_{e_av} ≲1.9×10^{20} m^{-3}), the higher is the electron temperature of plasma periphery, the stronger is the LHCD effect and, together, fewer is the spectral broadening. The occurrence of the causal link between

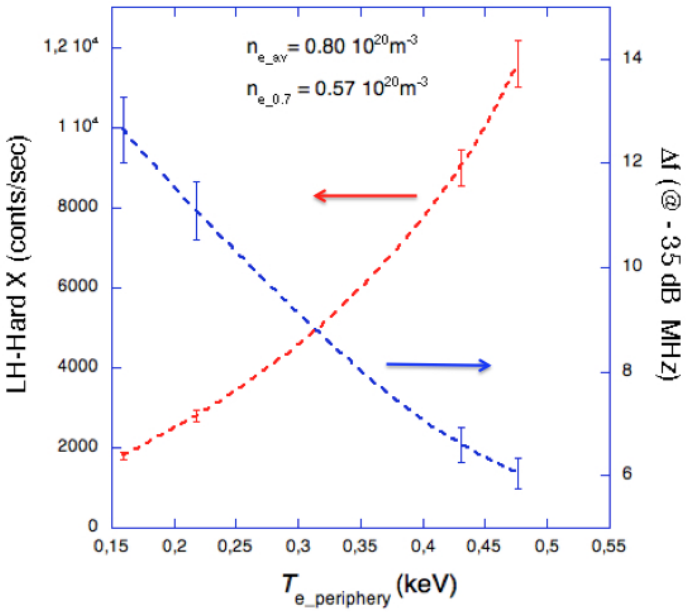

Figure 6.5. Hard-X ray level and spectral broadening of the RF probe signal plotted versus the plasma electron temperature at the plasma periphery ($r/a \approx 0.7$)

electron temperature in the outer plasma layer, spectral broadening and LHCD effect is now further backed.

6.2 Modelling results

Modelling of the plasma current evolution has been performed by the JETTO code [46] using the measured magnetic data, kinetic profiles, and LH-driven radial current density profile modelled by the LH^{star} code [21]. The following experimental data have been considered.

In the case of higher coupled LH power (P_{LH}≈0.52 MW) the proportionally higher hard X-ray signal (see Fig. 6.3b box 4) is accompanied by a higher central electron temperature (T_{e0}~0.8 keV instead of T_{e0}~0.6 keV, see Fig. 6.3b box 2) and a lower loop voltage (by about 20%) with respect to the case with standard LH power (P_{LH}≈0.35 MW). As the density profile and impurity concentration are similar in these plasmas (effective ion charge: Z_{eff}~1), the difference in temperature can be only attributed to the higher coupled LH power. Moreover, no significant changes of the T_e profile occur just after the beginning of the LH pulse (in particular at the radial location r/a~0.3–0.4 in which the LH deposition indicated by FEB signal has its maximum). Instead, the higher T_{e0} in the case with higher LH power occurs on a time scale of 40 ms, which corresponds to the evolution of current density profile and transport. On this time scale a higher current density is produced in the plasma core by the coupled LH power. Figure 6.6 shows the evolution of the profiles of safety factor (top box) and magnetic shear (bottom box) at two time points just before and during the LH power coupling phase. The LH deposition profiles used in the JETTO code are consistent with the measured hard X-ray profiles. The LH-driven current leads to the formation of local negative shear (≈ -0.5 in the region r/a~0.3–0.4), the effect being more pronounced in the case of higher LH coupled power, and accompanied by a reduced electron thermal conductivity (by about 20% in the inner half of plasma). In comparable experiments performed without LH power no significant change of temperature and current density profiles were seen. A possible interpretation of this result is that, operating at ITER-relevant plasma densities and with sufficiently high peripheral plasma temperature, the launched LH waves penetrate and drive current in the plasma core, which, in turn, produces an improvement in the plasma confinement through the generation of low magnetic shear [47].

Using the LH^{star} code, described in Ref. [21], the PI-induced spectral broadening has been calculated and used to determine the LH deposition in the plasma. Frequencies and growth rates of the ion-sound-quasi-mode-driven LH sideband waves are obtained by solving the parametric dispersion relation, Eq. 5.35 of Chapter 5.

From the measured data, in the standard plasma regime (discharge 32164 in Fig. 6.4), high growth rates ($\gamma / \omega_0 \approx 1 \times 10^{-4}$) are obtained for the LH sidebands, which are significantly shifted in frequency with respect to the pump wave ($\Delta f \approx 15$ –20 MHz in frequency, and $\Delta n_{//} \approx 30$ in wavenumber). The spatial amplification factor, which takes into account the convective loss due to plasma inhomogeneity, described in Sec. 5.4.3 of Chapter 5, has been calculated. Consequently, for the plasmas in the standard regime the PI amplification factor is in the range $A_{inhom} \approx 10 - 25$ for the different LH wave sidebands, and produces a small pump power depletion fraction (of about 0.1%) for the sidebands with highest wavenumber (with $n_{1//} \cong n_{1//\_cut\text{-}off} \approx 30$, see Sec. 5.4.5 of Chapter 5 for the pump depletion concept). The frequencies of these sidebands are shifted from the pump up to about 20 MHz. For the high T_{e_outer} regime (plasma discharge 32555 in Fig. 6.4) a much smaller spectral broadening is obtained as a consequence of lower PI growth

rates due to the higher T_e at the plasma edge. Consequently, a lower amplification factor (in the range 10 - 18) for the LH sidebands, which are less shifted from the pump in wavenumber ($n_{1//} \lesssim 7$) and frequency ($\Delta f \lesssim 10$ MHz).

Data available from measurement have been input to the ray-tracing and Fokker-Plank modules of the LH^{star} code. The numerical results showing the radial profile of LH-driven current density are plotted in Figure 6.6. For case of high T_{e_outer} regime (plasma discharge 32555 of Fig. 6.3) and PI-produced spectral broadening (up to $n_{1//}$=7.5) of antenna spectrum, the coupled LH power is mostly deposited at $r/a \approx 0.4$ in the first radial pass (see Fig 6.6, green curve).

It worth noting, that the contribution of all PI-produced LH wave sidebands is essential to produce the LH-driven current density profile, although only a little power (≈0.1% of the pump power) is carried by the components with the highest wavenumber, consistent with quasi-linear lower hybrid wave damping effect. Numerical simulations also show that LH waves accelerate plasma electrons, mainly at the same radial location of $r/a \approx 0.4$, at energies in the range 40 keV÷80 keV, which is consistent with the measured hard X-ray energetic spectra obtained in previous LHCD experiments [48]. Meanwhile, using the measured data from the standard regime (plasma discharge 32164 of Fig. 6.3) and the PI-induced spectral broadening (up to $n_{//}$ =30), the computed LH power deposition is localised very close to the plasma edge (see Fig. 6.6, red curve). In this case very low energy electrons are produced by the coupled LH power (tail electron temperature <10 keV), well below the FEB camera range of detection. This result is consistent with the detected FEB signal, which remains at the noise level in the high-density standard regime plasmas. Therefore the creation by the LH sideband waves of an electron distribution function tail near the plasma edge is sufficient to damp the lower $n_{//}$ components of the pump.

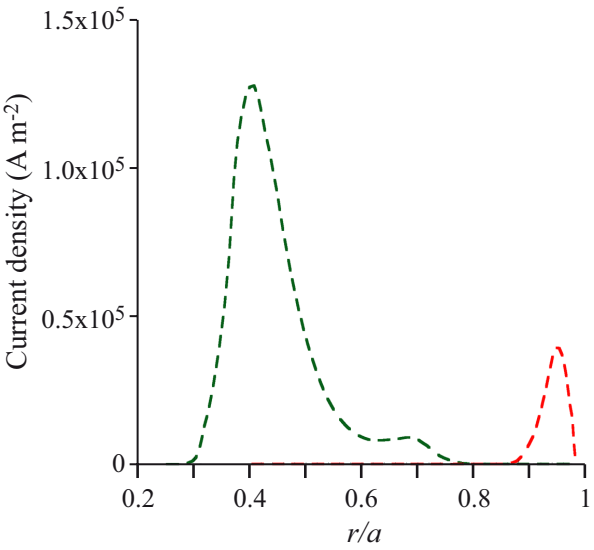

Fig. 6.6. LH-driven current density profiles in the standard and high T_{e_outer} regimes. r/a is the normalised minor radius of the plasma column. The profiles have been obtained by modelling with the LH^{star} code, considering the parameters of the plasma discharges of Fig. 6.3: standard regime (red curve), high T_{e_outer} regime (green curve).

The effects of wave-produced ionization and resistive losses [10,14] have been considered as a possible further cause for the LH edge deposition in the standard regime. These effects have been calculated to be around 2-3 % in a single radial pass in the most pessimistic edge conditions (i.e. considering the case of lowest temperature in the standard regime: pulse 32164 in Fig. 6.3, where the neutral density is less than $10^{17} m^{-3}$). These effects would thus require very many full radial passes to cause the full absorption of the coupled LH power at the plasma edge. But this kind of wave propagation would produce some $n_{//}$ up-shift of the launched antenna spectrum, effect of wave propagation in the toroidal plasma geometry; consequently, some wave interaction with tail electrons of the plasma core should occur, which is inconsistent with the absence of signatures of wave-accelerated plasma electrons in the high-density standard regime.

6.3 Discussion

The experiment confirms the theoretical prediction that operation at relatively high temperature at the plasma periphery is the key for reducing the spectral broadening produced by parametric instability, and allowing penetration of lower hybrid waves into high-density plasmas relevant for fusion power-plant.

Effects of ionization and resistive loss [10,14], which may cause full damping of the coupled radio frequency power at the very plasma periphery in the FTU standard regime, do not play a dominant role. Indeed these effects (of the order of 1%) are generally insufficient to explain the observed lack of LH power penetration in JET where the much higher core electron temperature (T_{e0}≈6 keV) than in FTU results in LH power that is mostly deposited during the first radial pass [27]. It is more likely in both cases that the parametric instability produces strong single pass wave damping at the edge, playing a dominant role.

Correlated with lower hybrid power penetration in the core, spectral broadening measured by radio frequency probes is significantly smaller than in reference plasmas without the reduced parametric instability, consistent with the theoretical predictions that have motivated this experiment [27,28]. The hard X-ray emission from the suprathermal electron population, generated by the LH waves in these favourable conditions, is considerably increased even at densities that have so far been considered the upper limit for efficient LHCD operation in FTU, namely line density $n_{e\,av} \approx 1.3\cdot10^{20}\,m^{-3}$, central density $n_{e0} \approx 1.5\cdot10^{20}\,m^{-3}$, peripheral density (at $r/a \approx 0.8$) $n_{e\_0.8} \approx 0.4\cdot10^{20}\,m^{-3}$. LHCD effects are now detected on FTU at $n_{e\_av} \approx 2\cdot10^{20}\,m^{-3}$, $n_{e0} \approx 5\times10^{20}\,m^{-3}$, $n_{e\_0.8} \approx 0.85\times10^{20}\,m^{-3}$.

The plasma-wall temperatures expected in the ITER device (Te<100eV for r/a=1.007-1.10) [34] are in the range of parameters considered in FTU experiments in the standard regime. Therefore the present work is useful for assessing the potential impact of lower hybrid current drive as a tool in a revised ITER design. In ITER, useful conditions should be produced to avoid the launched $n_{//}$ spectrum from being strongly broadened as it propagates through the cold layer of the plasma edge, which would prevent the LH wave penetration into the plasma core. Recent experiments at JET indicate that this undesirable condition can actually occur [49], but the related FTU results show how the problem can be solved.

The lower hybrid wave penetration and current drive produced in FTU at reactor-grade plasma densities provides a change of paradigm for driving current in tokamak plasmas by means of externally launched radio frequency power. Thus, an advance is produced in the understanding a crucial issue for fusion science, and in providing the know how to extend the range of usefulness of the LHCD effect to regimes of critical importance for fusion reactors.

6.4 Method summary

6.4.1 Experimental device description

FTU is a medium sized high magnetic field (up to 8 T) tokamak with a toroidal major radius on axis of 0.93 m and minor radius of 0.3 m. The machine produces plasmas with densities at or above the level of a reactor (line averaged density up to 4×10^{20} m^{-3}) with a plasma current flat-top of 1.5 s duration. The experiments described here have been performed with the option of displacing the plasma, with circular

cross section, both towards the toroidal limiter, which is located on the high field side and has a relatively large plasma-wall contact area (of about 1.7 m^2), or towards the poloidal limiter, located on the low field side, which has a much smaller plasma-wall contact surface (about 0.026 m^2).

6.4.2 FTU operations

FTU tools allow comparable high-density plasma regimes to be exploited with different electron temperatures at the plasma periphery. This capability provides the necessary conditions for testing the lower hybrid wave penetration and current drive effect, which linear theory expects to be produced at reactor-grade plasma densities, but which the results of previous experiments did not confirm. Two different configurations have been exploited with plasma displaced towards the two limiters structures. Using the toroidal limiter a stronger plasma-wall interaction occurs due to the larger plasma-wall contact area. In these conditions higher recycling and relatively low temperature at the plasma periphery generally occur. Conversely, in operation with the plasma displaced towards the poloidal limiter, the D-alpha emission level is about ten times smaller, and slightly higher electron temperatures are observed at the plasma edge than in similar experiments using the toroidal limiter.

FTU can operate with vacuum vessel covered either by boron or lithium. Such coatings are both useful for improving plasma operations and reducing the plasma impurity content. With lithium, sprayed on the walls from the limiter, where it is present in liquid form [36], the plasma is particularly protected from fluxes of impurities with high values of effective electric charge, and is characterised by a level of recycling significantly lower than with a boron-coated vessel [36-38].

Pellet injection has also been exploited to produce the initial plasma conditions needed in these LHCD experiments. FTU has a pneumatic single stage multibarrel pellet injector [39], capable of firing up to eight pellets per plasma discharge with a typical velocity of 1.3 km/s and a mass of the order of 10^{20} deuterium atoms. The FTU pellet operations are characterized by deep core fuelling, which produces high-density plasmas exhibiting a phase with relatively high electron temperature at the periphery of the plasma.

In order to reduce the recycling further, the technique of extra-gas fuelling in the early phase of discharge has been used. In the standard gas fuelling technique, the requested density value at the start of the LHCD pulse is set by the plasma density feedback control, which generally produces a continuous gas injection during the whole plasma discharge. Relatively high levels of recycling and low temperatures at the plasma periphery are obtained with this operation. In the technique of extra-gas fuelling in the early phase of discharge, a large amount of gas is injected in the early phase of discharge (but still during the plasma current flat-top), which transiently produces a plasma density slightly higher than the value required for the LHCD pulse. The density then falls to the required value after a delay during which a pause in the gas injection is programmed, so that low recycling occurs. This fuelling technique has been used to prepare plasmas with both very high-density and low recycling by means of pellets fired during the pause in the gas injection.

Using all these methods the highest temperatures at the plasma periphery have been produced in high-density plasmas, meeting the requirements of the experiment.

6.4.3 Systems of additional heating and current drive

Three additional heating and current drive systems are available on FTU: Lower Hybrid Current Drive (operating frequency: 8 GHz, coupled radiofrequency power more than 2 MW), Electron Cyclotron resonant heating (operating frequency: 140 GHz, coupled radiofrequency power up to 1.6 MW) and Ion Bernstein Wave heating (operating frequency: 0.433 GHz, coupled radiofrequency power up to 1 MW). In the experiments presented here only the Lower Hybrid Current Drive system has been used: two antennas are available in two FTU ports; each consisting of three grills superimposed poloidally. Each grill is an array of 4 rows and 12 columns of active and phase controlled rectangular waveguides. Each grill is fed by a gyrotron radio frequency power source and, given FTU compactness has small dimensions: L_z (toroidal) = 8 cm, L_y (poloidal) = 14 cm. The peak of the antenna spectrum, $n_{//Peak}$, can be adjusted continuously in the range 1.5 -3.8, $n_{//Peak}$=1.83±0.2, corresponding to a waveguide phasing of 90 degrees with 90% directivity, has been used here. The discussed experiments have been performed using only one antenna grill. Further experiments are planned on FTU where the ECRH system will be used to produce further local heating of the plasma periphery by properly setting the toroidal magnetic field. In this way, the related lower hybrid current drive regimes at reactor-grade plasma densities should be further sustained.

6.4.4 Production of the plasma discharges

About forty FTU plasma discharges have been produced in two regimes at reactor-grade high plasma densities characterised by different electron temperatures at the plasma periphery. The standard regime described in the paper has been produced using a boron-coated vessel, the plasma column displaced towards the toroidal (internal) limiter and the standard gas fuelling technique. In these conditions high-density plasmas have been obtained with relatively low electron temperature at the plasma periphery. The plasma current was 0.35 MA or 0.52 MA and the toroidal magnetic field was 5.2 T or 5.9 T, respectively.

The high T_{e_outer} regime described in the paper has been obtained using a lithium-coated vessel, plasma displaced towards the poloidal (external) limiter, extra-gas fuelling in the early phase of the discharge and pellet injection. The pellet has been fired (at t=0.7s) just before the LH power switch-on (with a 0.012 s delay) to prevent enhanced pellet ablation. The velocity and size of the pellets have been sufficient to produce the desired fuelling in the plasma core. A plasma current I_P= 0.6 MA and a toroidal magnetic field B_T=5.9 T have been used. The slightly lower magnetic field also used in the standard regime has been useful to obtain similar safety factors and plasma stability conditions in the two regimes.

6.4.5 Hard X-ray measurements

The generation of LH-accelerated supra-thermal electrons, has been detected by a high performance fast electron Bremsstrahlung (FEB) camera, detecting hard X-ray emitted in the direction perpendicular to the confinement magnetic field. The FEB has a time resolution of 4 μs and uses two independent pinhole cameras with 15 lines of sight each [28]. Considering the poloidal cross-section of the torus, the horizontal camera is centred on an angle of 0 degree, and the vertical one is centred on an angle of -90 degree (on the bottom). Both cameras are identical including the viewing angles. For each line of sight there is a C_dT_e detector with a thickness of 2 mm and a square surface of 25 mm^2. The absorbers and screens used allow transmission for an energy range from 20 keV to 200 keV. The detector is closely connected to an appropriate pre-amplifier.

6.4.6 Electron temperature measurements

The evolution of the plasma electron temperature profile has been monitored by electron cyclotron emission and Thomson scattering measurements. Both diagnostics have confirmed the occurrence, in the high $T_{\text{e-outer}}$ regime, of the central temperature increase produced by lower hybrid current drive. In the high $T_{\text{e-outer}}$ regime, the edge temperature has been taken only from the Thomson scattering diagnostic as the ECE temperature measurements in the periphery are affected by some supra-thermal emission located in the spectrum between the first and second harmonic (where the plasma is optically thin), due to the effect of second harmonic down-shift extending to the very plasma edge.

Chapter 7

7 Interpretation of recent results of EAST (Experimental Advanced Superconducting Tokamak)

This chapter considers results of Ref [36] (L Amicucci, et al., PPCF 2016) and Ref [37] (B J Ding, M H Li, L Amicucci, et al. Subm. to Physical Rev. Letters), which have made possible assessing, by theoretical model, the phenomenology occurring in spectra of radiofrequency (escaping away from the machine and documenting wave-plasma interactions) measured by a probe during recent experiments of lower hybrid current drive (LHCD) carried out on EAST (the major Chinese machine for fusion energy research).

In this work, for the first time, we have utilised the new (Matlab-Python) version of the numerical code LHPI (Lower Hybrid Parametric Instability) capable of solving in much reduced time the equations of parametric dispersion relation shown in Chapter 5. Also the output data are managed much more efficiently than in previous (Fortran 77) version of code.

This work has successfully enabled interpreting data that reveal signatures of parametric instability (PI) never observed before, consisting in a slight change of frequency of downshifted sideband that appears at around the operating frequency of 2.45 GHz. This frequency shift results dependent on plasma edge temperature and, consequently, following previous understanding, the spatial origin of PI phenomenon would also unrealistically move in opposite sides of plasma edge (from the low field side, where the antenna is located, to the high filed side of the column). This problem has been solved by original modelling work, which however identifies the PI origin in edge plasma layer near the antenna-plasma interface.

These results confirm validity of the parametric instability modelling, originally developed by ENEA Frascati, in predicting and interpreting outcomes of experiments aiming at approaching conditions useful for driving current at high plasma density (~10^{20} m^{-3}), as necessary for thermonuclear reactor.

7.1 Introduction

Parasitic effect of the parametric instability (PI), occurring in tokamak experiments utilising externally launched LH power, was originally studied on Alcator C [52] and FT [22] with the aim of interpreting the negative results of heating and current drive experiments at high densities. These experiments exhibited, indeed, only signatures of non-linear wave plasma interactions monitored by RF probe. This apparatus consists in a simple loop antenna (of dimension of a few centimetres) located outside the machine connected to a spectrum analyser. As distinctive feature of the LHCD experiments on EAST experiments operating at high plasma densities, a strong reduction of the LHCD effect at high density accompany RF

probe spectrum showing the phenomena of the pump broadening and down-shifted ion-cyclotron (IC) sidebands, which were observed also in early LH experiments aimed at heating the plasma ions, which also operated at frequencies in the range 1 GHz – 5 GHz, summarised in Chapter 5.

We focus hereafter on the IC sideband phenomenon with the aim of establishing weather the PI modelling tool, already utilised with success for interpreting the spectral broadening phenomenon, should be useful also to understand the IC sideband phenomenology.

The information of the radial position of the plasma where the PI mechanism takes place could not be obtained by spectral broadening measurements, as those of Figure 2 of Chapter 5. Indeed, the lack of IC sideband in the RF probe spectra prevents inferring the PI origin with the local toroidal magnetic field value. Conversely, this indication could be usefully provided by the feature of IC sideband occurring in the RF probe spectra of LHCD experiments performed on EAST at 2.45 GHz [53,54].

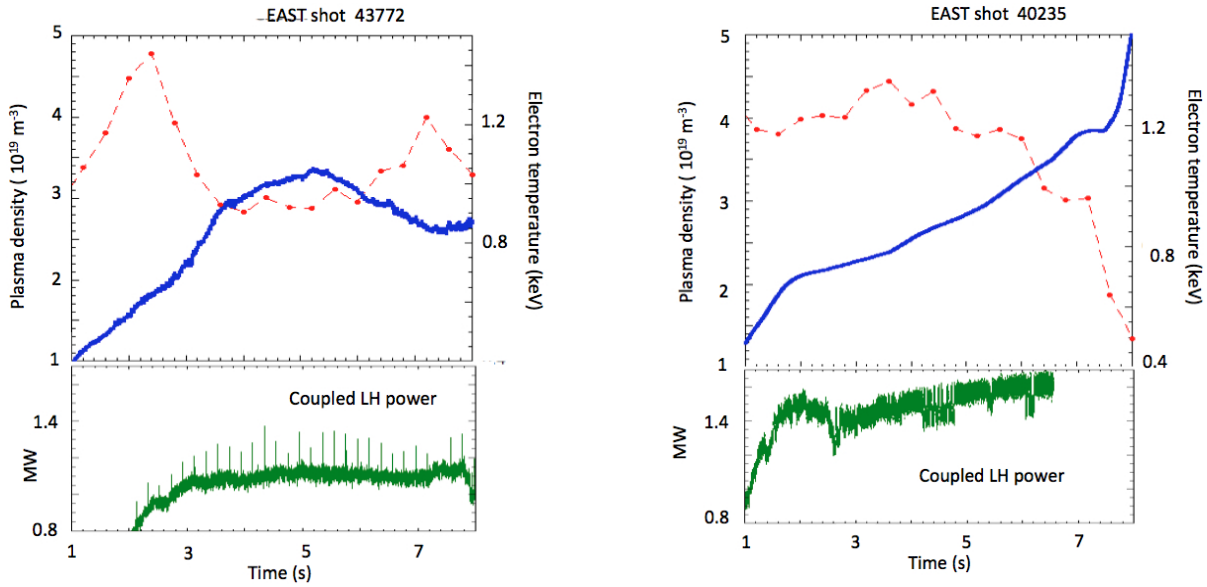

Figure 7.1. Time traces of the central line-averaged plasma density and electron temperature and coupled RF power of reference plasma discharges performed with weak lithisation (left), and strong lithisation of the chamber (right).

We show hereafter that the frequency shift of sideband in the RF probe spectra does not merely reflect the behaviour of an IC resonant layer, but the more complex, non resonant, PI mechanism which links together sideband and low frequency quasi-mode, under the presence of a pump wave electric field of finite amplitude.

7.2 RF probe spectra and PI phenomenology on EAST

LHCD experiments at high plasma densities have been carried out on EAST, supported by RF probe spectrum measurements, with the aim of assessing the PI phenomenology occurring at around the operating frequency of 2.45 GHz [53,54]. Two comparable discharges are considered here, performed with plasma current of 0.5MA and toroidal magnetic field: B_T= 2.23T (the major plasma radius is: R=1.87 m on axis, the minor radius of the last closed magnetic surface on the equatorial plane is: r=a=0.445m).

Figure 7.1 shows the time evolution of the central line-averaged plasma density and central electron temperature of these discharges during the phase of coupling of the RF power (of about 1 MW, and antenna spectrum peaked at parallel refractive index: $n_{//}$=2). Figs.7.1a and 7.1b refer to cases of weak lithisation (kept as reference), and strong lithisation, respectively. The latter regime has been produced on EAST aiming at a higher temperature profile of scrape-off layer (SOL) and radial periphery of the main plasma, and, consequently, diminishing the parasitic PI effects during LHCD, by following method assessed on FTU for enabling LHCD at high plasma densities [7]. The radial periphery of plasma is intended extending from the separatrix to layers having large normalised minor radius (lying in the range 0.7 ≳ *r/a* ≳ 1). In the considered plasmas the SOL width is of about 6.5 cm and the antenna is located about 1.5 cm inside the SOL.

The RF power is coupled during phases in which the plasma density is gradually risen up to about $3.5x10^{19}$ m^{-3}. In order to compare the RF probe spectral data, with density values, respectively, medium (~$2.3x10^{19}$ m^{-3}) and high (~$3.3x10^{19}$ m^{-3}) are considered.

Correspondingly, the central electron temperatures are similar in both discharges (of about 1.2 keV for medium density and 1 keV for high density). Conversely, differences in the compared regimes occur in the radial outer half of plasma, as shown in the kinetic profiles shown Figure 7.2. In discharge (40235) performed with strong lithisation the electron temperature is slightly higher (of about 20%), mainly in the SOL, than in reference shot. Incidentally, this change is weaker than (~50%) that occurred in previous FTU experiments that demonstrated the occurrence of LHCD effect at reactor relevant high plasma density accompanied by strong reduction of PI effect [24].

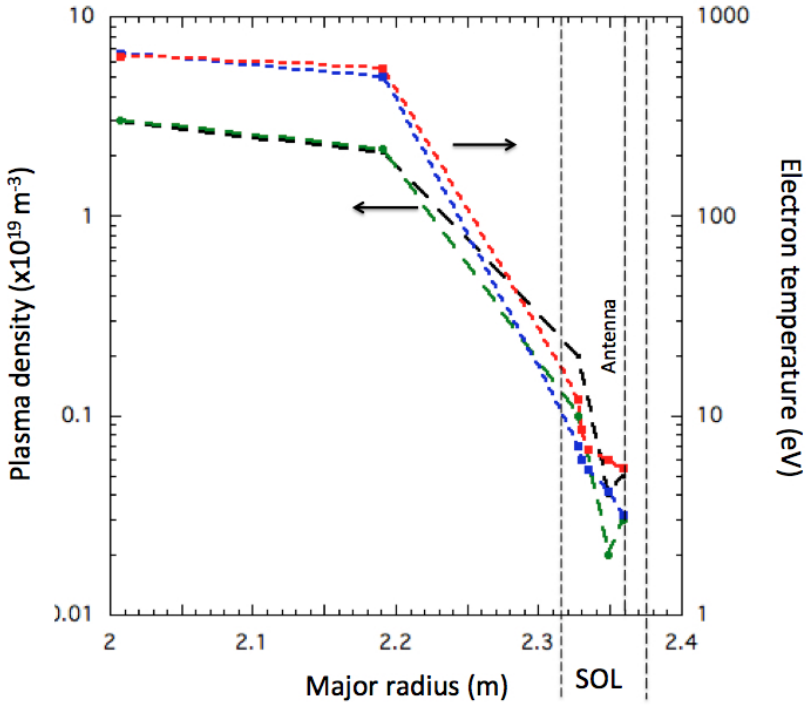

Figure 7.2. Electron density and temperature profiles of the outer radial half of plasma plotted vs. the major plasma radius for reference plasma discharges performed with weak (#43772, black-density/blue-temperature lines) and strong (#40235, green-density/red-temperature lines) lithisation of the chamber. The profiles have been obtained by interpolating the Langmuir probe data of SOL with those of the Thomson scattering diagnostic of the main plasma. No data are available in the radial gap between SOL and plasma bulk profiles. Linear interpolation has been utilised

Typical RF probe frequency spectra obtained during the experiments in object are displayed at the top and right of Figure 7.5. These spectra have been kept connecting the RF probe to a spectrum analyser displaying frequencies close to the operating frequency. The instrument has been set with

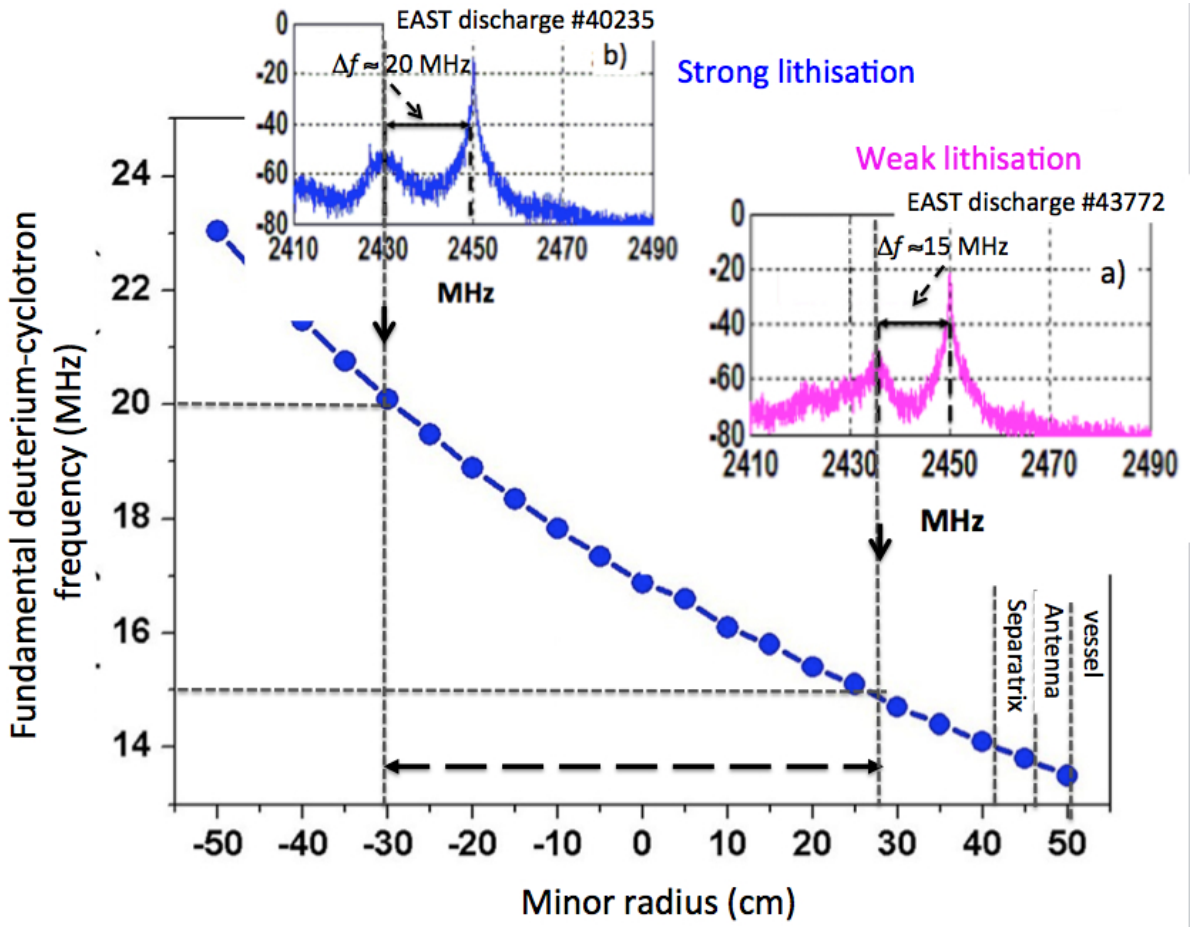

Figure 7.3. Top and right boxes: RF probe spectra obtained during LHCD experiments on EAST. Two reference plasma discharges are considered, performed respectively with: a) weak lithisation (shot number 43772, top box) and strong lithisation (shot number 40235, right box) of the vacuum chamber. The toroidal magnetic field is 2.23T, the line-averaged plasma density is: 2.3 10^{19} m^{-3}. Close values of coupled LH power have been utilised, namely, 1.1 MW for the case a) and 1.5MW for the case b), with antenna spectrum peaked at $n/_{/}$=2.
Main box: Profile of the fundamental deuterium frequency versus the plasma minor radius on the equatorial plane.

a frequency span capable of detecting power emissions shifted of amounts in the Deuterium-cyclotron resonant range, and bandwidth suitable for discriminating with sufficient precision (≲100 kHz) the sideband frequency. The spectra are kept (at t~3s) during medium density phase: the one in the box on the right of Fig. 7.3 refers to case with weak lithisation; that in the box at the top refers to case of strong lithisation.

We focus here on the following phenomena shown by the available RF probe spectra: *i*) in the considered two different regimes, Figure 7.3 shows that the frequency separation between the IC sideband and the line operating frequency is (~20 MHz) larger in case of strong lithisation than in condition of weak lithisation (~15 MHz), and compares these difference with the radial trend of the deuterium-cyclotron frequency; *ii*) in the late phase of discharge, when the line-averaged density is increased at 3.3 10^{19} m^{-3}, the difference in frequency shift disappears, see Figure 7.4.

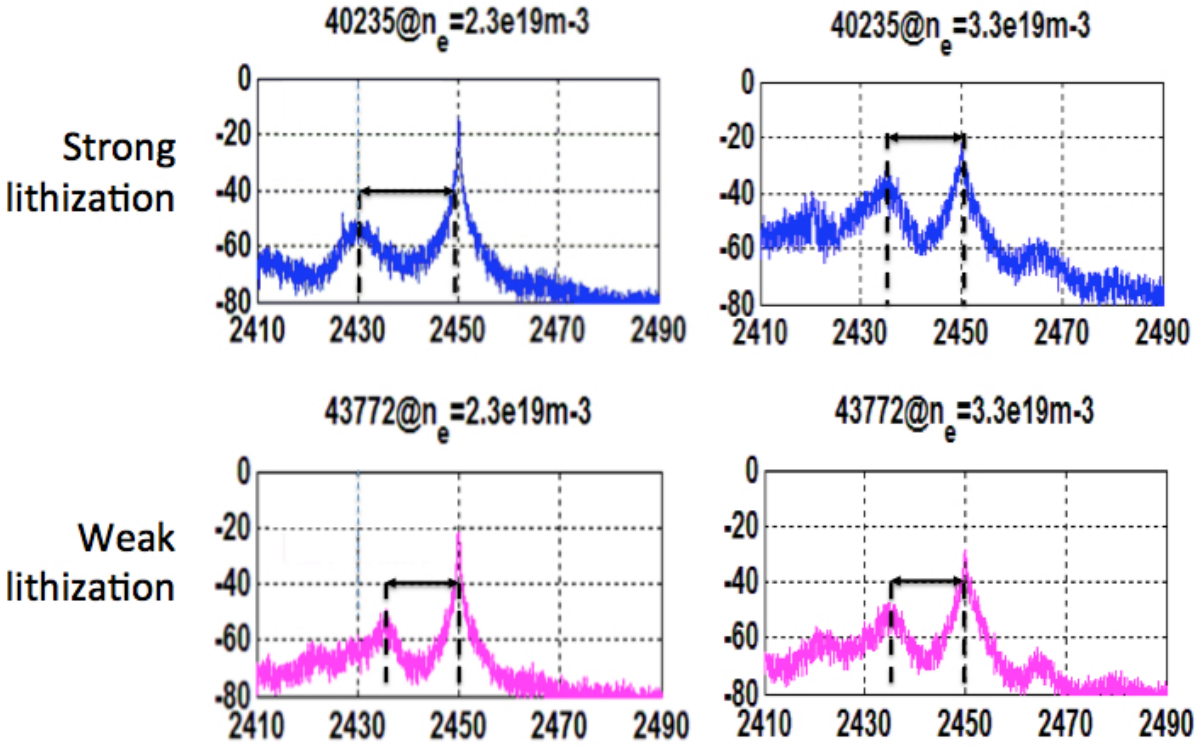

Figure 7.4. RF probe spectra in the two regimes of chamber lithisation of the same discharges of Figure 7.3, kept in phases with plasma densities medium (at $t\approx$ 3s, boxes on left) and high (at $t\approx$5s for #43772, and at $t\approx$ 6s for #40235, boxes on right).

In the latter condition, measurements indicate that consequent to larger gas puffing necessary for increasing density the increase of the edge plasma temperature vanishes.

It would be difficult interpreting the IC sideband phenomenology on EAST. Indeed, if we assumed valid the hypothesis that the sideband would merely reflect the behaviour of an IC resonant plasma layer, we would accept the idea that the spatial PI origin would jump from very distant radial layers of plasma periphery located in opposite sides of the low and high field sides, as effect of only a relatively small local change of kinetic profiles. Moreover, when the latter difference vanishes at higher operating density, we would imagine the IC sideband origin moving out to the low field side, as indicated by smaller frequency shift (of about 15 MHz) in boxes on the right of Fig 7.4.

We show hereafter that this *paradox* is removed considering appropriate PI modelling. New results show that the assumption that the relevant sideband would reflect the behaviour of an IC resonant mode is not funded. Consequently, the spatial origin of PIs occurring in the considered experiments is however situated at the plasma edge in the low field side, consistently with data available from early LH experiments. The higher temperature produced at the edge by chamber lithisation only on EAST should be responsible of the monitored increase in the IC sideband frequency shift of PI.

7.3 Modelling results

The utilised modelling approach has been summarised in Sec. 4 of Chapter 5.

The parametric dispersion relation, Eq.5.35 of Chapter 5, has been numerically solved on the basis of theory exposed in Chapter 5 by the LHPI code [21], utilising as inputs the EAST plasma parameters of discharges of Figure 7.2. Frequencies and growth rates of the modes driving the PI, taking into account the kinetic profiles available for the reference plasma discharges of EAST performed in regimes of weak

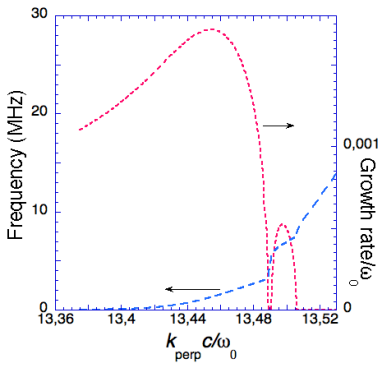

Figure 7.5a. Frequency and growth rate of modes driving the parametric instability. PI-coupled modes. Plasma parameters of the reference plasma discharge performed with weak lithisation (#43772, P_{LH}=1.1MW B=1.70 T have been considered, at a radial layer close to the antenna position (R=2.36 m). The following parameters have been considered for the computation: n_e=3.0 10^{17} m^{-3}, T_e = T_e =2 eV.

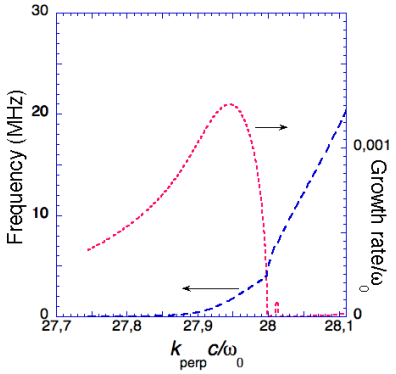

Figure 7.5b. Same parameters of Figure 7.5a, but kept at a radial position in the mid-outer SOL (R≈2.34 m): n_e=1.3 10^{18} m^{-3}, T_e = T_e =5 eV.

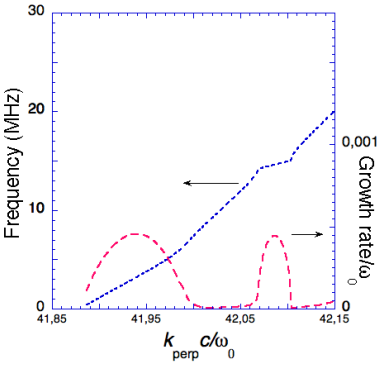

Figure 7.5c. Same parameters of Figure 7.5a, but kept at a radial position in the mid-inner SOL (R≈2.32 m): n_e=3.0 10^{18} m^{-3}, T_e = T_e =30 eV.

and strong lithisation, respectively.

The code provides also output useful for assessing whether the modes of PI are true propagating modes or not, i.e., whether the following equations: $\varepsilon_{Re}(\omega,\mathbf{k})=0$, $\varepsilon_{Re}(\omega_1,\mathbf{k})=0$, $\varepsilon_{Re}(\omega_2,\mathbf{k}_2)=0$ are respectively satisfied, or not, for any solution of the parametric dispersion relation (Eq. 5.35 of Chapter 5). Consequently, the condition $|\varepsilon_{Re}(\omega,\mathbf{k})|>>1$ generally occurs, i.e., the driving mode of PI is evanescent. Moreover, apart frequency of driving mode laying within a small shift from the pump, also the upper sideband is evanescent (i.e.: $|\varepsilon_{Re}(\omega_2,\mathbf{k}_2)|>>1$) and PI manifests in the growth of only the lower sideband which would reflect in a well separated down-shifted structure observable in the RF probe spectra. This justifies the main features of IC sidebands exhibited by RF probe spectra.

The utilised modelling tool is limited to PI of small intensity, i.e., sidebands marginally emerging from the background noise level. Moreover, since we are mainly interested assessing the radial position of plasma

layer where PI signatures of the RF probe spectra should be originated, we have limited the analysis to the first down-shifted sideband, which in the RF spectra generally exhibits larger amplitude.

As general result, the plasma is found unstable in regard to PI phenomenon in the radial regions of SOL and periphery, with higher growth rates occurring for colder plasma conditions. For plasma edge indicated in Figure 7.2, we have repeated the numerical runs of the code considering three layers located at different radial distances from the antenna mouth, respectively, at: $R\approx2.36$ m (in the outer SOL, in the low field side), $R\approx2.34$ m (in the mid-outer SOL), and $R\approx2.32$ m (in the mid-inner SOL. The separatrix is at $R\approx2.30$ m, the antenna mouth is located at $R\approx2.36$ m).

The obtained results are shown in Figure 7.5, representing, for different numerical runs, the PI growth rate plotted versus the perpendicular (to toroidal magnetic field) wavelength component of the low frequency mode driving the PI mechanism.

Higher growth rates (up to about $7\text{x}10^{-3}$) occur for driving modes with very low frequencies (i.e., for ion-sound frequencies up to few megahertz), especially in the colder region of outer SOL (for $n_e \lesssim 1.3\ 10^{18}$ m^{-3} and plasma temperatures up to few eV). By comparing Figs 7.5a and b, moving from the antenna-plasma layer to inner positions, driving modes of lower frequencies ($\lesssim$7 MHz) tends having lower growth rate. At further inner radii, Figure 7.5 c shows that IC modes (with frequencies between 10 MHz and 20 MHz) tend to have higher normalised growth rate ($\approx5\text{x}10^{-4}$). IC sideband approaches that of ion-sound sideband with maximum growth rate occurring for frequency ($\approx$15 MHz) consistent with that of RF probe spectra in Figure 7.5, for weak lithisation case, and in Figure 7.6 for both cases at high-density.

We have repeated the computations for same parameters of the mid-inner SOL of Figure 7.5c, but higher value of toroidal magnetic field corresponding to the last closed magnetic surface in the high field side (B_T= 2.93T at R=1.424 m). Consequently the IC sideband shift is of about 23 MHz.

As result of computations carried out considering parameters of further inner radial position, the growth rate of IC sideband (not shown) becomes dominant on that of the ion-sound branch. However, growth rates tend to further decrease and, for high enough temperature ($T_e \gtrsim 0.5$ keV), the plasma becomes stable in regard to all PI channels.

Finally, we have taken into account the effect of higher edge temperature that strong lithisation produces, by repeating the computation reported in Fig. 7.5c with same input parameters but higher temperature (i.e., with $T_e = T_e = 50$ eV in place of 30 eV). The result is shown in Figure 7.6: the maximum growth rate of IC sideband displaces slightly increases (from 15 MHz to about 20 MHz), consistently with case of IC sideband frequency shift occurring for strong lithisation, as shown in Figure 7.3. Considering same parameters of Figure 7.6 but toroidal magnetic field corresponding the high field side, the IC sideband shift increases at about 30 MHz.

In summary, as the maximum growth rate and the corresponding frequency are produced for given

plasma parameters at a certain radial layer of kinetic profiles, we can formulate hypothesis about PI origin. The IC sideband observed in spectra of Figures 7.3 and 7.4 would be mainly originated at radial position (R~2.32 m) situated in the mid-inner SOL in the low field side, as shown in Figure 5c: this indicates the occurrence of high normalised growth rate (≈5x10^{-4}) of IC sideband of large frequency shift. Consequently this sideband emerges as phenomenon well separated from contributions of pump broadening shown in Figs 7.5a,b. Indeed, owing to their conspicuous lower frequencies, LH sidebands driven by these quasimodes contribute to broaden the operating frequency line. These sidebands would be mainly originated at slightly more external radii in the SOL, as their growth rate is larger in colder and less dense plasma. Consequently, they could be responsible of the failure of LHCD effect observed at high density on EAST, consequent to large broadening of the $n_{//}$ LH wave spectrum. Quantitative assessment will be done by dedicated work now in progress.

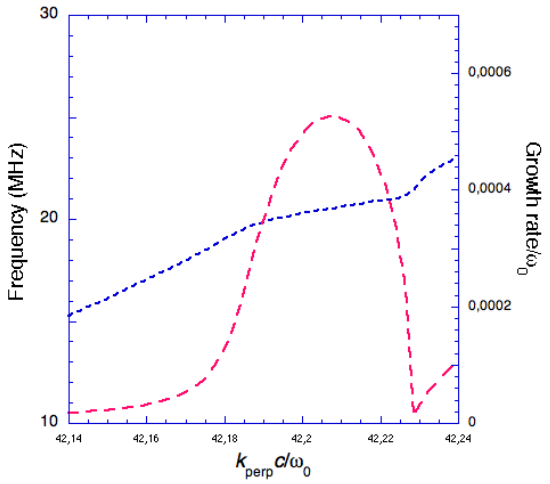

Figure 7.6. RF frequency and growth rate of the PI driving for same parameters of fig 7.5c but higher temperature (T_e = T_e =50 eV, in place of T_e = T_e =30 eV)

7.4 Discussion

Parametric instabilities are complex phenomena that analysis reported here, limited to homogeneous plasma approximation, is insufficient to fully assess. Indeed, convective loss effects should be retained especially for quantitatively interpreting the relevant LHCD regimes.

However the presented results are sufficient for addressing solution of the paradox about PI origin appearing by data of RF probe measurements performed during recent LHCD experiments on EAST at 2.45 GHz. When only data of spectral broadening are available, as in case of FTU experiments at 8 GHz, it is impossible establishing the position of the layer(s) that originates the signal collected by the RF probe, since to make a quantitative comparison between data from experiment and PI modelling, as a synthetic diagnostic would require, is problematic.

Considering the trend of the IC sideband frequency shift observed on EAST experiments, the PI origin results situated in the low field side of plasma edge, more specifically, mostly in slightly inner radial half of SOL.

The difference in frequency shift occurring in the considered operation regimes would reflect the effect that locally higher plasma temperature, occurring with strong lithisation, produces in displacing at higher frequency the IC sideband growth rate peak of PI.

This result is consistent with the IC sideband shift generally observed in LH experiments since almost four

decades ago. Indeed these experiments operated in standard conditions of high plasma densities that naturally produced low temperatures and, consequently, sideband shifts that remained situated quite close to the occurring IC resonant frequency.

Moreover, considering the growth rate maxima at lower frequencies (up to several MHz, i.e., relevant to ion-sound driving modes), they would reflect in sidebands not well separated from the pump, as in the IC sideband case. Being closer to the operating frequency line, these sidebands contribute to the phenomenon of pump broadening that would originate mainly at layers with low densities and low temperatures in the outer half of scrape-off. Further work now in progress for EAST experiments will assess this issue.

The same modelling approach that has enabled assessing the method for successful LHCD occurrence at reactor relevant, high plasma densities has been considered here. Accordingly to modelling results, the phenomenon of spectral broadening is originating at layers close to the antenna mouth, confirming the indication of modelling relevant to FTU experiments. The mechanism of well-separated downshifted IC sideband is favoured by larger growth rate expected to occur for the lower operating frequency of EAST. This sideband is not present in LHCD experiments operating on FTU at 8 GHz thanks to effect of the pump frequency in diminishing the PI growth rate.

Chapter 8

8 Solution of the problem n. 2: how to drive of current at high plasma temperature of thermonuclear reactor

This chapter summarises the results of Ref. [55] [L. Amicucci, et al., "Current drive for stability of thermonuclear plasma reactor", Plasma Phys. Controlled Fusion, 58 (2016) 014042] and Ref. [56] (A. Cardinali, R. Cesario, L. Amicucci, et al., to be submitted for publication on PRL) displaying solution of the problem of how to enable the RF power penetration into the bulk of reactor plasma and drive current in the presence of high electron temperature (~10 keV) at the radial periphery of plasma column.

In addition, the innovative method allows tailoring the current density profile in the plasma column by actively acting on antenna parameters. This goal failed from experimental attempts carried out for decades, but it can be successfully pursued in envisaged reactor plasma conditions thanks to results presented here.

Since discovery of the lower hybrid current drive (LHCD) effect, in 1980, too high plasma temperature was considered a serious obstacle for exploitation of the LHCD tool to tokamak reactor, and non linear effects described in Chapter 5 prevented obtaining the desired major dependence of the RF power deposition on the antenna parameters.

Considering theory of LHCD summarised in Chapter 4, the problem of propagation and damping in the plasma has been numerically solved, in innovative way, by highlighting the role of the width in refractive index of the power spectrum launched by the antenna in reducing the strong Landau damping at too high plasma temperatures. This is the consequence of a feature, displayed for the first time, of the interaction between wave spectral components and electron distribution function. Consequently, the way for enabling the lower hybrid current drive in a reactor consists of operating with an antenna capable to produce power spectra of moderate width in refractive index. This aspect will be discussed in Chapter 9.

8.1 Introduction

Analytical derivation of the equations that govern the lower hybrid current drive (LHCD) effect in tokamak plasmas has been summarised in Sec. 2 of Chapter 4. However, a mere analytical approach is incapable of properly describing the complex mechanism of wave-plasma interaction. Numerical results shown hereafter give a more complete assessment of wave plasma interactions and allow predicting the relevant radial profile of current density driven by RF power in the plasma.
Following quasi-linear (QL) wave theory, summarised by analytical results in Sec. 3 of Chapter 4, we have numerically modelled the LH wave propagation and damping effects that occur after many collision times, in reactor-relevant regime of high electron temperature. For this aim, we have performed ray-tracing

computation in toroidal geometry and solved the Fokker-Planck equation in two dimensions in velocity space. This method is fully adequate for describing, in reactor-relevant plasma conditions, the evolution of the distribution function of plasma electrons under the effect of a strong electromagnetic wave field [12].

The antenna spectra considered as inputs in the analysis have been obtained by numerical computation, whose details are shown in Chapter 9. Figure 8.1 displays these antenna spectra. A too narrow spectrum, as the one of the figure (with $\Delta n_{//} \cong 0.085$), could in principle not satisfy the QL theory limit, since it might significantly modify the electron orbits in the presence of too large RF power density (p_{RF}) values, and consequently produce a *trapping* effect incompatible with hypothesis, at the basis of the QL model, of trajectory linearization [12]. This is explicated hereafter.

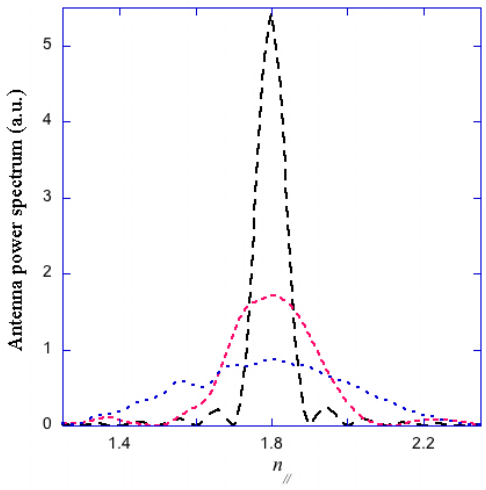

Fig. 8.1. Main lobe of the antenna spectra obtained by a passive-active multi-junction (PAM) waveguide antenna, with modules phased for launching spectra with same $n_{//}$ peak but with three different widths, respectively, $\Delta n_{//}$=0.085 (black curve), $\Delta n_{//}$=0.33 (red curve) and $\Delta n_{//}$=0.58 (blue curve). Minor lobes occurring in the full spectral range do not have displayed (see the text).

8.2 Condition for model validity

Theory is able describing the interaction of a power spectrum of finite width in refraction index with the distribution function of plasma electrons provided that their trajectories originated from acceleration by the wave electric filed should be linearized. In particular these trajectories would not meet condition of bouncing as shown in the middle box of Figure 8.2. This schematises the case, for a given amplitude of the wave electric field, of the reflection caused by a too close second maximum of the accelerating wave, consequence of too narrow wavenumber width of the RF power density spectrum, see Fig, 8.2, top box. The suitable condition for modelling validity is represented in the bottom box of Fig. 8.2 which refers to spectrum with sufficiently large width in Fourier *k* width.

In summary, the wave spectrum should not be too narrow to the point that, for the electron, accelerated by the given 1st E_{RF_max}, his trajectory should not be modified by the 2nd E_{RF_max} (trapping effect). Stronger E_{RF} would require broader spectra for maintaining QL theory valid.

8.3 Numerical results

For the analysis, the LH^{star} package [34,27,24,21,55,56] has been used. This tool incorporates modules suitable for calculating: *i*) the coupled LH antenna spectrum with complex geometries [35], ii) the effect of the PI-produced spectral broadening [27] and, iii) the consequent j_{LH} profile by means of coupled modules, respectively, dedicated to ray-tracing computation in toroidal geometry and 2-D relativistic Fokker-Planck analysis (the RayFP code) [34]. Ray-tracing is always used in condition of fulfilling the geometric optic approximation of LH waves, which holds at radial layers sufficiently far from the cut-offs (because of the lower density) located at the plasma edge. There, LH waves have too large wavelength, so

that quasi-optic approximation necessarily fails. In order to perform the LHCD modelling for DEMO (this concept of thermonuclear reactor is described in Chapter 2), we have considered the envisaged plasma parameters [57] and same antenna geometry proposed for ITER [58] whose details are given in Chapter 9. To model the RF power current density profile, $j_{LH,}$ the QL theory limit should remain valid for all the parameters considered for the analysis. QL theory retains the approximation of linearized trajectories, i.e., unperturbed orbits. Consequently, the important issue of the spectral auto-correlation time would be arisen for a too narrow spectrum [23]. For an evolving spectrum of dispersive waves, this pattern will persist for a limited lifetime (t_L). This should be compared to the bounce time (t_B) of a particle in this pattern. The latter time is that spent by a particle to reverse direction and come close to the initial position. QL limit requires that: $t_B >> t_L$. Consequently, the field pattern changes prior to particle bouncing, and the approximation of trajectory linearization remains valid. Conversely, the particle suffers a *trapping* effect, and the linearization fails owing to too high p_{RF} of wave packet.

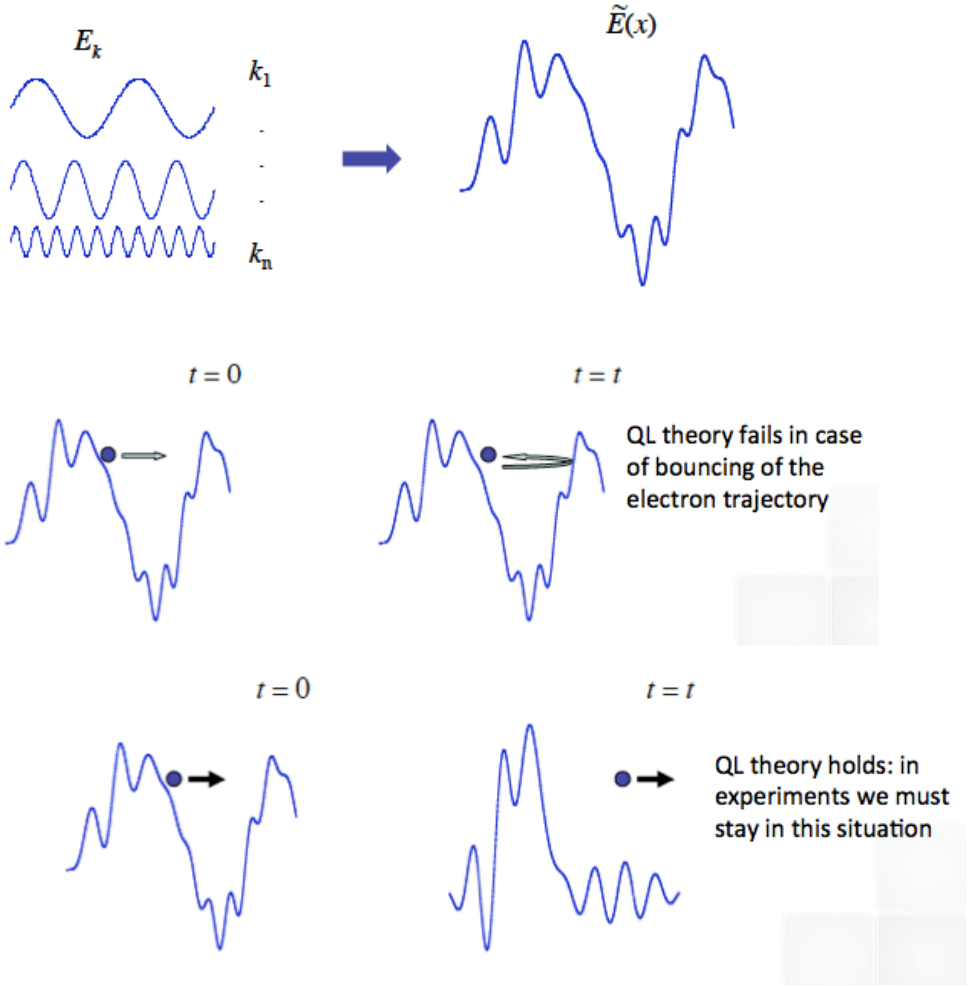

Figure 8.2. Top box: sketch of the electric field waveform at the initial time t=0 as result of the wavevector k- Fourier components.
Middle box: during time evolution, occurrence of bouncing of an electron accelerated by the 1st E_{RF_max} of the wave electric field (occurring close to the initial position of electron) consequence of proximity of the 2nd E_{RF_max}.
Bottom box. The undesired bouncing effect is avoided thanks to sufficiently broad k-vector spectrum that prevents, for given E_{RF} value, the formation of a second $E_{max.}$ too close to the initial one.

Consequently, we found that the phase velocity width is (□0.17c) found much larger than the trapping

velocity width (□0.002*c*), for p_{RF}≈30 MW/m^2 [27]. Realistic values of the minimum and maximum phase velocities of the propagating wave spectrum, consistent with production of EDF plateau, have been calculated near the peak of absorption radial layer (*r/a*≈0.5) of the correspondent j_{LH} profile that will be described in Sec.5. The latter data have been indeed obtained by ray-tracing and Fokker Planck analyses. A wave electric field with intensity (0.2 kV/cm), markedly larger than that (0.05 kV/cm) expected to occur at that layer, has been considered with the aim of overestimating the trapping velocity width. This choice has allowed checking QL theory validity with wider margin [19].

Consequently, also the narrower spectrum in Fig.3 can be retained sufficiently *broad* for largely satisfying QL theory limit.

As an example of reactor plasma parameters, we have considered two configurations with the density profiles, respectively, *peaked* and *flat* envisaged for the DEMO *pulsed* regime [57]. We have however verified that the main results maintain validity also for other reactor plasma configurations mentioned in Chapter 2.

The density and temperature radial profiles are shown in Figure 8.3. These plasma configurations will be refereed to as, respectively, DEMO-*peaked* and DEMO-*flat* cases. The highest T_e values occur for the DEMO-*flat* case of Fig. 8.3, which, on the basis of the previous understanding, would produce LHCD effects too far out in the plasma, precisely, as consequence of the too high $T_{e\_pedestal}$ [59,57]. For comparison, the figure displays also the respective profiles for the steady-state scenario envisaged for ITER [60,61].

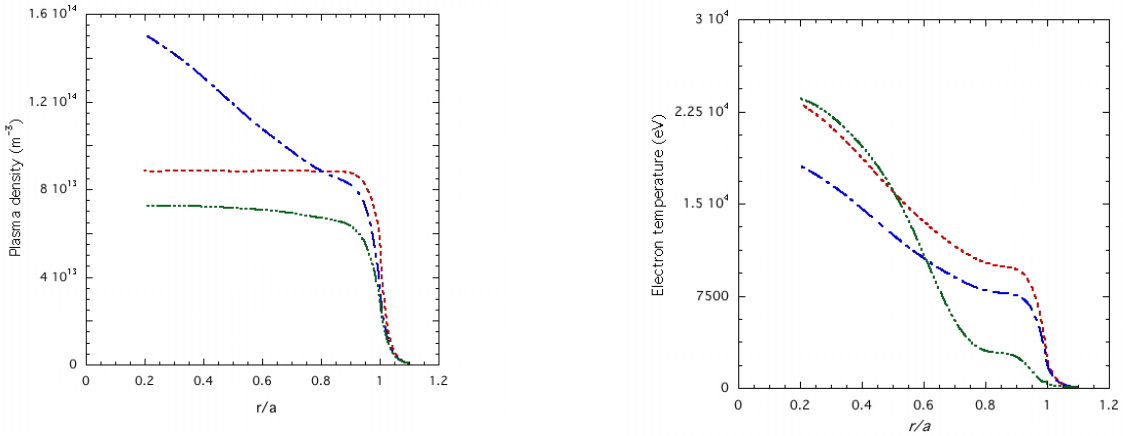

Figure 8.3. Electron plasma radial profiles of: a) density and b) temperature envisaged for the DEMO pulsed regime, with peaked (blue curves) and flat (red curves) scenarios. Steady-state regime profiles of ITER (green curves) are also displayed.

Considering the plasma density and temperature profiles of Fig. 8.3, we show hereafter the j_{LH} profiles modelled by using antenna spectra with the three different spectral widths of Fig. 8.1. On the other hand, Figure 8.4 shows the j_{LH} profiles obtained using the *peaked* density profile case: narrower antenna spectra produce j_{LH} profiles that are peaked at more and more inner radii (at *r/a* ≈ 0.9 for $\Delta n_{//}$≅0.58, at *r/a* ≈0.65 for $\Delta n_{//}$≅0.33 and at *r/a* ≈0.45 for $\Delta n_{//}$≅0.083). For the case of *flat* profile, considering the narrowest spectrum of Fig. 8.1, a slightly more off-axis deposition is obtained, as shown in Figure 8.5. This is due to the higher T_e value (at half plasma radius*:* T_e~16 keV, in front of T_e~14 keV for the *peaked* density profile case).

The peaks observed in Figures 8.4 and 8.5 in cases of narrow antenna spectrum (green curves) display a

typical, important, wave-particle mechanism whose interpretation will be illustrated in Sec. 8.4.

On the top of Fig. 8.5 it is displayed, for comparison, the j_{LH} profile obtained considering the whole antenna spectrum relevant to case of narrowest main lobe of Fig. 8.1, in front of effect of only the main antenna lobe that has been considered for producing the profiles at the bottom of Fig. 8.4. The total absorbed power (~80 MW) drives a net current (~3.8MA) consistent with the result (~3MA) obtained for the corresponding case of the bottom of Fig. 8.5. The latter has been obtained considering only the main lobe of spectrum in Fig. 8.1. The antenna directivity is: $dir \approx 60\%$, defined as:

$$dir \equiv \frac{P_+}{P_+ + P_-} \qquad (8.1)$$

where P_+ and P_- indicate, respectively, the wave power fraction travelling in the co- and counter plasma current directions. The co-current driven by minor lobe at high $n_{//}$ does not have been included. The LHCD efficiency, defined as:

$$\eta = R_0 n_{e\_av} \frac{I_{CD}}{P_{abs}} \left(\frac{Ampere}{Watt \times m^2} k \right) \qquad (8.2)$$

is: $\eta_{LHCD} \approx 0.3 \mathrm{AW}^{-1} m^{-2}$. In eq. 8.2, R_0 is the major plasma radius, n_{e_av} is the line-averaged central plasma density, I_{CD} is the total current driven by the RF power and P_{abs} is the absorbed RF power.

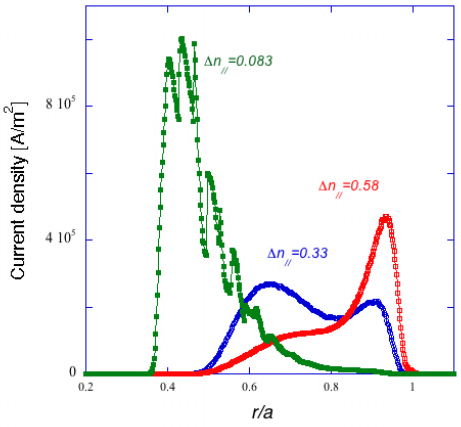

Figure 8.4. j_{LH} profiles obtained respectively using the narrow (green curve), intermediate (blue curve), and broad (red curve) main lobe of antenna spectra of Fig. 1. Toroidal magnetic field: B_T=6.8 T, plasma current: I_P= 18 MA, operating LH wave frequency: 5GHz, absorbed RF power: 80 MW, antenna directivity: 60%. The electron density and temperature profiles of Fig. 2 have been considered, relevant to the DEMO "peaked" density profile case (I_P = 18 MA).

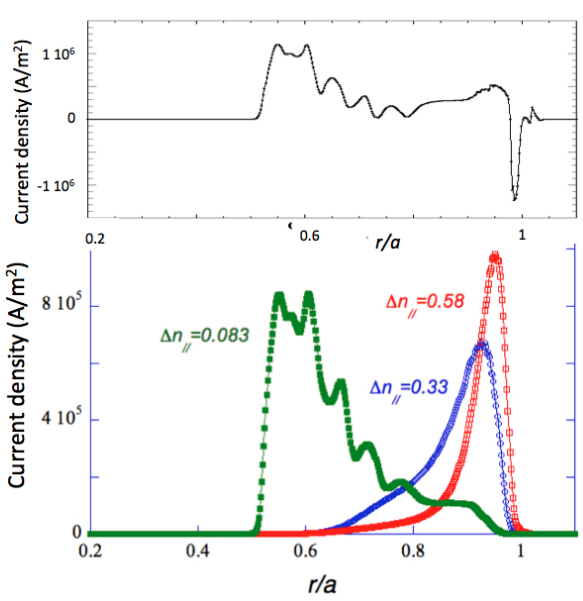

Figure 8.5. Bottom: j_{LH} profiles modeled, for the case of DEMO "flat" case of Figure 3, using the antenna spectra of Fig. 1. Top: j_{LH} profile obtained including, for the case of narrower lobe of Fig. 1, the effect of the minor lobes present at negative and positive $n_{//}$ of the launched antenna spectrum.

QL physics plays a beneficial key role in enabling the LHCD effect at high T_e of reactor plasmas. Indeed, by retaining only the limit of linear wave physics, i.e. the only ELD effect produced by a monochromatic LH power spectrum (concentrated at $n_{//}=n_{//0}$), the main peak of j_{LH} noticeably dislocates at outer radii ($r/a \approx$

0.94) with respect to the QL case ($r/a \approx 0.55$ using $\Delta n_{//} \approx 0.083$).

We have finally considered the case of ITER in steady-state scenario (B_T =4.83T, I_P = 9MA the kinetic profiles are displayed in Fig. 8.3) [60], and same antenna design of Ref. [58] (with P_{LH} =24 MW, $n_{0//}$ =2). Consequently, the driven total current is of about 1MA and, importantly, keeping fixed the antenna spectrum with $n_{0//}$ =2 and setting the antenna spectrum with $\Delta n_{//}$ in a suitable range (from $\Delta n_{//}$= 0.083 to $\Delta n_{//}$= 0.50, as enabled by hardware), the j_{LH} peak can usefully span in the outer radial half of plasma (respectively, from $r/a \approx 0.55$, where $T_e \approx$14keV, to $r/a \approx 0.64$, where $T_e \approx$8keV). This corresponds to markedly increase (up to~15%) the j_{LH} tailoring flexibility obtained by previous work (<4%) [60]. Acting also on the $n_{0//}$ parameter, the flexibility is further increased (the layer $r/a \approx 0.80$, where $T_e \approx$3keV, is reached using $n_{0//}$ =3.2, and $\Delta n_{//} \approx 0.15$).

Test of limit validity of QL theory (schematised in Figure 8.2) has been performed considering the worst case corresponding to the narrowest main lobe ($\Delta n_{//} \approx 0.083$) of Figure 8.1. The phase velocity width is found (~0.17c) much larger than the trapping velocity width (~0.002c, for $p_{RF} \approx 30$ MW/m^2). The realistic values of the minimum and maximum phase velocities of the propagating wave spectrum, capable of altering the equilibrium EDF, have been calculated near the absorption radial layer ($r/a \approx 0.5$), via ray-tracing and Fokker Planck analyses [12,34]. A wave electric field with intensity (0.2 kV/cm) conspicuous larger than that (0.05 kV/cm) expected to occur at this layer has been considered, with the aim of overestimating the trapping velocity width and checking the QL theory validity with larger margin.

About uncertainties of obtained results, a change of 10% of T_e profile produces change of about the same amount in the radial LH current profile. The precision in electronically setting the antenna parameters, $\Delta n_{//}$ and $n_{0//}$, is very good (~1%), which makes fully viable the present method.

8.3.2 Summary of the numerical code for calculating the LHCD profile

The LH^{star} code, used for the numerical simulations, consists of two computation sub-tools: *i*) the LHPI (lower hybrid parametric instability) module that is based on first principles of non-linear physics of plasma edge and calculates the PI-produced spectral broadening of the launched antenna spectrum, *ii*) the RAY^{star} module that utilises such initial spectrum and performs the ray-tracing in toroidal geometry and calculates, at any radial layer of wave propagation in the plasma and for any $n_{//}$ spectral component, the effects of wave propagation in toroidal geometry that can further broaden and upshift the LH wave spectrum. The ray-tracing analysis consists in solving the equation system for the position and wave vector allowing the reconstruction of the wave-phase and the power damping rate along the trajectory. Ray-tracing is performed in the framework of the geometric limit approximation, which holds for LH waves propagating far from the cut-off layers located at the plasma edge. This condition is fully satisfied for high electron temperature reactor plasmas, since the LH wave power coupled by the antenna is completely absorbed in the plasma bulk at the first radial pass, due to strong electron Landau damping. Moreover, at each radial step, the quasi-linear diffusion coefficient is evaluated, the 2-D Fokker-Planck relativistic equation for the electron distribution function is solved in velocity space, and the quasilinear damping is taken into account in the LH wave power equation. On this basis, at each radial step, the RF power density and LH-wave-driven current density radial profiles are determined.

8.4 Parasitic mechanisms for RF power penetration

In order to fully exploit the capability of the LHCD tool of shaping the plasma current density profile, it is

necessary to take into account phenomena that can potentially alter the $n_{//}$ power spectrum launched by the antenna and, consequently, the j_{LH} profile.

Modelling data showed that such an effect occurred at the plasma edge in experiments performed at high plasma densities even at the radial periphery of the plasma column as required for ITER ($n_{e0} \gtrsim 0.8\times10^{20}$ m^{-3}, $n_{e0.8} \gtrsim 0.7\times10^{20}$ m^{-3}), which showed tendency of the coupled RF power of not penetrating into the core. Indeed, in conditions of low electron temperatures generally occurring at the plasma periphery in standard high-density plasma regimes, parametric instability (PI) was expected to strongly broaden the launched $n_{//}$ spectrum. As summarised in Chapter 7, following the guidelines of these predictions, FTU experiments performed with higher temperature at large radii allowed sufficiently reducing the undesired PI effect. As described in Chapter 5, the PI mechanism consists in the building-up of a mutual transfer of energy and momentum from the low frequencies of density fluctuations of thermal background to the high frequencies of perturbations produced by the launched RF power. When a certain threshold in RF power density is exceeded, the low frequency mode that drives the instability produces the growth from the noise level of LH sideband waves, not present in the launched antenna spectrum, having larger $n_{//}$ values.

Further mechanisms were also invoked as possible causes of the parasitic RF power damping at the plasma edge, namely, the linear wave scattering (LS) [32], caused by the density fluctuations of the thermal background of plasma that give rise to angular deviation of the wavevector, and the collisional absorption effect [14] that becomes larger in the presence of lower plasma temperatures. In regard to the latter effect, it was found that, in reactor relevant condition of strong RF power damping per single radial pass, across the plasma column, this could not represent the main responsible of the observed strong RF power absorption at the edge. Consequently, we do not further consider this phenomenon. In regard to the LS mechanism, signatures were observed during experiments, however in concomitance of LHCD effect observed in FTU at reactor relevant, high plasma densities [24]. Consequently, LS would not be considered too ruinous in experiments performed so far. We will however take into account this effect, owing to reactor need of operating with sufficiently narrow antenna spectrum (as shown in the previous Section). Therefore, we will focus hereafter on the effects of PI and LS in possibly modifying the launched $n_{//}$ spectrum.

In order to evaluate the impact of PI in reactor plasma conditions, we have calculated the effect produced by such undesired spectral broadening on the j_{LH} profile, in condition of two different T_e radial profiles of scrape-off layer (SOL). The effect of temperature has been assessed assuming that they merge the main plasma profile in two different ways (respectively, by exponential and exponential-square functions), with marked T_e difference (of ~35%) at radii close to the antenna, for a certain radial gap (of ~25 cm) that separates the antenna from the LCMS layer (where $T_e \approx 2$keV). For the considered profiles, regions with relatively low T_e (~20eV–40eV), occur at slightly different radial distances from the antenna (respectively at: d_{ant} ~3 cm and d_{ant} ~7 cm for the exponential and exponential-square cases). The analysis performed using the LHPI numerical code [21] shows that the aforementioned cold plasma region results unstable for PIs driven by ion-sound, evanescent, low frequency modes (**~**1MHz). Consequently, some fraction (p_{PI}) of the RF power coupled by the antenna is redistributed over LH sideband waves (p_{PI}~1% and p_{PI}~10%, respectively, for the exponential and the exponential-square profiles), resulting in a larger spectral broadening for the colder plasma edge case (from $n_{//cut\text{-}off}$~3 to $n_{//cut\text{-}off}$~5). Cases of larger extension of the mentioned cold layer (≳10 cm) would increase the spectral broadening effect at amounts (p_{PI}>>10%) not valuable in the framework of the utilized available tool.

The effect of enabling LH power penetration into hot plasmas by QL physics is much stronger than the contrasting PI effect, since, for the considered case of marked spectral broadening (p_{PI}~10%), we have found that the j_{LH} peak dislocates outside only a little (from $r/a \approx 0.55$ to $r/a \approx 0.60$), with few current

(~10%) driven at large radii ($r/a \gtrsim 0.8$). The high temperature envisaged in reactor also at the plasma periphery enhances *a fortiori* this favourable effect, since results of FTU tokamak showed that the parasitic PI mechanism was usefully reduced even in condition of cooled metallic wall machine, at reactor-relevant high plasma density [24].
Therefore, thanks to the sufficiently high temperatures reasonably expected to occur in reactor even at large radii of the plasma column [59,57], the PI parasitic effect would not prevent the exploitation of the LHCD for actively shaping the current profile.
In regard to the spectral broadening effect produced by the LS mechanism, for the plasma parameters foreseen for DEMO and, in particular, considering a moderate value of toroidal magnetic field (6T), the LS effect, and its impact on the j_{LH} profile, are quite pronounced.
The primary effect of the scattering on the launched spectra is a large broadening in n_{pol}, the wavenumber corresponding to the poloidal direction (i.e., perpendicular to the confinement magnetic field), though not sufficient to produce significant RF power reflection. However, as a consequence of the magnetic shear effects, also a $n_{//}$ spectral broadening (from the nominal value $\Delta n_{//}$=0.08 to about $\Delta n_{//} \approx$ 0.2) is expected to occur at the radial periphery of plasma column. However, this effect can be significantly reduced operating at higher magnetic field, In this condition, magnetic shear effects do not transfer efficiently the broadening in n_{pol} into $n_{//}$. Since this effect is proportional to the nominal peak value of antenna spectrum, $n_{//0}$, the use of smaller values ($n_{//0}$~1.6) would help mitigating the undesired effect of LS mechanism. This is precisely the situation proposed for the fusion reactor ARC (mentioned in Chapter 2), which has safety factor (defined in Sec. 2 of Chapter 2) at the plasma edge of moderate value (q_a=4.7), large toroidal magnetic field (B_0=9.2 T), and the LHCD launcher located in the high field side of the machine.

For successful current profile tailoring utilizing the LHCD tool free from LS-produced spectral broadening effect, operations at high magnetic field and with relatively fast antenna spectrum (i.e., with smaller $n_{//}$ and $n_{//0}$~1.6) are recommended.

8.5 Interpretation of feedback wave-particle mechanism of RF power absorption

We give here a physical interpretation of the mechanism underlying the role of a narrower antenna spectrum in enabling the RF power to be deposited in the outer radial half of hot reactor plasmas. Results of numerical computations of the evolutions of the electron distribution function (EDF) and relevant spectral components of the propagating RF power spectrum, consistent with approximated analytical derivation shown in Sec. 3 of Chapter 4 (see Eqs. 4.16 – 4.21) support the new understanding presented here. The DEMO parameters shown in Figure 8.3 have been considered.
A peculiar feature of the current density profiles shown in Figs. 8.4 and 8.5 consists in the presence of the series of well observable relative maxima and minima in the profiles produced by narrow antenna spectrum (green curves), whilst a more regular trend occurs in cases of larger antenna spectrum (blue and red curves).

We have hypothesized that this behaviour would reflect feedback-like quasilinear mechanism that allows the components of the spectrum with slower phase velocities (i.e., larger $n_{//}$) promoting the absorption of the faster components via EDF distortion owing to QL effect. In order to test this

hypothesis, we have numerically calculated the evolutions, along the wave propagation from the edge to the core, of the EDF and the power $n_{//}$ spectrum, and focused on the respective behaviour at around the radial layer where a maximum of the green curve of Figure 8.3 occur (at $r/a \approx 0.61$). The evolution of EDF is displayed in Figure 8.6, and the respective behaviour of the RF power spectrum propagating in the plasma is shown in Figure 8.7. Similar trends occur at around the other relative maxima of the j_{LH} profile. In particular, in correspondence of a peak of LH wave-driven current density, the EDF plot exhibits (at $r/a \approx 0.61$) a slightly higher plateau (see Eqs. 8.3 – 8.6) with the corner at the right end (i.e., at large electron velocities) that is sharper than in cases of close radial layers (at $r/a \approx 0.55$ and at $r/a \approx 0.67$). Therefore, the j_{LH} peak in exam occurs however in concomitance of a larger density of electrons interacting with waves, especially with faster phase velocities. This behaviour is consistent with the concomitant larger RF power damping rate, Eq. 4.17 of Chapter 4, owing to the exponential function of expression containing the quasi-linear diffusion coefficient integrated on the velocity space in Eq. 4.17.

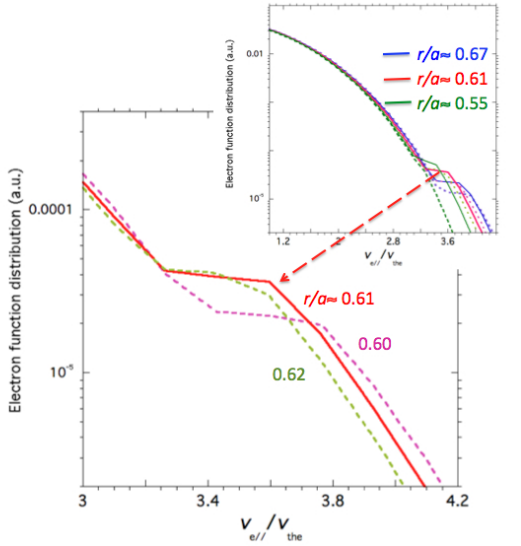

Figure 8.6. Evolution of the electron distribution function (EDF) under the wave electric field as numerically calculated by the Ray-FP module of the LHstar suite of codes [55].

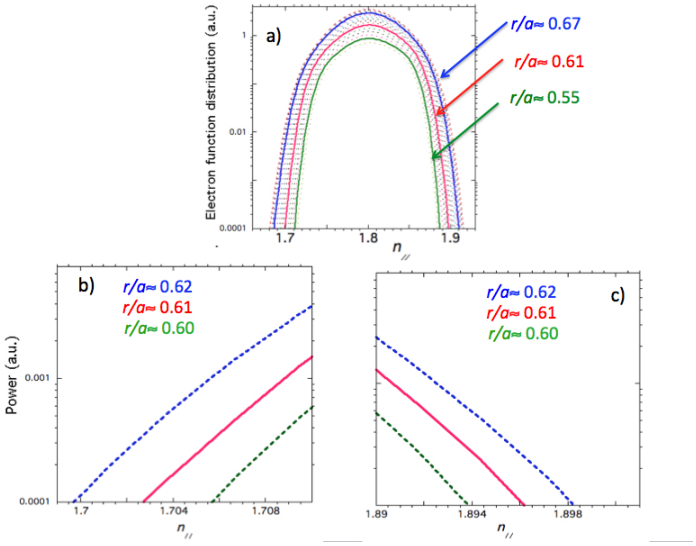

Figure 8.7. a) RF power $n_{//}$ spectrum propagating in the plasma corresponding to same radial layers considered in Fig. 6 ($n_{//}$ is the wave refractive index in direction parallel to the static magnetic field confining the plasma). b) Zoom of box a) for waves with fast phase velocities (low $n_{//}$ range). c) Zoom of box a) for waves with slow phase velocities (high $n_{//}$ range).

Since the plateau of EDF is regulated by the RF power carried by spectral components with larger $k_{// max}$ (see Eq. 4.20), and these components are absorbed quite regularly at the different radial layers, as shown by Figure 8.7c (which zooms the interval with larger $n_{//}$), as soon as these components are absorbed along the propagation path (from colder to warmer plasma layers), the damping of the whole power spectrum begins reducing. A relative maximum of j_{LH} consequently develops. For a same increment (of about 2%) of radial penetration of the RF power towards the plasma core, a fast spectral component (e.g., $n_{//}$= 1.7) erodes the carried RF power (of a factor 20, from 2e-5 to 4e-6) noticeably larger than the relative maximum of j_{LH} profile (of a factor 4, from 4e-6 to 1e-6). At slightly inner radius, owing to locally larger electron temperatures, the same *movie* takes place when new spectral components (with $k_{//} \sim k_{// max}$) begins being involved: the damping rate increases until these component are absorbed, and a new relative maximum of j_{LH} occurs. This mechanism works until the whole spectrum launched by the antenna is fully absorbed.

8.6 Schematisation of the role of the LH spectral width in preventing strong damping at high temperature of reactor plasma

We show here an original scheme of the feedback effect that promotes the damping of the whole spectrum despite of the fact that most of the spectral components are quite far from meeting condition of Landau resonance of electron velocity of the tail of the electron distribution function (EDF) and phase velocities of the launched spectrum.

The mechanism at the basis of the LHCD effect is much more complex than that occurring in resonant heating and CD schemes utilising EC and IC waves. This effect is well described by the quasi-linear (QL) theory (described in chapter 4), capable of taking into account the complex interaction of the launched antenna spectrum with the EDF, which leads far from Maxwellian thermal equilibrium condition.

This aspect is displayed by the key differential equation of the system, numerically solved by the LH^{star} code, relevant to ray-tracing and QL computations:

$$\frac{\partial P_j}{\partial \tau} = -2\Gamma_{QL}\left[f_e\left(\sum_j P_j\right),\ldots\right]P_j \qquad (8.3)$$

Eq. 8.3 is non-linear: the power carried by each LH ray, P_j, is coupled indeed to the power fraction carried by all rays that compose the propagating spectrum. Namely, all components of the spectrum determine the QL diffusion coefficient, consequent to EDF distortion and, in turn, determine the damping of the j^{th} ray, and vice-versa. Therefore, a feedback mechanism regulates the absorption of the propagating LH wave spectrum, by QL wave interaction with the EDF tail. This mechanism, described by available numerical modelling data relevant for DEMO (see Chapter 2), is consistently schematised by the sketch of Fig. 8.8.

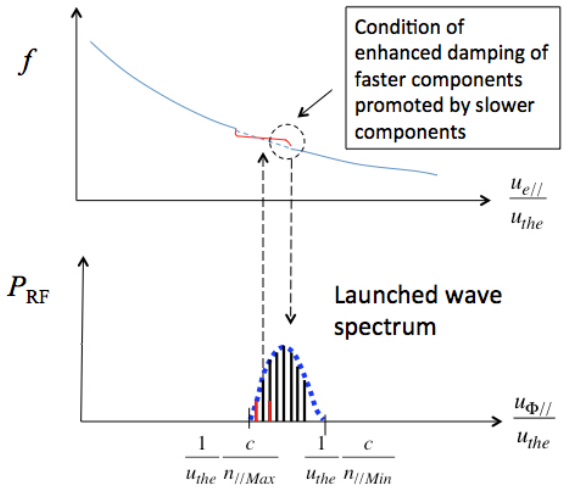

Figure 8.8. Electron distribution function in the vicinity of the particles resonating with components of the spectrum with slower phase velocity.

Propagating from the plasma edge towards the core, spectral components with slower phase velocity interact more strongly, via Landau damping, with colder plasma electrons accordingly with Eq. 8.4:

$$u_{\Phi//} \equiv \frac{\omega_0}{k_{//}} = \frac{c}{n_{//}} \approx 4u_{the} \qquad (8.4)$$

These components flatten the EDF, enhancing the population of fast electrons drifting along the confinement magnetic field and, consequently, promote the damping of the faster components of the

launched spectrum. A similar *movie* is re-proposed at more internal layer with higher T_e, until the coupled LH power spectrum is fully absorbed.
It is reasonable that by using a less broad antenna spectrum, this would activate such QL-damping loop mechanism in a layer with higher electron temperature, so that this spectrum would be absorbed at inner radial layer, for given electron temperature profile of reactor.

This picture of the lower hybrid current drive effect is consistent with the interplay of LH spectrum width and QL effect, which follows analytical derivation in Sec.3 of Chapter 4 and numerical results reported in Sec. 2 and 4 of this chapter.

Chapter 9

9 Assessment of the main antenna parameters for current profile control in thermonuclear reactors

This chapter gives a summary of results contained in a journal paper in preparation, Ref. 62 (L. Amicucci et al, to be submitted to Nuclear Fusion), useful for addressing the design of antennas suitable for driving current in thermonuclear reactor plasmas.

We consider the case of DEMO, the future reactor plant (see Chapter 2). In this condition, previous understanding has considered impossible producing current drive, as a consequence of too high temperatures envisaged even at the radial periphery of plasma column.

Conversely, by new method described in Chapter 8, this obstacle should be overcome by means of a proper antenna spectrum with reduced width in wave refractive index (in the direction parallel to the magnetic field that traps the plasma), as described in this chapter. The large dimensions of access ports of a reactor allow satisfying this desired condition of narrow antenna spectrum. Apart this crucial, new aspect, the remaining RF power system remains the same that was proposed for LHCD on ITER (International Thermonuclear Experiment Reactor), as described in Ref [58].

On the basis of numerical calculations, we show how to produce a RF power spectrum in wave refractive index suitable for setting a deposition profile of current density at a desired radial layer of the plasma column. These results are fundamental for solving the problem of how to predict the current control system that a thermonuclear reactor mandatorily requires (see Chapter 3). We present also original numerical results, produced by the Grill 3D code, useful for characterising the power reflection coefficient for different values of plasma density at the antenna mouth, as necessary for completing the assessment of the new antenna design. The utilised code has the special feature of retaining the effect of the angle that tilts the orientation of the static magnetic field and the waveguide array orientation owing to contribution of the plasma current (not only of the magnet). This allows obtaining the antenna spectra in more realistic conditions of operations.

The obtained results back the conclusion that current can be actively driven at a desired radial layer of the reactor plasma column by suitably feeding the phased array of waveguides.

9.1 The concept of waveguide array antenna for lower hybrid current drive (LHCD)

In order to couple power to the natural mode of plasma consisting in the lower hybrid (LH) wave, the following conditions should be satisfied, given the solution of the wave equation holding for magnetised, cold plasma as shown in Chapter 4.

Cut-off condition. LH waves cease of being evanescent and propagate for sufficiently high plasma densities given by the condition: $\omega_{pe} > \omega_0$ where $\omega_{pe} = \sqrt{\frac{4\pi n_e e^2}{m_e}}$ is the electron plasma frequency, ω_0 is the operating angular frequency and n_e is the plasma density.

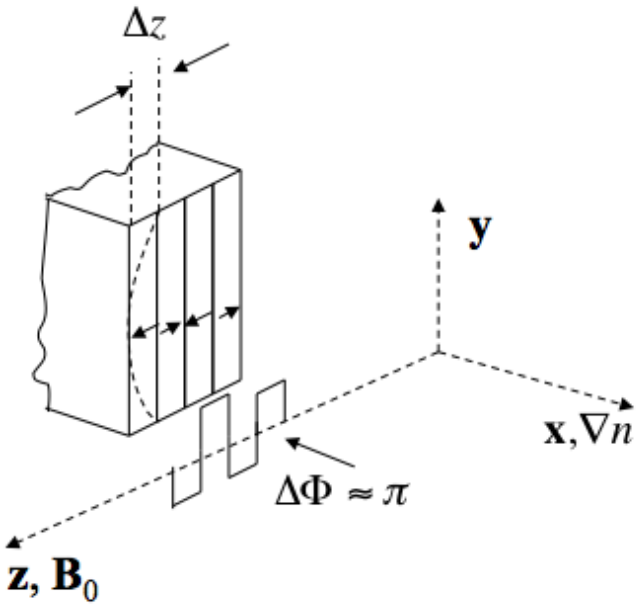

Figure 9.1. Sketch of the waveguide antenna at the plasma interface

Polarisation condition. For very high plasma densities, $\omega_{pe} >> \omega_0$, LH waves have the electric field almost fully aligned to the *x* direction of plasma gradients, see Figure 9.1 that represents the plasma in slab geometry. Conversely, for density close to cut-off condition, $\omega_{pe} \approx \omega_0$, the wave electric field is almost aligned to the z direction, $E_{rf} \sim E_z$, of the static magnetic field utilised for trapping the plasma. This condition can be satisfied by the polarisation of the fundamental TE_{10} mode of a rectangular waveguide. For plasma densities a few times higher than the cut-off density, LH waves behave as almost fully electrostatic plasma modes, i.e., have the electric field quasi aligned to the wavevector.

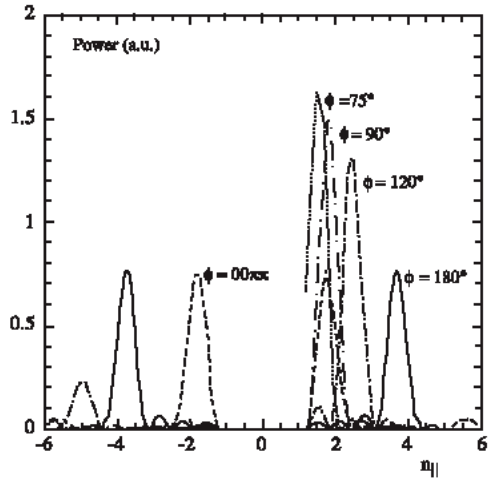

Figure 9.2. Antenna power spectra for different phasing conditions of waveguides numerically calculated by solving the wave equation

Slow wave condition. LH waves are plasma modes having phase velocity smaller than the light speed: $\frac{\omega_0}{k} \equiv u_\Phi < c$. In the direction of the static magnetic field, along which the electron can be freely accelerated by the wave electric field, slow wave condition can be written considering the wave refraction index: $\frac{c}{u_{\Phi//}} \equiv n_{//} > 1$.

The aforementioned conditions can be all met by a phased array of rectangular waveguides positioned at the plasma edge, where the density slightly exceeds the cut-off condition, see Figure 9.1. In particular, fortunately, the waveguides should be oriented in way suitable for fitting the gap available between the coils of the tokamak's magnet. For a frequency of 5 GHz the density should be of the order of 10^{18} m^{-3}, as in the tokamak

plasma experiments. The slow wave condition is produced by suitably phasing the waveguides in order to
form a periodic structure capable of tailoring the wavevector, as roughly shown by: $n_{//} \equiv \frac{c}{v_{\Phi//}} \approx \frac{c}{\omega}\frac{\Delta\Phi}{\Delta z} > 1$.

Numerically computation is necessary for calculating the $n_{//}$ antenna spectrum by properly solving the wave equation. An example of solution is shown in Figure 9.2, and the picture of the waveguide antenna of the Frascati Tokamak Upgrade (FTU) experiment is shown in Figure 9.3.

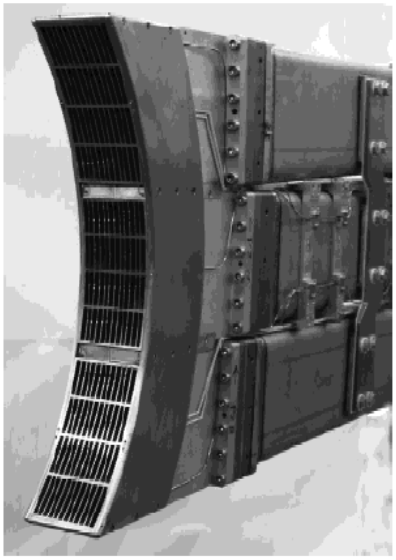

Figure 9.3. Picture of the FTU (Frascati Tokamak Upgrade) launcher of 1MW power at the frequency of 8 GHz for lower hybrid current drive

9.2 Launcher for LHCD in a thermonuclear reactor

We focus on the assessment of the principal parameters of antenna that original results of Chapter 8 have identified as essential for solving the crucial problem of how to enable non-inductively driving plasma current in a future thermonuclear fusion power station.

Before considering this important problem, we give a summary of the RF power system proposed for LHCD on ITER, described in Ref. 58.

The launcher is sketched in Figure 9.4, and a summary of the RF power system is given hereafter.

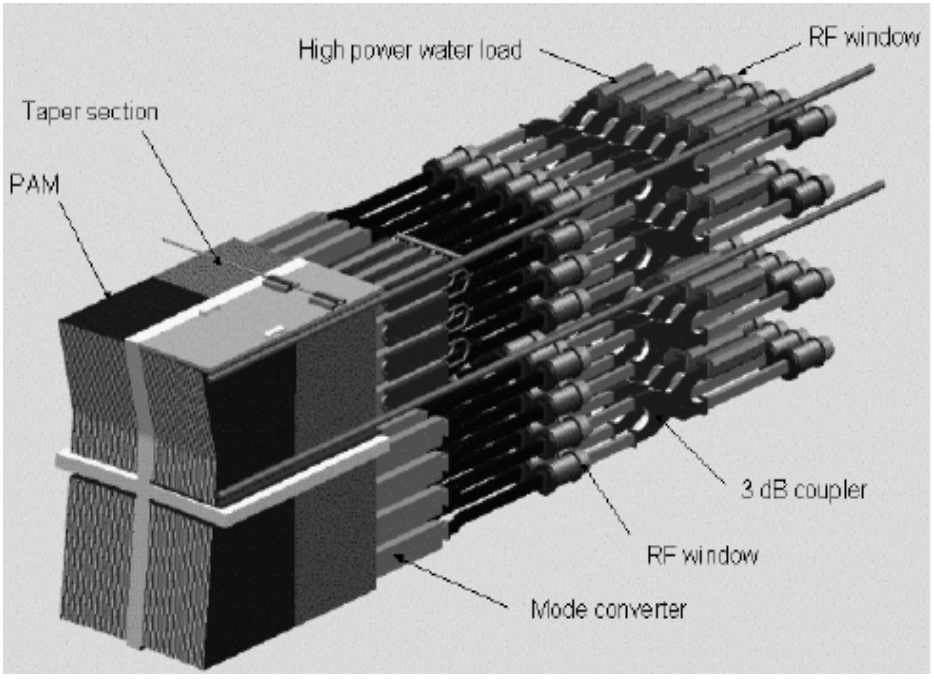

Figure 9.4. Picture of the launcher proposed for ITER. The antenna would couple 24 MW power at the frequency of 5 GHz for lower hybrid current drive.

The transmitter is composed of 24 CW klystrons of one MW. No circulators are used to protect the klystron from the reflected power. The protection is performed by hybrid junctions with water loads on their equilibrium port installed in the transmission line. High Voltage DC supplies power clusters of four tubes. The RF driver is based on 5 GHz components: solid state source, amplifier, attenuator, phase shifter and phase and amplitude loop. Each klystron is connected to the launcher by a 60 meters long oversized circular transmission line that includes: straight parts, mode converters, 90 degrees bends and mode filters, see Figure 9.5.

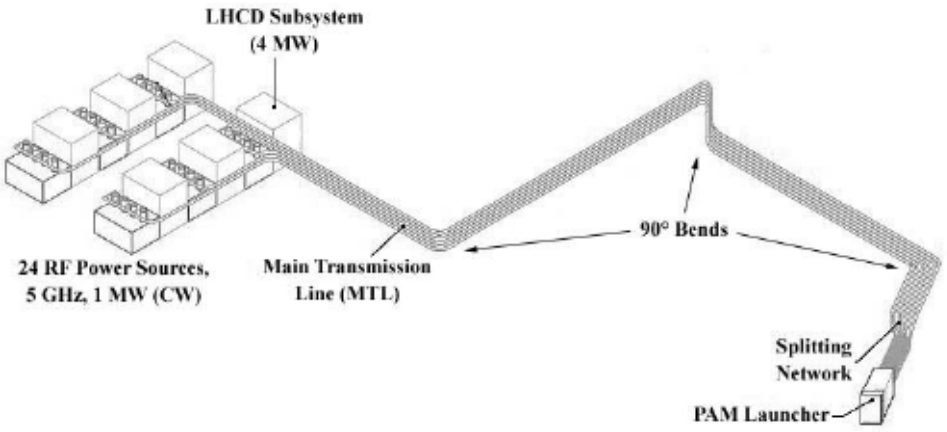

Figure 9.5. Overall view of the LH system for ITER

The klystron output T_{10} mode in WR229 (58.17 mm x 29.08 mm) rectangular wave guide is converted to the TE^{O}_{01} cylindrical mode via an adiabatic TE10 to TE^{O}_{11} mode converter and a TE^{O}_{11} to TEO01 snake like mode converter.

The expected power conversion efficiencies are respectively 99.9 % on a 100 MHz bandwidth for the first one and 99.5 % on a 32 MHz bandwidth for the second. The choice of the circular waveguide diameter (~120mm) is a compromise between the RF losses reduction (less than 5% in the straight lines) and avoiding the TE^{O}_{02} propagation.

The antenna is based upon the PAM (Passive Active Multi-junction) concept, which relies on passive wave guides wedged between active ones. Very efficient water cooling is set in the back of the quarter wavelength passive wave guides to remove the heat from plasma radiation, neutron damping and RF losses. The main RF components of the launcher are the RF windows, the rectangular TE_1 to TE_{30} mode converters and the bi-junction. In the present design, the antenna is made of 4 blocks. For each block, 3 x 2 RF windows are set on the secondary vacuum flange. The power is then divided in two using hybrid junctions. They are linked to 3 x 4 RF windows. Each of them feeds a TE_{10} to TE_{30} mode converter used to vertically divide the power by 3. On the three output waveguides are inserted 8 secondary output E plane 270 degrees multi-junctions. This leads to 12 horizontal rows of 24 active and 25 passive waveguides each. The active waveguide sizes are 58 x 9.25 mm^2. The periodicity between active waveguides is 22.5 mm.

The estimated activation produced by neutrons from fusion reactions on the antenna structures is represented in Figure 9.6.

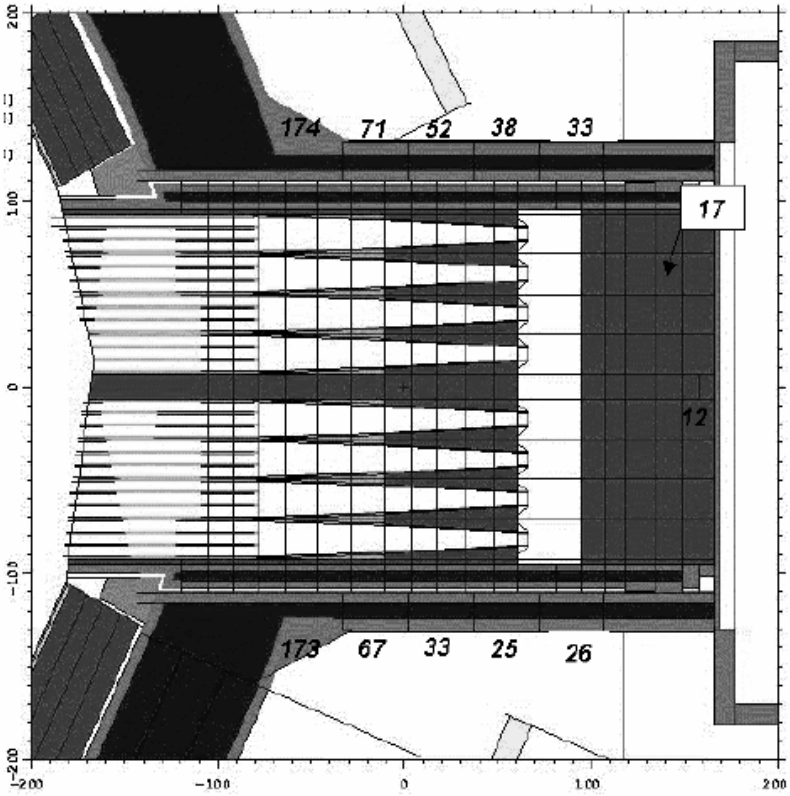

Figure 9.6. Dose rate (μS/h) in the launcher equatorial plane

9.2.2 Antenna geometry for DEMO

Following original results of Ref [56] (A. Cardinali, R. Cesario, L. Amicucci, et al., "Active current drive for thermonuclear fusion reactor", to be submitted on Science), on the basis of numerical calculations, we show how to produce a RF power spectrum in wave refractive index suitable for determining a deposition profile of current density at a desired radial layer of the plasma column, as required by a thermonuclear reactors (see Chapter 3). Moreover, we show original numerical results useful for completing the assessment of the new antenna design.

We consider an antenna consisting of the same modules proposed for LHCD launched for ITER [58].

For the relevant case of DEMO considered here, we have assumed a larger antenna-plasma interface (namely, with dimensions of about 1.2 m in toroidal direction, and 2.2 m in the perpendicular direction). The launcher should be capable of coupling to plasma a strong RF power (P_{LH} = 80 MW) at a frequency of 5 GHz: the frequency is the same of that proposed for ITER, whilst the power is about three times higher for satisfying the need of driving current in the larger plasma volume of DEMO.

These conditions guarantee safe operations since they correspond to power density (p_{RF}≈30 MW/m^2) of about half of the limit (~60 MW/m^2) expected from experiments at this frequency [16]. The antenna type is a passive/active multi-junction (PAM) waveguide array [58], consisting of two piles of (38) rows, placed side by side, and suitably fed for setting the desired $n_{0//}$ and $\Delta n_{//}$ parameters. Each row (large 615.5 mm) is aligned to the toroidal direction, and consists of (24) active waveguides and (25) passive waveguides (i.e. the latter are not fed).

We give hereafter details useful for producing the desired parameters of antenna.

The antenna consists in modules of rows combined along the toroidal and poloidal direction (the latter is perpendicular to the toroidal one). A single row (aligned to the toroidal direction) is formed by 24 couples of active-passive waveguides, and an additional passive waveguide is placed at the beginning of the row in order to have passive waveguides at both the ends. Therefore, there are 24 active waveguides and 25 passive waveguides in this row. The peak value $n_{0//}$ =1.8 of the spectra in Figure 9.7, described in the next subsection, has been obtained considering a single row using waveguide width of a=9.5 mm, height 58 mm, wall thickness 3 mm, and phase shift between active waveguides of 90 degrees. The size of the row is of 615.5 mm.

The full antenna size in the toroidal direction is 1215.5 mm. By feeding together identical modules piled along the poloidal direction, the spectrum does not change but the coupled power increases.

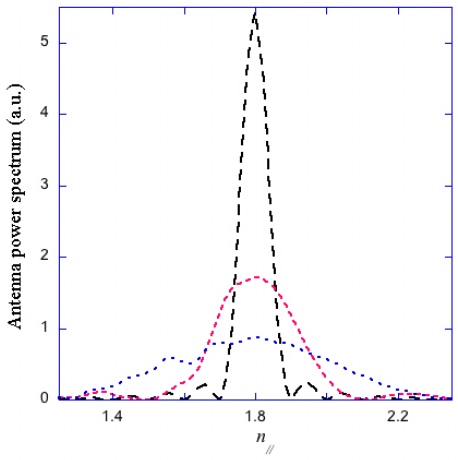

Fig. 9.7 Main lobe of the antenna spectra obtained by a passive-active multi-junction (PAM) waveguide antenna, with modules phased for launching spectra with same $n_{//}$ peak but with three different widths, respectively, $\Delta n_{//}$=0.085 (black curve), $\Delta n_{//}$=0.33 (red curve) and $\Delta n_{//}$=0.58 (blue curve). Minor lobes occurring in the full spectral range do not have displayed (see the text).

A coupled power of 80 MW can be coupled by an antenna consisting in a module pile of 37 rows, which would handle a power density of less than 30 MW/m^2, suitable for safe routine operations far from breakdown limit (which is of about 70 MW/m^2 at 5 GHz) met in experiments that used LH wave power coupled to tokamak plasmas in the last thirty years [16]. The reflected power, back to RF generator, can be kept low, under a quite large variation of the plasma edge density occurring during operations, by using a passive-active multi-junction (PAM) antenna with one or more bi-junction planes [58].

9.2.3 Numerical results of main antenna spectra

The antenna spectrum has been calculated by the Grill-3D numerical code [63]. This is a universal tool for simulation of waveguide antennas in 3D geometry, capable of considering also very complicated structures.

Consequently, Figure 9.7 shows the main lobe of two antenna power spectra having the same $n_{0//}$ (=1.8) value. The latter has been chosen for satisfying the LH wave accessibility condition for the considered dense plasma density profile. The obtained three different widths ($\Delta n_{//}\cong$0.083, $\Delta n_{//}\cong$0.33 and $\Delta n_{//}\cong$0.58), respectively, have been considered for modelling. Actually, the whole antenna spectrum, corresponding to case of narrow main lobe, exhibits well-separated secondary peaks (at $n_{//} \approx$ -3.2, -6, -8, and $n_{//} \approx$ +6.5: positive/negative values correspond to LH waves travelling in the co/counter sense of plasma current). The resulting net CD takes into account the antenna directivity ($dir \equiv P_+\left[P_+ + P_-\right]$, where P_+ and P_- indicate, respectively, the wave power fraction travelling in the co- and counter plasma current direction).

The possibility of producing different LH wave-driven current density radial profiles, necessary for active current profile control in a reactor plasma, relies on the capability of the antenna of launching RF power with different spectra. In order to produce a more off-axis current drive, the peak of the RF power

spectrum ($n_{0//}$) and its width ($\Delta n_{//}$) should be increased. Consequently, for given antenna geometry, the $n_{0//}$ and $\Delta n_{//}$ parameters can be set by properly feeding the waveguides and choosing the relative phasing. More specifically, the $n_{//}$ peak value can be changed using different waveguide width that, increased at a=12 mm, would produce a spectrum with lower peak, $n_{0//}$≈1.5, and, reduced at a=8.25 mm, produces a spectrum with a higher peak, $n_{0//}$≈2.0. Furthermore, with the waveguide width of a=9.5 mm, the $n_{0//}$ value should be increased by using lower phasing value for active waveguides. For instance, $n_{0//}$ increases to 1.96 for phasing of 65 degrees, and to $n_{0//}$ =2.1 for 45 degrees. It is necessary to design a suitable antenna structure that allows this phasing.

The spectral width is minimised (at $\Delta n_{//}$≈0.07) by setting the phase of 90 degrees between adjacent active waveguides. The two spectra of Fig. 9.7 with small and large width ($\Delta n_{//}$ =0.083 and $\Delta n_{//}$ =0.58) have been obtained by changing the number of fed modules.

9.2.4 Further numerical results for assessing the antenna behaviour

Considering the antenna geometry proposed for DEMO reactor described in Sec. 2.1, we show here further parameters that complete the assessment of the antenna behaviour in different condition of plasma density at the antenna mouth, necessary for optimising the antenna-plasma coupling, and different widths of waveguides that allow modifying the launched power spectrum in refractive index, $n_{//}$.

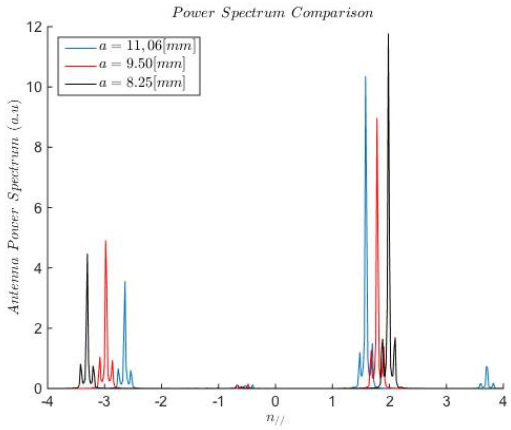

Figure 9.8b. Comparison of antenna patterns for positive and negative values of $n_{//}$ for same parameters of Fig. 9.8a.

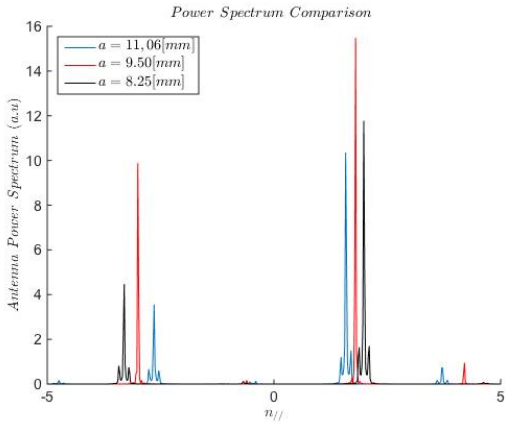

Figure 9.8c. Antenna spectra obtained with same parameters as in in Figure 9b but without including the effect of the angle tilting the static magnetic field with respect to the waveguide orientation.

This study allows completing the conceptual design of the RF power system of a thermonuclear reactor, which has been enabled by the new discovery of the key role of the spectral $n_{//}$ width of the launched RF power, as described in Chapter 8.

9.2.5 Power spectra and waveguide phasing

The assessment of the antenna spectra has been performed by further numerical results of the Grill 3D code shown in Figure 9.8 considering a phasing between active waveguides of 90 degrees.

Figure 9.8a displays the power spectrum coupled to the plasma versus the parallel refractive index, for different values of the waveguide width, *a*. Figure 9.8b extends the analysis to negative values of $n_{//}$, evidencing the capability of these antenna settings of producing a net current in the plasma in the same sense of the static magnetic field necessary for trapping the plasma.

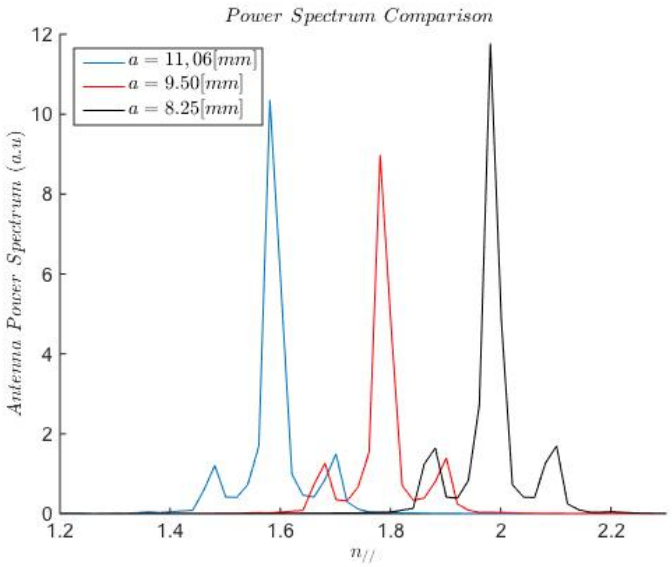

Figure 9.8a. Power spectra launched by the antenna for positive values of $n_{//}$ (which is the refractive index in direction parallel to the static magnetic field confining the plasma). Waveguide phasing: 90 degrees.

The effect on the antenna spectrum of the tilt angle occurring between the grill orientation and the effective direction of the static magnetic filed, calculated retaining the contribution of the plasma current (i.e., not only that produced by the magnet), can be assessed by comparing Fig. 9.8b and Fig. 9.8c. The latter refers to case approximating the tilt angle equal to zero. Consequently, for the relevant case of $n_{//\_peak}$=1.8 (utilised in Chapter 8 for modelling the RF power depositions in reactor), in the more realistic case of non-zero tilt angle, the spectral components of the launched power in the co-plasma current direction exceed more markedly those in the counter direction.

9.2.6 Different phasing between active waveguides.

Figure 9.9 displays the $n_{//}$ spectra in case of angle of 45 degrees between active waveguides and Figure 9.10 the spectra of case of 180 degrees. The latter spectra are not useful for current drive, but only for plasma heating, as similar amounts of the co- and counter plasma current would be produced by the coupled RF power, resulting in an overall negligible effect.

9.2.7 Power reflection coefficient

The capability of the antenna of coupling power for different plasma densities occurring at the antenna mouth has been tested by numerical results of the Grill 3D code summarised in Figure 9.11, which shows the power reflection coefficient of antenna plotted versus the plasma density at the antenna mouth, considering as parameter the peak of $n_{//}$ displayed in Figure 9.8 and same waveguide phasing of 90 degrees. Optimum behaviour for any $n_{//}$ peak value (which is important for operations with plasma) occurs for sufficiently high values of density at the antenna-plasma interface ($\gtrsim 5 \times 10^{17}$ m^{-3}), see Fig. 9.11a, consistently with theory of lower hybrid plasma waves exposed in Chapter 4. The optimum window of plasma density values which gives lower reflection coefficient is magnified in Figure 9.11b.

Figure 9.12 and 9.13 report the power reflection coefficient for phasing between active waveguides of 45 degrees and 180 degrees, respectively.

In summary, the main antenna parameters have been assessed by original numerical computations, showing that the power reflection coefficient is sufficiently low (≲20%) for ensuring safe operations of launched spectra with peak values in the range $n_{//} \approx$ 1.8–2.0, relevant for current drive in condition of fully accessible LH waves into the plasma interior without suffering mode conversion with the fast wave branch, see Chapter 4.

The presented results help addressing the design of the control system of reactor's current profile based on current drive by lower hybrid plasma waves.

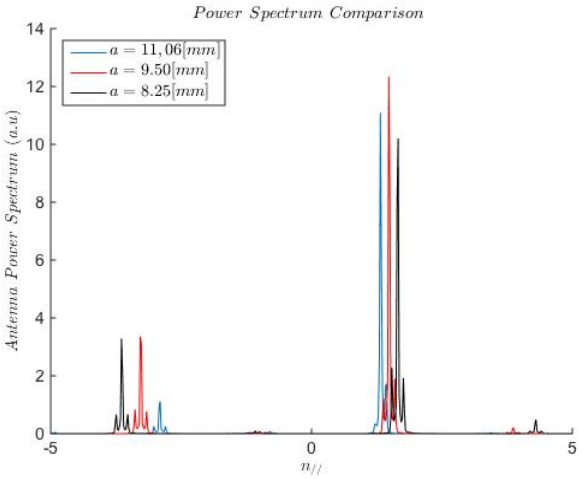

Figure 9.9. Antenna power spectra modelled considering a waveguide phasing of 45 degrees.

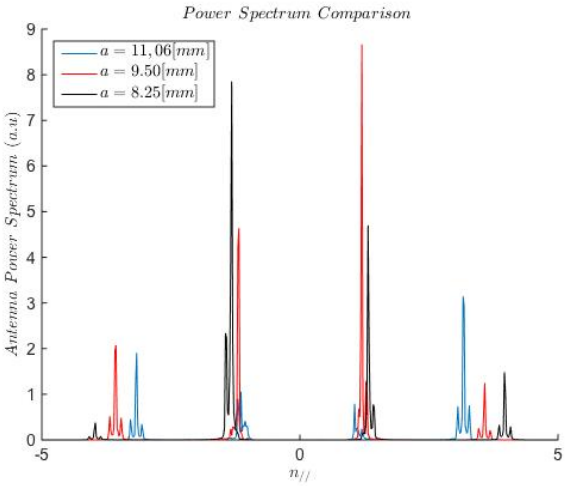

Figure 9.10. Antenna power spectra modelled considering a waveguide phasing of 180 degrees.

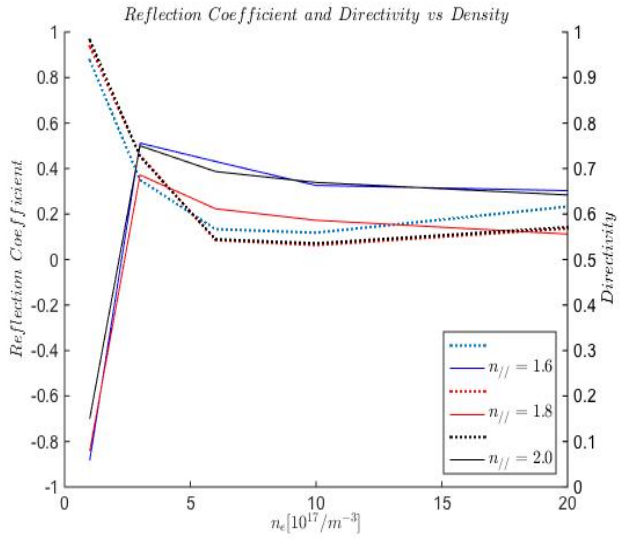

Figure 9.11a. Power reflection coefficient of antenna plotted versus the plasma density at the antenna mouth, considering the peak of $n_{//}$ as parameter. Waveguide phasing: 90 degrees.

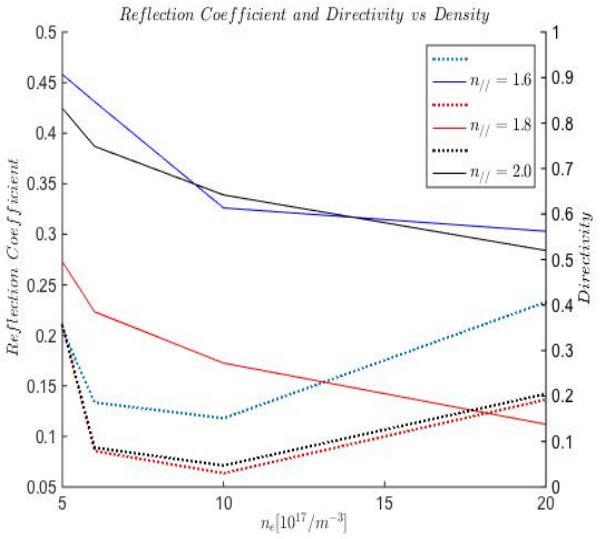

Figure 9.11b. Zoom of Fig. 9.11a evidencing conditions for optimum antenna coupling, which occur for $n_{//}$ values of 1.7–1.9.

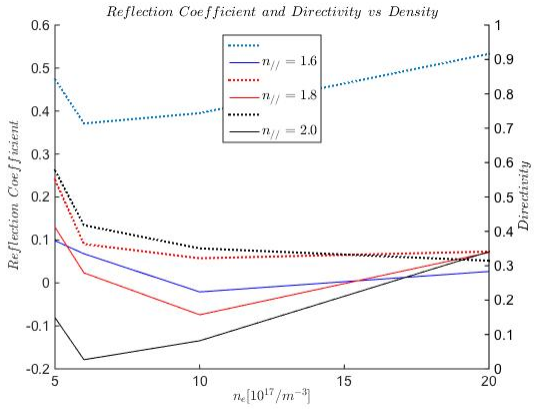

Figure 9.12. Power reflection coefficient of antenna plotted versus the plasma density at the antenna mouth, considering the peak of $n_{//}$ as parameter. Waveguide phasing: 45 degrees.

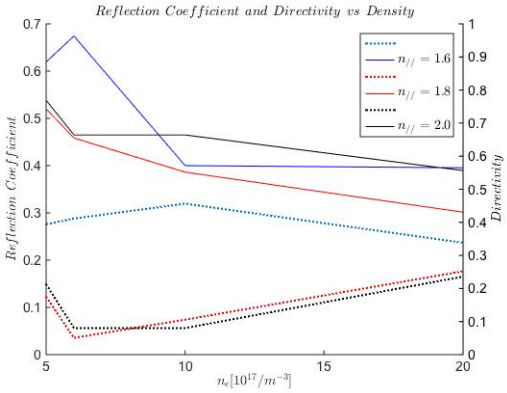

Figure 9.13. Power reflection coefficient of antenna plotted versus the plasma density at the antenna mouth, considering the peak of $n_{//}$ as parameter. Waveguide phasing: 180 degrees.

Chapter 10

10 Conclusions

The Thesis considers the major conceptual problem of research of energy by thermonuclear fusion, consisting in how to drive steady-state current at outer radii of the tokamak plasma column. This is necessary for matching the natural bootstrap current profile, spontaneously originated by radial profile of plasma pressure. Consequently, the current density should be properly imposed in the plasma column in order to ensure the fusion gain developing in the context of stability. Importantly, this fundamental condition would be reached and maintained by exploitation of the "*free meal*" represented by the bootstrap current, which consequently enables an affordably economic development of reactor.

The principal drawback of the existing tools proposed for driving current in ITER, the international fusion experiment, now in construction phase, is the incapability of efficiently and flexibly driving current at large radii, precisely where bootstrap profile would require being supported. This could consequently jeopardise the development of a reactor.

Solution of this problem has been found by new modelling results that enable reconsidering the use of the lower hybrid current drive. The possibility of exploiting this effect, well known for decades, has faced so far with impossibility, predicted by previous understanding, of enabling the launched RF power at several gigahertz penetrating into the plasma interior, owing to too high temperature envisaged to occur in a reactor even at large radii of the plasma column.

Importantly, the work produced for this Thesis has helped solution of a major problem of the LHCD concept. As shown by experimental results, the effect of RF power deposition in the plasma intolerably depend too much on variables different from antenna parameters. Non-linear wave-plasma effects at the edge parasitically broaden, indeed, the launched spectrum. The assessed conditions of plasma operations are useful for suppressing such undesired effect. This is essential for implementing the LHCD tool in the current profile control system required by a reactor.

From engineering point of view, the reported results help solution of the problem (existing for decades) of how to enable the antenna parameters in actually determining at a desirable radial layer of plasma the deposition of the coupled RF power. This goal enables the LHCD method to be really exploitable in a reactor.

The results have assessed condition of ineffectiveness of the parasitic effects of plasma edge for case of a reactor. Consequently, it has been removed the problem, expected by previous understanding, of lack of RF penetration into a too hot plasma bulk of reactor.

The novelty consists in a phased array of waveguide antenna capable of launching in the plasma a power spectrum sufficiently narrow in wave refractive index. This goal is facilitated, indeed, by the wide accesses envisaged for the DEMO reactor, which enable to conceive array of phased waveguides having a sufficient extension along the toroidal direction.

The solution of this problem requires a phased array of waveguide antenna that launches in the plasma a power spectrum sufficiently narrow in wave refractive index. As original numerical results have demonstrated, this diminishes the strong power damping to the point of enabling the RF power deposition at any desired layer of the outer radial half of plasma. This condition is possible thanks to tolerable parasitic effect of non-linear wave-plasma interaction of plasma edge, as new modelling results have demonstrated. Modelling relevant to the latter effect has been produced also for interpreting recent experimental results of the EAST tokamak (the major Chinese experiment on nuclear fusion energy).

The main antenna parameters have been assessed by original numerical computations, demonstrating that the current profile control can be based, indeed, on current drive by lower hybrid plasma waves.

References

11 References

1. Freidberg, *Plasma Physics and Fusion Energy*, Cambridge Univ. Press, 2007
2. Hughes, W. L. (2004). Energy 101. Rapid City, South Dakota: Dakota Alpha Press.
3. Rose, D. J. (1986). Learning About Energy. New York: Plenum Press.
4. Tester, J. W., Drake, E. M., Driscoll, M. J., Golay, M. W., and Peters, W. A. (2005).
5. Sustainable Energy. Cambridge, Massachusetts: MIT Press.
6. Reynolds, A. B. (1996). Bluebells and Nuclear Energy. Madison, Wisconsin: Cogito Books.
7. Waltar, A. E. (1995). America the Powerless, Madison, Wisconsin: Cogito Books.
8. Fowler, T. K. (1997). The Fusion Quest. Baltimore: John Hopkins University Press.
9. McCracken, G. and Stott, P. (2005). Fusion, the Energy of the Universe. London: Elsevier Academic Press.
10. Wesson, J. (2004). Tokamaks, third edn. Oxford: Oxford University Press.
11. R. Cesario, L Amicucci et al., Plasma Phys. Contr Fusion 2013. Plasma Phys. Control. Fusion 55 (2013) 045005 (14pp)
12. Fisch, N.J., "Confining a tokamak plasma with RF-driven currents", *Phys. Rev. Letters* **41** (1978) 873-876
13. Bernabei, et al., Phys. Rev. Letters **49**, (1982) 1255-1258
14. N. Fisch, Rev. Mod. Physics, 59, (1987) 175-234S
15. R. Cesario, L. Amicucci, A. Cardinali, C. Castaldo, M. Marinucci, L. Panaccione, F. Santini, O. Tudisco, M. L. Apicella, et al., "*Current drive at density required for thermonuclear reactors"*, Nature Communications, 1 (5) 55, 2010
16. R. Cesario et al. "*Modeling of Lower Hybrid Current Drive in Tokamak Plasmas by including the Spectral Broadening induced by Parametric Instability*", Phys. Rev. Letters, **92** 17 (2004) 175002
17. R. Cesario et al. "*Spectral broadening of lower hybrid waves produced by parametric instability in current drive experiments of tokamak plasmas"*, Nucl. Fusion 46 (2006) 462-476
18. Garcia, J. et al., Analysis of DEMO scenarios with the CRONOS suite of codes. *Nucl. Fusion* 48 075007 (2008)
19. L. Amicucci, et al., "Current drive for stability of thermonuclear plasma reactor" Plasma Phys. Controlled Fusion, 58 (2016) 014042 (8pp)

20. A. Cardinali, C. Castaldo, R. Cesario, L. Amicucci, A. Galli, et al., "Active current drive for thermonuclear fusion reactor", subm. to Physical Reviw Letters

21. Wilson, R, Porkolab, M., et al. RF power systems for plasma heating and current drive, Nuclear Fusion 1988.

22. Stix T. H., 1965, Phys. Rev. Letters **15**, 878 (1965)

23. Diamond, P.H., Itoh, S. and Itoh, K., *Modern Plasma Physics*, Vol.1, Cambridge University Press, 2010.

24. Bonoli, P., Englade, R.C., "Simulation Model for Lower Hybrid Current Drive", *Phys. Fluids* **29** 2937 (1986)

25. Brambilla, M., *Kinetic Theory of Plasma Waves*, Oxford Press, 1999

26. Charles F. F. Karney and Nathaniel J. Fisch, Phys. Fluids, Vol. 22, No. 9, 1979, page 1817

27. C. Gormezano, et al., Nucl. Fusion 25 (1985) 419

28. ITER Physics Expert Group on Energetic Particles, Heating and Current Drive and ITER Physics Basis Editors, *Nucl. Fusion* **39** 2495. doi:10.1088/0029-5515/39/12/306 (1999)

29. R. Cesario, L. Amicucci, C. Castaldo, et al., Spectral broadening of parametric instability in lower hybrid current drive at a high density. *Nucl. Fusion* **54** 043002 (2014)

30. PORKOLAB, M, Phys. Fluids 17, 1432 (1974)

31. LIU, C.S., and TRIPATHI, V.K., "*Parametric Instabilities in a magntized plasma*", *Physics Report*s **24** (1984) 1709

32. R. Cesario et al., "*Parametric instabilities excited by ion-sound and ion-cyclotron quasi-modes during lower hybrid heating of tokamak plasmas*", *Nucl. Fusion* **29** (1989) 1709-1719

33. R. Cesario et al., Nucl. Fusion, **32**, 2127 (1992)

34. R. Cesario et al., at the 15th European Conf. on Controlled Fusion and Plasma Heating, Dubrovnik, May 1988, Edited by J. Heijn Petten, European Physical Society 1988 Vol 12B part III, p 896

35. R. Cesario and V. Pericoli-Ridolfini, Nucl. Fusion, **27**, 435 (1987)

36. J. F. Drake , P. K. Kaw , Y. C. Lee , G. Schmid , C. S. Liu et al., Phys. Fluids 17, 778 (1974)

37. TAKASE, Y. et al., Phys. Fluids 26, 2992 (1983)

38. PAOLETTI, F., Thesis Dissertation: Parametric instabilities of Lower Hybrid waves in magnetised plasmas", Faculty of Mathematics, Physics and Natural Sciences, Department of Physics, University La Sapienza, Rome, February 1989

39. ANDREWS, P.I., and PERKINS, F.W., "*Scattering by lower-hybrid waves by drift-wave density fluctuations: Solutions of the radiative transfer equation*", *Phys Fluids* 26 (1983) 2537-2557

40. CHEN L., R. and L., Berger, Nucl. Fusion **17,** 779 (1977)

41. CARDINALI, A., Recent Research Developments in Plasmas, edited by S. G. Pandalai (Transworld Research Network, Trivandrum, India, 2000), Vol. 1, p. 185.

42. BRIGUGLIO, S., et al., Physics of Fluids B 1 (1989) p. 1449

43. NAPOLI, F., et al., Plasma Phys. Control. Fusion 55 (2013) 095004

44. SUCCI, S., et al., "*Plasma Phys. and Contr. Fusion* **27** (1985) 863-871

45. WALLACE, G.M., et al., "*Lower hybrid current drive at high density in Alcator C-Mod",* Nucl. Fusion 51 (2011) 083032

46. A. A. TUCCILLO, et al., *On the Use of Lower Hybrid Waves at ITER Relevant Density*, in Fusion Energy 2012 (Proc. 24th Int. Conf. San Diego, 2012 http://www.naweb.iaea.org/napc/physics/FEC/FEC2012/index.htm), ITR/P1-09

47. BERTELLI, N., et al., "*The effects of the scattering by edge plasma density fluctuations on lower hybrid wave propagation*", Plasma Phys. Controlled Fusion, **55** 074003 doi:10.1088/0741-3335/55/7/074003

48. PERICOLI-RIDOLFINI, V., et al., Nucl. Fusion 51 (2011) 113023

49. BARBATO, E., Nucl. Fusion 51 (2011) 103032

50. Kirov, K.K., Baranov, Y., Goniche, M., Mailloux, J., Mayoral, M.-L., Ongena, J., et al., "LH Wave Absorption and Current Drive Studies by Application of Modulated. LHCD at JET" Proceedings of the 36th European Phys. Society Conf. on Plasma Physics, Sofia, Bulgaria, 2009

51. Colas, L., Milanesio, D., Faudot, E., Goniche, M. and Loarte, A. "Estimated RF sheath power fluxes on ITER plasma facing components", *Journ. of Nucl. Materials* 390–391 (2009) 959–962

52. GONICHE, M., et al., Nucl. Fusion 53 (2013) 03301

53. Cenacchi, G., A. Taroni, "The JET equilibrium-transport code for free boundary plasmas (JETTO)" Proceedings of the 8th Computational Physics, Computing in Plasma Physics, Eibsee 1986, (EPS 1986), Vol. 10D, 57-60

54. Levinton, F.M., Zarnstorff, M.C., Batha, S.H., Bell, R.E., Budny, R.V., Bush, C., et al., "Improved confinement with reversed magnetic shear in TFTR", *Phys. Rev. Letters* **75** (1995) 4417

55. Cesario, R., Panaccione, L., Botrugno, Cardinali, A., Castaldo, C., Marinucci, M., et al., "Lower hybrid wave produced supra-thermal electrons and fishbone-like instabilities in FTU", *Nucl. Fusion* **49** (2009) 075034

56. Cesario, R, Amicucci, L., et al., *"Plasma edge density and lower hybrid current drive in JET (Joint European Torus)*", Plasma Physics and Controlled Fusion, Volume 53, Issue 8, pp. 085011 (2011)

57. Amicucci, L., et al., "*Parametric instability modelling of radio-frequency probe spectra in lower hybrid current drive experiment on EAST*", to be pub. on Nuclear Fusion

58. B J Ding, M H Li, L Amicucci, et al*., "Higher operating frequency improves LHCD effects", subm. to Physical Rev. Letters*

59. Y. Takase, M. Porkolab, J. J. Schuss, R. L. Watterson, C. L. Fiore, R. E. Slusher, and C. M. Surko: *Observation of parametric instabilities in the lower-hybrid range of frequencies in the high-density tokamak*, , Phys. Fluids 28, 983-994 (1985)

60. M. H. Li et al, Phys. Plasmas 21, 062510 (2014)

61. B. J. Ding et al, Nucl. Fusion 55 093030 (2015)

62. H. Zohm H., et al., On the physics guidelines for a tokamak DEMO. *Nucl. Fusion* **53** 073019 (2013).

63. Bibet P. et al., ITER LHCD plans and design. *Symposium on the Twenty-First IEEE/NPS Fusion Engineering*, Sept. 2005 Knoxville, TN DOI: 10.1109/FUSION.2005.252946 (2005).

64. G. T. Hoang et al, "A lower hybrid current drive system for ITER", Nucl. Fusion 49 (2009) 074001

65. P. T. Bonoli, et al ITPA Meeon Steady-State Operation 8–10 October 2003 General Atomics, San Diego, CA (USA) https://fusion.gat.com/conferences/itpa2003/steady_state/SSEP%20pdf/12_Forest_LHCD.pdf

66. Amicucci, L., et al., "Assessment of antenna design parameters for enabling LHCD in thermonuclear reactors", to be subm. to Nuclear Fusion

67. M.A. Irzak and O.N. Shcherbibin, "Theory of waveguide antennas fro plasma heating and current drive", Nucl. Fusion, Vol. 35, No. 11 (1995), 1341.